



Institut für Werkstoffe und Verfahren der Energietechnik  
IWV 2: Werkstoffstruktur und -eigenschaften

***Assessment of Beryllium as a  
Plasma-Facing Material for Next Step  
Fusion Devices***

*Alessandra Lodato*



# ***Assessment of Beryllium as a Plasma-Facing Material for Next Step Fusion Devices***

*Alessandra Lodato*

**Berichte des Forschungszentrums Jülich ; 3908**

ISSN 0944-2952

Institut für Werkstoffe und Verfahren der Energietechnik

IWV 2: Werkstoffstruktur und -eigenschaften Jül-3908

D 82 (Diss., Aachen, RWTH, 2001)

Zu beziehen durch: Forschungszentrum Jülich GmbH · Zentralbibliothek

52425 Jülich · Bundesrepublik Deutschland

☎ 02461/61-5220 · Telefax: 02461/61-6103 · e-mail: [zb-publikation@fz-juelich.de](mailto:zb-publikation@fz-juelich.de)



# Assessment of beryllium as a plasma-facing material for next step fusion devices

Alessandra Lodato

## Abstract

The selection of the armour materials for the plasma facing components (PFC) was one of the important challenging problems in the design of the International Thermonuclear Experimental Reactor (ITER). The working conditions of the plasma facing materials (PFM) are very complex. During normal operation they are subjected to high cyclic heat fluxes which originate thermal fatigue and simultaneously to high particle fluxes which produce erosion. During off normal operations the PFMs may suffer severe thermal shocks caused by plasma disruptions and by vertical displacement events of the plasma.

Beside carbon material and tungsten, beryllium will play an important role as PFM in ITER. For the construction of PFCs the beryllium tiles have to be attached to a heat sink of copper. Several techniques of joining such as brazing and hot isostatic pressing are under consideration.

During the operation of ITER the PFMs will suffer irradiation with 14 MeV neutrons generated in the fusion process. This irradiation will affect the thermal and mechanical properties of beryllium and beryllium-copper joints. To validate the choice of the reference beryllium grade and Be/Cu joint, there is a need to investigate their behaviour under combined exposure to thermal loading and neutron irradiation. To investigate the materials degradation processes, thermal shock samples from different beryllium grades, actively cooled Be/CuCrZr mock-ups and mechanical test samples have been neutron irradiated in the High Flux Reactor at Petten, The Netherlands.

In the present work the experimental assessment of neutron irradiation effects on Be material has been carried out by performing thermal shock tests on beryllium samples of different grades. The thermal shock behaviour of the different beryllium grades before and after neutron irradiation has been compared.

Furthermore, the experimental verification of neutron damage on Be/Cu joints has been achieved by performing thermal fatigue tests on beryllium-copper mock-ups. The heat removal efficiency and the thermal fatigue behaviour of mock-ups with CuMnSnCe braze and with InCuSil braze before and after neutron irradiation have been compared.

# Bewertung von Beryllium als plasmakompatibles Material für zukünftige Fusionsanlagen

Alessandra Lodato

## Zusammenfassung

Die Auswahl der Materialien für die plasmaaktiven Komponenten war eine der großen Herausforderungen beim Design des Internationalen Thermonuklearen Experimentalreaktors ITER. Die Betriebsbedingungen für diese Komponenten und ihre Materialien sind sehr komplex. Während des Normalbetriebes sind sie hohen zyklischen Wärmeflüssen ausgesetzt, die thermische Ermüdung verursachen. Gleichzeitig erfahren sie hohe Belastungen durch Neutronen- und Ionenflüsse. Während abnormaler Betriebszustände können die Materialien schwere thermische Schocks erleiden, die durch Plasma-Disruptionen und vertikale Plasma-Instabilitäten (VDE) verursacht werden.

Neben Kohlenstoffmaterialien und Wolfram, wird Beryllium eine wichtige Rolle als plasmakompatibles Material für ITER spielen. Zur Reduzierung der Betriebstemperatur müssen die Berylliumziegel mit einer aktiv-gekühlten Wärmesenke aus Kupfer verbunden werden. Verschiedene Verbindungstechniken, wie z.B. Löten und heiß-isostatisches Pressen (HIP) werden hinsichtlich ihrer Brauchbarkeit für diesen Anwendungsfall untersucht.

Während des Betriebs von ITER, sind die plasmaaktiven Komponenten einer Bestrahlung mit 14 MeV Neutronen ausgesetzt, die während des Fusionsprozesses entstehen. Diese schnellen Neutronen verändern die thermischen und mechanischen Eigenschaften von Beryllium und des Beryllium-Kupfer-Verbundes. Die Auswahl des Beryllium-Referenzwerkstoffes und die Ertüchtigung der Verbindungstechniken zwischen Beryllium und Kupfer, erfordern experimentelle Untersuchungen des Materialverhaltens unter kombinierten thermischen Belastungen und Neutronenbelastungen. Zur Untersuchung der Material-Degradation nach Bestrahlung, wurde ein umfangreiches Bestrahlungsprogramm im Hochflußreaktor (HFR) Petten (Niederlande) durchgeführt. Dieses betraf Thermoschock-Proben, aktiv gekühlte Be/Cu-Module und mechanische Testproben aus verschiedener Beryllium-Qualitäten.

Im Rahmen der hier vorliegenden Arbeit wurden Thermoschock-Tests an verschiedenen unbestrahlten und bestrahlten Varianten von Beryllium durchgeführt. Das Erosionsverhalten und die Rißanfälligkeit dieser Materialien wurden vor und nach Neutronenbelastung verglichen.

Weiterhin wurde der Einfluß von Neutronenschäden auf die Be-Cu Verbindungen in Thermozyklert-Experimenten untersucht. Dabei wurden das Wärmeabfuhrverhalten und das thermische Ermüdungsverhalten je eines Moduls mit CuMnSnCe-Lot und mit InCuSil-Lot vor und nach Neutronenbestrahlung verglichen.

## TABLE OF CONTENTS

<b>1</b>	<b>INTRODUCTION AND SCOPE OF THE WORK.....</b>	<b>1</b>
1.1	INTRODUCTION.....	1
1.1.1	Plasma facing components for ITER.....	2
1.1.2	Plasma facing materials.....	5
1.1.3	Armour/Heat sink materials joining.....	6
1.1.4	The R&D program on plasma facing components for ITER.....	6
1.2	SCOPE OF THE WORK.....	8
1.2.1	Experimental assessment of neutron effect on Be samples.....	8
1.2.2	Experimental assessment of neutron damage on Be/Cu joints.....	9
1.2.3	Theoretical verification of the structural adequacy of the first wall.....	9
<b>2</b>	<b>BACKGROUND.....</b>	<b>11</b>
2.1	BERYLLIUM.....	11
2.1.1	Introduction.....	11
2.1.2	Fabrication methods.....	11
2.1.3	ITER grades.....	15
2.2	HEAT SINK MATERIALS.....	18
2.2.1	CuCrZr ITER Grade.....	19
2.2.2	CuAl25 alloy, ITER Grade.....	20
2.3	BE/CU JOINING TECHNOLOGIES.....	20
2.3.1	Brazing.....	22
2.3.2	Hot Isostatic Pressing.....	25
2.4	LIFETIME DESIGN ISSUES FOR PFCs.....	25
2.4.1	Erosion lifetime.....	25
2.4.2	Thermal fatigue.....	29
2.5	NEUTRON IRRADIATION EFFECTS.....	29
2.5.1	Basic interaction phenomena between radiation and solids.....	29
2.5.2	Primary interactions of fusion neutrons with metallic materials.....	30
2.5.3	Change of macroscopic properties.....	33
2.5.4	Effects of neutron damage on Be.....	34
2.5.5	Effects of neutron damage on Be/Cu joining.....	38
<b>3</b>	<b>ELECTRON BEAM INTERACTION WITH MATERIALS.....</b>	<b>39</b>
3.1	THE ELECTRON BEAM IN TECHNOLOGICAL PROCESSES.....	39
3.2	PHENOMENOLOGY OF THE ENERGY DEPOSITION.....	39
3.2.1	X-Ray production.....	40
3.2.2	Secondary electrons.....	40
3.2.3	Thermionic emission.....	40
3.2.4	Electron backscattering.....	41
3.3	THE ELECTRON BEAM AS HEAT SOURCE FOR TESTING OF PFCs.....	42
3.4	THE ELECTRON BEAM FACILITY JUDITH.....	43
3.4.1	Technical specifications.....	44
3.4.2	Diagnostic.....	45
3.4.3	Improvement for testing of beryllium.....	45
3.4.4	Improvement for the handling of radioactive samples.....	45
<b>4</b>	<b>NEUTRON IRRADIATION PROGRAM.....</b>	<b>48</b>
4.1	PARIDE 1 AND 2.....	48
4.2	PARIDE 3 AND 4.....	50
<b>5</b>	<b>THERMAL SHOCK TESTS ON BE SAMPLES.....</b>	<b>52</b>
5.1	OBJECTIVES.....	52
5.2	EXPERIMENTAL DETAILS.....	53
5.2.1	Test specimen design.....	53
5.2.2	Experimental set-up.....	54
5.2.3	Quantification of thermal shock damage.....	55
5.3	TEST RESULTS.....	56
5.3.1	Measurements of absorbed current.....	57

5.3.2	<i>Thermionic electron emission: a hypothesis for the current drop</i>	59
5.3.3	<i>First test campaign</i>	60
5.3.4	<i>Second test campaign</i>	76
5.4	NUMERICAL SIMULATION OF THE EXPERIMENTS	90
5.4.1	<i>Analysis model</i>	90
5.4.2	<i>Thermal loads and input data</i>	91
5.4.3	<i>Results</i>	92
5.5	THERMAL SHOCK TESTS ON PRE-HEATED BE SAMPLES	94
5.5.1	<i>Objectives</i>	94
5.5.2	<i>Experimental details and loading conditions</i>	94
5.5.3	<i>Test results</i>	95
5.6	CONCLUSION AND RECOMMENDATIONS FOR FUTURE WORK	98
<b>6</b>	<b>ACTIVELY COOLED MOCK-UPS</b>	<b>100</b>
6.1	THERMAL FATIGUE TEST OF BE/CU JOINTS PRODUCED BY BRAZING	100
6.1.1	<i>Objectives</i>	100
6.1.2	<i>Numerical simulation of the experiment</i>	101
6.1.3	<i>Experimental details</i>	106
6.1.4	<i>Un-irradiated mock-ups test results</i>	109
6.1.5	<i>Neutron-irradiated mock-ups 8mm Be tile: results and comparison</i>	109
6.1.6	<i>Neutron-irradiated mock-ups 3mm Be tile test results</i>	114
6.1.7	<i>Experimental and analytical results comparison</i>	115
6.2	SHEAR TESTS OF BE/CU JOINTS	116
6.3	PRE-IRRADIATION CHARACTERISATION OF PW HIPED MOCK-UPS	117
6.3.1	<i>Objectives</i>	117
6.3.2	<i>Mock-ups fabrication</i>	118
6.3.3	<i>Testing procedure and loading conditions</i>	120
6.3.4	<i>Results</i>	120
6.3.5	<i>Numerical simulation of thermal fatigue experiments</i>	123
6.4	CONCLUSIONS	125
<b>7</b>	<b>PORT LIMITER ANALYSES</b>	<b>127</b>
7.1	INTRODUCTION	127
7.2	ANALYSIS MODEL	128
7.3	STEADY STATE ANALYSES WITH ELASTIC MATERIAL BEHAVIOUR	128
7.3.1	<i>Thermal loads and input data</i>	129
7.3.2	<i>Results</i>	130
7.4	TRANSIENT ANALYSIS WITH ELASTO-PLASTIC MATERIAL BEHAVIOUR	133
7.4.1	<i>Thermal loads and input data</i>	133
7.4.2	<i>Results</i>	133
7.4.3	<i>Lifetime estimation</i>	139
7.5	OFF NORMAL CONDITION	140
7.6	CONCLUSIONS	140
<b>8</b>	<b>SUMMARY</b>	<b>141</b>
<b>9</b>	<b>APPENDIX - LIST OF ACRONYMS</b>	<b>143</b>
<b>10</b>	<b>BIBLIOGRAPHY</b>	<b>144</b>

# 1 INTRODUCTION AND SCOPE OF THE WORK

## 1.1 Introduction

July 1998 marked the end of the Engineering Design Activities (EDA) for the International Thermonuclear Experimental Reactor (ITER). The 1998 ITER design fulfilled the overall programmatic objective of ITER, i.e. to demonstrate the scientific and technological feasibility of fusion energy for peaceful purposes. ITER would achieve this by demonstrating controlled ignition and extended burn of deuterium-tritium plasma<sup>1</sup>, by demonstrating technologies essential to a reactor in an integrated system and by performing integrated testing of the high heat flux (HHF) components under a nuclear environment [1].

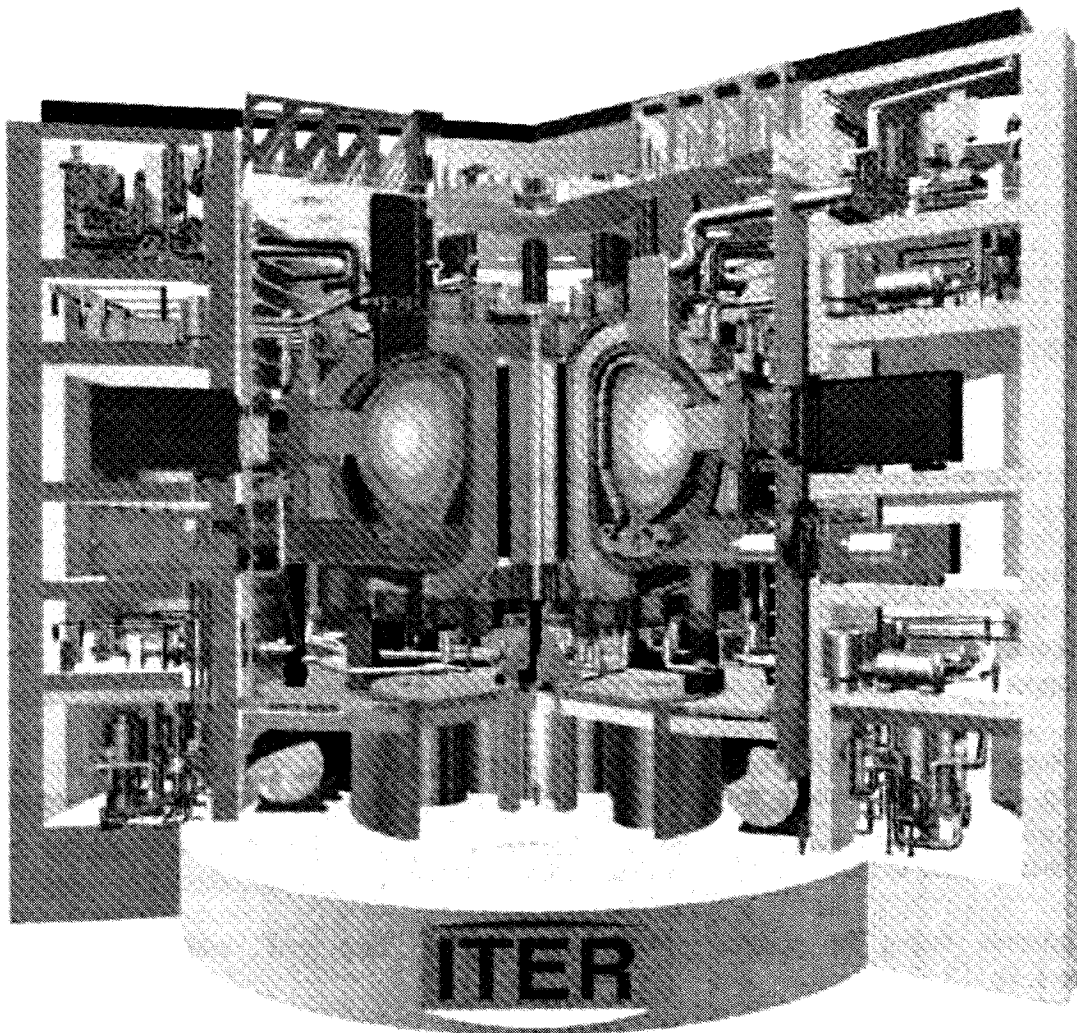


Figure 1.1 - Computer-generated model of the ITER tokamak.

---

<sup>1</sup> The conditions for controlled fusion on Earth can be created using magnetic forces to confine the fusion fuel while heating it by a variety of methods. The fuels to be used are deuterium and tritium, two isotopes of hydrogen. Ignition occurs when enough fusion reactions take place for the process to become self-sustaining. To achieve this the fusion fuel must be heated to temperatures high enough to overcome the natural repulsive forces of nuclei (about 100 million degrees Celsius) and kept dense enough and confined long enough to withstand energy losses.

The ITER design (Figure 1.1) by the end of EDA is presented in the ITER Final Design Report (FDR), Cost Review and Safety Analysis [2]. At the end of the EDA, the ITER Parties recognised the possibility that they might be unable, for financial reasons, to proceed to the construction of the device according to the FDR. Therefore several options for a reduced technical objectives / reduced cost (RTO/RC) ITER project, by reducing plasma performance and technical margins, have been studied. As a result a device referred to as ITER-FEAT (Fusion Energy Advanced Tokamak) has been defined. The outline design report on the ITER-FEAT is reported in [3]. In Table 1.1 the main parameter and dimensions of ITER according to the original design presented in the FDR and ITER-FEAT are collected. The material choices of the original design have been presently kept for the ITER-FEAT design but an effort has been required for improving and possibly reducing the costs of the manufacturing technologies. The results, which are presented here, make up a part of the material database on beryllium and beryllium-copper brazed joints after neutron irradiation.

<b>Table 1.1 - ITER Major Design Parameters</b>	<b>FDR* (1998)</b>	<b>FEAT** (2000)</b>
Plasma major radius [m]	8.14	6.2
Plasma minor radius [m]	2.8	2.0
Nominal plasma current [MA]	21	15 (17)
Toroidal field at major radius [T]	5.68	5.3
Burn time [s]	1000	≥ 300
Nominal fusion power [MW]	1500	500 (700)

\* FDR = Final Design Report; \*\* FEAT = Fusion Energy Advanced Tokamak

### 1.1.1 Plasma facing components for ITER

A particular effort was devoted in the associated European programme to the design and technological development of the plasma facing components (PFCs) for ITER [4, 5, 6]. The PFCs comprise the blanket and divertor systems and the radio-frequency antenna (Figure 1.2).

The blanket system consists of modules with a First Wall (FW) and neutron shield mounted on a supporting structure [7] and has three main functions:

- i. to remove the majority of the fusion power generated by the plasma;
- ii. to reduce the nuclear responses in the vacuum vessel structure and superconducting coils;
- iii. to contribute to the passive stabilisation of the plasma.

The structure facing the plasma, globally identified as “first wall”, can be subdivided into (Figure 1.3):

- i. *Primary Wall* (PW), providing the first generic protection to the components located behind it;
- ii. *Port Limiters* that in addition to the normal function of the primary modules defines the plasma boundary during start-up and shut-down phases;
- iii. *Baffles* that in addition to the normal function of the primary modules prevent the flow of neutral particles from the divertor region back to the plasma.

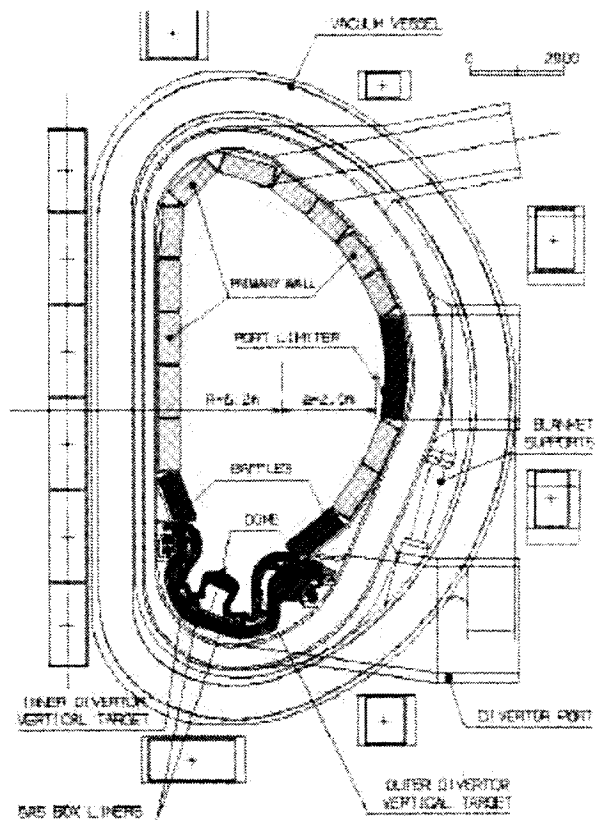
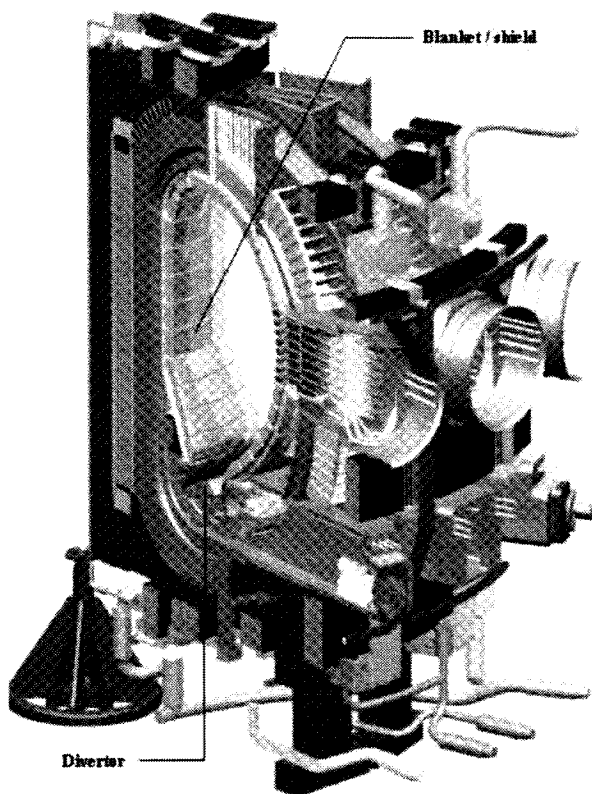
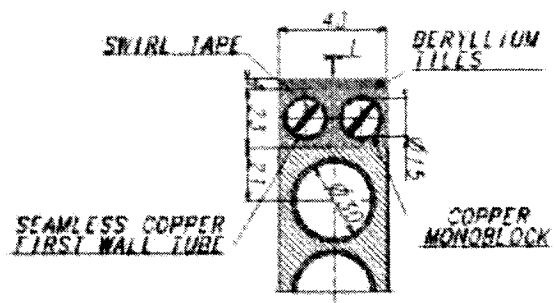
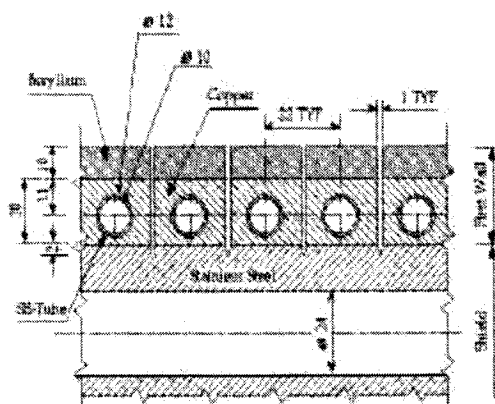


Figure 1.2 - Computer-generated model of the ITER- FEAT tokamak: isometric view of main in-vessel blanket system components (36° sector of the torus).

The primary wall, surrounding most of the plasma along the last closed magnetic surface, is exposed to a moderate heat flux ( $0.5 \text{ MW/m}^2$ ) but has to withstand the highest neutron load. The port limiter is subjected to the same loads as the primary wall during plasma burn conditions but higher peak heat flux ( $8 \text{ MW/m}^2$ ) when the plasma is leaning on its surface. The baffle is exposed to an intermediate heat flux (up to  $3 \text{ MW/m}^2$ ) and to severe erosion from neutral particles. The operating conditions of the ITER EDA and ITER- FEAT PFCs are presented in tables 1.2 and 1.3 [8].

PFCs in ITER are protected by sacrificial armour material that can be replaced in case of damage. The typical design of PFCs is a structure with the armour tiles metallurgically joined to an actively cooled heat sink for providing the necessary transfer of incident power to the cooling system (Figure 1.4) [9 - 16]. The general lay-out of each component, its functions, requirements and specifications can be found in the ITER FDR [2].



a) b)

Figure 1.4 – ITER FDR design - Horizontal cross section of PFCs heat removal structure: a) primary module; b) port limiter.

Table 1.2 – ITER 1998 Design – Main data for the shielding blanket components [8].

Specifications	Units	PW	Port limiter	Baffle	
				Lower	Upper
Peak heat flux	MW/m <sup>2</sup>	0.5	~8	3	1
Average heat flux.	MW/m <sup>2</sup>	0.2	2.6	1.8	0.5
Neutron wall load	MW/m <sup>2</sup>	1.19	1.17	0.77	0.90
BPP <sup>2</sup> Radiation damage	dpa	~1	~1	~0.4	~0.5
BPP He production	appm	~1000	~1000	~400	~500
Irradiation temperature	°C	230-280	230-280	200-500	200-500
Number of cycles	--	13000	26000	13000	13000
Water temperature inlet	°C	140			
Water pressure inlet	MPa	4			
Central disruption <sup>3</sup> energy	MJ/m <sup>2</sup>	1			
No. of central disruption	--	500			
VDE <sup>4</sup> peak H. Load/dur.	MJ/m <sup>2</sup> - s	60/0.3	--*	60/0.3	60/0.3
No. of VDE	--	10	--	10	10
Runaway electrons/dur.	MJ/m <sup>2</sup> - s	50/0.3	--	50/0.3	50/0.3
Baking	°C	240			

\*VDE are assumed not to strike the limiter.

Table 1.3 – ITER-FEAT Design – Expected main data for the shielding blanket components [8].

Specifications	Units	FW	Port limiter	Baffle
Maximum heat flux	MW/m <sup>2</sup>	0.5	~8	1-2
Maximum fluence	MW/m <sup>2</sup>	0.5		
Maximum wall loading	MW/m <sup>2</sup>	~0.8		
Average wall loading	MW/m <sup>2</sup>	~0.6		
Water temperature inlet	°C	100		
Water pressure inlet	MPa	3		
Baking	°C	240		

<sup>2</sup> Two performance phases are foreseen for ITER 1998 design reactor: Basic Performance Phase (BPP) and Extended Performance Phase (EPP). In the BPP of ITER operation the shielding blanket has three main functions: 1) to remove the majority of the fusion power generated by the plasma; 2) to reduce the nuclear responses in the vacuum vessel structure and superconducting coils; 3) to contribute to the passive stabilisation of the plasma. During the EPP, a tritium breeding blanket will replace all or a large proportion of the shielding blanket.

<sup>3</sup> Plasma disruption, a sudden, uncontrolled termination of the plasma current and plasma confinement, with the thermal and magnetic energy contained in the plasma being dumped on the FW and divertor plates (ref. Chapter 2.4).

<sup>4</sup> Vertical Displacement Event (VDE), a plasma instability during which the whole plasma moves up (or down) away from its equilibrium position (ref. Chapter 2.4).



### 1.1.2 Plasma facing materials

The selection of the armour materials for ITER PFCs was one of the important challenging problems in the ITER design [17 - 23]. The working conditions of the plasma facing materials (PFMs) are very complex. During normal operation they are subjected to high cyclic heat fluxes which originate thermal fatigue and simultaneously to high neutron and ion fluxes which produce erosion. During off normal operations, the PFMs may suffer severe thermal shocks caused by plasma disruptions and by vertical displacement events (ref. Table 1.2).

The factors that affect the selection come primarily from the requirements of plasma performances, component lifetime, and safety [24, 25]. Beryllium, together with carbon materials and tungsten [26], will play an important role as a plasma facing material in ITER [8, 27, 28]. In the ITER 1998 design, beryllium was foreseen for the first wall, upper baffle and for the port limiter surfaces, carbon fibre composites near the strike points of the divertor vertical target and tungsten elsewhere in the divertor and lower baffle modules. In Figure 1.5 the plasma facing materials for the ITER-FEAT design are shown.

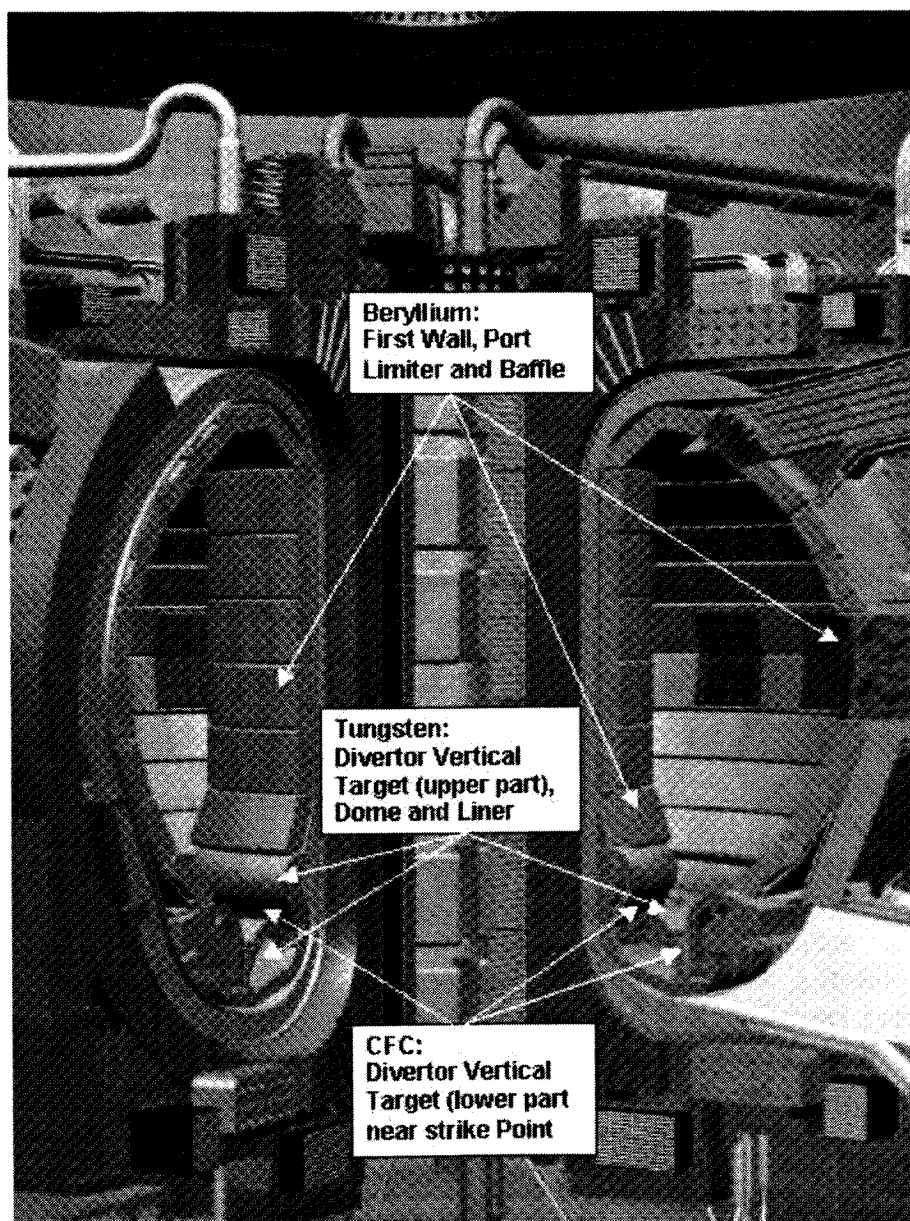


Figure 1.5 - Plasma facing materials in ITER-FEAT design.

All candidate materials have some advantages and disadvantages as an armour for PFC. Table 1.4 summarises the main design issues related to their selection. Inside each class of PFMs there are several different industrial grades, which were developed to meet a variety of requirements. Each grade has been compared with the fusion applications features in order to select a reference candidate grade for each type of materials and to develop the data base on material properties that is needed for the design evaluation. The characteristics of different beryllium grades investigated in the present work have been summarised in chapter 2.

### **1.1.3 Armour/Heat sink materials joining**

For the construction of PFCs the beryllium tiles have to be attached to a heat sink of copper (Figure 1.4). Several techniques of joining have been proposed and studied: low and high temperature hot isostatic pressing (HIP) with or without interlayer, brazing, low and high temperature diffusion bonding, plasma spray, explosion bonding, joint rolling etc.

A short description of the joining technologies, which have been investigated in the present work, is reported in chapter 2.

The joints must withstand the thermal, mechanical and neutron loads and the cyclic mode of operation. They must be able to operate under vacuum, while providing an acceptable design lifetime and high reliability. For the ITER FDR design preliminary recommendations have been worked out for Be/Cu joining technologies: high temperature HIPing and plasma spray (PS) are recommended as the most promising methods for the large surface and the low heat flux of the Be Primary Wall. For the Be Port Limiter, it seems that HIP joining with an AlBeMet compliant layer is a viable technique. Brazing technologies could be applied to low and intermediate heat flux components, but the scaling of brazing to the manufacture of large and complex components is still to be demonstrated.

### **1.1.4 The R&D program on plasma facing components for ITER**

A research and development (R&D) project (Large Project-4) has been conducted as a collaborative effort between the ITER JCT and the Home Teams of European Union, Japan, Russian Federation and United States for assessing the manufacturing feasibility, the performances and the integration of the most important components of the ITER blanket system [29, 30]. This R&D project was organised as a broad collaboration involving several EU laboratories and several industrial companies.

An extensive effort of this R&D technology project for ITER has been devoted to the development and selection of the reference PFMs and to the development of reliable Be/Cu joining technologies for application in ITER PFCs [31].

Several beryllium grades have been investigated taking into account the critical issues for Be application in ITER PFCs (Table 1.2). Some issues addressed do not depend on the material grade (joining to the Cu heat sink, erosion, behaviour of melt layers, etc.) [28]. The selection of the optimum Be grade was therefore driven by those properties which are very sensitive to the impurity levels, grain size, methods of production, thermomechanical treatment, and which usually differ for the different Be grades, such as thermal fatigue resistance, mechanical properties, swelling, neutron irradiation response, tritium-retention. High heat flux tests have been conducted in several electron beam facility, for simulating the severe thermal shocks on PFMs, caused by plasma disruptions. Mainly due to its excellent thermal fatigue/thermal crack resistance (demonstrated for unirradiated Be), excellent mechanical properties, industrial availability, and larger data base in comparison with other industrial grades, Be S65C vacuum hot pressed (VHP - Brush Wellman, US) was selected as reference grade for the ITER PFCs. The Russian grade DShG-200 is proposed as back-up.

For investigating different joining techniques several small scale mock-ups, the design of which was intended to be similar to that of the typical high heat flux PFCs, have been

manufactured and tested [32-35]. Figures 1.6 to 1.9 show some mock-ups which has been created for investigating design and manufacturing issues of some PFCs in the frame of the R&D program. The response of the Be/Cu joint when subject to surface heat loads has been investigated by performing thermal fatigue test in electron beam facilities. Based on the results of the R&D program on the small scale mock-ups, full scale but partial size components or group of components will be manufactured and tested and the reference technology for manufacturing the ITER PFCs will be established [36, 37].

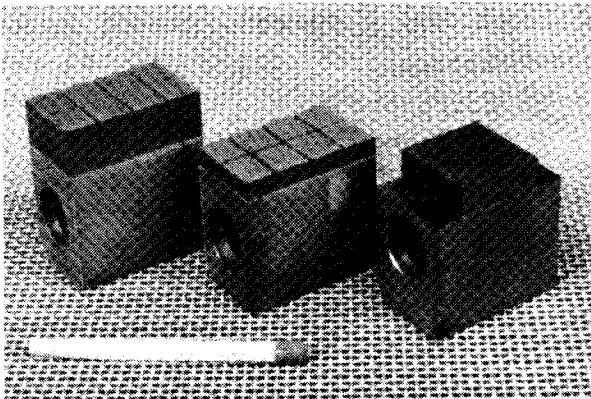


Figure 1.6 - Miniaturized Be/Cu mock-ups for neutron irradiation and HHF test in JUDITH.

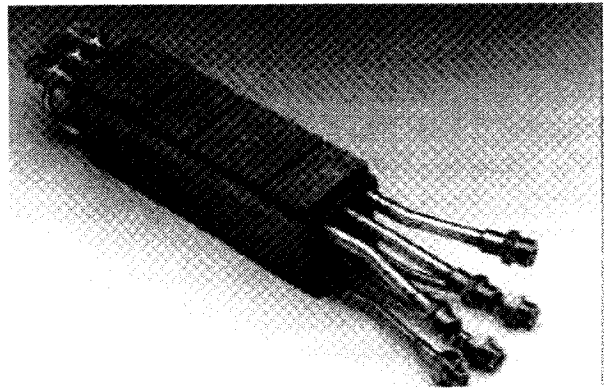


Figure 1.8 - FW mock-up with HIPed Be tiles [by courtesy of EFDA CSU Garching].

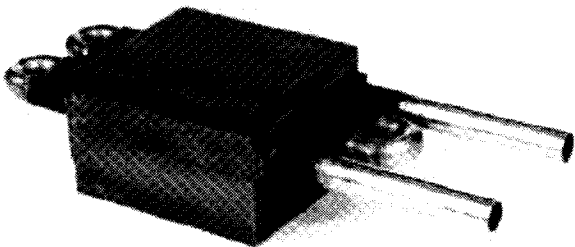


Figure 1.7 - FW mock-up with large Be tile tested in JUDITH [by courtesy of EFDA CSU Garching].

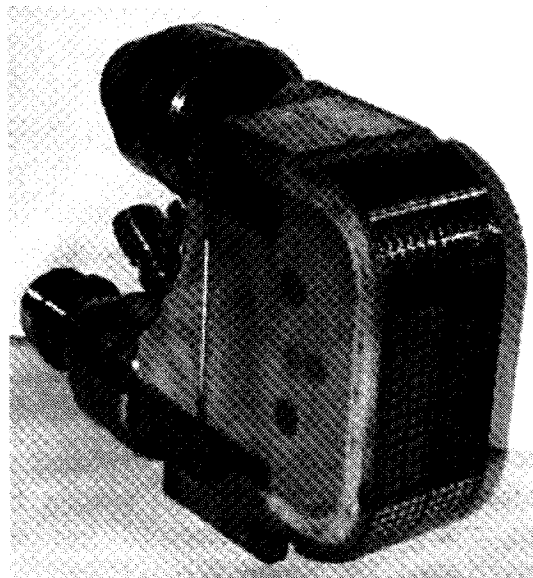


Figure 1.9 - Port Limiter mock-up - brazed two panel [by courtesy of V. Barabash ITER Team Garching].

## 1.2 Scope of the work

During the operation of ITER the PFMs will suffer irradiation with 14 MeV neutrons generated in the fusion process which will affect the thermal and mechanical properties of beryllium and beryllium-copper joints. To validate the choice of the reference beryllium grade there is a need to investigate the beryllium behaviour under combined exposure to thermal loading and neutron irradiation. An ITER R&D program was therefore dedicated on the production of data on the influence of neutron irradiation on the properties of Be and Be/Cu joints. To investigate the materials degradation processes, several neutron irradiation campaigns have been carried out in HFR at Petten, The Netherlands. Actively cooled Be/CuCrZr mock-ups, mechanical test samples and thermal shock samples from different beryllium grades have been irradiated up to 0.35 dpa at 350 °C and 700 °C during the first campaign and up to 1 dpa and 200 °C during the second campaign.

The objective of the present work was the assessment and experimental verification of the beryllium armoured plasma facing components for ITER. This objective has been achieved by:

- Experimental assessment of neutron irradiation effects on Be material performing thermal shock tests on beryllium samples;
- Experimental verification of neutron damage on Be/Cu joints performing thermal fatigue tests on beryllium-copper mock-ups;
- Detailed theoretical verification of the structural adequacy of the first wall performing specialised analyses to assess the components and to predict their lifetime.

Chapter 2 summarizes the numerous topics, which constituted the scientific background of the present work.

All tests have been carried out in the Electron Beam (EB) facility JUDITH, located in the hot cells of Forschungszentrum Jülich (FZJ). The simulation of high heat loads by electron beams has become a frequently used technique but the phenomena regarding the interactions of high energy electrons with the metal should be taken into account for the correct interpretation of the experimental results. These phenomena are discussed in chapter 3.

A short description of the two neutron irradiation campaigns is reported in chapter 4.

### 1.2.1 Experimental assessment of neutron effect on Be samples

The behaviour of the neutron irradiated samples when subject to thermal shocks has been studied experimentally and the erosion behaviour of the irradiated test coupons has been compared with the un-irradiated test specimens. These grades include beryllium S65C manufactured by Brush Wellman Inc., (USA), and the Russian beryllium grades TR30, DShG200, and TShG56. Beside these, powder-metallurgically (PM) produced materials, plasma sprayed (PS) beryllium (Los Alamos National Laboratory) and condensed beryllium (D.V. Efremov Institute, St.Petersburg) were investigated both as armour materials and coating technologies. The results of two test campaigns have been summarised in chapter 5. However, from the first test campaign, it was clear that the test conditions were not always reproducible and a change of some characteristics of the beam may occur between different series of tests. Therefore, during the second test campaign, for achieving the most accurate comparison of the material behaviour before and after nuclear irradiation, beryllium samples which were un-irradiated, irradiated at 350 °C and at 700 °C have been tested in sequence without any break of vacuum. A direct comparison of un-irradiated and irradiated material has been carried out only for samples tested in the same test campaign; the results of the two campaigns should not be mixed.

All thermal shock tests described so far have been performed on cold (i.e. not preheated) test specimens. PFCs in future thermonuclear fusion reactors will experience severe thermal shocks primarily during plasma operation, i.e. at elevated temperatures. Plasma disruptions on the first wall are expected to occur at surface temperatures above 400 °C. Under these conditions beryllium behaves more ductile compared to room temperature. Hence, additional tests on few un-irradiated beryllium test coupons have been carried out under experimental conditions, which take care of this effect. The erosion damage of the beryllium grades S65C and TR30 at different temperatures after thermal shock test has also been presented on chapter 5.

### **1.2.2 Experimental assessment of neutron damage on Be/Cu joints**

During the normal operation of ITER, the beryllium-copper joint will be stressed by cyclic heat loads, which may cause a fatigue failure. Thermal fatigue endurance is a necessary but not sufficient prerequisite for the joint. In fact, all plasma facing components will suffer irradiation with 14 MeV neutrons generated in the fusion process. The influence of neutron irradiation will play an important role in the selection of the joining technologies. This is particularly true for the first wall components, where the joint will experience a rather high fluence. According to one of the repair schemes envisaged for the primary wall [38], the armour is refurbished several times by plasma spraying new beryllium onto the old eroded beryllium surface. Therefore, the joint has to withstand the total fluence of the basic performance phase of operation, while the armour will be periodically renewed.

The heat removal efficiency and the thermal fatigue behaviour of a mock-up with CuMnSnCe braze and a mock-up with InCuSiI braze have been compared, before and after neutron irradiation. The results are presented in chapter 6. In this chapter, besides the post-irradiation tests, also the pre-irradiation characterisation tests on five primary FW beryllium-copper mock-ups produced by hot isostatic pressing are presented.

### **1.2.3 Theoretical verification of the structural adequacy of the first wall**

The assessment of the feasibility and adequacy of the ITER PFCs under normal and off-normal conditions has been carried out performing Finite Element (FE) thermo-mechanical analyses. Existing analytical methods have been applied to study these components and to predict their lifetime. The work has been focused on the most critical parts of the PFCs and the studies performed may be classified in three main categories:

- Assessment of the port limiter;
- Assessment of the separable FW design for the ITER FEAT;
- Study of an alternative FW design with replaceable armour tiles.

The assessment of the port limiter was one among the most complex and exhaustive study on PFCs. Therefore only the theoretical verification of this component has been included in the present work and is presented in chapter 7. The results of the assessments on the other PFCs can be found in [10 - 16, 39 - 45].

Table 1.4 – ITER FDR design - Main design issues which affect the plasma facing material selection [46].

Component	Loads	Effects and Issue	Armour	Advantages	Disadvantage
Primary Wall	Plasma radiation loads; Plasma contact during VDE disruptions; n-irradiation.	Evaporation/melting; Erosion.	Be	Plasma compatibility (low atomic number, Z); Relatively high thermal conductivity; Possibility of in-situ repair; Low activation.	Low melting point; Short erosion lifetime (erosion, loss of melt layer during disruption); Low neutron radiation resistance (concerning swelling, high He generation and embrittlement); Poor oxidation resistance above 800°C; Explosive dust potential; Needs special safety rules (toxicity). see above.
Port limiter	Plasma radiation loads; High start-up and shut down heat loads; Plasma contact during disruptions; n-irradiation.	Evaporation/melting; High peak loads resulting from misalignment effects.	Be CFC (alternative)	see above. Low Z (large experience in currents tokamaks); High thermal conductivity; High thermal shock resistance; Low disruption erosion (no melting); Large experience for applications as a high heat flux components.	High tritium retention; Loss thermal conductivity at neutron irradiation; High CTE mismatch with Cu heat sink; Poor oxidation resistance; Needs cleaning procedure.
Upper baffle	Plasma contact during VDE disruptions; High heat loads; n-irradiation.	Evaporation/melting; Erosion.	Be CFC (alternative)	see above.	see above.
Lower baffle	Large fluxes particles-high E; High heat loads; n-irradiation.	High sputtering Evaporation/melting.	W	High melting point; Low erosion (high energy threshold for sputtering); High thermal stress resistance; High thermal conductivity; Low swelling; Low tritium retention; Possibility of plasma spray repairing.	High Z (low allowed concentration in plasma, poor database on behaviour in large tokamaks); Neutron embrittlement; High radioactivity; Potential loss of melt layer during disruption; High CTE mismatch with Cu heat sink; Explosive dust potential; Poor machinability. see above.
			Be (alternative)	see above.	

## 2 BACKGROUND

### 2.1 Beryllium

#### 2.1.1 Introduction

Beryllium is one of the lightest metals known [47]. It has the atomic number 4 and an atomic weight of 9.012. Be has a hexagonal close packed (hcp) crystal structure (Figure 2.1) that partly accounts for its limited ductility at room temperature. Due to its structure, Be is characterised by the anisotropy of its properties with crystallographic orientation. A single crystal of Be will have very different mechanical properties depending on which crystallographic direction is tested. There is limited slip in directions not parallel to the basal planes, resulting in very small ductility perpendicular to the basal direction [48, 49]. Polycrystalline Be with fine grain size hides some of the anisotropy of the unit cell. There is an averaging effect whose magnitude depends on how randomly the single crystal grains are oriented [50]. Various production processes yield material with different impurities levels, grain structures and texture<sup>5</sup>. Processing methods are directed at producing as little texture as possible.

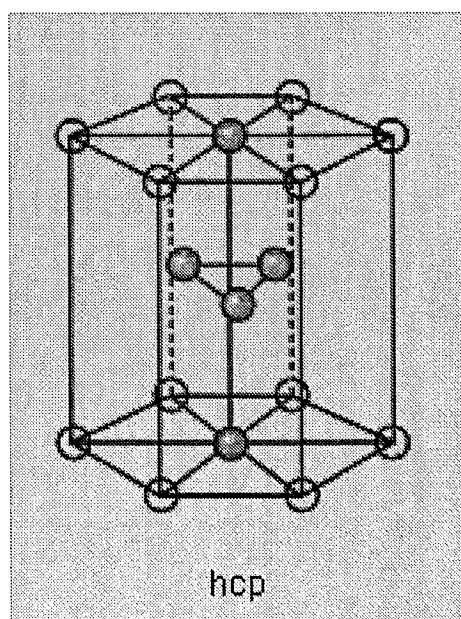


Figure 2.1 - Be crystal structure

Be in structural applications is notable for a combination of stiffness and low density. It has high specific heat and excellent thermal conductivity and it retains useful properties at both elevated and cryogenic temperatures. The combination of high specific heat, high thermal conductivity, low coefficient of thermal expansion with its structural properties makes Be components dimensionally stable under transient thermal loads. Nuclear reactors, inertial guidance instrumentation, military aircraft disc brakes, audio components, high speed computer parts, and satellite structures are among the many applications for this versatile material. Due to its low mass absorption coefficient for X-rays, Be foil windows are widely used in X-ray analytical and medical instruments. Excellent reflectivity for infrared radiation is observed. Because of its high neutron scattering cross-section, low thermal neutron capture cross-section and high (n, 2n) neutron multiplication cross-section, Be is used for neutron reflectors and as neutron multiplier in the design of reactors.

Be has a very high affinity to oxygen, and all oxygen in Be is in the form of beryllium oxide (BeO).

#### 2.1.2 Fabrication methods

Industrial production of primary Be is carried out in the USA, and in Kazakhstan [49]. Be is produced from betrandite ( $\text{Be}_4\text{Si}_2\text{O}_7(\text{OH})_2$ ) and Beryl ( $3\text{BeO} \cdot \text{Al}_2\text{O}_3 \cdot 6\text{SiO}_2$ ) ores. The production of engineered Be metals begin with the extraction of the metal from the ore. Through a combination of chemical and mechanical methods, Be metal ingots are obtained

<sup>5</sup> significant preferred crystallographic orientation of grains.



from the ore [51-53]. However, the material in Be ingots has a coarse grain structure that results in poor mechanical properties. For these reasons, virtually all Be enters service as powder metallurgy-derived product [54]. Powder is prepared by chipping the ingots and mechanically grinding the chips to the appropriate particle size distribution for consolidation into essentially full density billets by powder metallurgy techniques. Through this powder metallurgy process dense, homogeneous, fine-grain microstructures are attained, which are required for outstanding mechanical properties.

#### 2.1.2.1 Powder production

The first step in the production of Be powder is machining the cast ingots into large, flat chips by lathe-turning. These chips are too large to manufacture a useful product, so they are sent through one of several powder-making operation: attrition milling, impact grinding, ball mill grinding or inert gas atomisation [52, 55-59]. The mechanical grinding system used to manufacture Be powder of a given particle size distribution has been shown to have an effect upon the characteristic of the fully dense body prepared with the powder [60].

In *attrition milling*, plate-like particles are produced (Figure 2.2), which tend to align preferentially during powder consolidation steps, resulting in anisotropic mechanical properties. This technique is not presently used in production. Through the *impact grinding process* finer and more symmetric particles are produced (Figure 2.3), which result in a less textured microstructure and more uniform properties in all directions than attrition milling. The largest volume of Be is made using impact ground powder. *Ball mill grinding* produces extremely fine particles (Figure 2.4), which in turn produce an extremely fine grained microstructure in the final product. This expensive and time consuming method is used to obtain resistance to mechanical distortion in precision guidance components.

Useful technologies which produce a Be material that is totally isotropic and overcomes the basic anisotropy of the Be crystal are the *atomisation methods* under controlled inert gas atmosphere [49, 54, 58, 59]. These methods involve break up and rapid cooling of a molten Be stream to form spherical Be powder (Figures 2.5 and 2.6).

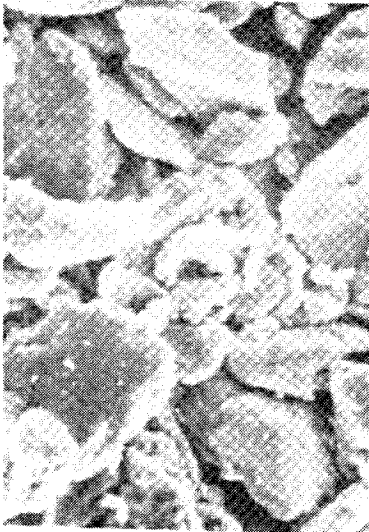


Figure 2.2 – Be powder particles produced by attrition system. Be chips are ground into powder between a fixed, grooved Be plate and a rotating, grooved Be plate [53].



Figure 2.3 – Be powder particles produced by impact grinding system. Be chips suspended in a stream of high velocity gas collide with a solid Be target. [53].

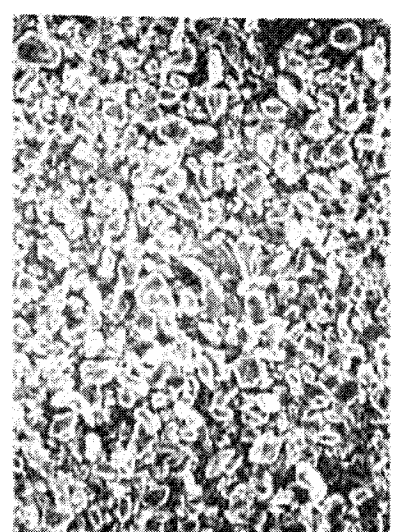


Figure 2.4 – Be powder particles produced by ball mill system. Ball milled powder has been either impact or attrition ground before it is ball milled [53].



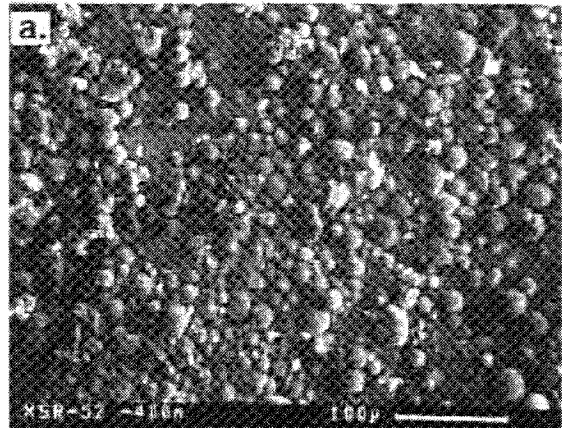
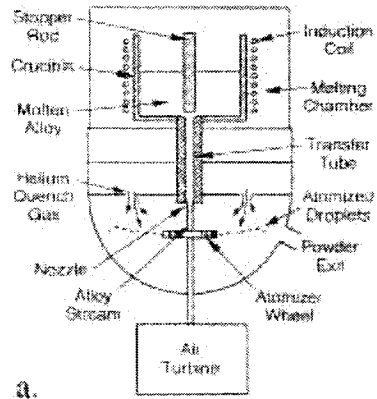


Figure 2.5 – Left: Be centrifugal atomization process. Vacuum melted Be is directed through a transfer tube onto the surface of a rapidly spinning wheel, whereby the liquid metal is mechanically atomized into finely divided droplets. The droplets are solidified in flight inside the atomizing chamber by a transverse flow of He gas that also carries the Be powder product into a cyclone separator. Right: Spherical morphology of produced Be powders [59].

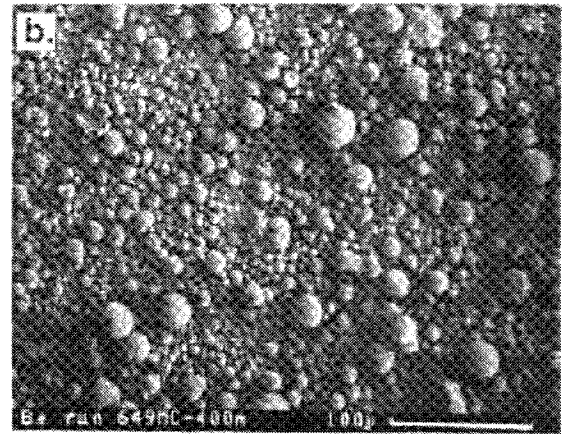
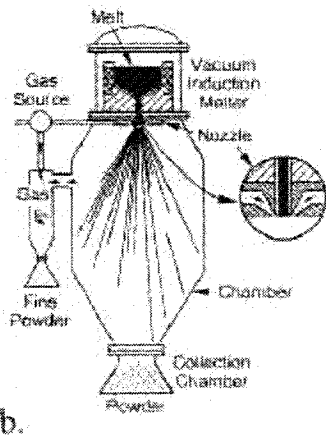


Figure 2.6 – Left: Be inert gas atomization process. Solid stock of Be are vacuum melted and poured through a fine nozzle. Fine droplets are produced by directing a high pressure inert gas jets at controlled angles onto the metal stream which exits from the nozzle. Particles are subsequently cooled and solidified during free-flight in an inert atmosphere [59]. Right: Spherical morphology of produced Be powders [59].

During the powder metallurgy process, each particle of powder rapidly develops a surface layer of BeO because of the high affinity of Be for oxygen even at room temperature. There is a clear connection between type of grinding process and oxidation of the powder surface. The content of BeO characterises the ductility of the several Be grades [61]. In fact, the grain size of the Be, which because of its anisotropy is an important factor in determining the ductility of various components, can be controlled by oxide content.

Via the specific choice of methods, conditions and atmosphere of grinding powders can be produced by the powder technology in a wide range of sizes (from 5 to 200 μm) with a controllable content of oxygen (up to 3%) [62].

#### 2.1.2.2 Powder consolidation

Be powder must be consolidated at elevated temperatures to form products. The method of powder consolidation has a strong effect on anisotropy of mechanical properties [63]. In the process of compacting, the oxide film covering the Be powder particles breaks down resulting in inclusions the size of which depends on the process parameters and chemical composition of an initial ingot. The large amount of Be oxide present in the material pins the grain boundaries which retard grain growth during the high temperature processing [64, 65]. Powder consolidation can occur by all the conventional powder metallurgy consolidation

techniques including vacuum hot pressing (VHP), cold pressing (CP) and sintering, hot isostatic pressing (HIP), cold isostatic pressing (CIP) and HIP, CIP and sintering, CIP and extrusion, and so on. VHP and HIP are the most widely used consolidation routes for Be (Figures 2.7 and 2.8).

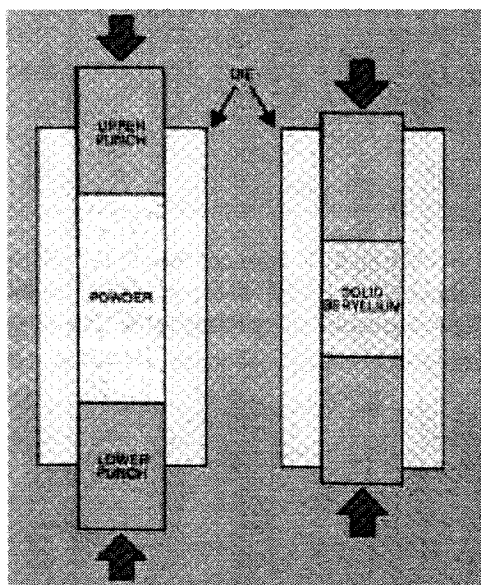


Figure 2.7 – VHP process. A column of loose Be powders is compacted under vacuum by the pressure of opposed upper and lower punches (left). Temperature is increased and the powder is simultaneously compacted and sintered in the final stage of pressing (right), bringing the billet to final density [53].

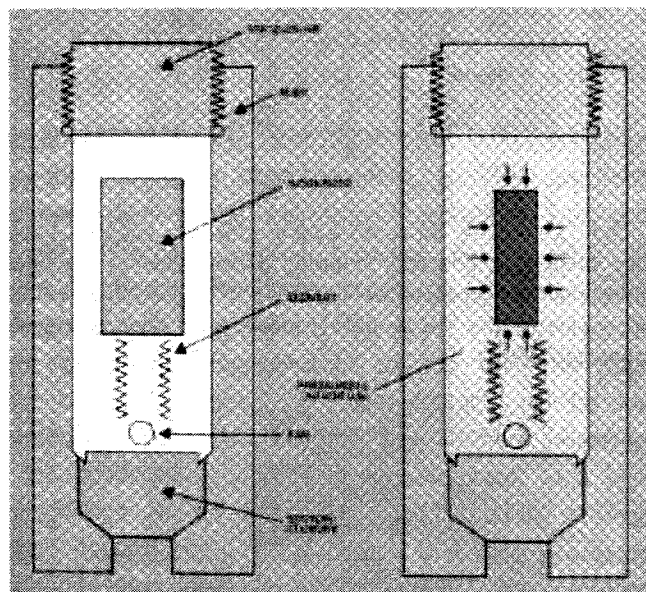


Figure 2.8 – Cutaway view of hot isostatic press. The powder container fits inside of a resistance-heated furnace that is installed in a pressure vessel. The pressurization medium is argon, an inert gas. Pressure is exerted evenly on the entire surface of the container. During the HIPing cycle (right), the container collapses, and the powder is simultaneously compacted and sintered to full density [53].

Mechanical properties of Be shapes obtained by VHP are anisotropic whereas simple shapes made by HIP have minimal anisotropy in mechanical properties. Complex near net shapes can be made by HIP. This process significantly reduces the amount of machining required to produce a finished part and at the same time impart properties that are superior to those of standard vacuum hot-pressed material.

### 2.1.2.3 Plasma-sprayed beryllium

The plasma spraying (PS) of Be is in essence one of the methods of consolidating Be powder: molten Be droplets are sprayed onto a substrate where they solidify into a partially dense deposit. However, it is expedient to discuss this process individually because of its attractiveness for a fusion reactor application both as a method for depositing Be coatings on damaged plasma facing Be surfaces and as an alternative to powder metallurgy produced Be to protect the FW [62, 66, 67].

ITER R&D activities showed that coating technologies can be also considered as a manufacturing method for the initial fabrication of PFCs [49]. A large variety of coating methods were considered potentially suitable for the Be armour of low and medium heat load PFCs. Table 2.1 lists the coating technologies investigated in the initial phase of the R&D programme. A brief description of the various methods can be found in [49].

Table 2.1 - Coating Technologies for beryllium.

Vacuum Plasma Spraying (VPS)
Rotating Rod Arc (RRA)
Vacuum Arc (VA)
Physical Vapour Deposition (PVD)

On the basis of the experimental results of R&D activities [49], VPS (Figure 2.9) has been selected as reference Be coating technology for low heat flux PFCs [66, 68, 69]. PS of Be involves a complex layering of individual splatted particles which creates a three-dimensional array of interweaving splats, unmelted particles, and entrained oxides. This layered structure results in anisotropic behaviour in both the thermal and mechanical properties of Be. The quality of the Be deposit and the coating adhesion depend on the characteristics of the powder feedstock material and on the large number of process variables (Figure 2.9) [49, 59, 66]. Powder produced by atomisation processes are used in PS of Be, since the spherical morphology of this powder allow easy feeding/flow of Be powder into the plasma-spray torch.

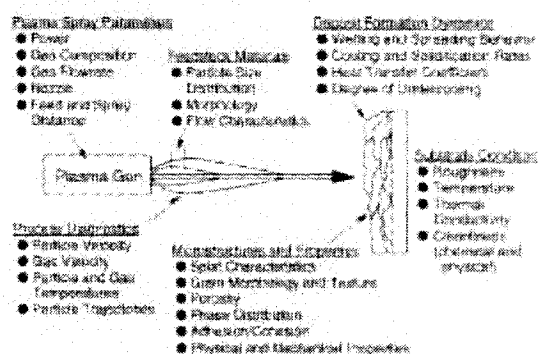


Figure 2.9 – VPS process and variables which can influence the quality of the coating. A feedstock coating material in the form of powder is melted with heat from a plasma torch that generates a non-transferred arc. The feedstock material is superheated and propelled at high speeds against the substrate by the hot ionised gas issuing from the torch. The process is done in a controlled environmental chamber at a reduced argon pressure [59].

## 2.1.3 ITER grades

### 2.1.3.1 Chemical composition

The design and R&D activities were focused on the characterisation of several grades of US and Russian Federation Be in ITER relevant condition [49, 70]. Table 2.2 lists the various grades of Be that were obtained from Brush Wellman and from Efremov Institute, St. Petersburg and that were tested in the frame of the present work [49, 52, 71 - 74].

The Brush Wellman Be S-65C is a VHP Be grade made from impact ground Be powder. [73].

The Russian Federation Be DShG-200 is a high purity distilled grade which is made by taking less than 200 micron distilled Be powder and hot pressing it to partial density and then punching to full density [73]. It has high thermal stress resistance, coarse grain structure and it is expected to show good neutron irradiation properties.

The Russian Federation Be TShG-56 is a technical purity grade made from less than 56 micron Be powder by hot pressing to partial density and then punching to full density [73]. It is a cheaper grade with intermediate properties; it has an intermediate grain size and is a compromise between TR-30 and DShG-200.

The Russian Federation Be TR-30 is a technical purity grade made from less than 30 micron Be powder by hot isostatic pressing to partial density and then punching to full density [49, 74]. It has been developed with respect to the best neutron irradiation behaviour concerning swelling. It has a fine grain structure, but due to high oxygen content it has relatively poor ductility [75].

The Russian Federation condensed Be is obtained by vacuum evaporation-condensation coating method. Deposited Be is characterised by coarse-grained (50-100  $\mu\text{m}$ ) columnar

structure [74, 76]. It has higher coefficient of thermal expansion values and is a material with more expressed anisotropy of thermal expansion in comparison with industrial powder Be. PS Be is made by VPS coating technology at Los Alamos National Laboratory.

Table 2.2 - Investigated beryllium grades [49, 52, 71, 73 - 77].

Grade	Producer	wt% Be Average	Wt% BeO Average	Production form	Consolidation process
S-65C	Brush Wellman	99.4	0.6	PM	VHP
DShG-200	Russian Federation	99.34	0.79	PM	VHP, punching
TShG-56	Russian Federation	99.10	0.95	PM	VHP, punching
TR-30	Russian Federation	97.64	3.2	PM	VHP
Condensed Be	Russian Federation	99.85	0.15	scrape & waste products	Condensed from vapour
Plasma Spray	Los Alamos National Laboratory	see table 4	see table 4	PM	VPS

PM = Powder Metallurgy; VHP = Vacuum Hot Pressed; HIP = Hot Isostatic Pressing;  
VPS = Vacuum Plasma Spray

First screening experiments based on thermal fatigue resistance [73] and thermal shock experiments [78] indicated that the most resistant grades are S-65C VHP and DShG-200. Therefore S-65C VHP was selected as the reference grade, also on the basis of its availability, better data base, and previous experience in JET. DShG-200 was selected as the back-up [49]. The standard chemical composition of some Be grades [49] is given in Table 2.3. Being produced from distilled Be powder, DShG-200 has the lowest BeO and impurity content. A typical chemical composition of Be powder used in PS Be and resulting Be plasma sprayed deposit on copper heat sink is given in Table 2.4 [49]. Differences in the chemical composition of the powder feedstock material used for the plasma-spraying operation and Be armour are attributed to the potential erosion and wear of system components used in the plasma spray operation which can contaminate the Be coating [68]. The observed increase in the Al and Cu contents were attributed to erosion of the copper anode inside of the plasma spray torch and erosion of Al parts inside of the powder feeders while the increases in the N, C and BeO were attributed to the commercial purity of the processing gases used during the plasma spraying process. [68].

Table 2.3 - Chemical composition of Be grades [71].

Element, wt.%	S-65C	DShG-200	TShG-56	TR-30
Be	99	99.34	99.10	97.64
BeO	0.98	0.79	0.95	3.2
Al	0.018	0.0045	0.013	0.015
C	≤0.1	0.077	0.077	0.05
Fe	0.09	0.024	0.10	0.12
Mg	<0.003	0.003	-	0.006
Si	0.026	0.013	0.014	0.013
Average grain size, μm	18-20	22-25	22-25	9

Table 2.4 - Chemical analysis of Be powder and Be coating material used in PS Be [49].

Element	Be Powder	Be on CuCrZr
*BeO	.34	.98
*C	.074	.104
Fe (ppm)	920	980
Al (ppm)	440	625
Si (ppm)	310	385
Ni (ppm)	110	105
Cu (ppm)	35	90
N (ppm)	80	395

\* wt.%

### 2.1.3.2 Thermophysical and thermomechanical properties

Although Be is an anisotropic metal, the physical properties of the polycrystalline grades can be considered, to a first approximation, as isotropic [79, 80, 81]. The recommended data on thermophysical properties of Be needed for the design assessment have been collected in ITER Material Properties Handbook (MPH) [82]. These properties are reported in Table 2.5. The thermomechanical properties of the ITER grade S-65C, which have also been adopted in the FE analyses (cf. Chapters 5-7), are collected in Table 2.6. The physical properties are in first approximation the same for the various Be grades.

Table 2.5 - Be thermophysical properties [82]

Melting point	1283 °C
Boiling point	2869 °C
Heat of fusion	1300 kJ/kg
Heat of vaporization	32827 kJ/kg
Vapor press.* [T=°C]	$\log (P_{\text{Be}}) = 11.192 + 1.454 \cdot 10^{-4} (T+273) - 1.6734 \cdot 10^4 / (T+273)$

\*recommended correlation

Table 2.6 - Be S-65C Thermo-mechanical properties - Best-fit equations [82]

Properties	Fitting equations [T = °C]	Temp. [°C]
Thermal conduct. [W/mK]	$189.8 - 0.2694 \cdot T + 2.5429 \cdot 10^{-4} \cdot T^2 - 1.0104 \cdot 10^{-7} \cdot T^3$	20 - 1000
Specific heat [J/kgK]	$1741.8 + 3.3358 \cdot T - 3.1125 \cdot 10^{-3} \cdot T^2 + 1.2748 \cdot 10^{-6} \cdot T^3$	20 - 1500
CTE* $\cdot 10^6$ [K <sup>-1</sup> ]	$11.0388 + 1.0859 \cdot 10^{-2} \cdot T - 4.4735 \cdot 10^{-6} \cdot T^2 + 8.6305 \cdot 10^{-10} \cdot T^3$	20 - 1200
Young's modulus [GPa]	$306.78 - 2.9281 \cdot 10^{-2} \cdot T - 4.5069 \cdot 10^{-5} \cdot T^2$	20 - 800
Density [kg/m <sup>3</sup> ]	$1823 - 0.06933 \cdot T - 1.5139 \cdot 10^{-5} \cdot T^2$	20 - 1250
Poisson's ration	$0.0715 - 2.5 \cdot 10^{-5} \cdot T$	20 - 800
Yield strength [MPa]	$224.64 + 0.0448 \cdot T - 4.1428 \cdot 10^{-4} \cdot T^2 + 8.5157 \cdot 10^{-8} \cdot T^3$	20 - 800

\*CTE = Coefficient of thermal expansion

**Emissivity.** Emissivity has an influence on temperature measurement by infra-red system (cf. Chapter 6). The emissivity of Be strongly depends on the surface conditions (BeO level, roughness, etc.). Even for the same grade, S-65C, used in experiments in Juelich and JET, the data show a large scatter. This effect is due to the different surface conditions resulting from different heat treatments during joining of Be to Cu and to mechanical treatments after the joining procedure. The data collected from the open literature, are presented in Figure 2.10 [49]. The analysis of the limited available data indicates that emissivity of Be increases with temperature.

At low temperature (RT-600°C) the emissivity depends on the presence of the BeO surface layer, which is a function of temperature and time spent in the oxidising environment and is removed e.g. by melting. Accordingly, emissivity values ranging from 0.1 to 0.6 are measured, even for the same grade in the same experiment. At temperatures of 600-800°C, the oxidation rate starts to become high and the emissivity increases rapidly to above ~0.4, reaching a value of 0.65-0.85 at temperatures >1000°C. This represents an intrinsically safe behaviour of the Be armour, which in accidental conditions is likely to be heavily oxidised.

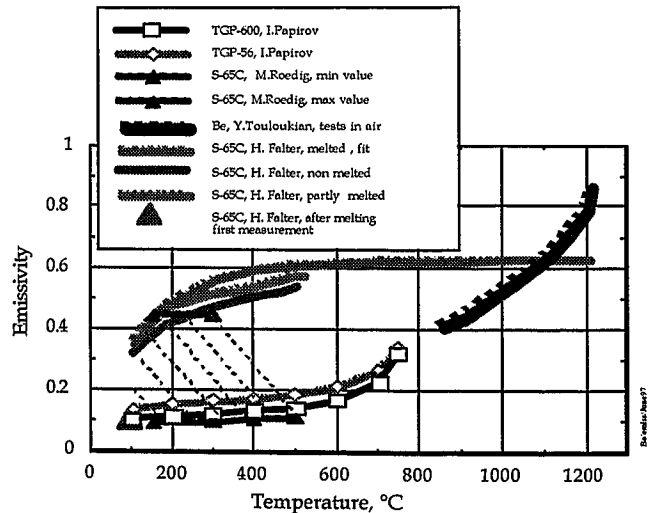


Figure 2.10 - Emissivity of beryllium [49].

## 2.2 Heat sink materials

A key property for the copper alloys to be used as heat sink material in the PFCs is a high thermal conductivity. For its elevated thermal conductivity, pure copper would be the best choice as heat sink material. However, its high sensitivity to radiation damage and low strength at moderate temperature do not allow copper to be used in a high neutron flux and in the presence of mechanical loads, which, although mainly taken by the structural material, are not negligible. Two families of copper alloys exhibit high thermal conductivity and strength and radiation resistance: precipitation hardened<sup>6</sup> (PH) and oxide dispersion strengthened<sup>7</sup> (DS) alloys. Within each class different alloys are commercially available [49]. As a result of the first stage of R&D, two materials have been retained as candidate heat sink material for the high heat flux components and for further investigation: CuCrZr among the PH alloys and

<sup>6</sup> PH alloys represent a wide family of heat-treatable alloys differing in chemical composition and/or in thermo-mechanical treatment. PH alloys reach an optimum in strength after a thermo-mechanical treatment involving first a solution annealing (SA) at high temperature to dissolve the alloying elements, then a water quench (WQ) to keep the alloying elements in supersaturated solid solution at room temperature, and finally an ageing (A) treatment at intermediate temperatures to decompose the supersaturated solid solution into a fine distribution of precipitates. Cold working (CW) of the supersaturated solid solution, if compatible with the component manufacturing cycle, would provide a better homogeneity of the precipitate distribution through the copper matrix and a higher strength after ageing.

<sup>7</sup> Dispersion-strengthened materials typically obtain their strength from a combination of cold working and the presence of a uniformly-dispersed insoluble particles. DS copper alloys are powder metallurgy products, characterised by a fine dispersion of nanometric second phase particles, that gives strength and thermal stability to the copper matrix. For dispersion strengthened copper, the dispersoid is Al<sub>2</sub>O<sub>3</sub> (alumina). The presence of insoluble ceramic particles suppresses the recrystallization and allows this class of material to retain its strength almost up to the melting point of the material. For DS copper this temperature is around 950°C.

GlidCop® Al25<sup>8</sup> among the DS alloys. Starting from the original specification, the composition, manufacturing process and heat treatment were optimised with the definition of the ITER grade (IG) specification: CuCrZr-IG and CuAl25-IG.

## 2.2.1 CuCrZr ITER Grade

Copper-chromium-zirconium is a precipitation-strengthened alloy, which have a good combination of thermal conductivity and strength in the temperature range of interest for ITER [49, 82]. It is a candidate for high heat flux components manufacturing when the correct heat treatment can be integrated in the component manufacturing cycle.

The main problems of CuCrZr alloys are the low ductility of irradiated material at temperatures below 120-150°C, the instability of precipitates that causes softening at irradiation temperatures >300°C and finally, the sensitivity of the material to the heat treatment.

The chemical composition and the recommended heat treatment of CuCrZr-IG can be found in [49]. Thermophysical and thermomechanical properties have been collected in the Material Properties Handbook [82]. Because there is a strong dependence of material properties vs. heat treatment, depending on the proposed application, the heat treatment is usually specified in accordance with required material properties [83-85]. During the component manufacturing (e.g. welding, brazing, HIPing, etc...), the base material is in general subjected to additional thermal cycles which may affect the physical properties of CuCrZr by dissolution and/or coarsening of the precipitates. If the manufacturing heat cycles can be made consistent with the recommended heat treatment or if the latter can be applied afterward, a complete recovery of base material properties occurs. The recommended data for the design analysis are given in Table 2.7.

Table 2.7 - CuCrZr-IG – Thermo-mechanical properties for design analysis [82].

Temperature [°C]	20	50	100	150	200	250	300	350	400	450	500
Thermal conduct. [W/mK]	379	373	365	359	355	352	351	351	352	354	357
Specific heat [J/kgK]	388	389	392	396	400	405	410	416	422	429	437
CTE*·10 <sup>6</sup> [1/K]	15.7	15.9	16.3	16.7	17.0	17.3	17.6	17.9	18.2	18.4	18.6
Young's modulus [GPa]	128	127	125	123	121	118	115	112	109	105	102
Density [g/cm <sup>3</sup> ]	8.92	8.91	8.89	8.86	8.84	8.82	8.79	8.77	8.74	8.72	8.69
Poisson's ratio	0.34	0.34	0.34	0.34	0.34	0.34	0.34	0.34	0.34	0.34	0.34
Yield strength [MPa]	297	293	285	277	268	257	246	234	222	208	194

\*CTE = Coefficient of thermal expansion

<sup>8</sup> GlidCop® is the commercial trade name for American version of dispersion strengthened copper. It is produced by an internal oxidation process: Al-25 refers to the grade which has an aluminium oxide content of 0.48 percent by weight. The material is produced through a powder metallurgy process in which a Cu-Al alloy melt is atomized into powder, then exposed to an oxidizing treatment whereby the Al combines with oxygen to form alumina (Al<sub>2</sub>O<sub>3</sub>) within the copper matrix. The treated powder is then consolidated to full density by hot extrusion or HIPing. Since there is an inherent residual amount of oxygen not combined with aluminium in the process, this material is subject to embrittlement from hydrogen. Boron is intentionally added to this alloy to scavenge the "free" oxygen and thereby avoiding embrittlement when the material is intended for hydrogen or vacuum exposure during fabrication or service.



## 2.2.2 CuAl25 alloy, ITER Grade

The CuAl25-IG is made optimising the commercial GlidCop® AL-25 LOX<sup>9</sup>-80 process whereby an improvement of ductility and reduction of anisotropy is achieved.

CuAl25-IG exhibits a good thermal stability up to almost the melting point and shows much less sensitivity to heat treatments compared to CuCrZr [86, 87]. This allows a wider flexibility in the use of different joining technologies for high heat flux components. However, a certain variation of the mechanical properties is observed as a function of different manufacturing procedures, test conditions and measuring laboratory.

The chemical composition and the recommended fabrication process of CuCrZr-IG can be found in [49, 88]. Thermophysical and thermomechanical properties have been collected in the Material Properties Handbook [82]. The recommended data for design analysis are reported in Table 2.8.

CuAl25-IG was selected as the first option for the primary wall because the stresses are within the design allowable including fracture criteria, and it has better thermal stability under the manufacturing heat treatment. For the divertor components, local stresses are very high due to high heat flux and existence of singularity zones that may result either in fatigue life or fracture limitation, in particular for the 20 MW/m<sup>2</sup> transients considered for the design. CuCrZr-IG, which has the same fatigue endurance and much better fracture toughness than CuAl25-IG is the recommended option [49].

Table 2.8 - DS Cu Al25 IG Physical Properties - Best-fit Equations [82]

Properties	Fitting equations [T = °C]	Temp. [°C]
Thermal Conduct. [W/mK]	$350 - 0.2612 \cdot T + 3.07 \cdot 10^{-4} \cdot T^2$	20 - 500
Specific Heat [J/kgK]	$383.3267 + 0.11413 \cdot T - 2.9794 \cdot 10^{-5} \cdot T^2$	20 - 500
CTE $\cdot 10^6$ [K <sup>-1</sup> ]	$16.0734 + 8.3710 \cdot 10^{-3} \cdot T - 3.4349 \cdot 10^{-6} \cdot T^2$	100 - 500
Young's Modulus [GPa]	$126.4176 - 3.7884 \cdot 10^{-2} \cdot T - 1.8237 \cdot 10^{-5} \cdot T^2$	20 - 500
Density [kg/m <sup>3</sup> ]	$8872 - 4562.8 \cdot 10^{-4} \cdot T - 8703.8 \cdot 10^{-8} \cdot T^2$	20 - 500
Poisson's Ration	0.343	20 - 500
Yield Strength [MPa]	$334.41 - 0.21416 \cdot T - 6.6692 \cdot 10^{-4} \cdot T^2$	20 - 450

\*CTE = Coefficient of thermal expansion

## 2.3 Be/Cu joining technologies

An extensive R&D program has been carried out to develop reliable joining technologies between Cu alloys and Be in ITER PFCs (cf. Chapter 1) [89]. Be in PFCs is used under widely varying operational conditions (cf. Chapter 1). Because of the different functions and hence of the different neutron and heat loads the design of the PFCs includes various combinations of joints between Be armour and Cu alloy heat sink materials [90]. The joints must withstand the thermal/mechanical and neutron loads, the cyclic mode of operation and operate under vacuum, while providing an acceptable design lifetime and high reliability [91]. A critical issue related to joining processes is the compatibility of the joining heat cycle with the overall manufacture process of PFCs, in particular with the requirement to maintain adequate properties of CuCrZr alloys. The main problem of bonding Be to Cu alloys is that

<sup>9</sup> LOX refers to a reduced oxygen content process whereby 200 wppm elemental boron is added to the powder prior to consolidation and -80 refers to the fineness of the powder prior to consolidation.



Be reacts with almost all metals at moderate and high temperatures and forms brittle intermetallic phases that are detrimental for the joint reliability and the fatigue lifetime. The direct interaction and reactivity of Be with Cu is very high in comparison with other metals. Recent studies [92, 93] have demonstrated that intermetallic phases are already formed at 350-400°C and with temperature increasing the rate of interaction increases significantly. Only a few metals do not form stable beryllides below 760°C, i.e. Al, Si, Zn, Ag and Ge. The goal of the joining technology developments is to avoid or control BeCu intermetallic formation for an increased reliability and lifetime of the joints [94].

To solve the problem of the extensive formation of the brittle phases and provide the good quality of Be/Cu joint the different approaches have been studied. These approaches could be summarized as following [91]:

- The use of materials as fillers or interlayers between Be and Cu alloy which not form intermetallics phases with Be (e.g. Al, Ge, Si, AlSi);
- The use of diffusion barriers materials (Ti, Cr, Ti/Ni, Al/Ni, Ti/Cu, Al/Ti/Cu, Cr/Cu) with less affinity to the formation of beryllid intermetallics (typically for this type of joint HIP is used as joining procedure at temperature range 500-850°C);
- The use of low temperature joining processes (less than 500°C) to avoid or control the formation of intermetallic phases;
- Direct bonding of Be to Cu alloy during short time at moderate temperatures (~ 500-700°C) e.g. explosion bonding [95, 96], joint rolling [95], vacuum plasma spray [97, 98], or joining of Cu interlayer to Be at low temperature (e.g. electroplating) and next joining to Cu alloy by low temperature HIP [91].

Low temperature joining processes have the additional advantage of not overageing the CuCrZr alloy and reducing the residual stresses.

The list of the joining technologies proposed and investigated during the ITER EDA is given in Table 2.9 [49].

Table 2.9- Be/Cu joining technologies [49].

Type of joint	Process Parameters
Diffusion soldering	~ 690°C, few min
Brazing, CuMnSnCe	720°C, few minutes
HIP, Mo/Al-interlayer	500°C, 1.5 h, 100 MPa
HIP Ti interlayers	800-850°C, 1h, 100 MPa
HIP without diffusion barrier	850°C, 2h, 140 MPa
Cu electroplating onto Be + Diffusion Bonding	450°C, 0.5 h, 150 MPa
Brazing: Cu-Mn	~ 930°C, few min
Brazing: CuInSnNi	~ 800°C, < 1 min
Brazing: Ti-Zr	~ 800°C, few min
Diffusion bonding	~ 800°C
Explosion bonding	RT-700°C
Joint rolling	800°C, 30% deformation
Cu electroplating onto Be + Low Temperature HIP	450°C, few hours
Plasma Spraying with/out diffusion barriers	substrate temp. >500°C
HIP AlBe - Al/Ti - Expl. Bond to Cu	~ 625°C,
HIP ass. brazing Al-Si - Al/Ti - Expl. Bond to Cu	~ 625°C,
Copper brazing: Ag-Cu	700-980°C, tens min

Some of above-mentioned technologies have been cancelled in stage of initial development due the bad results; the most promising technologies have been used for the manufacturing of the representative mock-ups, which have been tested at conditions simulating ITER environment. The preliminary results of these tests [49] can be summarized as following:

- High temperature HIPing and VPS are recommended as the most promising methods for the large surface and the low heat flux of the Be PW, both giving adequate performance and ease of fabrication;
- For the Be Port Limiter, it seems that HIP joining with a compliant layer is a viable technique;
- Brazing technologies could be applied to low and intermediate heat flux components, but the scaling of brazing to the manufacture of large and complex components is still to be demonstrated.

This recommendation on joints has to be confirmed on larger and more representative mock-ups and the influence of neutron irradiation has to be studied. For the final selection, cost and reliability will also have to be considered [99, 100].

### 2.3.1 Brazing

Brazing technologies have demonstrated promising results during the ITER R&D. Brazing is a process used to join materials by introducing an interfacial metal that has a melting point lower than that of the base metals [94]. The prerequisites to a successful braze include:

- a braze alloy that wets the materials being joined,
- filler metals that are compatible with the substrate materials and the service environment,
- materials that are compatible and do not form brittle intermetallics up to the liquidus temperature of the braze alloy,
- surfaces that are clean and free from contaminants (such as oils and oxides) and remain clean during the brazing process, and
- a joint design that provides close proximity between the two materials to be joined and designed for shear.

Wetting is described as the ability of the filler material to adhere to the surface of the substrate in the liquid state. If wetting occurs, a thin film of the filler material is drawn by capillary flow along the joint area resulting in a void free braze joint. Besides wetting, the ability for the filler metal to flow along the joint region is important. Among others, the viscosity is dependent on the temperature, surface conditions, melting range of the filler metal, and the reaction of the filler metal with the substrate.

During the braze process interactions are occurring which influence the flow characteristics including: alloy formation between the filler metal and the substrate; diffusion of the materials; grain boundary precipitation dissolution; and the formation of intermetallic compounds. These factors are usually minimised by selecting the correct filler metals and reducing the temperatures, times, and cooling rates.

Filler metals are selected based on several characteristics including: the ability to wet the substrate materials; melt temperature compatible with the substrate materials; ability to alloy or react with the substrate materials without forming brittle intermetallic compounds; and proper flow characteristics at the brazing temperatures. An ideal brazing system is one in which embrittling intermetallics are not formed but there is sufficient mutual solubility to permit the formation of a diffusive interface.

Ideal situations are difficult to achieve and Be tends to have low mutual solubility with potential braze materials.

Brazing of Be to Cu-Cr-Zr presents several problems, associated with the presence of a highly tenacious and stable layer of BeO on the surface of Be components and with the intermetallics that form between Be and heavy metals, such as copper, silver and nickel, which are the prime constituents of established brazing alloys [101 - 104].

For the Cu/Be joints, the brazing filler metal must possess the following properties: the ability to wet the surface of the copper base metal and Be and form a strong, sound bond; a melting point compatible with those of heat sink material and Be; the ability to form brazed joints possessing suitable high temperature properties; a composition well matching those of heat sink material and Be. Previous studies demonstrated that Be wetting is promoted by increasing temperature.

Surface preparation is a very important aspect of the Be brazing process. Due to its high affinity for oxygen, an adherent refractory oxide film (BeO) rapidly forms on Be surfaces inhibiting wetting, flow and melting during brazing. Therefore surfaces must be properly cleaned prior to joining. However, if the surface finish of the heat sink material is too smooth, the filler metal may not be distributed throughout the entire joint and may leave voids. Very smooth or polished facing surfaces have to be roughened to assure adequate flow of the filler metal throughout the joint. For preventing oxidation during joining operation the brazing process has to be performed in a vacuum system. Standard methods of Be brazing are based on an aluminium or copper/silver brazes. Aluminium brazes have the advantage of not forming brittle intermetallic compounds with Be but are not compatible with copper substrates and have lower strengths than copper/silver brazes.

#### **2.3.1.1 Vacuum induction brazing Incusil-ABA**

At brazing temperature above 700°C (which is typical for brazing with Ag or Cu based brazing alloys) BeCu intermetallic formation takes place. A way to reduce this process is the reduction of the reaction time.

The Be/Cu joint quality after conventional furnace heating and induction heating with Ag-Cu brazing alloy has been studied [105] and it was concluded that the quality of joints is much better after induction brazing. Induction brazing offers the advantages of high heating rates and short, accurately controlled dwell times. With induction brazing it is possible to bring the Be and CuCrZr to the liquidus temperature of the braze in a very short time. This can prevent overaging of the CuCrZr and it also prevents the formation of intermetallics between the braze and the Be.

Brazing techniques using the silver-based filler metals have been studied at the Joint European Torus (JET) Undertaking Facility in Abingdon, Oxfordshire [100, 106, 107]. In this study several filler metals were explored using similar parameters for joining CuCrZr alloy to Be. Heating was accomplished using induction coils in vacuum ( $5 \times 10^{-5}$  Torr). The pressure on the braze assembly was 0.3 MPa. Comparisons of shear strength values for all braze assemblies clearly showed the superior performance of the Ag-Cu alloy InCuSil-ABA brazed at 720°C for 60 seconds. Incusil ABA is an active braze containing Ag (59%) Cu (27.25%) In (12.5%) Ti (1.25%) with solidus and liquidus of 605°C and 715°C. The beneficial effects from the active titanium content was investigated and titanium was considered to be gettering the outgassing products from the brazed joint. Indium was associated with the silver in both the matrix and the interaction with the copper workpieces [100, 106]. The essential features of the joint microstructures are illustrated schematically in Figure 2.11.

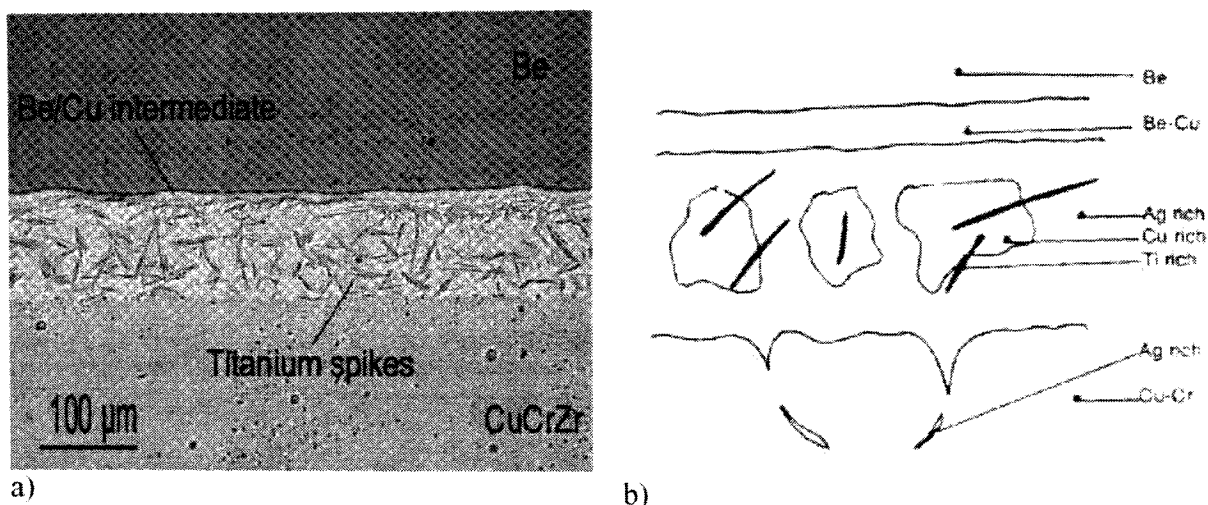


Figure 2.11 - InCuSi1 Ti brazed joint: a) metallography; b) schematic illustration. The braze alloy is based on the silver-27.25% copper eutectic and the braze had a silver rich matrix containing copper rich islands. Within the matrix needles or plates of a titanium-copper compound are recognisable. A Be-Cu reaction product layer is formed at the Be/braze interface. At the braze/copper workpiece interface there are some grain boundary grooving and penetration by silver [100, 106].

The good quality of the Be/Cu joints produced by induction brazing with use of Incusil ABA brazing alloy has been reported in [100]. The shear strength at optimal brazing temperature which has been determined at  $\sim 720^{\circ}\text{C}$ , was  $\sim 120\text{-}160\text{ MPa}$  in temperature range  $20\text{-}500^{\circ}\text{C}$ . This strength was equal or better than strength of Be and CuCrZr alloy.

### 2.3.1.2 Vacuum induction brazing CuMnSnCe

Due to the incompatibility with the fusion reactor environment silver may be considered unacceptable in filler alloys for PFCs. To avoid poisoning of the cryo-pumps, elements with high vapour pressure, e.g. Cd, are not allowed as brazing/filler materials, nor those which form these elements by neutron transmutation, such as Ag or Au [49]. Therefore, the use of silver-based alloys has been forbidden for ITER application due to the Cd transmutation during neutron irradiation. The burn up of silver in a high neutron flux is described as producing  $1.64 \times 10^{22}$  atoms per  $\text{cm}^3$  of braze [94]. After only 168 s of thermonuclear operation the maximum allowable Cd in the plasma would be exceeded. Furthermore, over time Cd transmutation within a silver-base filler metal could diffuse out of the braze joint area and evaporate into the vacuum chamber.

Different types of silver-free brazing technologies have been developed for ITER application. Brazing alloys based on Al, but also on intermetallic forming elements like Cu, Mn, Ce, Sn etc. have been proposed. In the latter case the brazing temperature was kept low and the brazing time short, in order to limit the metallurgical interaction between braze and Be. For this reason, all these alloys have been applied together with "fast" heating technologies (via induction brazing or heating by e-beam). Typically the shear strength of these joints is less than the strength of joints produced with Ag brazing alloys. Nevertheless the metallurgical quality and, more important, high heat flux performance were found to be acceptable.

A vacuum brazing process using a silver-free alloy CuMnSnCe which also showed promising thermal fatigue performance of the joints, has been developed and assessed by GEC-Marconi Ltd., UK [101, 102]. The proposed braze has the composition 60Cu 9Mn 30Sn 1Ce (wt%) and a melting range of  $640\text{-}700^{\circ}\text{C}$ . The addition of cerium greatly improves the alloy wetting on oxidised metal interfaces.

## 2.3.2 Hot Isostatic Pressing

An other technique for joining beryllium onto copper alloy [108-110] is the Hot Isostatic Pressing (HIP) diffusion bonding. HIP diffusion bonding of Be to GlidCop® has been developed both for low and high in-service temperature [111]. Diffusion bonding is a process that produces solid-state joining by diffusion under pressure and temperature [112, 113]. HIP diffusion is particularly suitable for large surfaces to be joined and complex geometries. It allows high quality junction that is necessary for a good heat transfer through the interface.

Direct diffusion bonding between dissimilar materials may be sometimes difficult to achieve. The thermal and mechanical properties of a joint are mainly dependent on the interface microstructure and its stability under service conditions. The joining process parameters, i.e. temperature, pressure and time, must take into account the in-service requirement, and the mechanical as well as the metallurgical properties of each material. The reactivity between Be and Cu is very high: reactive layer begins to appear at the interface at 400°C and becomes very large at 700°C. It is recommended that temperature should be lower than 620°C for direct Be/Cu diffusion bonding. It should be noted that in operation the joint temperature may be exposed to temperatures higher than 400°C during transient events. Thus, it seems that interlayers have to be used, to avoid the excessive growth of brittle Cu-Be intermetallics. The use of silver as an interlayer is out of consideration because of its transmutation to cadmium under neutron flux. Aluminium and titanium interlayer have been used.

## 2.4 Lifetime design issues for PFCs

### 2.4.1 Erosion lifetime

A major issue for design and construction of a nuclear fusion reactor with magnetically confined plasma is the interaction of the hot plasma with the material of PFCs [114 - 117]. The plasma wall interaction processes lead to two main problems:

- the contamination of the plasma by impurities released from the blanket structure; and
- the alteration of the material of PFCs by the particle bombardment and the high energy flux which may limit significantly the lifetime.

Erosion/ redeposition is one of the crucial physical issues to be faced in the design of a fusion reactor such as ITER. The erosion of PFCs produces impurity influxes, which degrade fusion performance and the redistribution of wall material due to poloidally asymmetric transport. This results in areas of the first wall and divertor that experience net erosion and other areas where there is a build-up of redeposited material. The net erosion not only limits the lifetime of wall components but also determines the tritium wall inventory via co-deposition of the tritium along with eroded material in regions of re-deposition. Different erosion mechanisms such as physical sputtering and thermal erosion during disruption and transient events are responsible for the erosion lifetime of the individual ITER PFCs. Local erosion effects, such as erosion due to electric arcs and hot spot formation, can also play a significant role.

#### 2.4.1.1 Physical sputtering

The main erosion process for Be surfaces exposed to a plasma is physical sputtering, i.e., the removal of surface atoms due to the impact of energetic plasma neutrals and ions, including the fuel ions, impurity ions such as carbon and oxygen, and the beryllium ion themselves. When a ion or neutral atom is hitting a solid surface, it follows a complicated trajectory because of collisions with the lattice atoms in the solid. During this collision cascade the incident particle will be reflected, if its path leads it back to the surface, or trapped either at grain boundaries or at vacancies in the bulk.

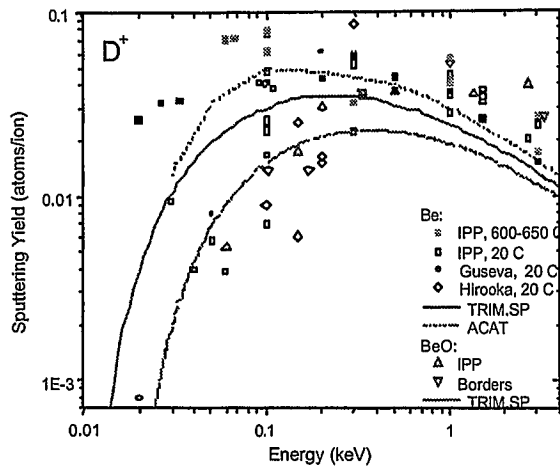


Figure 2.12 - Energy dependence of the sputtering yield of Be and BeO bombarded with  $D^+$  at normal incidence [49].

In addition, if a surface atom receives sufficient energy from a collision, it is sputtered away from the solid. This is only possible if the energy of the incident particle is above a threshold energy  $T_e$ . The database for beryllium physical sputtering is reasonably well established, including measurements and calculations [49].

In Figure 2.12 the energy dependence of the sputtering yield of Be and BeO bombarded with D at normal incidence is shown. It includes experimental data and results obtained with computer simulation. BeO surfaces are reported to have significantly reduced sputtering yields [49] compared to pure Be.

The dominant effect seems to be an increase in the surface binding energy leading to an increase in the threshold energy for sputtering, from about 8 eV to 30 eV. A conservative approach to estimate the Be release from the first wall of ITER should assume sputtering from non oxidised beryllium. However, the function of Be is to provide a low-Z wall surface which getters oxygen. Be is reported to diffuse through BeO at temperatures above 700K, yielding fresh surface layers for gettering. Thick BeO layers will eventually accumulate. The mechanical properties of the layers are not well known. Note that large area oxide coverage on the first wall will lead to oxygen release by sputtering.

#### 2.4.1.2 Plasma disruption

A plasma disruption is a sudden, uncontrolled termination of the plasma current and plasma confinement, with the thermal and magnetic energy contained in the plasma being dumped on the FW and divertor plates [116]. The basic phenomenology and causative factors for disruption in tokamaks can be described in terms of the three classical phases of a disruption: precursor development, thermal quench and current quench.

Disruption typically proceeds with onset of a *precursor phase* wherein slowly evolving external causes (e.g. radiative losses) initiate onset of unstable distortions of the shape of the plasma/magnetic field system. These distortions in turn result in destruction of the internal magnetic surfaces which leads to an ensuing rapid loss of plasma thermal energy (*thermal quench*). The thermal quench is followed by a *current quench* in which rapid decay of the plasma current occurs. Plasma energy loss in this phase is caused primarily by more-or-less uniform impurity radiation losses to the surrounding vacuum vessel or first-wall surfaces.

This explosive-like phenomenon, which lasts for a few milliseconds ("fast" disruption), results in a substantial increase of the heat flux to the PFCs for very short times, causing significant Be armour erosion due to vaporisation and partial loss of melt, brittle destruction, but having little thermal effect on the actively cooled heat-sink substrate and coolant.

Another feature of disruptions is the generation of fast beams of "runaway" electrons which might drill holes in the PFCs. *Runaway electrons* are electrons in a plasma that gain energy from an applied electric fields produced by disruptions at a faster rate than they lose it through collision with other particles. These electron tend to "run away" in energy (not position) from the cooler remainder of the background plasma, because the collision cross-section decreases as the particle's velocity increases, so that the faster the particles goes, the less likely it is to be stopped. A conversion up to 80% of plasma current to runaway electron current following

a disruption is possible. Subsequent loss of the runaway current to the surfaces of in-vessel components can result in localized high surface and near-surface power loadings.

The number of disruptions that could be accommodated would depend on the occurrence of mitigating effects resulting from vapour shielding, on the extent of melt layer loss and on the redeposition pattern.

#### 2.4.1.3 Vertical Displacement Event

At some locations, the PFCs must also withstand a certain number of so called “slow” high-power plasma thermal transients caused by “loss-of-vertical-control” (VDE), whose duration is anticipated to be much longer than that of disruptions, and of the same order as the characteristic thermal diffusion time of the actively cooled component itself.

VDEs from loss-of-control (hot-plasma) start with appreciable plasma thermal energy and with a slow drift phase and onset of wall contact that then leads to high plasma energy deposition, typically  $\sim 60 \text{ MJ/m}^2$ , over times up to 300 ms.

In contrast to fast disruptions, such “slow” plasma transients not only produce substantial erosion of the armour through vaporisation and melting, but lead to large heat flux propagation from the armour to the heat sink and to the coolant, potentially resulting in high temperatures and stress at the interface between the armour and the heat sink and in severe changes in the coolant heat removal capability.

‘Slow’ high power transients resulting from VDEs result in high armour and heat sink temperatures and severe surface erosion of the tile because of vaporisation and partial loss of the melt layer.

During a VDE, the plasma comes in contact with the limiter component and starts to be scraped off. This effect induces a fraction of the plasma to flow in the scrape-off layer, i.e. in the outer layer of a magnetically confined plasma (ca. 2 cm thick), where the field lines penetrate a material surface (limiter) rather than close upon themselves. Current flowing in this region (*halo current*) can intercept a material surface, where the current will take the path of lowest electrical resistance, causing intense heating and deformation of the material.

Figure 2.13 shows an axisymmetric simulation of a loss-of-control VDE in ITER developed with the Tokamak Simulation Code (TSC) modeling code.

The ITER PFCs, vacuum vessel, and magnet system must be designed to withstand several thousand plasma disruptions, and also a lesser number ( $\sim 100$ ) of plasma VDEs due to loss of vertical equilibrium control.

The combination of the effects of plasma disruptions and VDE pose a challenging and interconnected set of thermal, structural and lifetime design issues for the ITER in-vessel plasma-facing-components and their supporting structures [118].

Design of these components and evaluation of their performance requires specification of disruption, VDE and runaway conversion parameters. Physics R&D has been carried out for

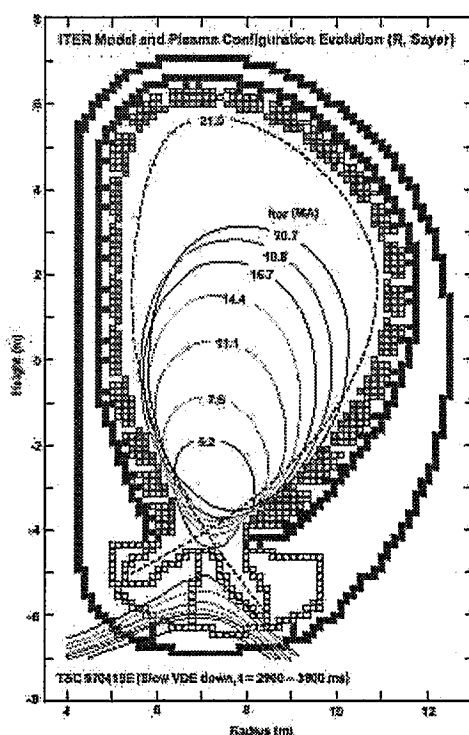


Figure 2.13 - Plasma equilibrium evolution for a loss-of-control VDE in ITER, simulated with TSC code [116].

developing design specifications on disruptions, VDEs and runaway electrons. Design basis specifications for plasma-wall interaction are summarized in Table 2.10.

Table 2.10 - ITER Disruption and disruption-related design basis [116, 119].

Event	Key Characteristics	Major Consequence(s) and/or comment(s)
Plasma disruptions	frequency: ~10-30%; Number in BPP (~11000 pulses) = 500; thermal energy $W_{th}=1\text{GJ}$ ; thermal quench duration: 1-10 ms; magnetic energy $W_{mag}=1\text{GJ}$ ; current quench duration: 50-1000 ms; max. current decay rate: 500 MA/s.	<ul style="list-style-type: none"> <li>- vaporisation (and also melting for metals) and brittle destruction of divertor targets, and nearby surfaces;</li> <li>- during the thermal quench, 80-100% of the thermal energy (<math>W_{th}</math>) is transported by conduction to divertor; 30% by radiation to first-wall or conduction to baffle;</li> <li>- during the ensuing current quench phase, 80-100 % of the energy (<math>W_{mag}</math>) is transferred to the first-wall by radiation, with a poloidal peaking factor of ~2; 20% by conduction and localised radiation during VDEs;</li> <li>- initiates VDE<sup>10</sup> and runaway conversion.</li> </ul>
VDEs (following disruption thermal quench) <sup>10</sup>	thermal energy $W_{th} \leq 1\text{GJ}$ ; magnetic energy $W_{mag}=1.1\text{GJ}$ ; duration = current quench duration; direction = up or down (depending on changes of plasma current and inductance); halo current $\leq 40\%$ .	<ul style="list-style-type: none"> <li>- follows each disruption;</li> <li>- slow current quench <math>\rightarrow</math> worst VDE;</li> <li>- part of the magnetic energy (<math>W_{mag}</math>) is lost to the first-wall;</li> <li>- produces in-vessel halo currents and forces on in-vessel components.</li> </ul>
Loss-of-equilibrium-control VDE	thermal energy $W_{th} \leq 1\text{GJ}$ ; magnetic energy $W_{mag}=1.1\text{GJ}$ ; frequency: 1% of pulses; drift = 1-5 s to wall contact onset: first-wall contact initiates H-mode loss, $W_{th}$ loss, melting, rapid current quench or disruption.	<ul style="list-style-type: none"> <li>- initiated by poloidal field control failure;</li> <li>- electromagnetic effects (halo current/vertical force);</li> <li>- major thermal effects on first-wall;</li> <li>- affected first-wall region: upper/inside or divertor entrance baffles.</li> </ul>
Runaway (RA) current conversion	knock-on avalanche; $E_{RA}=10-15\text{ MeV}$ , up to 15 MA; $W_{th}=500\text{ MJ}$ { $W_{th}=60\text{ MJ}$ for ITER FEAT}	<ul style="list-style-type: none"> <li>- may occur following disruption, loss-of-control VDE or fast plasma shutdown;</li> <li>- local damage effects are potentially severe;</li> <li>- onset and magnitude may be sensitive to MHD loss effects;</li> <li>- magnitude of runaway current, FW deposition and total RA thermal energy to FW are predicted to be sensitive to plasma MHD<sup>11</sup> loss effects;</li> <li>- toroidal localisation depends on first-wall alignment;</li> <li>- shutdown species will influence runaway electrons current</li> <li>- substantial uncertainties.</li> </ul>

<sup>10</sup> The major changes in the plasma current and pressure profiles that occur following onset of disruption typically result in a loss of vertical equilibrium and plasma shape control (MHD). The vertical control is usually lost following onset of rapid current quench. In this after-disruption control loss situation, in which most of the plasma thermal energy is lost before the onset of vertical motion, the resulting event is called after-disruption (cold-plasma) vertical disruption (VDE).

<sup>11</sup> Unstable distortions of the shape of the plasma/magnetic field system.



## 2.4.2 Thermal fatigue

Due to the high heat fluxes arriving at the FW of the PFCs and due to the necessity to cool these parts, there will be large thermal gradients in these structures, which generate considerable thermal stresses. Thermal stresses result when the change in dimensions of a member as the result of a temperature change is prevented by some kind of constraint [120]. As a consequence of the cyclic operation of ITER, whenever PFCs are heated, as during start up, and cooled, as during shut down, the resulting thermal gradients give rise to pulsed stresses. The continuous change of such stresses, due to the operational cycles of the components causes a thermal fatigue. Under these circumstances it is possible that failure occurs at a stress level considerably lower than the tensile or yield strength for a static load. The stress range will depend mainly upon the thermal loads and the physical properties of the material such as the coefficient of expansion, the thermal conductivity, the elastic modulus and so on.

Thermal fatigue seems to be the main concern of the ITER FW [73, 121 - 124]; the PFCs work under fatigue conditions, which influence the lifetime of the material. For predicting the lifetime of the PFCs, beside thermo-mechanical analyses of PFCs [125] for evaluating the self-induced stresses caused by a temperature gradient, thermal fatigue experiments have been performed during the ITER R&D [126 - 135].

## 2.5 Neutron irradiation effects

The investigation of neutron irradiation influence is very important for prediction of the lifetime of Be armoured PFCs. High energetic neutrons can displace atoms from their regular lattice sites and thus change the physical and mechanical properties of materials.

Irradiation conditions in fusion reactors are different from typical irradiation conditions in fission reactors. The flux of neutrons for unit energy is four times greater in a fusion reactor than in a fission reactor. The energy of the neutrons is higher (14 MeV) and therefore radiation damage in fusion reactor is much more severe than in a fission reactor.

Special analysis is required to predict property changes in fusion environment based on data from fission irradiation [136]. However, there is expected to be an overlap in energy between fission test reactor neutron spectrum and neutron spectrum produced by reflection of 14 MeV neutrons from the ITER stainless steel supporting structure, so testing in existing fission reactors may provide valuable baseline data [137].

The degradation of the Be properties by neutron irradiation could lead to a decrease in the erosion lifetime, to a loss in the mechanical integrity of the material itself and in the joining with heat sink. This would lead to a loss of the required functions as armour material in protecting the cooled structures and avoiding plasma contamination by impurities.

### 2.5.1 Basic interaction phenomena between radiation and solids.

#### 2.5.1.1 Types of energy loss

All macroscopically observed radiation effects are caused by one or more of three elementary interactions between the radiation and the atoms of the solid: elastic collisions, electronic excitations, and nuclear reactions [138- 140]. When a particle of initial energy  $E$  traverses a distance  $dx$  in a solid, these interactions result in an energy loss  $dE$ , characterized by the stopping power  $dE/dx$ , given by:

$$\frac{dE}{dx} = \frac{dE}{dx}|_d + \frac{dE}{dx}|_e + \frac{dE}{dx}|_n$$

The term  $dE/dx|_d$  refers to elastic collisions in which a bombarding particle transfers a recoil

energy  $T$  to a lattice atom (called the primary knock-on atom, PKA). If  $T$  is larger than  $T_d$ , a material-dependent threshold energy, the PKA can leave its original site, thereby creating a vacancy-interstitial (Frenkel) pair.

The term  $dE/dx|_e$  refers to losses due to excitation, ionization, or exchange of electrons in the target. In insulators the electronic losses can cause permanent property changes, whereas in metals all electronic excitations are quickly thermalized.

The term  $dE/dx|_n$  describes inelastic collisions between the bombarding particle and the nuclei of the solid that set in above an isotope-dependent threshold energy  $E_h$ . For most elements,  $E_h$  is in the MeV range.

### 2.5.1.2 Structure of point defects

A permanent displacement of lattice atoms occurs if the recoil energy transferred from a bombarding particle exceeds the material-dependent threshold energy  $T_d$ .

After receiving a recoil energy  $T > T_d$ , the PKA starts a so-called replacement collision sequence by pushing out one of its neighbours, which in turn replaces its neighbour, and so on. This kind of shock wave travels with supersonic velocity along an atomic row until so much energy has been lost to the surrounding lattice that the last atom in the sequence does not have enough energy to displace its neighbour, and thus tends to return to its starting point.

This site, however, is occupied by the preceding atom in the row, so an *interstitial* must be formed there while a *vacancy* is left back in the original site of the PKA.

In most metals, the stable self-interstitial atom has the so-called dumbbell configuration in which two atoms share a lattice site (Figure 2.14). Because there are "easy" and "difficult" directions for starting a replacement collision sequence, the threshold energy for displacement is direction-dependent.

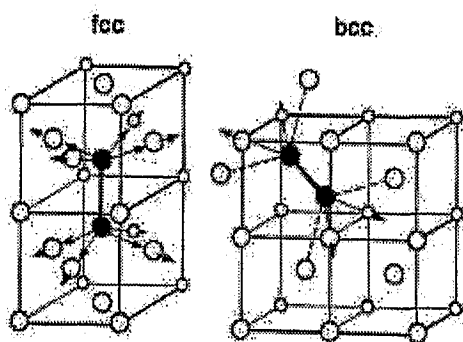


Figure 2.14 - Configuration of self-interstitial atoms in faced centered cubic (fcc) and body centered cubic (bcc) metals. For clarity, the two dumb-bell atoms are shown differently from the surrounding atoms [138].

## 2.5.2 Primary interactions of fusion neutrons with metallic materials

The interactions of fusion neutrons with the atoms of metallic structural materials cause two types of primary defects [141]:

- vacancies and interstitial atoms in and around displacement cascades; and
- foreign elements as reaction products of nuclear transmutations.

For neutrons, as uncharged particles, the electronic losses vanish.

### 2.5.2.1 Defect pattern produced by fusion neutrons

Structural fusion materials are exposed to high-energy neutrons, transferring recoil energies that are much larger than  $T_d$ . In this case the PKA, during slowing down, will by itself displace neighbouring atoms in the lattice, thereby creating a so called *displacement cascade*. This is a hierarchy of secondary, tertiary, etc., displacements from which, after some atomic rearrangements, a stable defect pattern evolves.

Since the sequence of these events lasts only some 10 ps, it cannot be followed experimentally and our knowledge of the defect production process mainly stems from computer simulation studies. The stage in evolution of defect pattern produced by fusion neutrons is reported in Table 2.11 and the main features can be summarized as follows. During slowing down, a high-energy PKA generates secondary, tertiary, and higher generation recoils in the lattice. The spatial and temporal region of these events is termed a *collision cascade*. Depending on the PKA energy collision cascades can develop lobes or break up into *subcascades*, which can be considered as new independent units of the damage (Figure 2.15). The collision-cascade phase ends when all recoils have slowed down to energies below  $T_d$ , so they cannot knock out further lattice atoms. It is succeeded by the so-called *spike phase*, where the cascade is considered a local region in which the majority of the atoms are in violent motion. From there on, a temperature,  $T_{sp}$ , can be defined by equating the average kinetic energy of the atoms in the spike core to  $3/2k_B T_{sp}$ . The central spike temperature typically reaches values of several times the melting temperature  $T_m$ , and thus the existence of a (hot) molten zone in the spike has to be considered. The atomic density within the core of a nascent spike is reduced whereas a ridge of compressed material at the periphery of the spike is built up (Figure 2.16). After about 0.3 ps the spike region begins to cool down, and after a typical time of around 3 ps,  $T_{sp}$  has fallen below  $T_m$ . In this *spike-relaxation* phase the core volume changes from a superheated to an undercooled liquid, while in the outer regions stable interstitial defects are formed. During this stage intense atomic mixing takes place. The free volume necessary for vacancy formation in the molten core is reduced by a partial backflow of compressed material in the shock rim. Only so many vacancies survive, as stable interstitial atoms have been deposited outside the melt zone. When the spike core solidifies the vacancies are quenched in and form the so-called *depleted zone* in the spike center. The defect pattern remaining when the temperature in the spike center has dropped to ambient is interstitials (single and clustered) in the periphery, and vacancies (single and clustered) in the center of the original collision cascade. A fraction of these defects can escape subsequent intracascade recombination ("escaping" or "freely migrating" defects) and interact with the microstructure of the material.

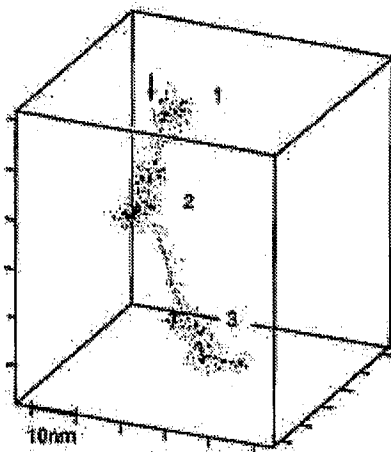


Figure 2.15 - Three-dimensional view of a 100-keV collision cascade in Cu generated by the MARLOW computer code showing three well separated subcascades with lobes [138].

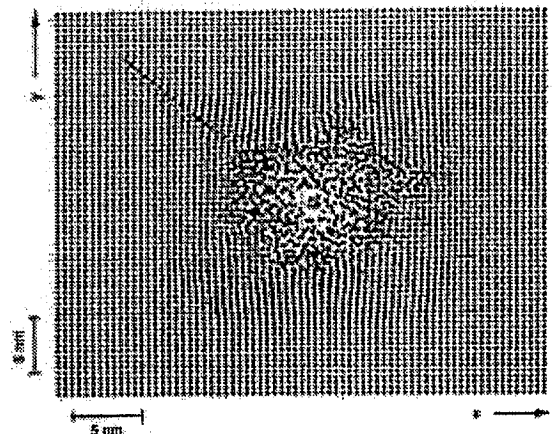


Figure 2.16 - Atomic configuration at 1 ps after a 10 keV PKA event in Au [138].

Table 2.11 - Stage in the evolution of defect pattern produced by fusion neutrons [138]

Time [ps]	Event	Result
$10^{-6}$	Transfer of recoil energy from neutron to lattice atom	Primary knock-on atom (PKA)
$10^{-6} - 0.2$	Slowing down of PKA Generation of collision cascade	Vacancies and subthreshold recoils Subcascades
$0.2 - 0.3$	Spike formation	Hot molten droplet Shock front
$0.3 - 3$	Interstitial ejection Transition from superheated to undercooled liquid spike core	Stable interstitials Atomic mixing
$3 - 20$	Spike core solidification and cooling to ambient temperature	Depleted zone Disordered zone, (amorphous zone) Vacancy collapse
$20 - \infty$	Thermal migration and reactions of defects	Defect recombination Evolution of microstructure

The irradiation damage is described by the number of displacements per atom (dpa). It is a measure for the number of defects produced and remaining after the cascade has cooled down to ambient temperature. H. Ullmaier and H. Trinkaus define the dpa number as [138]:

$$\text{dpa} = \int_E \int_T v_{\text{NRT}}(T) \frac{d\sigma}{dT}(E, T) \frac{d\Phi(E)}{dE} dT dE$$

where  $d\sigma$  is the differential cross section for the production of PKAs with energies between  $T$  and  $T+dT$ , and  $d\Phi(E)$  is the dose of irradiating particles with energies between  $E$  and  $E+dE$ .  $v_{\text{NRT}}(T)$  is the damage function, i.e., the average number of displacements produced by a PKA of energy  $T$ , calculated by the NRT (Norgett-Robinson-Torrens) approximation:

$$v_{\text{NRT}}(T) = \begin{cases} 0.8 T_{\text{dam}} / 2T_{\text{d,av}} & \text{for } T_{\text{dam}} > 2.5T_{\text{d}} \\ 1 & \text{for } T_{\text{d}} < T_{\text{dam}} < 2.5T_{\text{d}} \\ 0 & \text{for } T_{\text{dam}} < T_{\text{d}} \end{cases}$$

where  $T_{\text{d,av}}$  is the average threshold energy for single displacements and  $T_{\text{d}}$  is an effective displacement threshold energy which is either fixed by convention or otherwise taken as  $T_{\text{d}} \approx 25$  eV. In the fusion-relevant range of high recoil energies,  $v_{\text{NRT}}(T)$  overestimates the number of displacements leading to stable Frenkel pairs; thus a displacement efficiency  $\xi(T) = v/v_{\text{NRT}}(T)$  been introduced to account for this difference. In most metals  $\xi(T)$  approaches a constant value of around 0.25 for  $T \geq 20$  keV.

### 2.5.2.2 Transmutation products

During the lifetime of reactor components in most cases solid transmutation products do not seem to be a problem since the amounts of these produced are far below their solubility limits in the corresponding materials.

However nuclear transmutation reactions in which gaseous elements are generated are particularly important, because gases, especially helium, are known to affect materials properties at very low concentrations. The cross sections for  $(n, \alpha)$  processes are often maximal between 10 and 15 MeV. Although the cross sections for fast neutrons vary from isotope to isotope (Figure 2.17), they are substantial for all nuclei; i.e., the production of He cannot be avoided by selecting alloys of special composition.

The extraordinary role of He among all other impurities is due to its extremely low solubility in solids. Considering the high He generation rates in the plasma facing components, even for the shortest conceivable operation times, the He concentration will be far above the solubility limit.

Therefore, after a very short incubation period, He precipitation in the form of bubbles will take place.

The production of hydrogen by (n, p) reactions is not considered to cause severe problems in structural fusion material because, in most metals, the diffusion of hydrogen isotopes is so fast that their stationary concentrations during exposure should always remain far below the solubility limits, even at moderate temperatures.

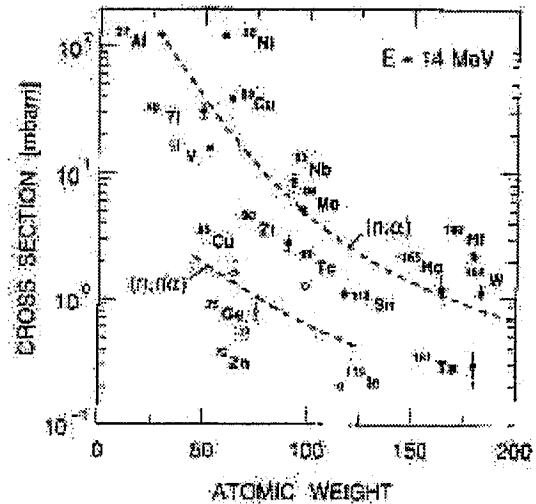


Figure 2.17 - Cross sections for 14-MeV neutron-induced He production in different elements. The dotted lines indicate the gross trends of the cross sections for (n,  $\alpha$ ) and (n, n'  $\alpha$ ) reactions, respectively, as a function of the atomic weight [138].

### 2.5.3 Change of macroscopic properties

The primary defects induced by fusion neutrons (displacements and transmutations) cause macroscopic responses, i.e. changes in physical and mechanical properties, of metallic structural materials subjected to neutron bombardment.

The large-scale, long-term defect accumulation controlling the macroscopic properties of metals under neutron irradiation is the result of reactions between the primary irradiation-induced defects with defects that were already present before irradiation (such as impurity atoms, precipitates, dislocations, and grain boundaries). For example, defects caused by atomic displacement events can act as barriers to dislocation motion, causing metals to become stronger and less ductile. The increase in hardness upon radiation is called *irradiation hardening* whereas the decrease of percent elongation is called *irradiation induced embrittlement*. Other macroscopic changes of neutron irradiated metallic structural materials and their dependence from primary irradiation-induced defects are given in Table 2.12.

Table 2.12 - Physical and mechanical property changes due to n irradiation.

Primary irradiation-induced defect	Macroscopic property change
Displacements Transmutation	Dimensional instabilities Change in yield strength Loss of ductility Change in creep rate Change in fatigue life Loss of fracture toughness
Displacements	Swelling Change in electric resistance
Transmutations	Radioactivity and after heat Composition change

## 2.5.4 Effects of neutron damage on Be

Be is degraded by radiation damage, both as result of displacement damage and of transmutation [142]. Displacement damage leads to point defect clustering, irradiation hardening and embrittlement. Transmutation produces helium and lithium (which eventually becomes tritium), resulting in high levels of gas-driven swelling and embrittlement at high temperature.

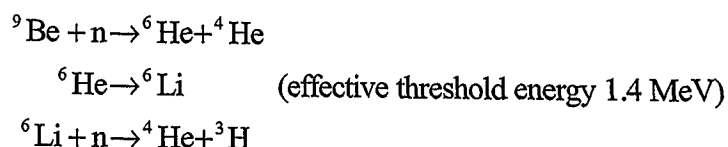
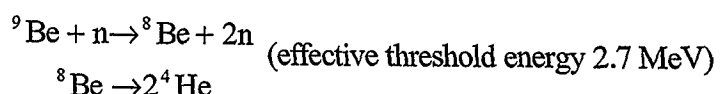
The changes of Be properties under neutron irradiation strongly depend on the irradiation temperature [143]. At low irradiation temperature (<300°C) the major changes are due to the displacement damage which leads to hardening and embrittlement of Be, whereas at high temperatures (>500°C) the He production by gaseous transmutation results in a high level of gas driven swelling and grain boundary embrittlement.

Therefore, for high temperature properties the value of He generation is important and has to be taken as a base for comparison, whereas to predict the mechanical properties at low temperatures the value of displacement damage has to be compared because the He remains in the solid solution.

The following paragraphs summarise and analyse recently generated data with the main emphasis on the properties of the Be ITER grade.

### 2.5.4.1 Transmutation reactions

Helium and tritium are produced in Be from (n, 2n) and (n, α) reactions. Each Be atom can transmute to two He atoms upon absorption of a high energy neutron. Absorption of a lower energy neutron produces two He atoms and one tritium atom. The controlling reactions are as follow [144, 145]:



As a consequence, under high energy neutron bombardment, He is generated in much greater quantities in Be than in any other metal.

Displacement damage and transmutation products during neutron irradiation depend on the neutron spectrum. For the ITER Be armoured PFCs the design value of damage during the BPP ranges from 0.4 to 1 dpa and the corresponding amount of He from 400 to 1000 appm (see table 1.2).

### 2.5.4.2 Microstructure changes

Radiation damage in Be can best be characterised by distinguishing between point defect accumulation, point defect coalescence and gas driven swelling [142]. Strength and ductility changes, as well as swelling, for beryllium are strongly dependent on the irradiation temperature. Responses can be divided into four regimes of temperatures:

1. low temperature (<20°C) response where point defects are created, but mobility is so low that coalescence is rare;
2. somewhat higher temperatures (20-300°C), where point defects are mobile but gas atoms are practically immobile;
3. still higher temperature (300-600°C), where gas atoms become mobile; and
4. very high temperatures where gas pressure driven swelling becomes dominant (>600°C).

The microstructural evolution in these temperature regimes is as follows:

- At temperatures where point defects are mobile, but gas atoms are not, point defects coalesce into dislocation loops and the loops grow and evolve into a complex dislocation network forming obstacles to dislocation motion. Gas atoms become trapped in the microstructure. Therefore, at these temperatures, Be displays swelling, at a modest rate, and hardening, which leads to embrittlement. In this regime swelling in Be is directly proportional to fast fluence. Growth (change in shape under irradiation) can also be anticipated.
- At temperatures where He and tritium gas atoms become mobile, gas bubbles form, most visibly on grain boundaries, but are also probably present on dislocations. The accumulation of He at bubbles is probably by a mechanism similar to solute segregation, dragging impurity atoms to point defect sinks by interaction with moving point defects. These bubbles again produce obstacles to dislocation and grain boundary motion and they can provide nucleation sites for cracking. Therefore swelling and mechanical property degradation occur at somewhat different rates than for lower temperature response.
- At temperatures where He and tritium mobility becomes large enough to allow consolidation into large bubbles, the swelling accumulation during neutron irradiation is larger by more than a magnitude, and it depends other than from neutron fluence from Be powder oxygen content and grain size. In particular it increases with decreasing oxygen content and with increasing grain size.

In the first-wall and the blanket-of-fusion reactors, high-temperature embrittlement by He is supposed to be the lifetime-limiting effect [146 - 150].

#### 2.5.4.3 Thermal conductivity

Few data exist on the effect of neutron irradiation on physical properties of Be (thermal conductivity, thermal expansion coefficient, elastic modulus). An estimation of the thermal conductivity of irradiated Be is present in literature [49].

Thermal conductivity of irradiated Be decreased to about 90% of the original value at low test temperature ( $<200^{\circ}\text{C}$ ) and to about 95% at higher temperatures (Figure 2.18).

After high temperature annealing, in specimens with 29 and 63% swelling, thermal conductivity decreased to about 70% and 40% of the unirradiated value, respectively. A significant reduction in thermal conductivity is not expected unless the material is irradiated in the temperature and fluence range where swelling becomes effective.

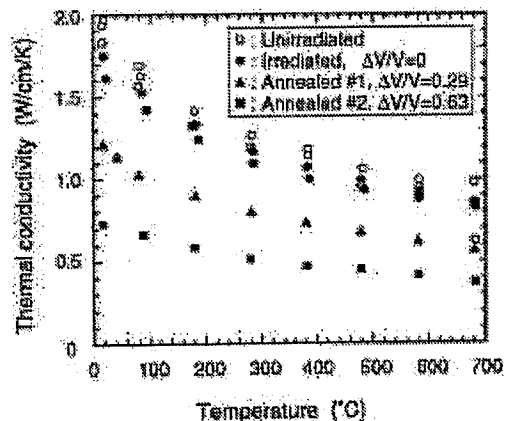


Figure 2.18 - thermal conductivity of beryllium specimens [49].

#### 2.5.4.4 Swelling

The largest part of the available data on irradiation induced swelling of different Be grades is based on the results of in-pile radiation tests in fission reactors.

However, to compare the irradiation data generated in different nuclear reactors correctly, to take into account the differences between the fusion and the fission spectra, as well as to predict damageability of Be in various component of fusion reactors, it is important to consider the accumulation and mobility of irradiation produced gases. Recently the ANFIBE

(ANalysis of Fusion Irradiated Be) code has been developed, which described the kinetics and dynamics of He induced swelling and which allows calculation of the swelling in Be over wide temperature and fluence ranges [151]. The agreement of prediction by ANFIBE and previous experimental data is excellent [146]. This code could be therefore used for preliminary prediction of the Be armour swelling.

The available information on swelling of different Be grades at low and elevated irradiation temperatures is shown in Figure 2.19 (including the predictions from existing correlations) as a function of He content and as a function of neutron fluence [49, 145, 150]. Further results of studies on the modern Russian Federation Be grades and S-65C VHP can be found in [72, 152 - 155].

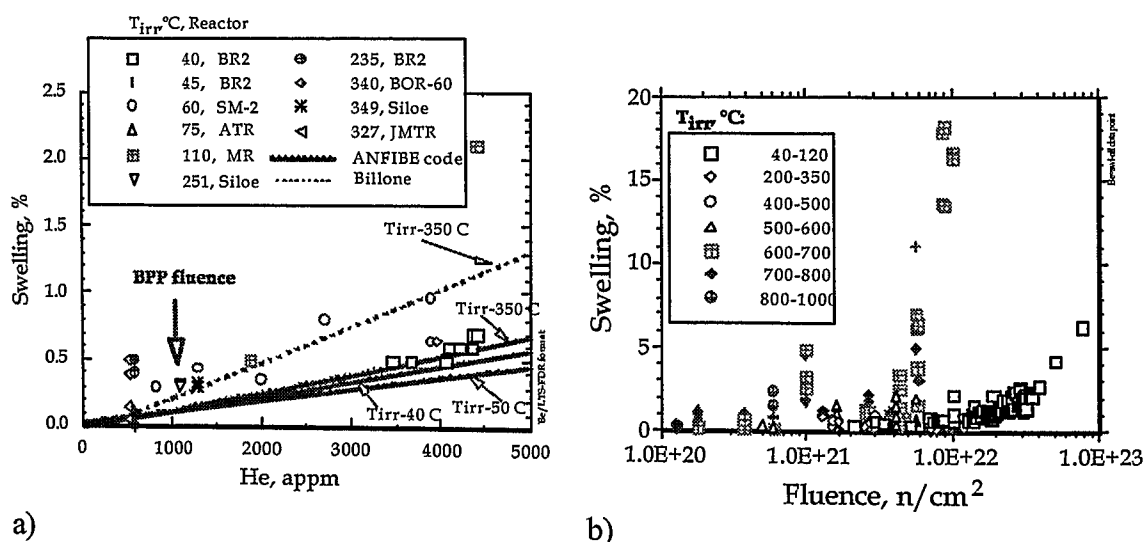


Figure 2.19 - Swelling of different Be grades: a) vs. He content; b) vs. neutron fluence [49].

#### 2.5.4.5 Mechanical properties.

The general qualitative trends in the strength and ductility behaviour of neutron irradiated Be, as anticipated above, are the following [143]:

- at low and moderate (20 - 500°C) irradiation temperatures the strength is typically increasing, while ductility is decreasing, in some cases to zero;
- at high temperature (more than 600°C) the ductility decreases without increase in strength;
- increasing of fluence leads to saturation in the behaviour of the strength and ductility.

Data on the influence of irradiation on mechanical properties of S-65C VHP and DShG-200 are still very limited [156]. As shown in Figure 2.20, low temperature (230°C) irradiation up to ~2 dpa leads to an increase of strength and to severe embrittlement. At higher irradiation temperature (300-500°C) ductility improves and up to ~1-5 dpa remains above a few % in the longitudinal direction [49].

Still there is no data on the mechanical properties of Be at low irradiation temperatures (100-270°C) and at a dose of ~1 dpa.

At high irradiation temperatures (>600°C), a sharp decrease of strength and ductility was observed [49, 149, 157], as a result of the He embrittlement (Figure 2.21).



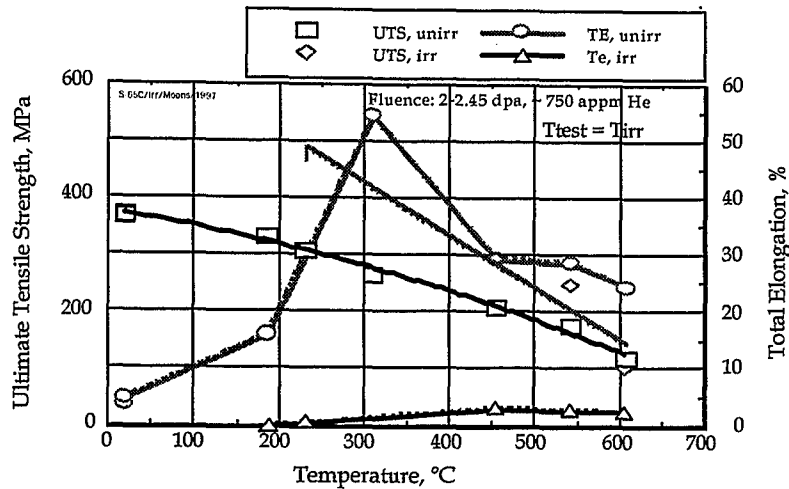


Figure 2.20 - Influence of neutron irradiation on mechanical properties of S-65C VHP [156].

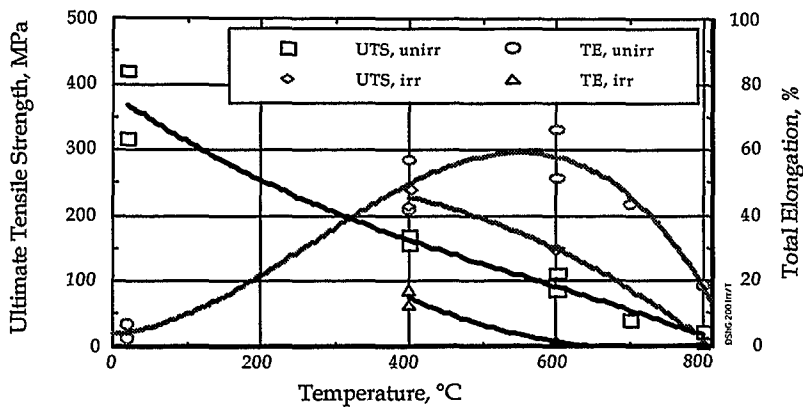


Figure 2.21 - Embrittlement and loss of strength of DShG-200 at  $T_{irr} = \sim 700^{\circ}\text{C}$ , fluence  $\sim 4$  dpa [49].

An interesting feature is observed in more anisotropic materials (DShG-200, TGP-56). Irradiation leads to an increase of the anisotropy level, [158]. The elongation of DShG-200 in the direction transverse to the moulding pressure at  $T_{irr} = 350\text{--}400^{\circ}\text{C}$  and fluence 4.5 dpa, is still  $\sim 30\%$ , whereas in the longitudinal direction the elongation drops from 25 % down to 0%. This effect has to be checked for the reference grade S-65C VHP and for other irradiation temperatures. If confirmed, it has to be taken into account in the selection of the armour tile orientation.

The saturation of hardening and embrittlement of DShG-200 occurs already at a fluence of  $<0.7$  dpa ( $T_{irr} \sim 550^{\circ}\text{C}$ ) and remains almost without change up to a fluence of  $\sim 5$  dpa [49]. Irradiation at high temperatures (more than  $650^{\circ}\text{C}$ ) leads to a decrease in the ductility. The main reason is the He embrittlement due to the large He bubble formation in the grain boundaries. This is accompanied by a loss of strength. The fracture mode is intercrystalline. Similar behaviour of irradiated Be was observed for S-65C irradiated up to a total fast neutron fluence of  $1.3\text{--}4.3 \cdot 10^{21}$  n/cm<sup>2</sup> ( $E > 1$  MeV) at  $327\text{--}616^{\circ}\text{C}$  [49]. The results of the bending tests at room temperature show that the fracture stress of Be grade S-65C rapidly decreases above  $450^{\circ}\text{C}$ . This reduction of the fracture stress is assumed to be due to He bubbles observed at the grain boundaries. However, the fracture stress of the larger-grained specimens (cast Be, S-200F HIP) was almost constant, although larger He bubbles were observed at their grain boundaries. Kuprijanov, [150, 152, 155, 158], has studied the mechanical properties of the modern Be grades with different content and morphology of the BeO, grain size etc. after high temperature irradiation ( $700\text{--}750^{\circ}\text{C}$ ). The typical loss of ductility has been observed. However

for grades with high swelling resistance (e.g. high BeO content and low grain size) some ductility at the level of a few % still remains while for other grades with low BeO content the failure was brittle. As for swelling resistance this could be explained by the reduced He migration in these materials.

Neutron irradiation decreases the fracture toughness of S-65 C VHP and of other grades [49].

### **2.5.5 Effects of neutron damage on Be/Cu joining**

During operation in ITER the PFCs will be subjected to cyclic temperature variations and thermal stresses. The influence of irradiation on fatigue and creep-fatigue properties will thus be of utmost importance for future fusion devices. The behaviour of joints between Be protective armour and heat sink under irradiation is of great importance. The behaviour of the neutron irradiated joints at these specific conditions cannot be predicted based on knowledge of the material properties, and has to be studied experimentally. The effect of neutron irradiation on beryllium/copper brazing joints under thermal fatigue loads has been investigated in the present work [159 -161]. The results are presented in chapter 6.

### 3 ELECTRON BEAM INTERACTION WITH MATERIALS

#### 3.1 The electron beam in technological processes

An electron beam (EB) is generated inside an electron gun. Such gun is based on the emission of free electrons, their acceleration and shaping into a beam in an electrostatic field, and beam focusing and deflection via magnetic and electric fields [162, 163, 164].

The generation and unrestricted propagation of a beam is only possible in high vacuum; so it is necessary to pump down the beam-generating and guidance systems. In general, this is also the case for the work chamber. Vacuum systems are therefore among the most important components of an EB system. The vacuum required in the beam-generating chamber of a gun is usually on the order of  $10^{-2}$ – $10^{-4}$  Pa, and that in the work chamber is generally around  $10^{-2}$  Pa.

When the beam impinges on the matter to be processed, the kinetic energy of the electrons is converted into various kinds of energy owing to interactions with the atoms in a series of elementary processes [165]. When the beam is utilised for melting, welding, evaporation, or thermal processing, for example, it is the produced thermal energy that is used.

#### 3.2 Phenomenology of the energy deposition

When an acceleration voltage  $U_B$  is applied, electrons are accelerated in the electrostatic field of the beam source so that they attain a kinetic energy  $E = eU_B$ .

At the point of beam interactions with the atoms of the matter, the kinetic energy of the beam electrons is converted into heat or atomic or molecular excitation energy [162, 166, 167]. A certain portion of the incident electrons will be backscattered. In addition, secondary processes produce X-ray, secondary-electron, and thermionic electron emission at the point of the beam incidence. The generated heat results in a rise in temperature on the work site, heat conduction from the zone of energy conversion to the environment, as well as heat radiation from the heated surface (Figure 3.1). To estimate the energy deposited in the target material, the various mechanisms of electron-material interaction have to be taken into consideration.

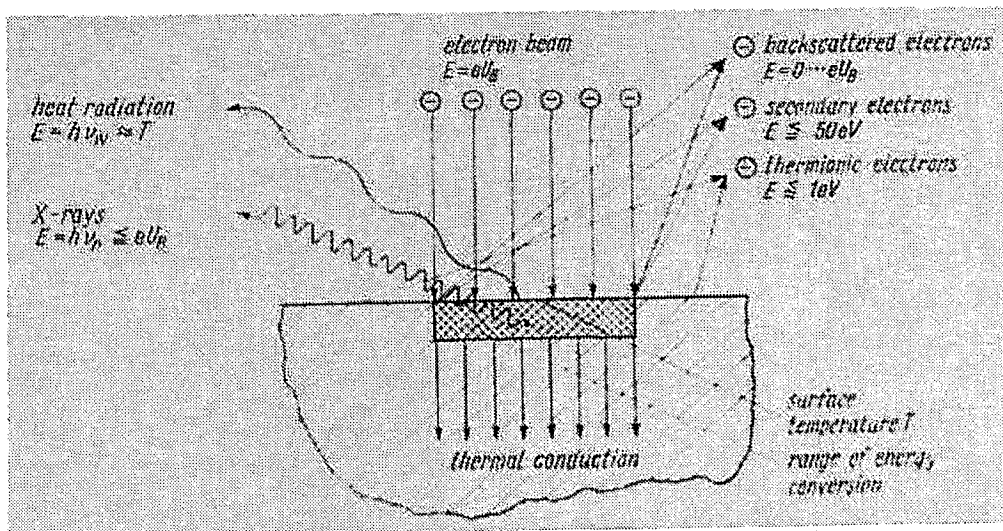


Figure 3.1 - Beam action upon impingement on matter [162].

### 3.2.1 X-Ray production

As with other particle or wave radiations, X-radiation is biologically active and, if a particular intensity is exceeded, represents a health hazard. Because its occurrence is inevitably linked to all EB processing techniques, suitable shielding is required for the protection in the immediate vicinity of EB facilities.

The continuous X-rays produced by deceleration of the electrons are directed towards the interior of specimen and, therefore, deposit all their energy in the material in a few millimeters of path. The emitted X-rays consist of two components: characteristic radiation and bremsstrahlung. The characteristic spectrum results from the ionization of the inner electron shells of target atoms and gives rise to discrete characteristic wavelengths associated with the binding energy. The resultant energy in the total X-ray emission can be neglected. The production of characteristic X-rays caused by ionization is extremely low; therefore the thermal emission from the melted spot is negligible. But bremsstrahlung, on the other hand, results in a wavelength spectrum with a maximum quantum energy:

$$h\nu_{\text{max}} = eU_B \quad (h = \text{Planck's constant})$$

and an intensity maximum at an energy that amounts to about 60% of the electron energy. Energy losses on the work site caused by X-radiation are on the order of 1% or less; they depend on the energy of the beam electrons and on the atomic number  $Z$  of the material hit by the beam [164].

### 3.2.2 Secondary electrons

If electrons impinge on the surface of a solid metal in a vacuum and inelastic collisions occur between the loosely bound outer electrons in the metal and the incoming beam, energy is lost from the beam electrons and the loosely bound electrons are ejected. The ejected electrons have an energy typically less than or equal to 50 eV and are called secondary electrons [165, 168]. If these secondary electrons are produced close to the surface and the energy of the secondary electrons is greater than the surface barrier energy (2-6 eV), the secondary electrons have a high probability of escaping from the surface. The emitted flow of secondary electrons depends on the target material – in particular, its surface – as well as the angle of beam incidence and the electron energy. At higher energies, the primary electrons penetrate so far below the surface before losing energy that the excited electrons have little chance of reaching the surface and escaping. Due to their low kinetic energy, the contribution of secondary electrons to the removal of energy from the sample is small. At high incident electron energies the energy carried away by the secondary electrons can be neglected.

### 3.2.3 Thermionic emission

A metal contains mobile electrons in a partially filled band of energy levels i.e., the conduction band. These electrons, though mobile within the metal, are rather tightly bound to it. The energy that is required to release a mobile electron from the metal (work function) varies from about 1.5 to approximately 6 eV, depending on the metal. In thermionic emission, some of the electrons acquire enough energy from thermal collisions to escape from the metal. When EB processes are performed with adequate heating of the corresponding material, a noticeable emission of thermionic electrons takes place [162, 168, 169]. The number of electrons emitted and therefore the thermionic emission current depend critically on temperature at the work-piece surface and on its material properties. Hence it is related to the beam current merely by temperature.

A formula known as Richardson's law (first proposed by the English physicist Owen W. Richardson), which is roughly valid for all metals, relates the emission current density ( $J$ ) to the temperature and to the work function of the metal:

$$J = AT^2 e^{-W/kT} \text{ [A/cm}^2\text{]}$$

where  $T$  is the temperature in Kelvin,  $W$  is the work function of the metal and  $k$  is Boltzman's constant ( $1.38 \times 10^{-23}$  J/K). The factor  $A$  is known as Richardson's constant and has a theoretical value of  $120 \text{ A/cm}^2\text{K}^2$ , although its experimental value changes dependent on the quality of the surface being considered and on the metal [170, 171]. Due to their low kinetic energy, their emission is practically meaningless as far as the energy balance of the EB process is concerned.

### 3.2.4 Electron backscattering

Electrons backscattering causes emission of electrons within the range of beam action, the energy spectrum of which goes up to the energy of the beam electrons. The portion of backscattered beam electrons and their energy spectrum and directional distribution are determined by the atomic number  $Z$  of the target material as well as by the angle between the normal to the target surface and the direction of beam incidence.

With increasing atomic numbers, there is a very pronounced energy maximum that corresponds to the most probable energy level of backscattered electrons; the higher the atomic number the more this maximum is shifted toward higher energy levels. Electron backscattering increases with the angle between the direction of beam incidence and the normal to the surface.

In contrast to thermionic emission, electron backscattering is independent of temperature and, compared to secondary electron emission, also independent of surface. The beam current backscattered is dependent on the atomic number  $Z$  of the material and it is not affected by the energy of the incident electrons (Figure 3.2).

The energy lost during the actual process because of electron backscattering may reach considerable magnitudes. The averaged kinetic energy of backscattered electrons ranges from 0.45 to 0.8 times the energy of the incident electrons. In computing the energy deposited in the sample by the EB the energy removed by the backscattered electrons needs to be taken into account.

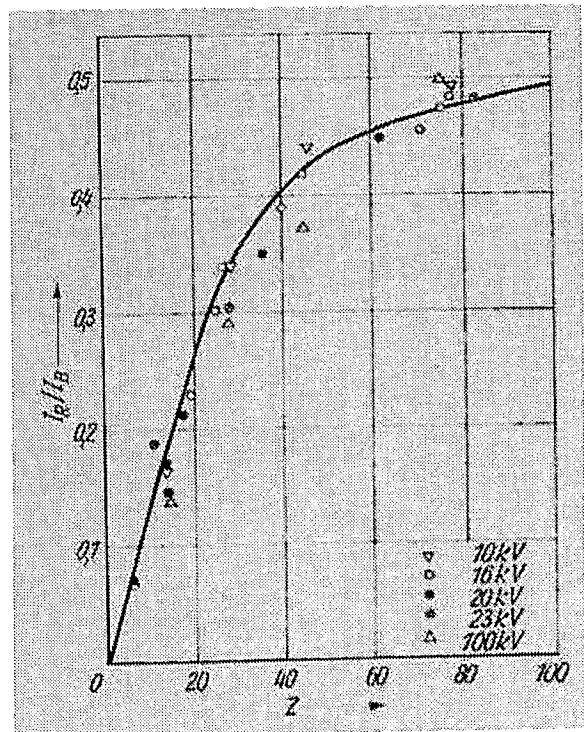


Figure 3.2 - Ratio  $IR/IB$  of backscattered electron current, plotted as function of the atomic charge  $Z$  of the target material for normal beam incidence [162].

### 3.3 The electron beam as heat source for testing of PFCs

Laser light, electron beam, ion beam and plasma gun devices have all been used world-wide to study disruption effects and erosion damage in plasma facing materials. Each of these methods has its merits and its demerits. Up to now there is no experimental facility which allows to simulate the disruption conditions adequately in term of plasma flow parameters.

The simulation of these high heat loads by electron beams has become a frequently used technique [172 - 175]. Electron beam facilities such as those as the JUDITH, JEBIS (Jaery, Naka, Japan), TSEFEY (Efremov Institute, St. Petersburg, Russian), FE200 (Framatome, Le Creusot, France), EBTS (Sandia National Laboratory, USA) have been utilised for testing of high heat flux (HHF) components of next step fusion devices [176]. Two basic kinds of tests are performed in these facilities:

- Simulation of normal operation with actively-cooled samples, in order to study the HHF behaviour of plasma facing components (PFCs), in particular the performance of joints between plasma facing materials and the heat sink materials (steady state heating or thermal fatigue);
- Simulation of thermal shock to study the materials erosion behaviour during off-normal plasma scenarios (e.g. simulation of disruptions or vertical displacement events).

To perform HHF simulation experiments, a heat source which can provide fast rise and intense heat fluxes on targets is required. The heat flux on the target should be spatially uniform to facilitate comparison of the experimental data with the analytical prediction. In fact, initiation and growth of cracks caused by intense heating could also be affected by a non-uniform profile of the heat flux distribution [177]. However it is not easy to obtain a spatially uniform high heat flux over a relatively large surface area with an electron beam. The comparison between the different facilities showed that a defocused beam can provide relatively uniform heat flux only in the low heat flux region even for a small test surface. For providing a high heat flux uniformly over a wide area with an efficient use of the beam power, a beam rastering is necessary.

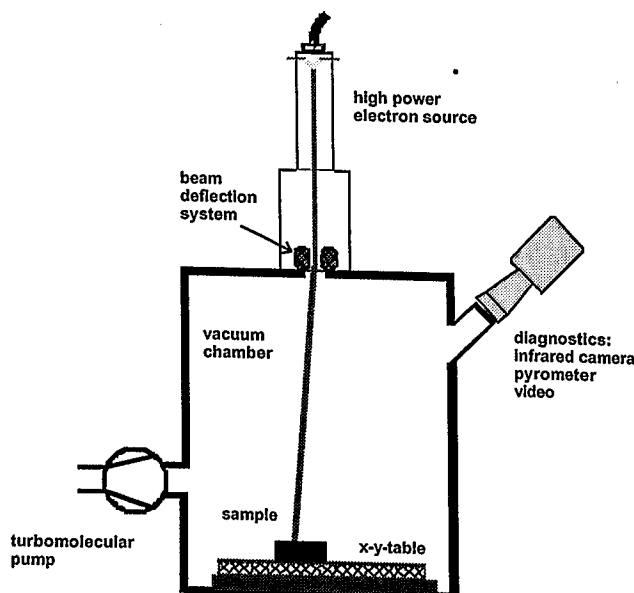


Figure 3.3 - EB test facility working principle [176].

An EB can easily be oscillated by means of beam rastering coils (Figure 3.3). Two-dimensional oscillation of the beam by a combination of two sets of rastering coils is expected to provide almost uniform heat flux in the test area [176]. However, in contrast to the static beam, the rastering beam fundamentally provides cyclically changing heat flux. The rastering frequency should be high enough for the heat flux to be regarded as temporally unchanged. Since the duration of the disruption is predicted to be on the order of 10 ms in the next generation machines, the rastering frequency should be higher than 100 kHz to provide a heat flux that can be regarded as temporally unchanged in disruption simulation experiment [177].

A merit of the EB facilities is their possibility to define the beam parameters with sufficient accuracy and to control them in a wide range. A disadvantage is the rather high energy of the beam electrons [178]. In fact, because of the high electron kinetic energy in these devices (100-150 keV), the electrons have a much longer range in both target material and vapour zone than in laser or plasma gun device. As result a volumetric heating is originated in the condensed target and the deposited energy density in the developed vapour cloud (cf. chapter 5) is relatively low [179, 180].

The response of metallic materials during electron beam loading in HHF simulation experiments is shown schematically in Figure 3.4 [181]. Unlike the conditions in a thermonuclear fusion device, the electron beam deposits its energy in the volume of the plasma facing material. The penetration depth depends strongly on the acceleration voltage and on the density of the material. The volumetric heat deposition of high energy incident electrons (120 keV) in Be occurs in a depth of approx. 150  $\mu\text{m}$ .

The high electron kinetic energy is deposited deep inside the target material, causing its melting and vaporization. Melt-layer erosion can be caused by melt splashing due to the formation, growth and bursting of bubbles inside the liquid layer. Splashing due to volume bubble explosion is a result of the continuous heating and overheating of the liquid layer during energy deposition. The surface temperature of the liquid layer will exceed the equilibrium vaporization temperature, this overheating leading to the growth and explosion or vaporization of volume bubbles as they reach the free surface. This explosion of bubbles, in turn, leads to ejection and loss of parts of melt layer, as shown in Figure 3.5 [182, 183].

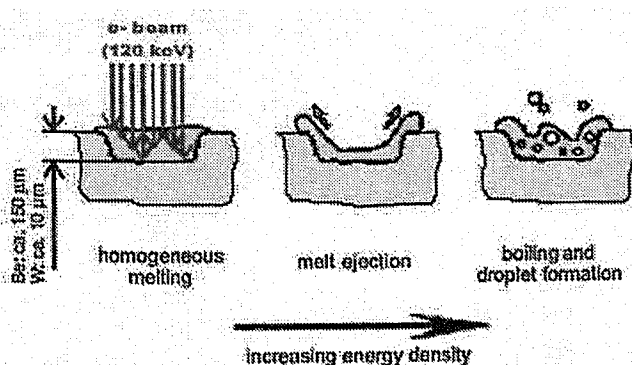


Figure 3.4 - Metal materials response during thermal loading with intense localized electron beam [181].

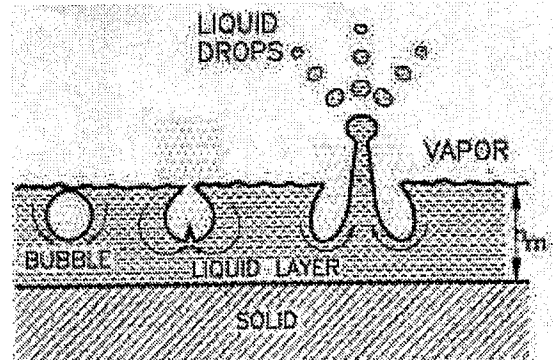


Figure 3.5 - Melt layer splashing due to bubble growth and explosion [182].

### 3.4 The Electron Beam facility JUDITH

All the experiments described in this work has been performed in the electron beam test facility JUDITH (Juelich Divertor Test Equipment in Hot Cells) located in the Hot Cells Laboratory of the Forschungszentrum Jülich (FZJ), Germany [184, 185].

The electron beam facility JUDITH (Figure 3.6) consists of an electron beam unit with a beam power of 60 kW, a stainless steel vacuum chamber of 800 x 600 x 900 mm<sup>3</sup>, and a number of diagnostic devices. The electron gun is placed on the top of the vacuum chamber and the beam is discharged downward to the surface of the test piece. A rather homogenous heat load distribution to the sample is obtained by fast scanning. The focused electron beam with a diameter of 1 mm and with typical energies of 120 keV is swept across the surface of the test coupon in two directions at frequencies up to 100 kHz.

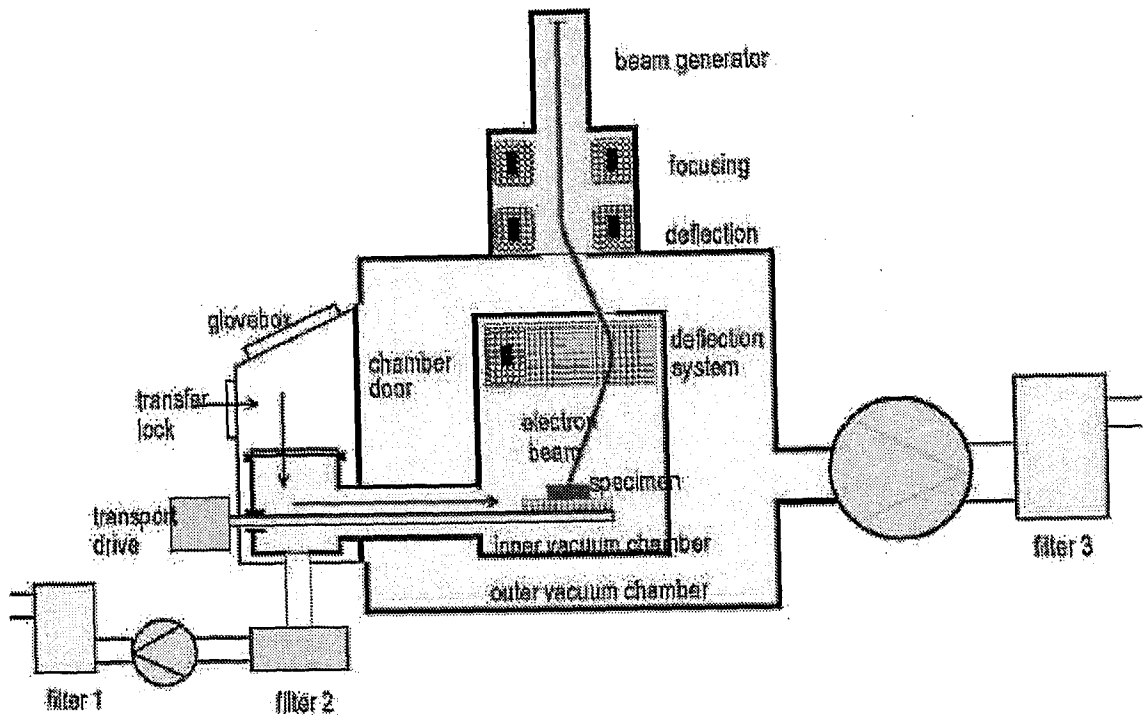


Figure 3.6 - EB facility JUDITH. Cross section of the vacuum chamber [185].

The beam power is defined as the product of the acceleration voltage and the total beam current: the acceleration voltage is held constant and the total beam current generated at the gun is controlled to provide the desired heat flux on the test surface.

In the present work, applied heat fluxes loaded surface areas of typically  $4 \times 4 \text{ mm}^2$  up to  $15 \times 25 \text{ mm}^2$  have been selected; the former for the simulation of disruption heat loads; the latter for the imitation of thermal fatigue on actively cooled modules. The maximum deposited energy density was  $15 \text{ MJ/m}^2$ .

### 3.4.1 Technical specifications

Table 3.1 summarises the main specifications of the electron beam facility. Short pulses from 1 ms up to 100 ms (as they were used in the thermal shock tests) are produced by means of a charged capacitor. The typical pulse duration was 5 ms (beam rise time 130  $\mu\text{s}$ ).

Table 3.1 - The technical data of JUDITH facility

beam potential:	$\leq 150 \text{ kV}$
beam current:	$\leq 400 \text{ mA}$
beam power:	$\leq 60 \text{ kW}$
pulse duration	$\geq 1 \text{ ms}$
pulse rise time:	130 $\mu\text{s}$
beam deflection:	$\pm 50 \text{ mm}$ (in x- and y-direction)
scanning frequency:	$\leq 100 \text{ kHz}$
max. loaded area:	$100 \times 100 \text{ mm}^2$



### 3.4.2 Diagnostic

The following diagnostic devices have been installed:

- two infra-red pyrometers, for point measurements of temperature from 200°C to 1100 °C and from 1000 °C to 3500°C (two colour system);
- a fast pyrometer from 1500 to 3500°C (rise time <10 µs);
- an infra-red camera system (scanner) calibrated for temperature monitoring in the range between RT and 3000°C;
- a video camera for visual monitoring of the tests;
- several thermocouples;
- quadrupol mass spectrometer for rest gas analysis;
- instrumented cooling loop for controlling pressure, flow rate, inlet and outlet temperature of cooling water during the experiment.

### 3.4.3 Improvement for testing of beryllium

In the thermal shock tests the evaporation and erosion of Be particles has to be taken into consideration, and due to the toxicity of Be special safety requirements has to be taken. The safety concept is guided from the considerations on one hand to avoid the spreading Be particles in the laboratory, and on the other hand to avoid contamination of the electron gun and of the vacuum chamber.

The EB facility JUDITH has been provided with the following improvements (Figure 3.6):

- insertion of a second containment inside the vacuum chamber being evacuated separately (inner vacuum chamber),
- magnetic electron beam deviation system to prevent sputtered positive ions contaminating the electron beam cathode,
- glove box for dust free loading and un-loading of samples,
- lock mechanism between glove box and inner containment, to allow sample change at vacuum conditions,
- filters in both vacuum systems,
- safety lock to put on protection equipment in case of accident.

Due to the location of the JUDITH facility in a hot cell (Figure 3.7), a containment exists and several safety systems are installed. This made the mastering of safety requirements relatively easy. Room ventilation is filtered through high efficiency filters to minimise Be emission to the atmosphere. A safety interlock has been established, which can be removed for non-beryllium testing campaigns. Wiping tests are performed in different regions of the JUDITH facility. All wiping tests outside the inner chamber showed a Be contamination which was below the detection limit. By these results the efficiency of the inner chamber for the retention of evaporated Be has been proved.

### 3.4.4 Improvement for the handling of radioactive samples

On flat tile Be/Cu modules, the coolant tubes for the connection to the coolant loop have been omitted. To guarantee tight sealing of the high pressure loop the clamping mechanism shown in Figure 3.8 has been developed [185].

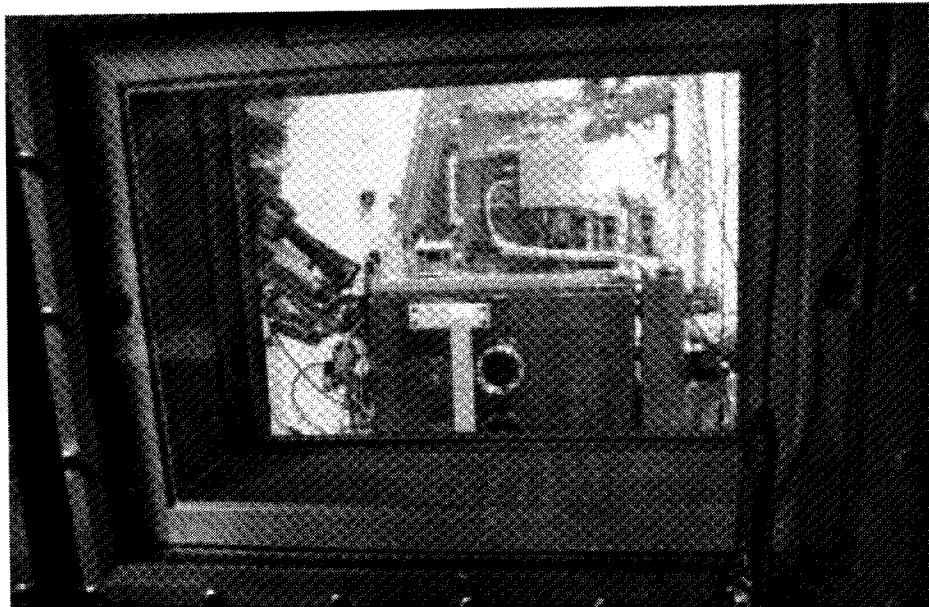


Figure 3.7 - EB facility JUDITH inside the Hot Cell [185].

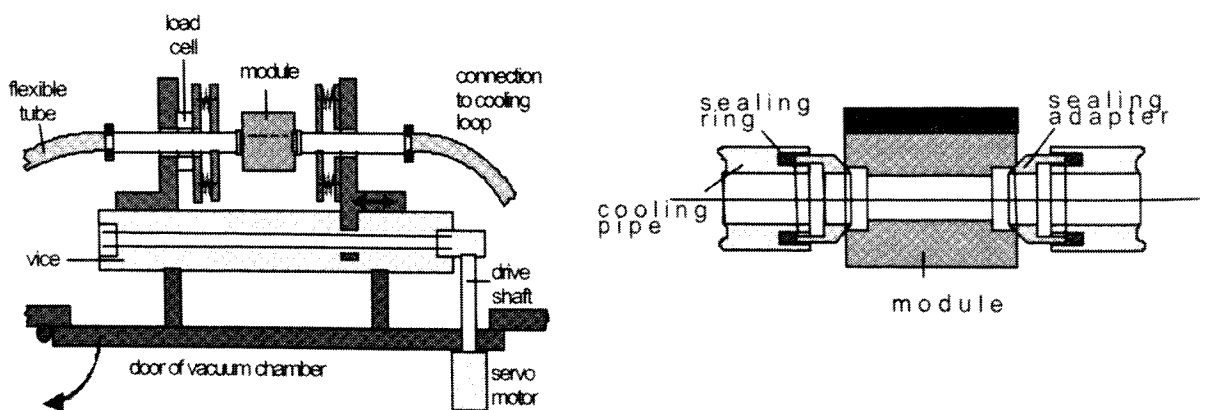


Figure 3.8- Clamping mechanism for water cooling of miniaturized mock-ups in JUDITH [185].

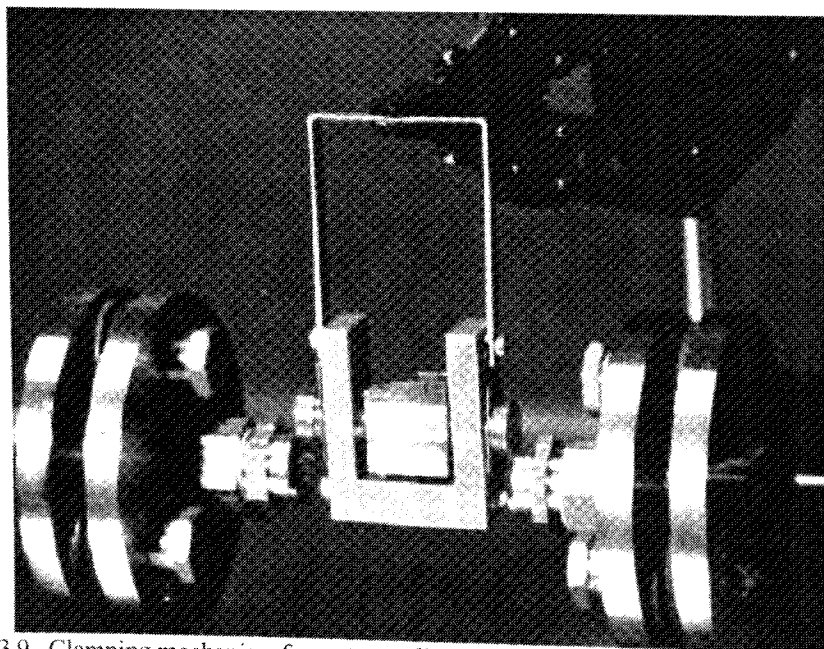


Figure 3.9 - Clamping mechanism for water cooling of miniaturized mock-ups in JUDITH [185].

Two sealing adapters machined from oxygen free copper in combination with O-ring sealings on the cooling pipes provide sufficient safety against water leaks.

The mechanism is motor driven, and it can be operated by remote handling techniques (Figure 3.9).

This system is installed at the door of the vacuum chamber (Figure 10).

The mock-up can be placed in the sample holder by means of a manipulator. After the door of the vacuum chamber is closed, the sample is positioned under the electron gun and is ready for testing.

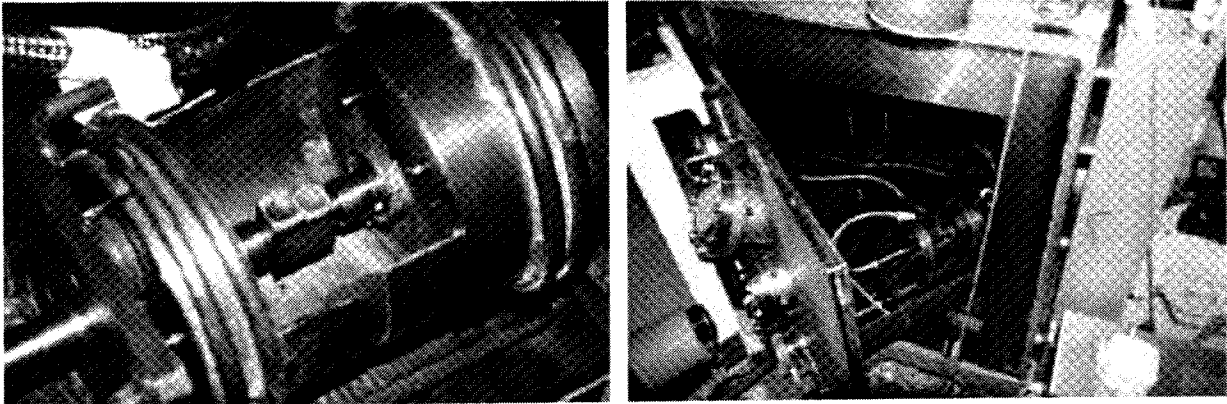


Figure 10 - Remote-controlled installation of neutron-irradiated mock-ups [185].

## 4 NEUTRON IRRADIATION PROGRAM

### 4.1 PARIDE 1 and 2

In order to study the influence of neutrons on the integrity of PFCs for ITER, the neutron irradiation program PARIDE has been carried out in the High Flux Reactor (HFR) at Petten, The Netherlands [186]. Beside Be, test specimens made from different CFC materials and tungsten alloys have been irradiated. Some promising newly developed joining techniques were not available at the time when the irradiation was started and hence they were not included. The HFR (Figure 4.1) is a light water moderated and cooled test reactor with a power of 45 MW. It contains 19 in-core positions, with a maximum thermal neutron flux of  $1.5 \cdot 10^{18} \text{ m}^{-2} \text{ s}^{-1}$ . The maximum fast neutron flux ( $E > 0.1 \text{ MeV}$ ) is  $4.65 \cdot 10^{18} \text{ m}^{-2} \text{ s}^{-1}$ .

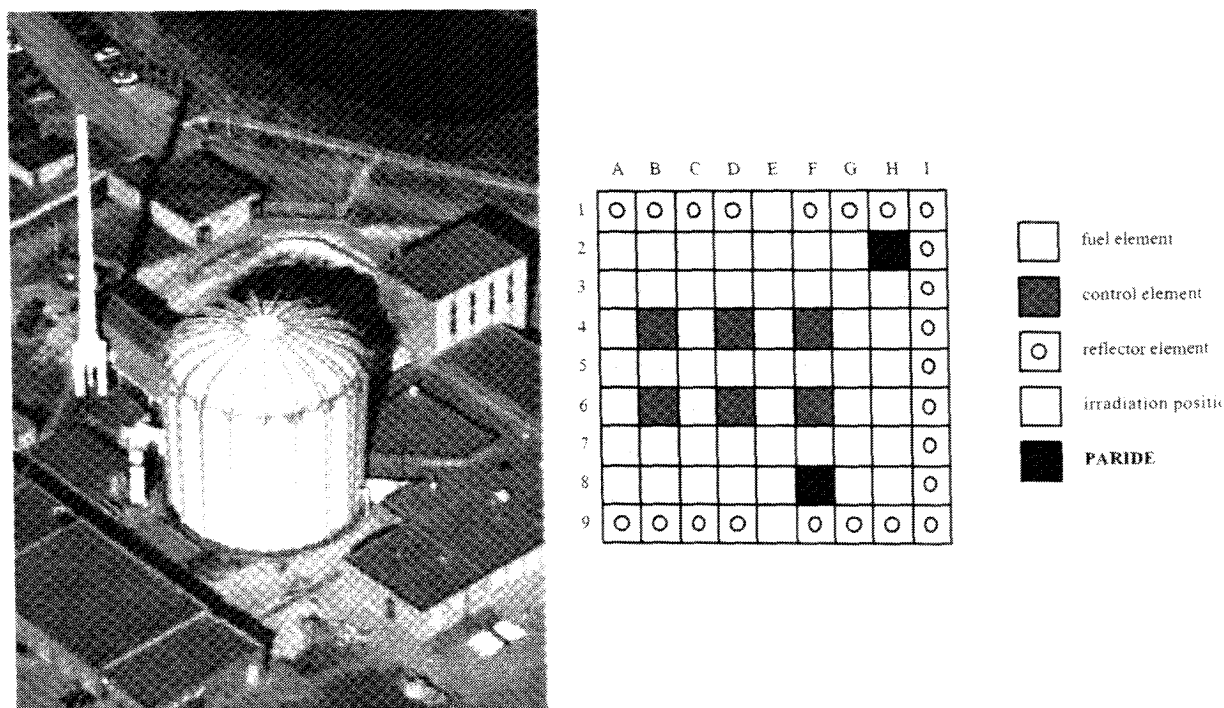


Figure 4.1 – Left: High Flux Reactor (HFR) Petten, The Netherlands. Right: Scheme of the core with position of irradiation rigs.

The neutron irradiation has been started by the end of 1995 and lasted two months in total. The material have been irradiated in stainless steel rigs and aluminium rings, respectively under the following nominal conditions:

- 350°C/0.5 dpa (PARIDE 1): this rig was placed in an outer position with relatively low flux, the irradiation time was two month approximately (two irradiation cycles of HFR);
- 700°C/0.5 dpa (PARIDE 2): this rig was placed in a position with higher flux, and the damage of 0.5 dpa was reached within one month (one irradiation cycle of HFR).

For both conditions temperature ranges were  $\pm 50^\circ\text{C}$  and  $\pm 0.2 \text{ dpa}$ . Figure 4.2 shows the relative vertical fluence rate of HFR. Over a length of 450 mm approximately, the fluence is homogeneous. Therefore irradiation rigs of this length have been used. To be precise the rig used for irradiation at 350°C was 511 mm long and consisted of four aluminium irradiation capsules, whereas the irradiation rig used for irradiation at 700°C was 558 mm long and due

to the high temperature it consisted of five stainless steel irradiation capsules [187]. Capsules were of 68 mm diameter and 60 to 165 mm length (Figure 4.3).

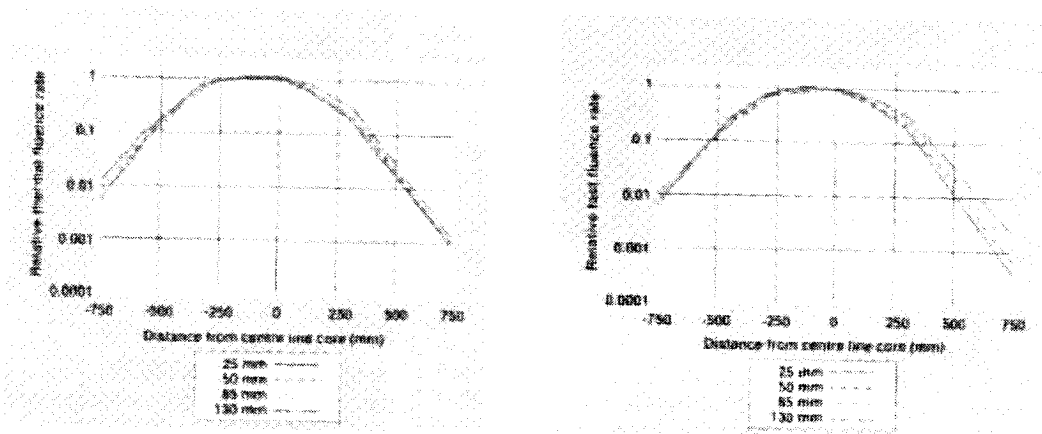


Figure 4.2 - Relative vertical fluence rate in the HRF Petten [188].

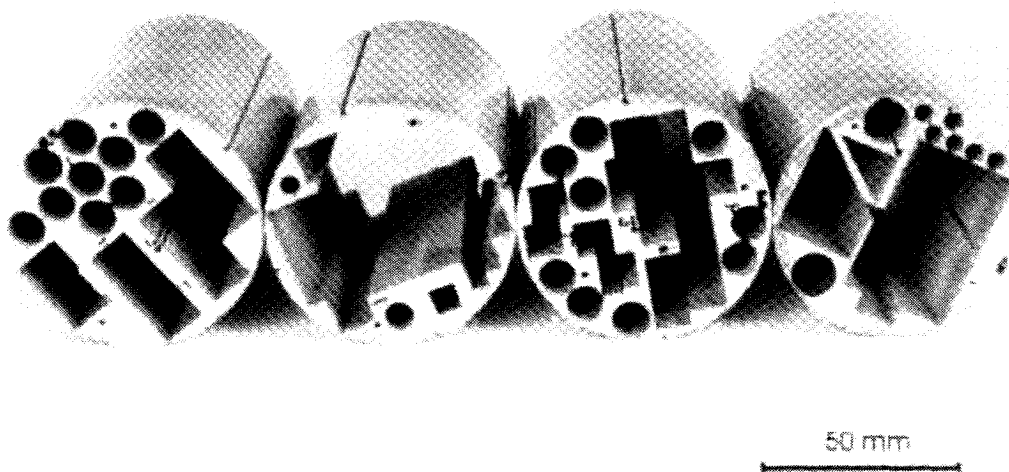


Figure 4.3 - Capsules for neutron irradiation at 350°C [188].

Figure 4.4 shows a cross section of those capsules which contained the Be samples and components.

The in-pile position of those capsules used for irradiation of Be materials and the exact position of each sample within the irradiation capsules can be found in [188].

Each rig was instrumented with thermocouples, dosimeters and was provided with equipment for temperature control.

Due to flux and temperature gradients in the irradiation rigs, the real irradiation conditions differed more or less from these values. In general the fluences were somewhat lower than the nominal values (approx. 0.35 dpa for both rigs). The irradiation temperatures and fluences were dependent on the position of the individual sample in the rig [189]. For the different beryllium samples and Be/Cu mock-ups the actual irradiation conditions are given in tables 1.1-1.3. More details on irradiation process are reported in [190].

In order to be not too confusing, in the frame of this work the following "mean values" are used: 0.35 dpa at 350°C and 0.35 dpa at 700°C.

After irradiation, the sample carriers have been transported to FZJ and dismantled in a hot cell.

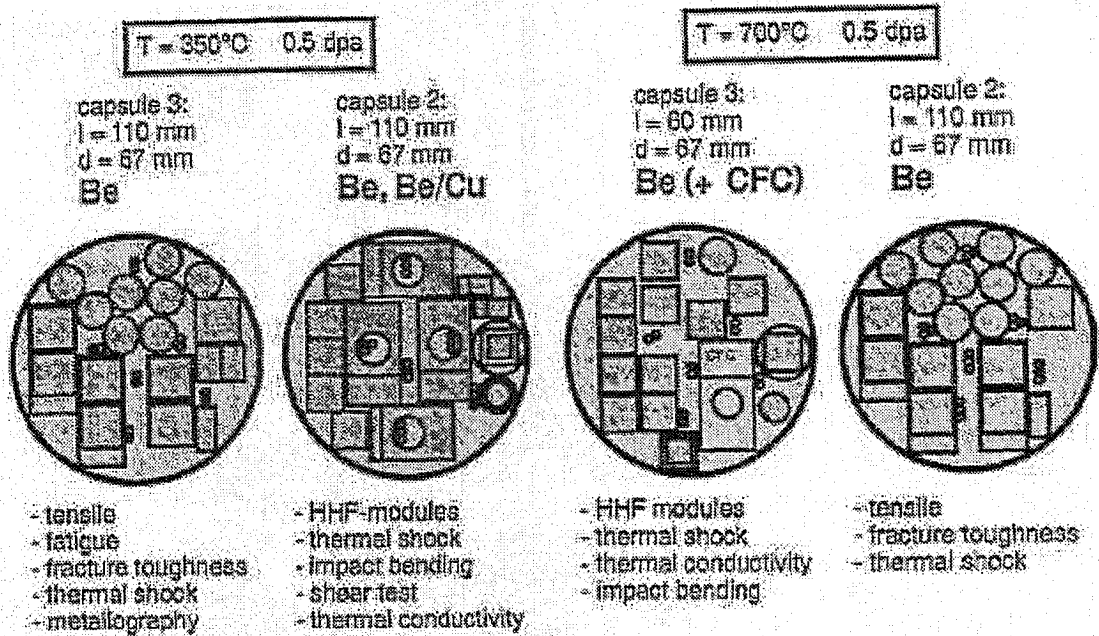


Figure 4.4 - Cross section from test samples and capsules (Be capsules only) irradiated in the HFR [191].

## 4.2 PARIDE 3 and 4

Further irradiation experiments PARIDE 3 and PARIDE 4 with more relevant fluence and temperature have been planned in order to test new joining technologies and new material grades [192]. New series of samples and small scale mock-ups have been produced for the second neutron irradiation campaign [193]. As for the previous irradiation campaign, the neutron irradiation has been carried out in the HFR at Petten, The Netherlands. The neutron irradiation has been started in 1999 and lasted eight months in total. The material have been irradiated under the following target conditions:

- PARIDE 3: 200 °C/0.2 dpa; approximately one irradiation cycle of HFR;
- PARIDE 4: 200 °C/1 dpa; approximately five irradiation cycles of HFR.

Irradiation capsules were of 60 mm diameter and 500 mm length. Screening test on Be/Cu mock-ups before irradiation have been carried out at the FZJ. After irradiation, the capsules have been sent back to FZJ for the post-irradiation thermal fatigue tests on the irradiated mock-ups and the tests on the irradiated specimens.

In the present work only the pre-characterisations tests of the primary wall mock-ups has been carried out for this campaign (cf. Chapter 6).

Table 4.1 - PARIDE 1 - irradiation conditions of Be samples - Cumulative full power days 49.64

Material	Sample type <sup>12</sup>	Sample No.	Capsule No.	T range [°C]	Neutron fluence•10 <sup>25</sup> m <sup>-2</sup> (E>0.1 MeV)	dpa
S65C	F	S12, S13, S14 S15, S17, S19 S20	3	310 - 340	0.334	0.344
DShG-200	F	1.1, 1.2, 1.3	3	310 - 340	0.334	0.344
TShG-56	F	2.1, 2.2, 2.3	3	310 - 340	0.334	0.344
TR-30	F	3.1, 3.2, 3.4	3	310 - 340	0.334	0.344
Cond. Be	F	4.1, 4.5, 4.3, 4.4	3	310 - 340	0.334	0.344
PS Be	F, CC	K1, K9, K13, K5, K17	3	310 - 340	0.334	0.344

Table 4.2 - PARIDE 2 - irradiation conditions of Be samples - Cumulative full power days 23.75

Material	Sample type <sup>12</sup>	Sample No.	Capsule No.	T range [°C]	Neutron fluence•10 <sup>25</sup> m <sup>-2</sup> (E>0.1 MeV)	dpa
S65C	F	S31, S32, S33	2	630 - 725	0.319	0.335
DShG-200	F	1.5, 1.6, 1.7	2	630 - 725	0.319	0.335
TShG-56	F	2.11, 2.12, 2.14	2	630 - 725	0.319	0.335
TR-30	F	3.6, 3.7, 3.8	2	630 - 725	0.319	0.335
Cond. Be	F	4.8, 4.9, 4.10	2	630 - 725	0.319	0.335
PS Be	F, CC	K2, K11, K6, K18	2	630 - 725	0.319	0.335

Table 4.3 - PARIDE 1 - irradiation conditions of Be/Cu mock-ups - Cumulative full power days 49.64

Material	Braze metal	Sample No.	Capsule No.	T range [°C]	n fluence•10 <sup>25</sup> m <sup>-2</sup> (E>0.1 MeV)	dpa
S65C/CuCrZr (GEC)	CuMnSnCe	FT 41/1	2	340 - 390	0.267	0.275
S65C/CuCrZr (GEC)	InCuSil	FT 36/1	2	340 - 390	0.267	0.275
S65C/CuCrZr (Accel)	InCuSil	FT 29/2	2	340 - 390	0.267	0.275

<sup>12</sup> Cf. Chapter 5.

## 5 THERMAL SHOCK TESTS ON BE SAMPLES

### 5.1 Objectives

Material erosion of PFCs during plasma disruptions is a serious problem that limits reactor operations. During plasma instabilities an intense flow of energy is directed outward from the plasma core to the PFCs. As a result, the Be armour of the PFCs is subjected to intense heat loads with a sharp deposition of energies of several ten MJ/m<sup>2</sup> within a few milliseconds (cf. chapter 2.4). However, during the early stage of this energy deposition, a dense cloud of ablated material from the exposed surface will form in front of the incoming plasma particles, thereby significantly reducing the net energy flux to PFM to values in the order of 10 MJ/m<sup>2</sup>.

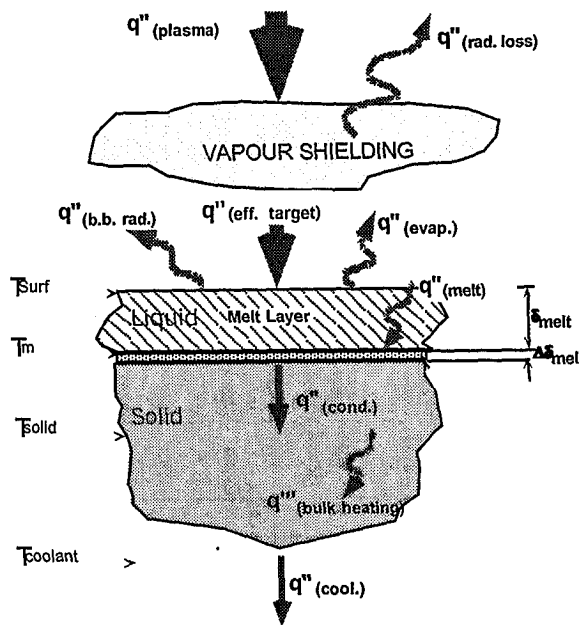


Figure 5.1 - Schematic illustration of different processes encountered during a plasma disruption on metallic armour [194, 195].

The plasma energy, which is carried by the escaping ions and electrons, is first deposited on the solid wall structure. Melting and vaporization of the wall material immediately follows and the vapour formed due to erosion in front of the wall expands towards the incoming plasma particles (Figure 5.1). The plasma particles then deposit part of their energy into the vapour and the rest of the energy is deposited into the condensed phase of the wall behind the vapour. As a result more vapour is produced and consequently more plasma energy is deposited into the vapour. Soon after, the plasma particles will completely stop in the vapour and no plasma particles kinetic energy will be able to penetrate through to the condensed wall material. The net power flux reaching the target surface will determine the net erosion and therefore the lifetime of PFCs.

The expected conditions during a plasma disruption in ITER reactor have been simulated in laboratory experiments using electron beam test facilities. The thermally induced material damage such as melting, evaporation and cracking formation on un-irradiated plasma facing materials have been investigated by electron beam experiments before [196 - 202]. However, during the operation of ITER, PFMs will suffer irradiation with 14 MeV neutrons generated in the fusion process, which will affect thermal and mechanical properties of materials. To validate the choice of the reference Be grade there is a need to summarise the data on Be



behaviour under combined exposure to thermal loading and neutron irradiation. In order to study the material degradation caused by fast neutrons, different Be grades have been neutron irradiated in the HFR at Petten (cf. chapter 4).

In the present work, the behaviour of the neutron irradiated samples when subjected to thermal shocks has been studied experimentally and the erosion behaviour of the irradiated test coupons has been compared with the un-irradiated test specimens. These grades include Be S65C manufactured by Brush Welman Inc., (USA), and the Russian Be grades TR30, DShG200, and TShG56. Besides these, powder-metallurgically produced materials, plasma sprayed (PS) Be (Los Alamos National Laboratory) and condensed Be (D.V. Efremov Institute, St.Petersburg) were investigated; both as armour materials and coating technologies. The characteristics of these different grades have been summarised in chapter 2.

The results of two test campaigns are summarised in the following. However, from the first test campaign, it was clear that the test conditions were not always reproducible and a change of some characteristics of the beam may occur between different series of tests. Therefore, during the second test campaign, for achieving the most accurate comparison of the material behaviour before and after nuclear irradiation, Be samples which were un-irradiated, and irradiated at 350°C and at 700°C, have been tested in sequence without any break of vacuum. In the present work a direct comparison of un-irradiated and irradiated material has been carried out only for samples tested in the same test campaign; the results of the two campaigns should not be mixed.

## 5.2 Experimental details

For comparing the Be response to plasma disruption before and after neutron irradiation, high heat flux (HHF) tests on small scale test coupons have been carried out in the 60 kW EB test facility JUDITH located in the Hot Cells of FZJ, Germany. The technical data of the electron beam test facility have been reported in chapter 3. The facility was upgraded with respect to the handling of the irradiated samples by means of a mechanical manipulator. The mounting of samples in a remote-controlled holder and the remote-controlled weighting of samples before and after the high heat flux test was performed by means of the mechanical manipulator.

### 5.2.1 Test specimen design

Test coupons used in disruption simulation experiments consist of polished specimens for single spot loading (Type F: 12x12x5 mm<sup>3</sup> -

Figure 5.2). This type of test samples have been designed in the view of neutron irradiation experiments and for also allowing weight loss measurements, in addition to profilometry. Surfaces of all samples have been polished to allow precise surface profile measurements from the erosion craters after high heat flux loading by laser profilometry. After polishing all samples were cleaned in an ultrasonic bath.

In case of PS-Be, thicker coupons (Type CC: 12x12x10 mm<sup>3</sup> -

Figure 5.2) have been also prepared for testing it as a coating technology. The bottom half of these specimens consists of a 5 mm powder metallurgy (PM) Be (S65C) substrate and an upper half consisting of 5 mm PS-Be.

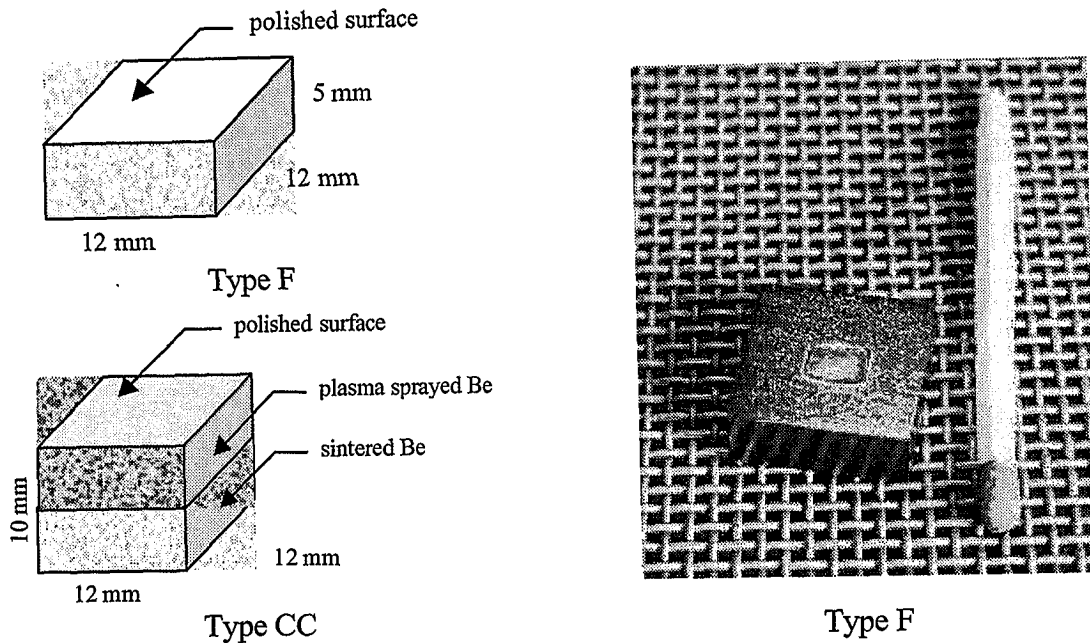


Figure 5.2 - Test coupons for plasma disruption simulations.

### 5.2.2 Experimental set-up

The exact amount of material eroded from both ablation and melting during a disruption is critically important to reactor design and its component lifetime. To investigate these phenomena extensive diagnostics are required to evaluate the actual material loading and to characterize the resulting material damage. It is essential to characterize the incident beam energy and the fraction which is absorbed by the specimen surface. For a given incident power the fraction of that power deposited in the material has been monitored by current measurements. In fact not all of the incident electrons deposit their energy in the material. They are influenced by effects of emission and reflection, material ablation, erosion, etc. During the electron beam loading the test samples were electrically isolated and grounded by a resistor of 100  $\Omega$ . The electrical current absorbed by the test samples was determined from the voltage drop at this resistor (Figure 5.3).

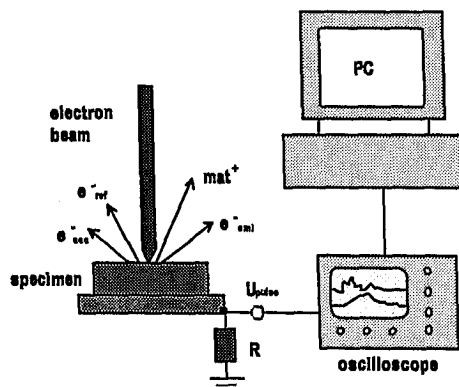


Figure 5.3 - Measurement of the beam current flowing into the sample.

The fraction of back-scattered electrons is relatively low for Be materials (typically a few percent for electron energies of 120 keV). At higher surface temperatures beside electron reflection a second phenomenon, namely thermionic emission is becoming essential (cf. chapter 3). To control this current as well, during some tests a Faraday cage encircling the incident electron beam has been installed in the vacuum chamber of the test facility (Figure 5.4).

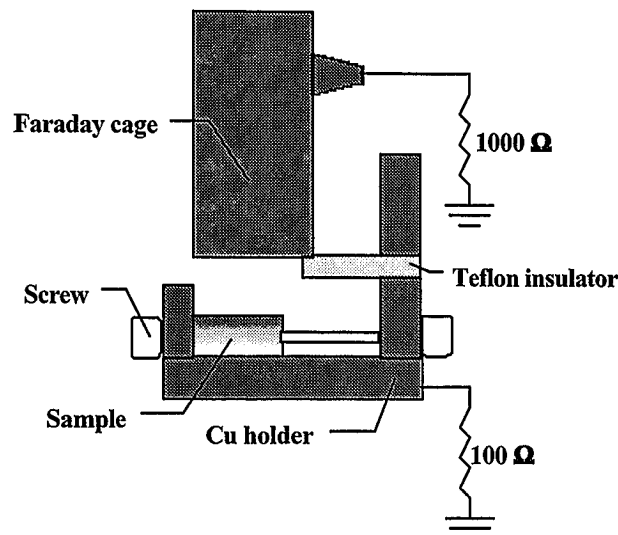


Figure 5.4 - Mounting scheme of Faraday cage during HHF test.

The Faraday cage was an isolated tube of aluminium of 24 mm inner diameter, 2.5 mm thickness and 70 mm length which was positioned at approximately 9 mm from the sample surface. The cage was connected to the ground by a resistor of 1 k $\Omega$  and the current was measured by connecting an oscilloscope to the terminals of the resistor.

### 5.2.3 Quantification of thermal shock damage

Beside comprehensive measurements of the current absorbed by the test samples, the thermal shock damage has been quantified by weight loss measurements, laser profilometry and different metallographic and optical procedures.

**Weight loss measurements.** Weight measurements of tests coupons have been accomplished before and after e-beam loading to determine the amount of material ablation due to the electron beam exposure. Ultrasonic cleaning before measurements had to be applied for removing beryllium dust originating both from transport and from erosion due to the test. The resolution of the micro balance used for these measurements was  $10^{-5}$  g; however, due to temperature instabilities, impurities on the test coupons or unavoidable weight losses (ablated particles during sample handling or mounting in the sample holder) the actual accuracy of the weight loss measurements was approximately one order of magnitude smaller. This implies that some of the measured data were below the detection limits [202].

**Laser profilometry.** Profilometer measurements have been performed by an UBM microfocus laser scanning [203] after e-beam loading to determine the maximum depth of erosion craters. Area scans (3D-shape of sample surface) have been carried out. This method supplied additional information on the melt motion during electron beam loading.

Figure 5.5 shows a 3D surface profile of a beryllium sample (S65C, neutron irradiated at 350 °C and 0.35 dpa) after 5 electron beam shots at 13.5 MJ/m<sup>2</sup>.

For determining the maximum crater depth value, an alignment of the measured 3D profile to a reference plane perpendicular to the beam direction was necessary for each sample. However, as it can be noted from Figure 5.5, in order to save time after the tests, not the entirely surface of the samples has been measured but only a portion surrounding the loaded area. Because the UBM software uses selected parts of the surface outside the loaded area for determining the reference plane, a perfect alignment of the sample was impossible, as indicated from the z quotes of the measured area in Figure 5.5, but an acceptable alignment was nevertheless achieved. The profile of Figure 5.5 shows clearly the melting rim

surrounding the loaded area. By laser profilometry it was also possible to measure the “free” volume of the crater, the crater section on the reference plane and the volume occupied by the material overflowed from the crater. For some samples the ratio between the free crater volume and the crater section was used for determining a medium crater depth value. For most samples, the difference between the free crater volume and the volume occupied by the material overflowed from the crater did not reflect the erosion value determined by weight loss measurement. This effect was already observed during previous test campaigns [204, 205] and indicates a swelling of the material during the e-beam load.

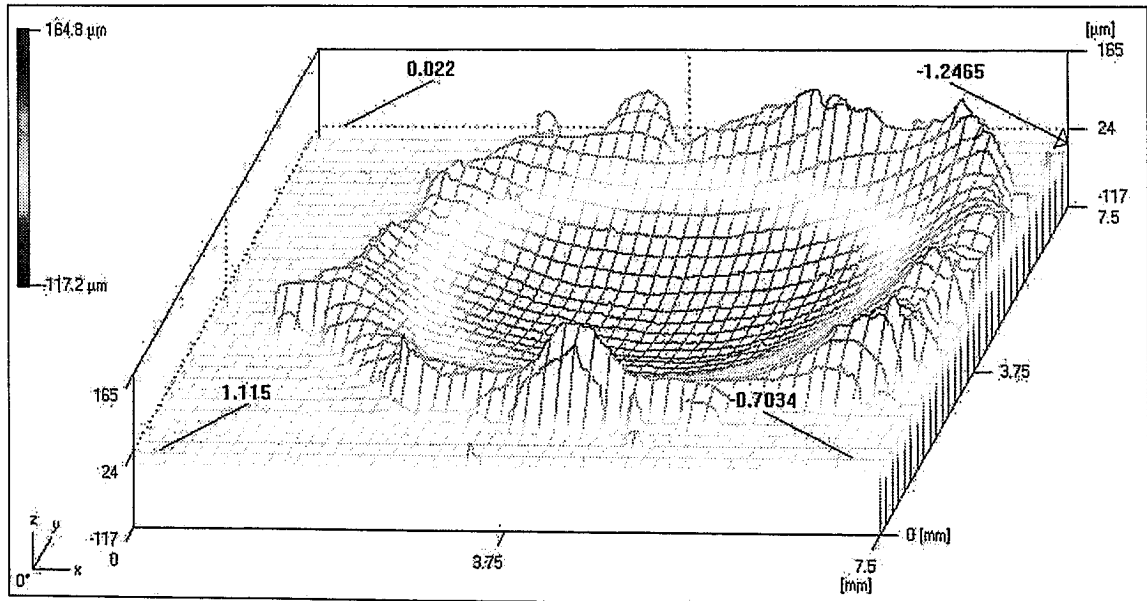


Figure 5.5 - 3D surface profile of a n-irradiated (350°C, 0.35 dpa) S65C Be sample (Id. no. S15) after 5 EB shots each at 13.5 MJ/m<sup>2</sup> incident energy density.

**Optical microscopy.** Microphotographs of all samples have been taken after e-beam loading to determine surface changes optically.

**Metallography.** After the exposure to the EB load, the specimens were sectioned at the centre of the spot and prepared for metallurgical examination. Metallographic pictures have been taken in a plane perpendicular to the surface of samples. The maximum and minimum depth of the melted zone was measured. The measured depth may underestimate the effective melted layer if the specimens was not sectioned exactly at the centre of the loaded area.

### 5.3 Test results

Test coupons made from different un-irradiated and irradiated Be grades have been exposed to intense EB pulses to simulate the thermal load during plasma disruptions. The investigated materials include the grade S65C by Brush Wellman, three Russian grades (DShG200, DShG56, and TR-30) PS Be (Los Alamos National Laboratory) and condensed Be (D.V. Efremov Institute, St.Petersburg). All tests have been carried out at room temperature. From previous test campaigns was clear that, except for the brittle Be grade TR30, erosion depth was not to be influenced by multiple shots [204]. Therefore, to eliminate surface conditioning, standard tests were five shots tests.

### 5.3.1 Measurements of absorbed current

For each Be sample the current absorbed during the first and the fifth EB shot has been recorded. In Figure 5.6 the absorbed current behaviour of un-irradiated Be S65-C during the first and the fifth e- beam shot at  $13.5 \text{ MJ/m}^2$  incident energy density is shown. Pulse duration was 5 ms. An interesting phenomenon has been observed. During about 2 ms from the beginning of the shot, the absorbed current is approximately 90% of the incident value due to the fraction of backscattered electrons. Then it drops to 50% of the initial value. This is common for all samples and a small difference in the amount of the drop has been observed between the first and the fifth shot. Similar behaviour has been monitored in case of irradiated S65C samples (Figure 5.7 and Figure 5.8).

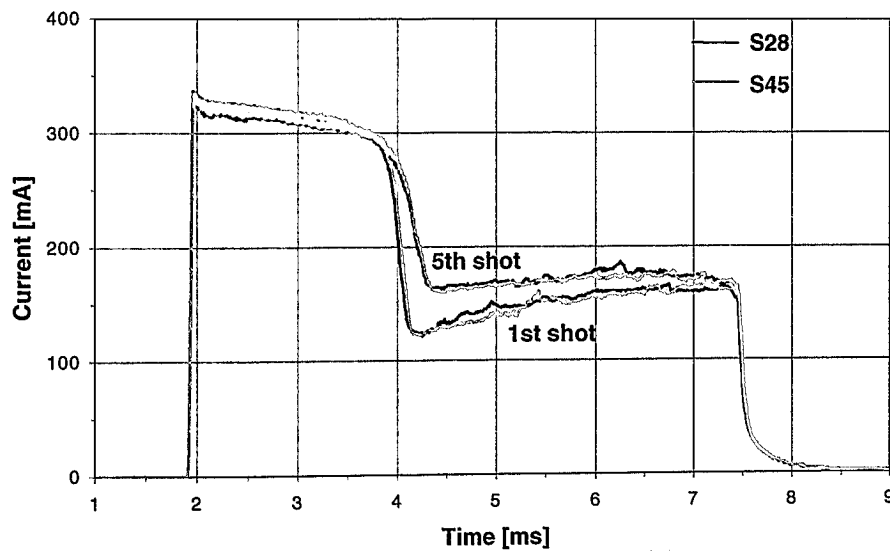


Figure 5.6 - Absorbed current during the 1st and 5th EB shot at  $13.5 \text{ MJ/m}^2$  on Be S65C un-irradiated samples.

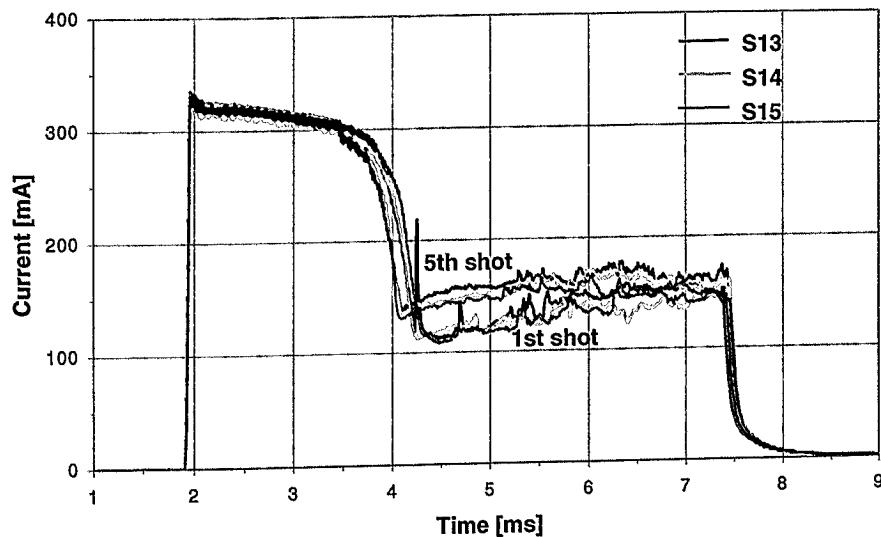


Figure 5.7 - Absorbed current during the 1st and 5th EB shot at  $13.5 \text{ MJ/m}^2$  on Be S65C irradiated at  $350^\circ\text{C}$  and 0.35 dpa.

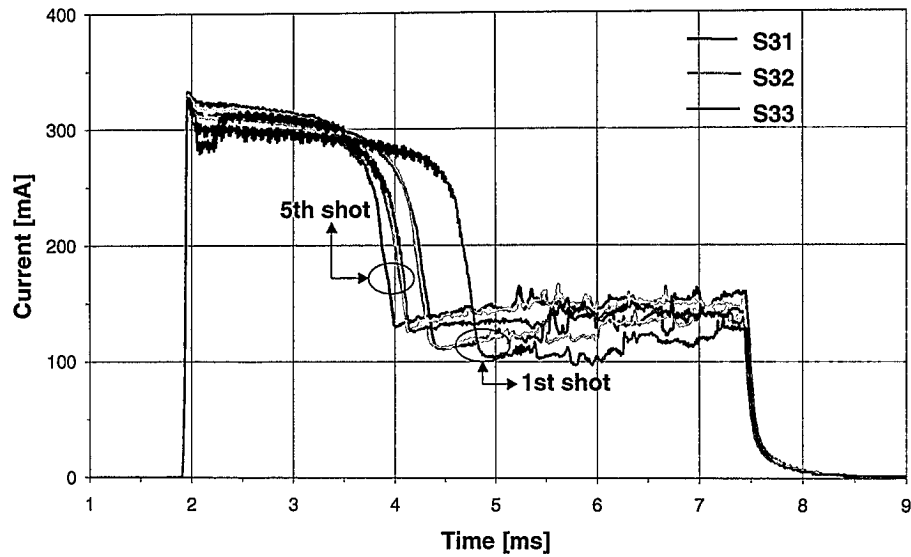


Figure 5.8 - Absorbed current during the 1st and 5th EB shot at  $13.5 \text{ MJ/m}^2$  on Be S65C irradiated at  $700^\circ\text{C}$  and 0.35 dpa.

Figure 5.9 shows the comparison between the absorbed current monitored during the fifth shot at  $13.5 \text{ MJ/m}^2$  on S65C un-irradiated, irradiated at  $350^\circ\text{C}$  and at  $700^\circ\text{C}$ . In Table 5.1 the values of the significant points of Figure 5.9 are reported. In case of samples irradiated at  $700^\circ\text{C}$  the drop is  $\sim 10\%$  bigger with respect to the un-irradiated sample and appears  $\sim 0.34 \text{ ms}$  earlier.

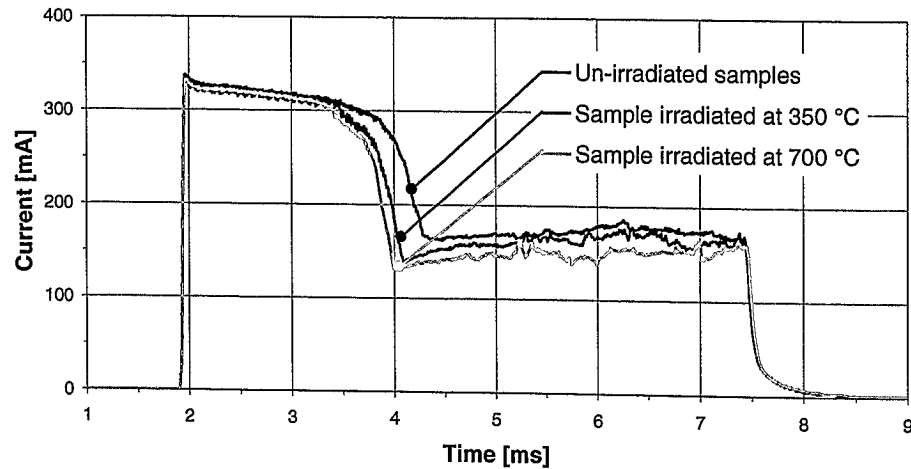


Figure 5.9 - Absorbed current during the 5th EB shot at  $13.5 \text{ MJ/m}^2$  on Be S65C un-irradiated and irradiated samples.

Table 5.1 - Time and absorbed current values during the 5<sup>th</sup> EB shot on Be S65C.

Sample un-irradiated		Sample irradiated $350^\circ\text{C}$		Sample irradiated $700^\circ\text{C}$	
Time [ms]	$I_{\text{abs}}$ [mA]	Time [ms]	$I_{\text{abs}}$ [mA]	Time [ms]	$I_{\text{abs}}$ [mA]
0	323	0	323	0	323
1.56	300	1.36	300	1.28	300
2.22	165	1.97	139	1.88	130
5	175	5	165	5	150

Several effects could originate this drop. The high incident power density could lead to a very fast ablation of the material so that the incoming electrons could be somewhat shielded by evaporated material [206]. On the other hand due to the high temperature of the sample the electron thermal emission could have a significant effect [207-209]. However, in the former case, i.e. that vapour shielding takes place, the resulting material damage has to be associated to a reduced absorbed energy value whereas in the latter case, i.e. that the drop in the absorbed current is due to thermionic emission, the energy of the incident electrons is deposited in the melt layer, because the energy of the thermally emitted electrons can be neglected compared to the incident energy of 120 keV per electron.

It is therefore important to fully understand the nature of the current drop. Looking to the results, electron thermal emission seems more likely than vapour shielding.

### 5.3.2 Thermionic electron emission: a hypothesis for the current drop

Because high energy electrons penetrate the target material deeply, no significant vapour shielding is expected to occur during the tests and the more likely explanation for the drop of the absorbed current is that electron emission takes place.

The current behaviour shown in figures 6 to 9 seems to be related to a threshold effect as for the thermionic emission: when the heat supplies some electrons with at least the minimal energy (work function) required to overcome the attractive force holding them in the structure of the metal, electrons will begin to be emitted from the metal. A Faraday cage (Figure 5.10) was installed during some tests for catching the thermionically emitted electrons. An increase of current through the cage was expected in connection with the absorbed current drop; but unfortunately this effect was not observed. The reason for that was probably due to a non-correct set-up of the cage.

In fact the latter was grounded by a resistor of 1 k $\Omega$  and since some of the incident electrons and/or the back-scattered electrons deposited their energy in the Faraday cage, a small current (~30 mA) was absorbed by this from the beginning of the electron beam shot, holding the cage at negative potential (~30 V). Due to a relatively large space (9 mm) between the sample surface and the Faraday cage, which was imposed by geometrical limitations of the sample holder, the electrons thermionically emitted escaped then through this space moving towards the vacuum chamber walls, which were at ground potential.

Due to the installation of the Faraday cage, which optically shielded the heated surface of the test coupons, the use of diagnostics (e.g. pyrometer) for monitoring the beryllium surface temperature was in that case not possible during the e-beam loading.

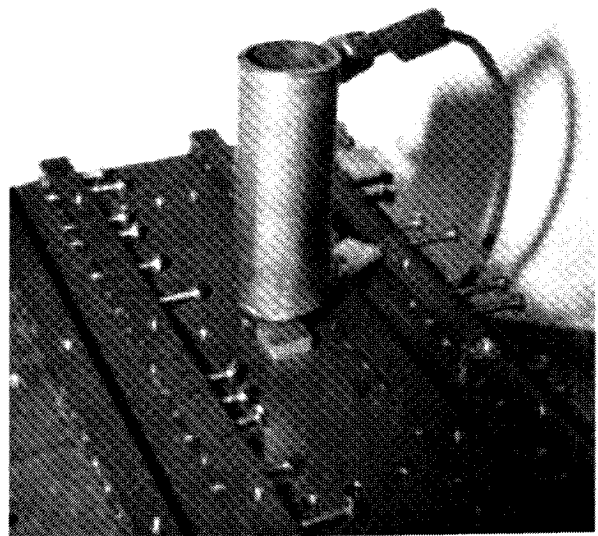


Figure 5.10 - Faraday cage installed during thermal shock tests.

This could have been helpful for understanding the effect [206]. Nevertheless, since a computational simulation of the experiment has been carried out [210], an indication of the sample temperature has been obtained from the analysis (ref. paragraph 5.4).

The electronic thermal thermionic emission current depends critically on temperature. The value of this current can be related to the temperature according to Richardson's law:

$$J = AT^2 e^{-W/kT} \text{ [A/cm}^2\text{]}$$

where T is the temperature in Kelvin, W is the work function of the metal<sup>13</sup> and k is Boltzman's constant ( $1.38 \times 10^{-23}$  J/K). The factor A is known as Richardson's constant and has a theoretical value of  $120 \text{ A/cm}^2 \text{K}^2$ , although its experimental value changes dependent on the quality of the surface being considered and on the metal [211, 212]. The thermionic work function for pure beryllium between 900 K and 1200 K was found to be 3.67 eV with slight temperature dependence [213 - 216].

Assuming that the Richardson's equation is the best fit for our data we try to fit our data to this function considering a possible interpretation of the origin of the current drop [217]. Due to the relatively large penetration depth of 120 keV electrons in a low-Z material ( $\sim 150 \text{ }\mu\text{m}$  in beryllium), the formation of a melt layer is not restricted to the outer surface alone but according to the computational simulation of the experiment a relatively thick layer will undergo phase transition. Now intense electron beam-induced convection will take place in the melt layer; the temperature will further increase until an equilibrium of beam heating, conduction and evaporation cooling is reached. For beryllium this temperature has been calculated to be about 2100 K. At this temperature, the thermally induced electron emission of a metallic surface according to the Richardson's equation is  $8 \text{ mA/mm}^2$ . Hence, the electron beam heated spot ( $4 \times 4 \text{ mm}^2$ ) should emit an electrical current of about 130 mA, which is confirmed by measurements obtained during test at  $13.5 \text{ MJ/m}^2$  incident energy density.

Therefore the absorbed current drop could be explained by electron thermionic emission. The small differences observed between the first and the fifth shots and between un-irradiated and irradiated samples could be related to changes of the work function and/or Richardson's constant, which are sensitive both to the surface conditions and to the temperature surface, the latter being influenced also by localised changes of the electrical resistivity and/or thermal conductivity in case of irradiated samples.

All the investigated Be grades showed a similar absorbed current behaviour during the electron beam shots. In case of samples tested at lower energy density ( $7.5 \text{ MJ/m}^2$  per shot; pulse duration 5 ms) the measured current drop was less and the drop occurred later (compare Figure 5.9, un-irradiated sample curve and Figure 5.13, sample on big Cu holder curve). The time delay is due to the fact that the samples absorbed less energy and therefore they reached the temperature at which the thermionic emission starts later. The smaller entity of the drop is due to a corresponding lower temperature at which the equilibrium of beam heating and evaporation cooling is reached.

### 5.3.3 First test campaign

During this test campaign six grades of un-irradiated beryllium and four irradiated grades at  $350^\circ\text{C}$  and 0.35 dpa have been investigated.

#### 5.3.3.1 Loading conditions

During the tests 5 electron beam shots of incident energy densities up to approx.  $13.5 \text{ MJm}^{-2}$  have been applied; pulse duration was typically 5 ms. All tests have been carried out at room

---

<sup>13</sup> minimal energy required to overcome the attractive force holding the electrons in the structure of the metal.



temperature. In Table 5.2 and Table 5.3 the investigated Be grades and the corresponding applied loading conditions are listed.

Table 5.2 - First test campaign. HHF tests on un-irradiated Be samples. Investigated grades and applied loading conditions.

Be grades	$I_{\text{beam}}$ [mA]	$V_{\text{acc}}$ [kV]	$A_{\text{spot}}$ [mm <sup>2</sup> ]	No. of shot	$t_{\text{pulse}}$ [ms]	P/A [MW/m <sup>2</sup> ]
S65C DShG200 TShG56	200	120	4*4	5	5	~ 1500
S65C DShG200 TShG56 TR30 Cond. Be PS Be (F) PS Be (CC)	360	120	4*4	5	5	~ 2700

Table 5.3 - First test campaign. HHF tests on irradiated Be samples (350°C and 0.35 dpa) samples. Investigated grades and applied loading conditions.

Be grades	$I_{\text{beam}}$ [mA]	$V_{\text{acc}}$ [kV]	$A_{\text{spot}}$ [mm <sup>2</sup> ]	No. of shot	$t_{\text{pulse}}$ [ms]	P/A [MW/m <sup>2</sup> ]
S65C	200	120	4*4	5	5	~ 1500
S65C Cond. Be PS Be (F) PS Be (CC)	360	120	4*4	5	5	~ 2700

### 5.3.3.2 Experimental features

For each Be sample the current absorbed during the 1<sup>st</sup> and the 5<sup>th</sup> e-beam shot has been recorded.

Figure 5.11 shows the absorbed current behaviour during the 5<sup>th</sup> e-beam shot for some un-irradiated samples which have been tested at 13.5 MJ/m<sup>2</sup> incident energy density. It can be noted that the behaviour of the absorbed current was almost the same for all specimens. Only the behaviour of condensed Be is shifted of to some extent. This effect could be originate from a material discontinuity along the thickness of the sample due to its fabrication method, which consists of a condensed layer deposited on a pre-existent substrate of same material.

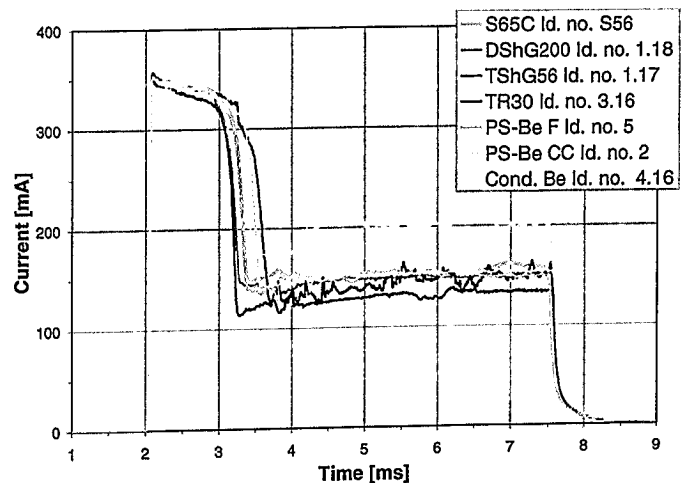


Figure 5.11 – HHF test on un-irradiated Be samples during the 1st test campaign. Absorbed current behaviour during the fifth EB shot at 13.5 MJ/m<sup>2</sup> energy density.

Due to normal difficulties in operating with irradiated samples, it has been decided, during this test campaign, to execute first the tests on all un-irradiated Be specimens and then the tests on all irradiated Be samples.

For avoiding possible contamination of the un-irradiated samples, two different copper holders have been used for the tests. The un-irradiated specimens were placed on a small copper holder, whereas the irradiated samples were fixed by means of screws on a bigger copper holder. Figure 5.12 shows the copper holder, which has been used for the irradiated samples. The different experimental set up influenced the behaviour of the current absorbed by the samples. For the specimens placed on the small copper holder the drop of the current appeared earlier than for the samples fixed by screws on the bigger copper holder (Figure 5.13).

This difference has been ascribed to the different thermal contact between samples and copper holder, which takes place in the two different arrangements. A reasonable explanation is that in case of samples placed without screw on a small copper holder the temperature at which thermionic emission starts is reached earlier with respect to the samples fixed on the bigger copper holder. By measuring the absorbed current before the occurrence of the drop, it has been determined that up to maximum 10% of the incident electrical power density has been reflected during the tests. This value corresponds to the value determined in previous test campaigns [198, 200, 201].

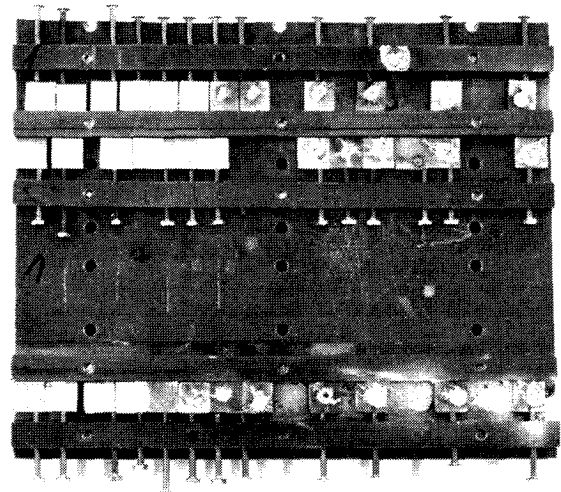


Figure 5.12 - Cu holder used for measuring the current absorbed by the n-irradiated Be samples during the first test campaign (1998).

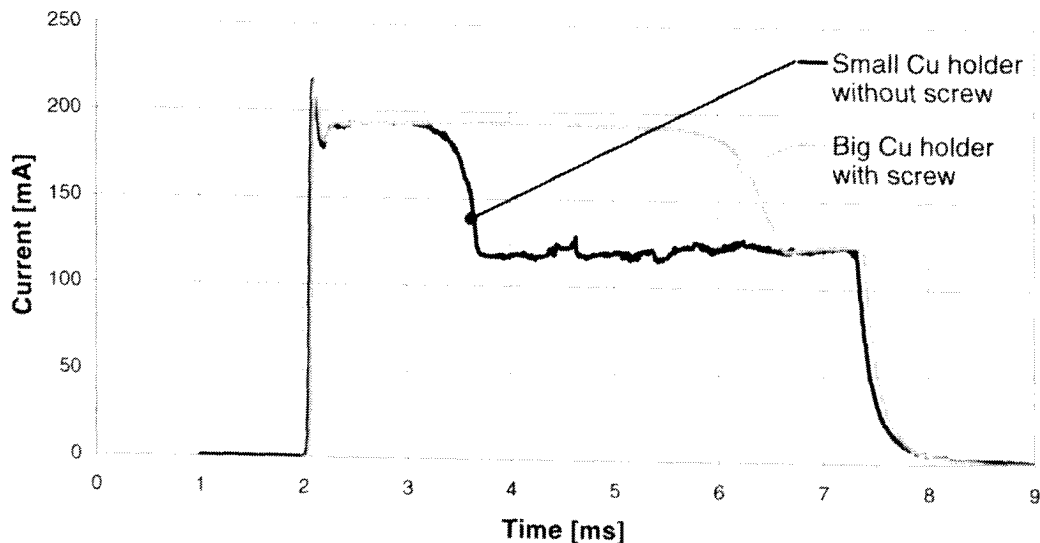


Figure 5.13 – Absorbed current behaviour of two un-irradiated Be S65C samples during an EB shot of 7.5 MJ/m<sup>2</sup>. Comparison between two different mounting systems.

### 5.3.3.3 Thermal shock damage – comparison of Be grades

After thermal shock tests, all samples have been investigated by weight loss measurement and 3D surface profilometry. Figure 5.14 shows the mean weight loss comparison of the un-irradiated Be grades after 5 EB shots at 7.5 MJ/m<sup>2</sup> and 13.5 MJ/m<sup>2</sup> incident energy density respectively.

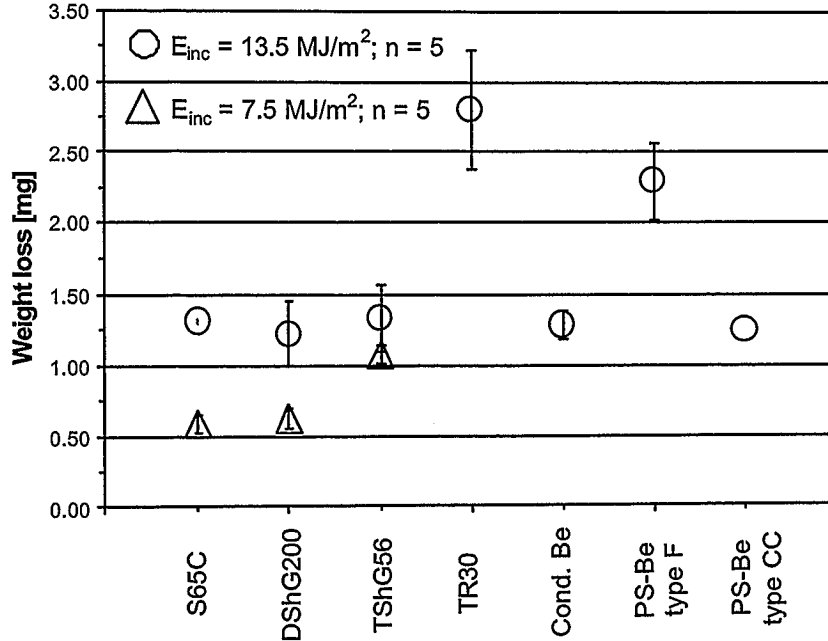


Figure 5.14 - HHF test on un-irradiated Be samples during the 1st test campaign. Mean weight loss after 5 EB shots at 7.5 MJ/m<sup>2</sup> and 13.5 MJ/m<sup>2</sup>.

The grade S65C showed at both energy densities the lowest mean weight loss, taking into account that for this grade the smallest scattering in the results has been obtained.

Figure 5.15 shows the maximum crater depth measured on the un-irradiated samples after 5 EB shots at 7.5 MJ/m<sup>2</sup> and 13.5 MJ/m<sup>2</sup> incident energy density, respectively.

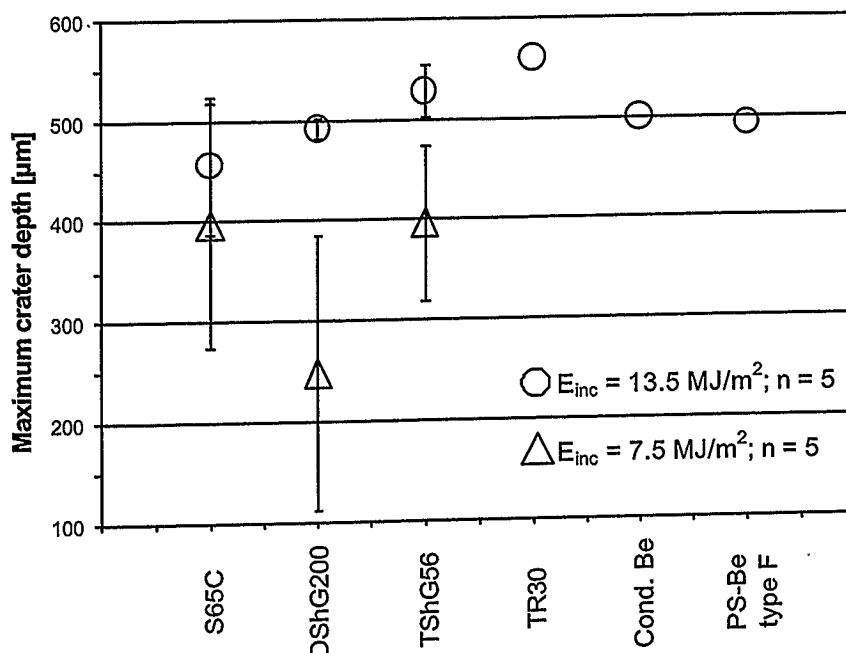


Figure 5.15 - HHF test on un-irradiated Be samples during the 1st test campaign. Mean value of maximum crater depth after 5 EB shots at 7.5 MJ/m<sup>2</sup>.

A very larger scattering in the measurements has been found mainly for the samples tested at of  $7.5 \text{ MJ/m}^2$ . The origin of this scattering should probably be ascribed to a not always reproducible distribution of the electrical current on the samples, which causes different melt movements. Figure 5.16 shows microphotographs of two S65C sample surfaces loaded by 5 EB shots of  $7.5 \text{ MJ/m}^2$  from which the above mentioned effect is clearly visible. Figure 5.17 shows the corresponding profilometer area scans for one of these samples.

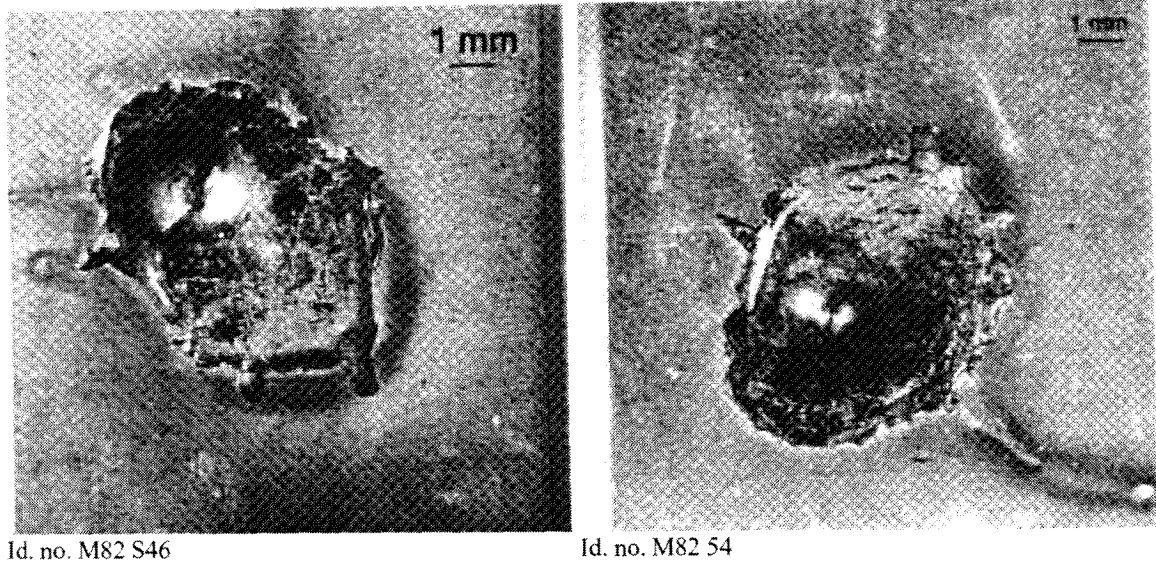


Figure 5.16 - HHF test on un-irradiated Be samples during the 1st test campaign. Microphotographs of two S65C samples after 5 EB shots of  $7.5 \text{ MJ/m}^2$ .

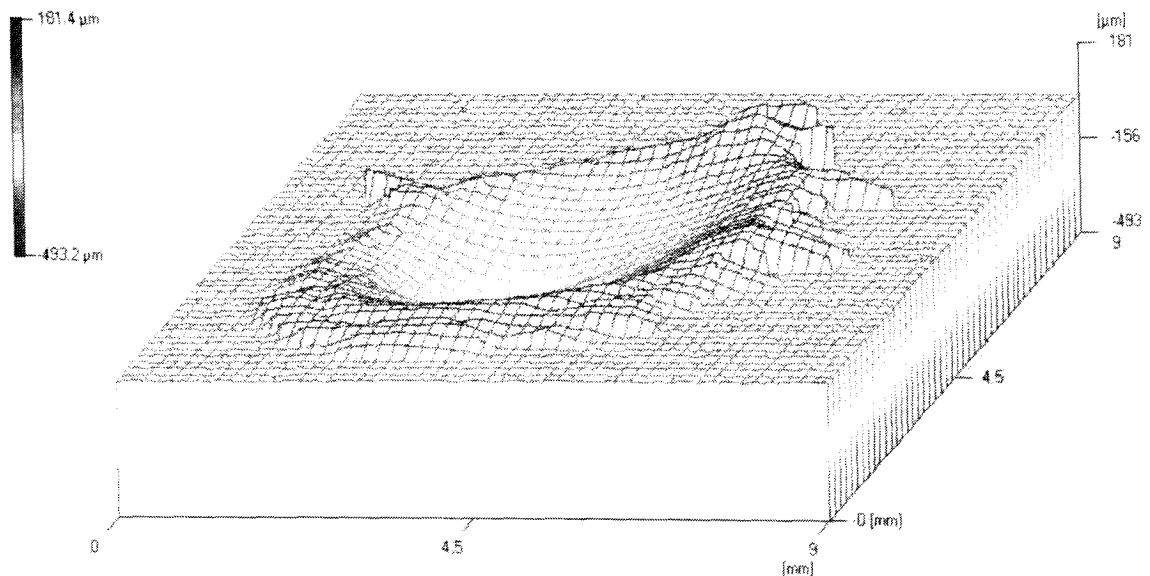


Figure 5.17 - HHF test on un-irradiated Be samples during the 1st test campaign. 3D surface profile of a S65C sample (Id. no. M82 54) after 5 EB shots at  $7.5 \text{ MJ/m}^2$ .

Therefore, taking into account the unavoidable experimental uncertainties, the general trend of the un-irradiated Be grades, which was already observed in previous test campaigns [197-201] at lower energy density, was confirmed also at higher energy up to  $13.5 \text{ MJ/m}^2$ . The S65C grade confirmed its best thermal shock performance in comparison to the other grades.

### 5.3.3.4 Thermal shock damage - comparison of un-irradiated and irradiated Be

#### Be S65C

In Figure 5.18 the weight loss of un-irradiated and irradiated Be S65C is shown as function of the incident energy density. The material shows higher erosion after neutron irradiation.

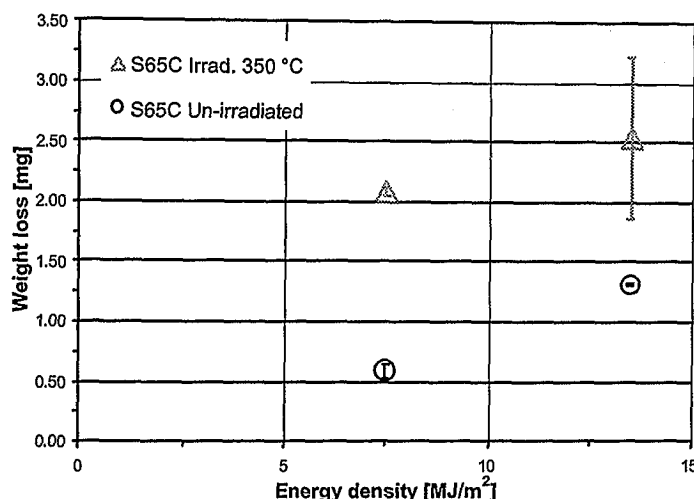


Figure 5.18 - First test campaign. Weight loss comparison of un-irradiated and irradiated (350°C; 0.35 dpa) Be S65C after 5 EB shots at 7.5 MJ/m² and 13.5 MJ/m².

The mean weight loss of the irradiated material after the HHF load is between two and three times higher than that of the un-irradiated material. However from the metallography investigation (see Figure 5.23-C) it seems that the loaded area of irradiated samples was smaller than that of un-irradiated specimens. Therefore these results should be considered conservative, in the sense that the erosion values corresponding to the irradiated samples could pertain to higher values of absorbed energy density.

The medium value of the maximum crater depth determined by laser profilometry vs. incident energy density is shown in Figure 5.19 for Be S65C un-irradiated and irradiated at 350 °C and 0.35 dpa.

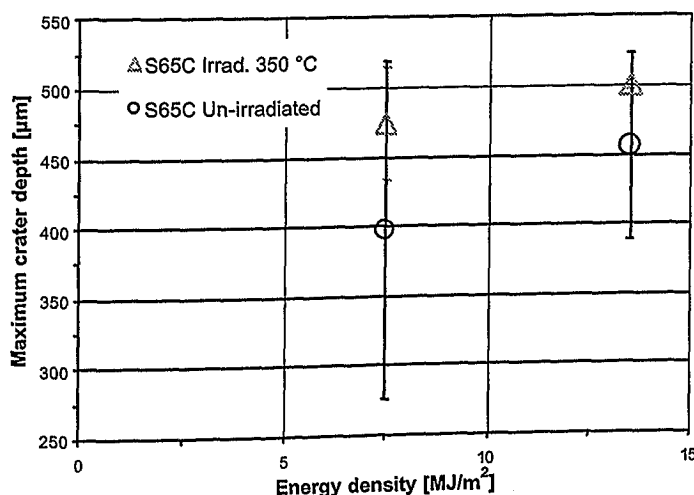


Figure 5.19 - First test campaign. Mean value of maximum crater depth of un-irradiated and irradiated (350°C; 0.35 dpa) Be S65C after 5 EB shots at 7.5 MJ/m² and 13.5 MJ/m².

Deeper craters have been measured on irradiated samples, i.e. the irradiated material showed higher erosion compared to the un-irradiated.

### S65C – Condensed Be – PS-Be

The comparison of material erosion before and after neutron irradiation for four different Be grades is shown in figures 5.20 and 5.21. The graph of Figure 5.20 represents the mean weight loss after 5 EB shots at  $13.5 \text{ MJ/m}^2$  incident energy. Apart from the condensed Be, all grades show an increased erosion after neutron damage. This result could be ascribed to the presence of gas bubbles in the crater and to the brittle destruction, which can take place in the neutron irradiated samples.

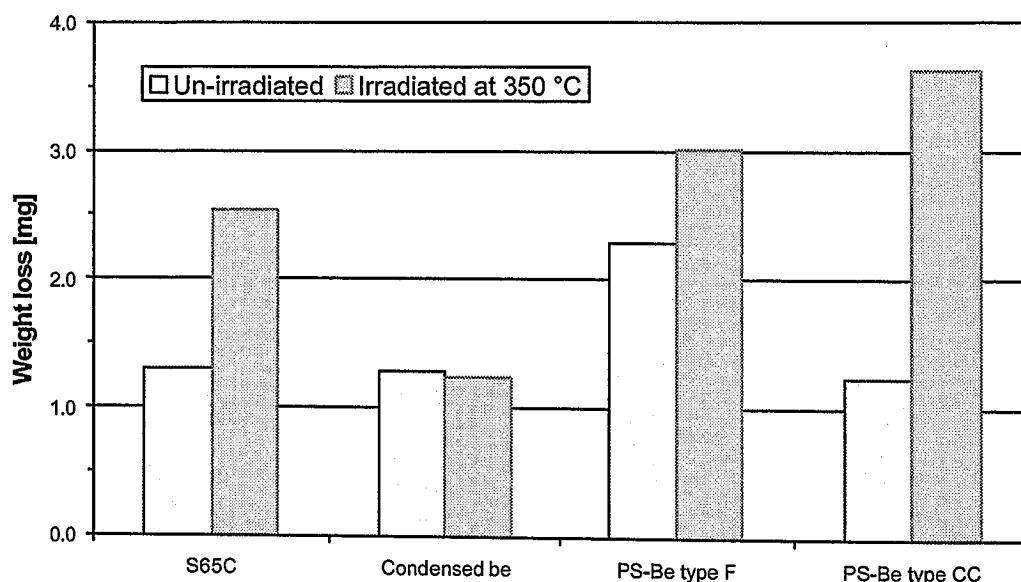


Figure 5.20 - First test campaign. Mean weight loss after 5 EB shots at  $13.5 \text{ MJ/m}^2$ . Comparison between un-irradiated and irradiated grades.

In Figure 5.21 the mean value of the maximum crater depth determined from 3D-profiles has been plotted. Five electron beam shots at  $13.5 \text{ MJ/m}^2$  energy density have been applied.

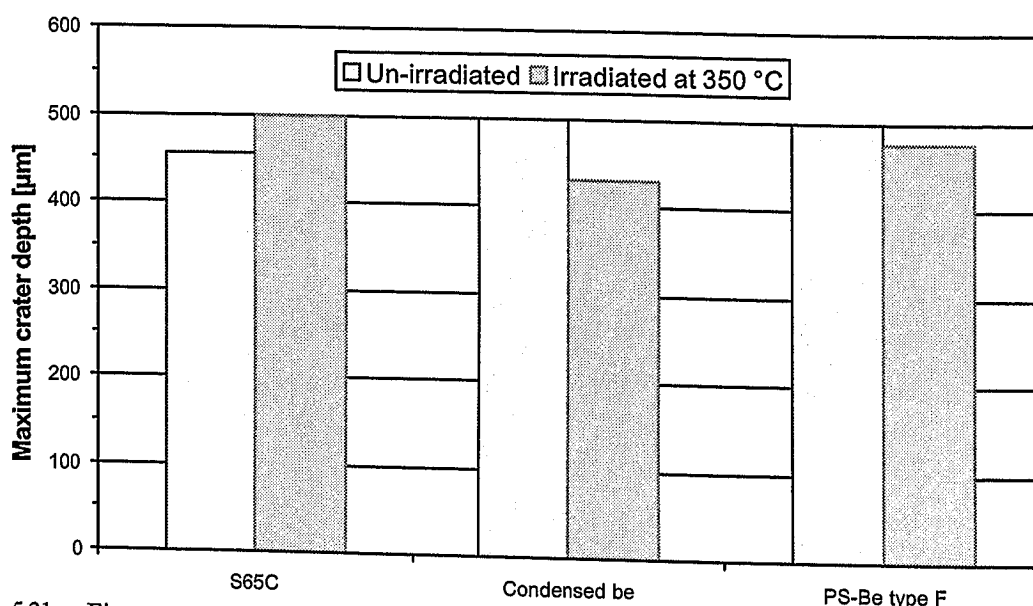


Figure 5.21 - First test campaign. Mean value of maximum crater depth after 5 EB shots at  $13.5 \text{ MJ/m}^2$ . Comparison between un-irradiated and irradiated grades.

The values of the mean weight loss per electron beam pulse obtained during this test campaign are reported in Table 5.4. The values of the corresponding standard deviation are

also indicated. In the light of the latter, the Be grade S65C remains the material, which shows the best thermal shock performance also after neutron irradiation.

Table 5.4 - First test campaign. Mean weight loss per pulse after 5 EB shots at different incident energy density.

Material grade	$E_{inc} 7.5 \text{ MJ/m}^2$				$E_{inc} 13.5 \text{ MJ/m}^2$			
	Un-irradiated weight loss [mg]	$\sigma$	Irradiated weight loss [mg]	$\sigma$	Un-irradiated weight loss [mg]	$\sigma$	Irradiated weight loss [mg]	$\sigma$
S65C	0.117	0.012	0.416	0.006	0.261	0.002	0.509	0.135
DShG200	0.124	0.014	-	-	0.244	0.046	-	-
TShG56	0.215	0.014	-	-	0.265	0.048	-	-
TR30	-	-	-	-	0.560	0.084	-	-
Condensed Be	-	-	-	-	0.256	0.020	0.248	0.012
PS-Be Type F	-	-	-	-	0.459	0.055	0.602	0.118
PS-Be Type CC	-	-	-	-	0.248	-	0.724	-

### 5.3.3.5 Post-mortem analysis

#### Be S65C

For comparing the erosion behaviour of the irradiated coupons with that of the corresponding un-irradiated specimens, metallurgical examination of all irradiated samples and one un-irradiated as reference has been carried out.

Figures 5.22 to 5.26 show microphotographs of the sample surface and correlative metallographic pictures of un-irradiated and irradiated S65C samples after thermal shock tests.

Figure 5.22 and 5.23 concern un-irradiated and irradiated specimens respectively loaded at  $7.5 \text{ MJ/m}^2$  incident energy density.

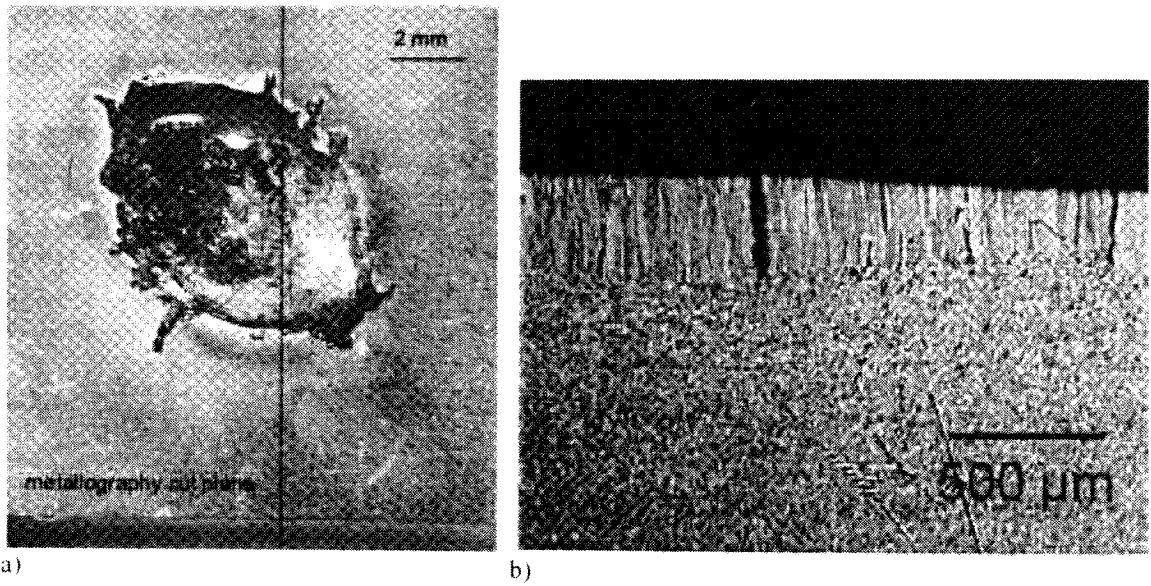
Figure 5.24 shows the surface and corresponding metallographic section of S65C un-irradiated sample loaded at  $13.5 \text{ MJ/m}^2$  whereas figures 5.25 and 5.26 show the damage obtained on the corresponding irradiated samples.

The metallographic pictures have been taken in a plane perpendicular to the surface of samples, which is indicated for the un-irradiated samples.

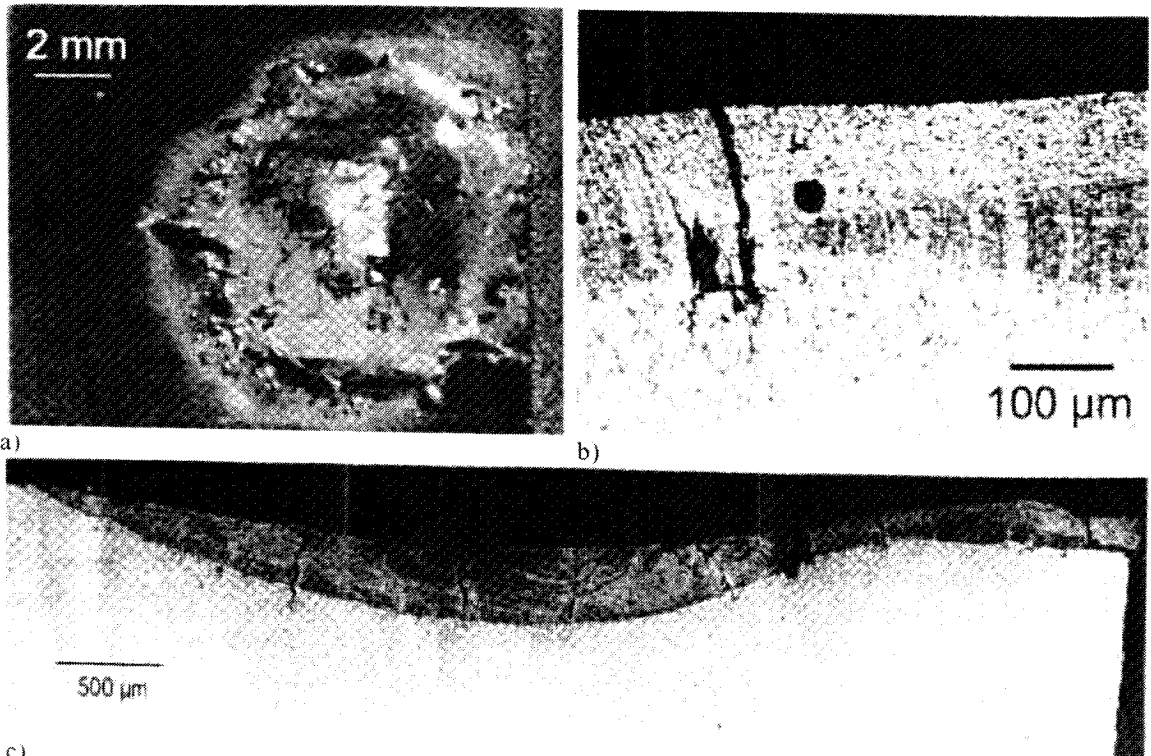
Different crater shapes have been obtained after the e-beam load on the samples. A more circular hole is observed in case of irradiated material whereas the craters of the un-irradiated samples are more oval in shape (Figure 5.22-a).

An estimation of the crater width is possible from the metallographic sections. It should be noted that if, for example, the loaded area during the tests at  $7.5 \text{ MJ/m}^2$  on the irradiated samples corresponded to a circle of  $\sim 4 \text{ mm}$  diameter (Figure 5.23), the energy density absorbed from these specimens was  $\sim 10 \text{ MJ/m}^2$  and an overestimation of the erosion presented from the material after neutron irradiation has to be considered. For the irradiated samples which have been tested at higher energy density ( $13.5 \text{ MJ/m}^2$ ) the estimated value of crater width was  $\sim 4.5 \text{ mm}$ , which correspond, in case of circular crater shape, to a loaded area of  $\sim 16 \text{ mm}^2$ . Thus the comparison of the material damage before and after neutron irradiation at higher energy density is more realistic than that at lower energy density.

The microphotographs of all specimens show severe melting and a dense crack pattern throughout the loaded surface with a slightly increased number of cracks on the irradiated samples. Molten rim around the crater and droplet formation is clearly visible on all test coupons. Drops spray out of the melt and re-solidify on the surface of the material. Outward movement of melt material on the solidified surface takes place.

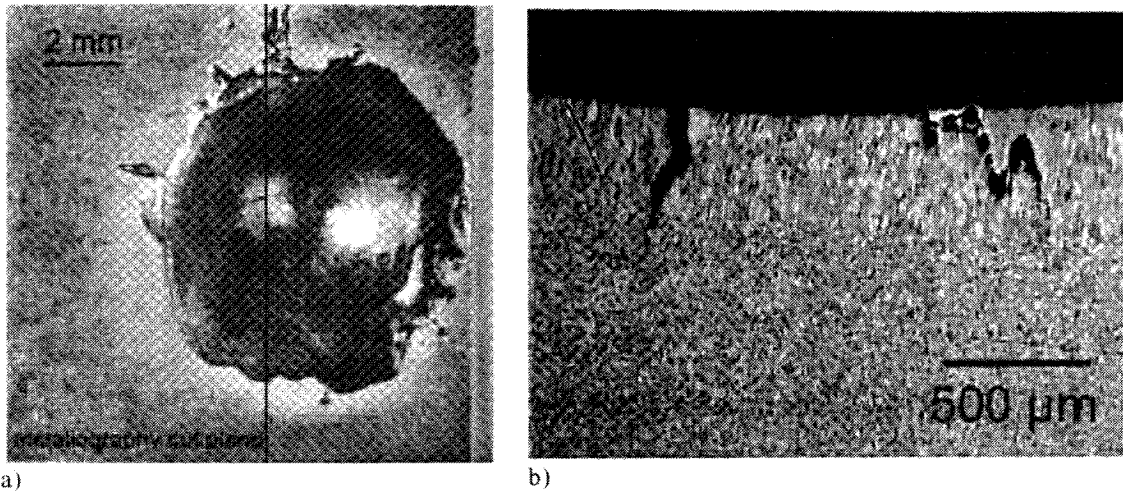


a) b)  
Figure 5.22 - First test campaign. Be S65C un-irradiated (Id. no. M82 52) after 5 EB shots at  $7.5 \text{ MJ/m}^2$ . Microphotograph and corresponding metallographic picture.

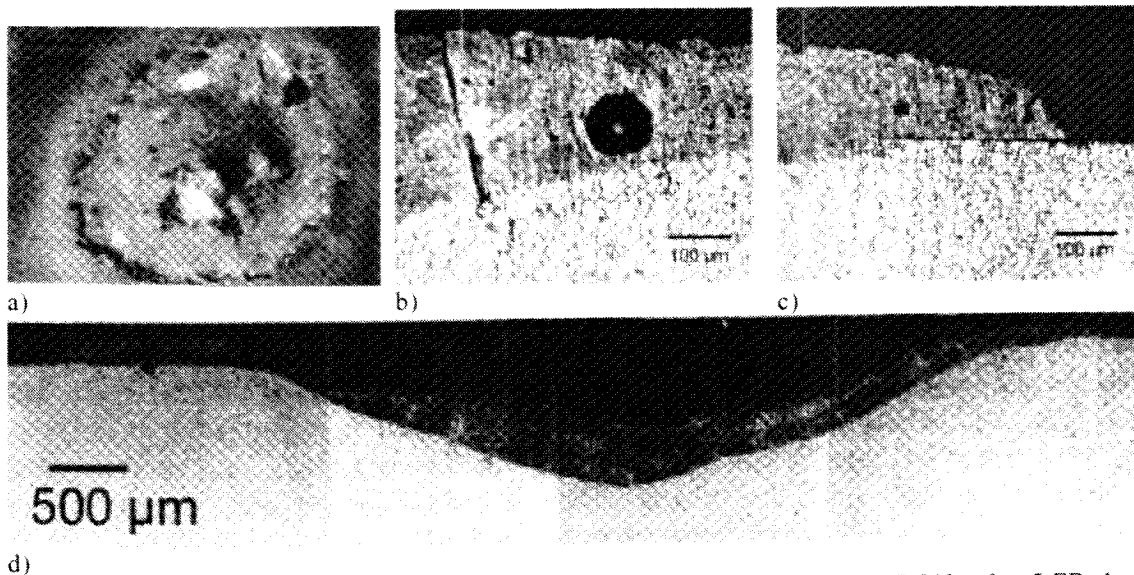


a) b) c)  
Figure 5.23 - First test campaign. Irradiated ( $350^\circ\text{C}$ ; 0.35 dpa) Be S65C (Id. no. M77 S19) after 5 EB shots at  $7.5 \text{ MJ/m}^2$ . Microphotograph and corresponding metallographic pictures taken in a plane perpendicular to the surface of sample.





a) b)  
Figure 5.24 - First test campaign. Be S65C un-irradiated (Id. no. M82 53) after 5 EB shots at  $13.5 \text{ MJ/m}^2$ . Microphotograph and corresponding metallographic picture.



a) b) c) d)  
Figure 5.25 - First test campaign. . Irradiated ( $350^\circ\text{C}$ ; 0.35 dpa) Be S65C (Id. no. M77 S12) after 5 EB shots at  $13.5 \text{ MJ/m}^2$ . Microphotograph and corresponding metallographic pictures taken in a plane perpendicular to the surface of sample.

From the metallographic sections of all samples, the fine grain, homogenous zone of the base material is easily recognisable from the heat affected zone. The re-crystallized material shows a columnar grain structure with grains orientation perpendicular to the loaded surface due to the direction of the thermal gradient.

Thermally induced cracks appear perpendicular to the surface and they only extend to the bottom of the melt layer and not into the base material. This pattern of cracks in the re-crystallized zone is very advantageous for the plasma facing components design, since it contributes to the release of thermally induced stresses.

Nevertheless, at incident energy densities of  $13.5 \text{ MJ/m}^2$ , the resulting cracks in one irradiated sample (Figure 5.26) penetrate deep into the base material and move in a direction parallel to the sample's surface, that is very dangerous for the component's integrity and life time.

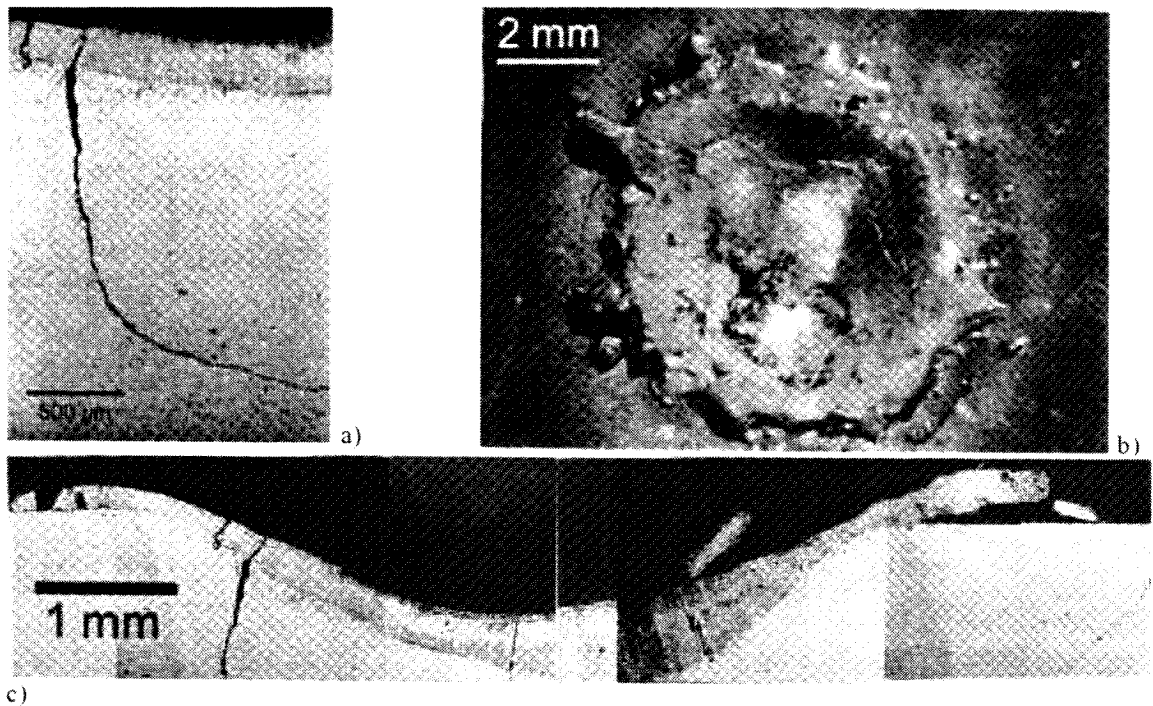


Figure 5.26 - First test campaign. . Irradiated (350°C; 0.35 dpa) Be S65C (Id. no. M77 S20) after 5 EB shots at 13.5 MJ/m<sup>2</sup>. Microphotograph and corresponding metallographic pictures taken in a plane perpendicular to the surface of sample.

Neutron irradiated samples show more porosity in comparison with the un-irradiated samples. A clear pore formation is recognisable in the melt layer of the samples after EB loading (see figures 5.23-b, 5.25-b and 5.25-c). The cavities in the melt layer arise from coalescence of gases present in the material during the liquid phase. These gas may be both tritium and helium produced during the neutron irradiation and some gaseous impurities (BeO) which may remain trapped between the grains of Be powder during the manufacturing process. Unfortunately, due to the location of samples inside the hot cells, it was not possible to carry on scanning electron microscopy for investigating the origin of this porosity.

The depth of the melted zone was measured for all irradiated samples and for the un-irradiated reference sample. Figure 5.27 shows the mean value of the maximum thickness of the melt layer vs. incident energy measured on un-irradiated and irradiated S65C test coupons.

The measured depth may underestimate the effective melted layer if the specimens was not sectioned exactly at the centre of the spot. This is also the reason why the value of maximum crater depth estimated from the metallographic section may differ from the value detected by 3-D laser profilometry.

For the samples tested at higher energy density, melting takes place up to a depth of approximately 370 μm for un-irradiated and 475 μm for irradiated samples. Therefore an increase of ~ 28% has been found after neutron irradiation.

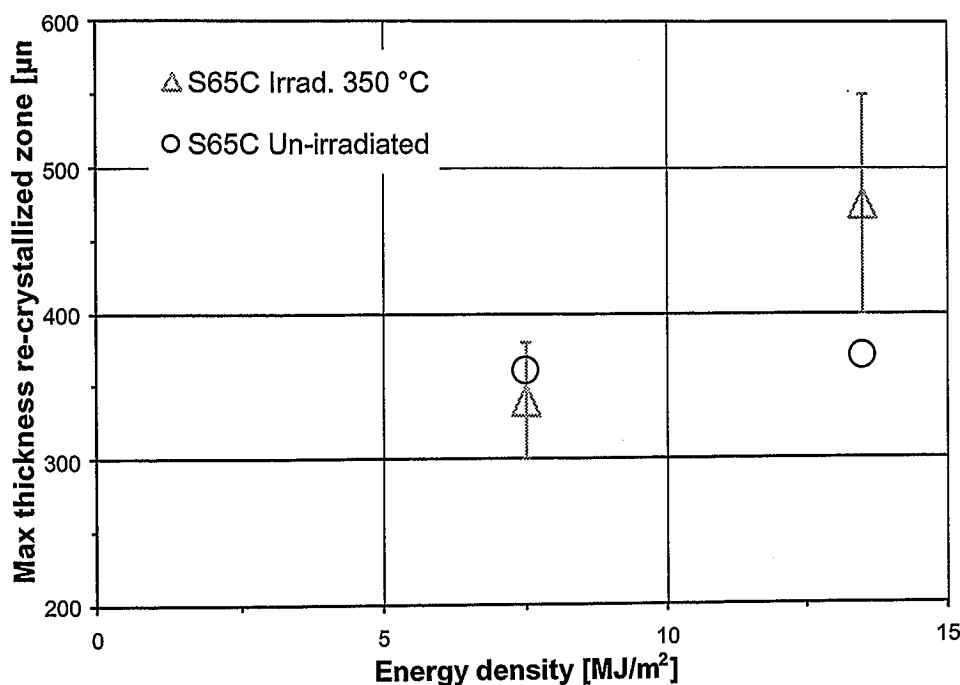


Figure 5.27 - First test campaign. Be S65C un-irradiated and irradiated (350°C; 0.35 dpa) comparison. Mean values of maximum thickness of re-crystallized zone after 5 EB shots at 7.5 MJ/m² and 13.5 MJ/m².

### Condensed Be – PS-Be

Metallographic investigation have been carried out also for the other Be grades. The erosion damage of the irradiated test coupons have been compared with that of the corresponding un-irradiated samples.

Figures 5.28 to 5.34 show microphotographs of the loaded surfaces and corresponding pictures of metallographic sections for condensed Be and PS-Be (type F and type CC) resulting from tests at 13.5 MJ/m² incident energy densities.

Also for these samples, a marked dynamic melting process with overflowing of the melt from the crater and ejection of drops has been observed. Cracks throughout the loaded area are easily recognizable

Each metallographic sections is characterized by a well-defined melted zone, recrystallized with long, columnar grain.

### Condensed Be

Figure 5.28 and Figure 5.29 show respectively the un-irradiated and irradiated condensed Be samples. These specimens present the peculiarity of elongated grain's shape also in the base material due to their fabrication method (cf. chapter 2). The irradiated test coupons consist of a layer of Be condensed onto a pre-existent layer of the same material resulting in a non homogenous junction (Figure 5.29-c).

More thermally induced cracks are observed on the irradiated samples of condensed Be. The cracks are perpendicular to the surface and extend to the base material (Figure 5.29-b). The random absence of grains in the melted zone (Figure 5.29-d) derives probably from the sample's preparation for the metallography. Also for this material, more porosity, especially in the melted area, characterizes the irradiated samples after the electron beam load.

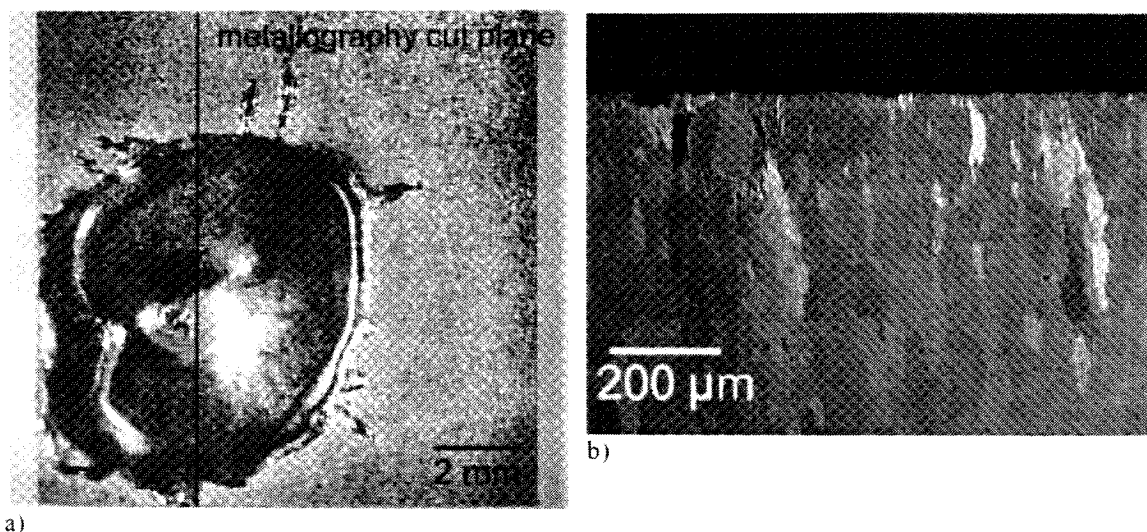


Figure 5.28 - First test campaign. Un-irradiated condensed Be (Id. no. M93 4.16) after 5 EB shots at  $13.5 \text{ MJ/m}^2$ . Microphotograph and corresponding metallographic picture.

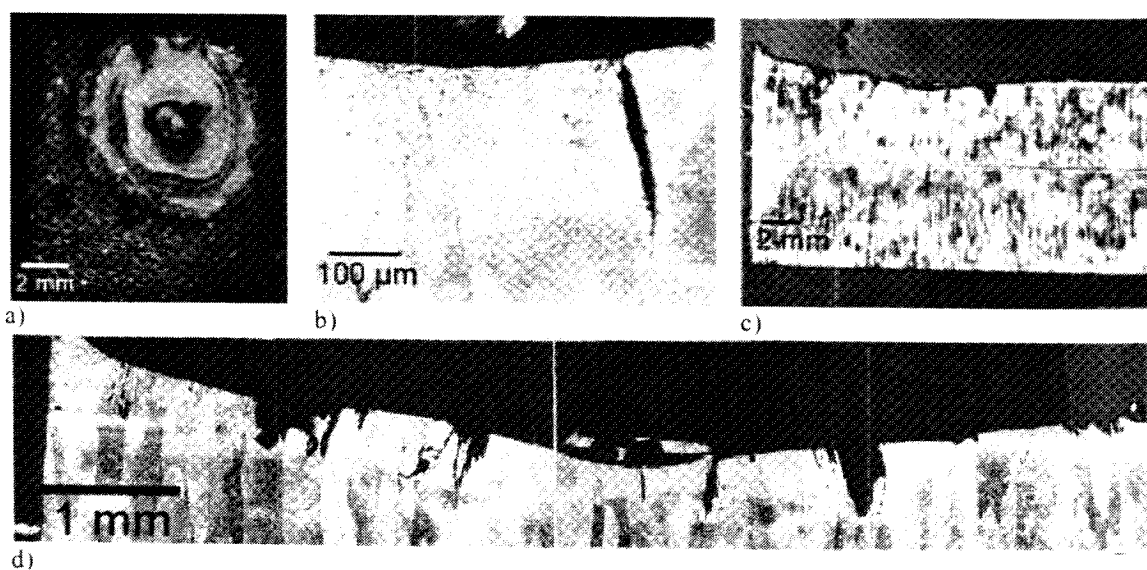


Figure 5.29 - First test campaign. Irradiated ( $350^\circ\text{C}$ ; 0.35 dpa) condensed Be (Id. no. M72 4.1) after 5 EB shots at  $13.5 \text{ MJ/m}^2$ . Microphotograph and corresponding metallographic picture.

### PS-Be

In figures 5.32 to 5.34 the erosion behaviour of PS-Be type F before and after neutron irradiation is presented. For this material severe damage after 5 electron beam shots at  $13.5 \text{ MJ/m}^2$  has been detected both in case of un-irradiated and irradiated samples.

The typical stratified structure due to their fabrication process characterizes the base material of these samples (figures 5.30-d, 5.31-b and 5.32-b). Un-melted particles between the layers are recognisable in all specimens. Only a slightly increase of porosity is observed in the material after neutron irradiation. In fact, in this material, the large part of cavities originates from coalescence of gas particles (argon) entrapped during the production of the test coupons and the influence of helium or tritium produced during neutron irradiation is not considered to be relevant. In all samples deep cracks perpendicular to the surface are observed within the resolidified zone and in the base material. In the un-irradiated test coupon cracks propagate through the thickness of the melted layer, then turned  $90^\circ$  and extend along the interface between the layers of the base material (Figure 5.30).

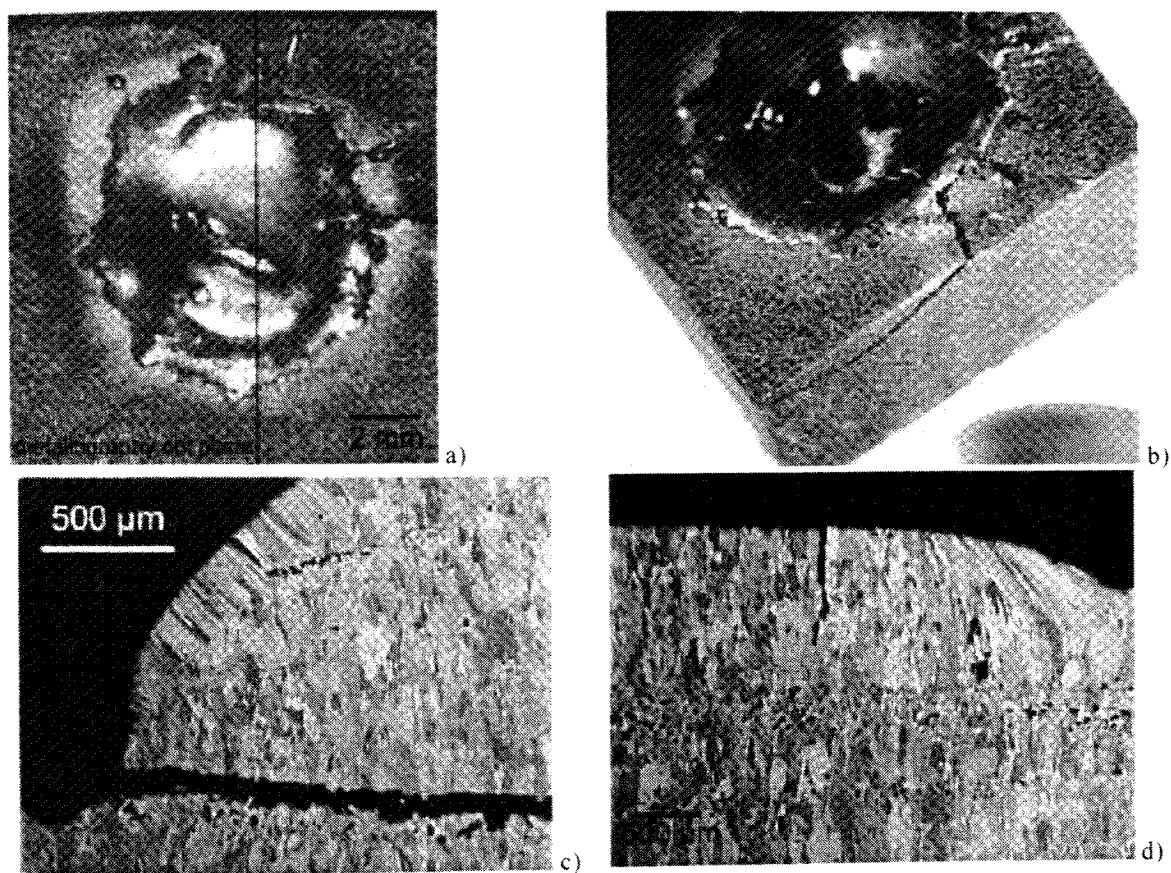


Figure 5.30 - First test campaign. PS-Be type F un-irradiated (Id. no. M119 7) after 5 EB shots at  $13.5 \text{ MJ/m}^2$ . Microphotographs and corresponding metallographic pictures.

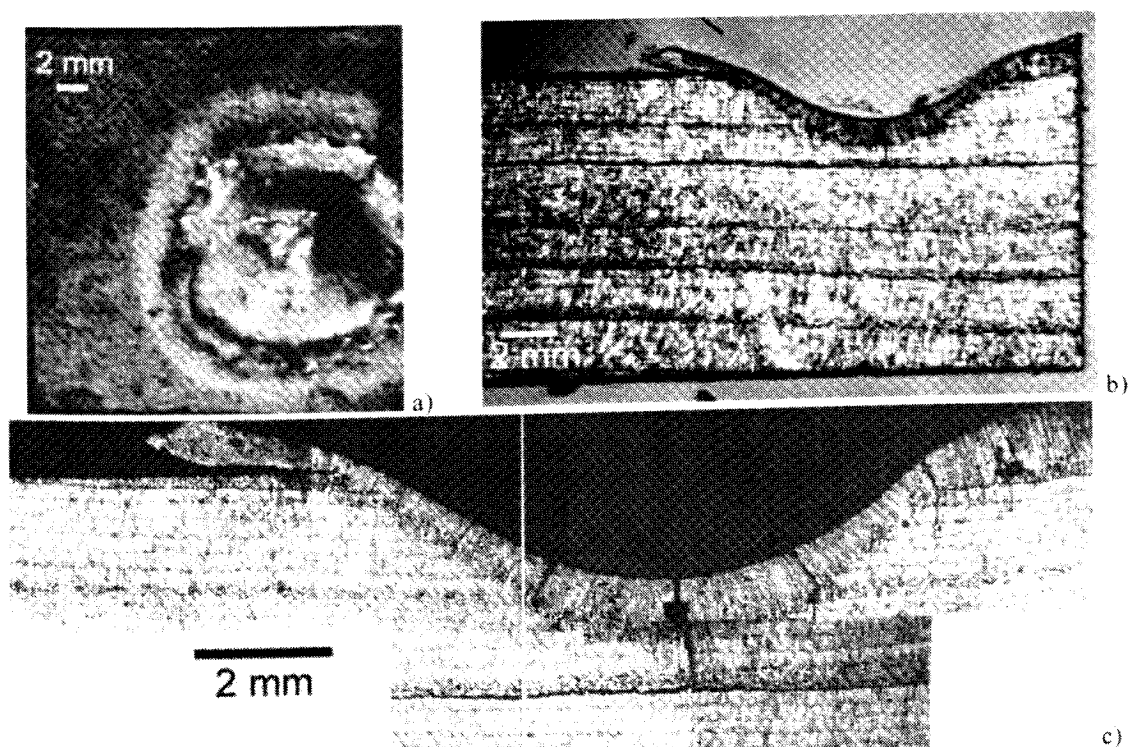


Figure 5.31 - First test campaign. Irradiated ( $350^\circ\text{C}$ ; 0.35 dpa) PS-Be type F (Id. no. M119 K9) after 5 EB shots at  $13.5 \text{ MJ/m}^2$ . Microphotograph and corresponding metallographic pictures.



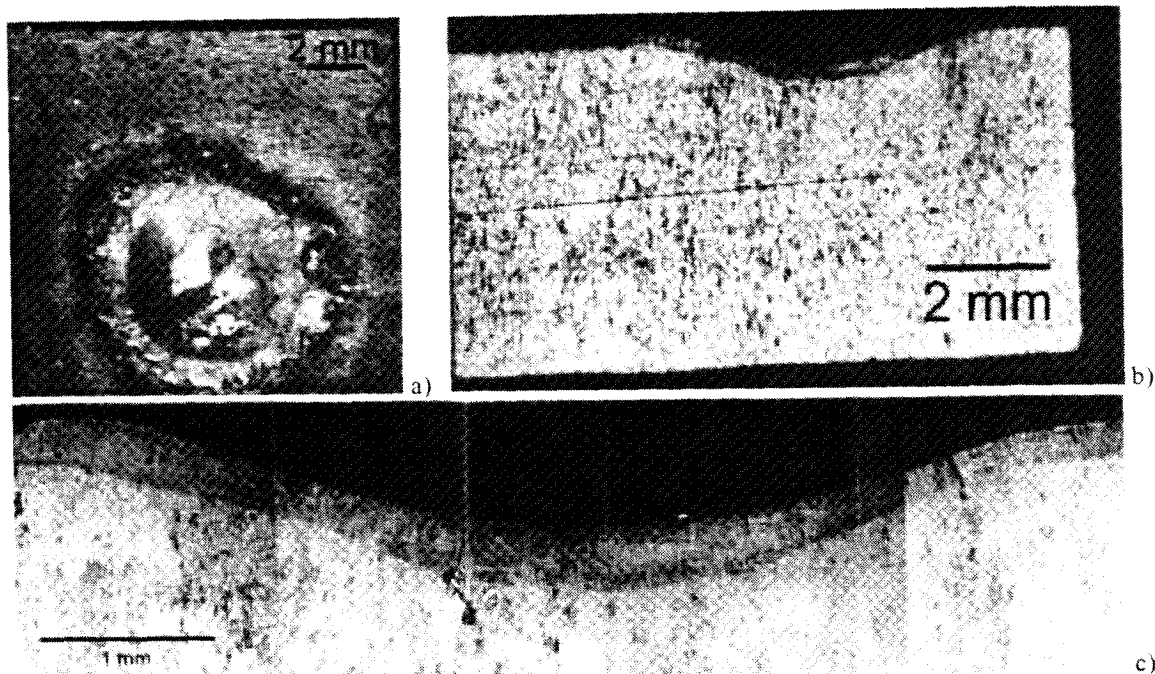


Figure 5.32 - First test campaign. Irradiated (350°C; 0.35 dpa) PS-Be type F (Id. no. M121 K13) after 5 EB shots at 13.5 MJ/m<sup>2</sup>. Microphotograph and corresponding metallographic pictures.

The metallography section of an irradiated PS-Be specimen after test is shown in Figure 5.31-c. Also in this case cracks are generated not only perpendicular to the surface but also in parallel direction. The origin of cracks which extend parallel to the surface of samples is ascribed to the fabrication method. This crack behaviour would suggest that a total detachment of a piece of Be could take place if the tile is subjected to thermal fatigue after a disruption.

However, Figure 5.32-c shows the metallographic section of a second irradiated sample after the electron beam load, and in this case only cracks perpendicular to the surface are found.

Figure 5.33 and Figure 5.34 show microphotographs and corresponding metallographic sections of PS-Be samples type CC, un-irradiated and irradiated, respectively. Deep cracks perpendicular to the specimens surface are observed in both test coupons.

The comparison of the erosion behaviour of the investigated Be grades before and after neutron irradiation is illustrated in Figure 5.35. Figure 5.35 shows the maximum thickness of the melt layer inside the crater obtained for each material grade after 5 electron beam shots at 13.5 MJ/m<sup>2</sup> incident energy density. The values reported are the medium values obtained from the measurements on each test coupons. Unfortunately it was not possible to measure the thickness of the re-crystallized zone of the un-irradiated condensed Be sample and therefore this value is omitted. The value assessed on the irradiated sample is reported for comparison with the other Be grades after neutron irradiation.

The Be grade S65C shows an increased thickness of the melt layer after neutron irradiation. The re-crystallized zone of the un-irradiated sample has been estimate ~370 µm whereas that of the irradiated samples was ~475 µm, i.e. ~28% bigger.

The irradiated PS-Be grade shows a smaller thickness of the melt layer with respect to the un-irradiated material. This result arises despite the fact that the weight loss of the irradiated samples is bigger than that of un-irradiated (Figure 5.20). Since the thermal conductivity of the irradiated Be has been measured without any considerable decreasing having been observed [218, 219], it seems that the more remarkable effect induced by neutron irradiation in Be is embrittlement. In case of PS-Be this effect is more accentuated and a more brittle disruption during the electron beam loading takes place.

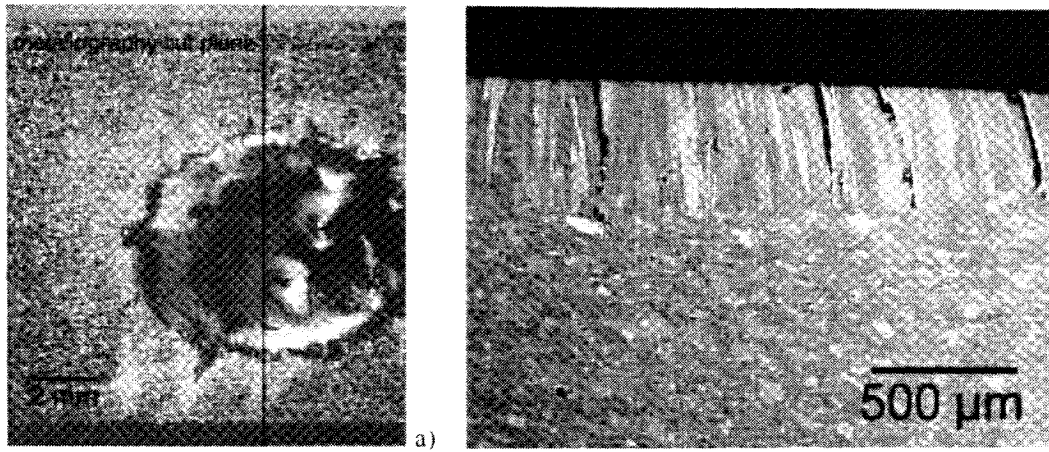


Figure 5.33 - First test campaign. Un-irradiated PS-Be type CC (Id. no. M118 2) after 5 EB shots at  $13.5 \text{ MJ/m}^2$ . Microphotographs and corresponding metallographic picture.

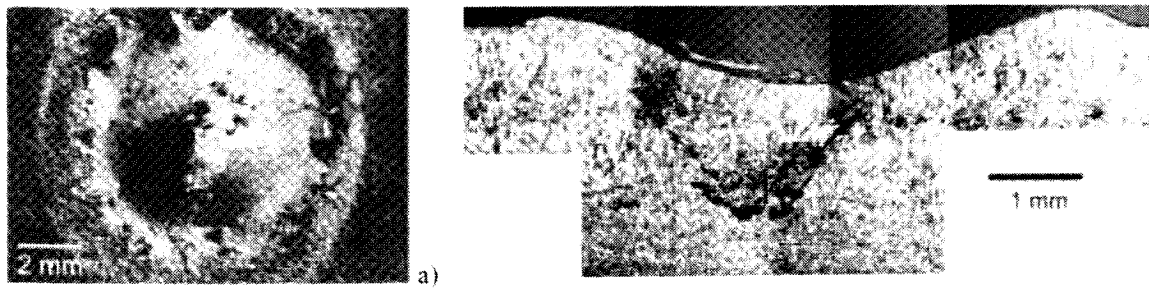


Figure 5.34 - First test campaign. Irradiated ( $350^\circ\text{C}$ ; 0.35 dpa) PS-Be type CC (Id. no. M118 K5) after 5 EB shots at  $13.5 \text{ MJ/m}^2$ . Microphotograph and corresponding metallographic picture.

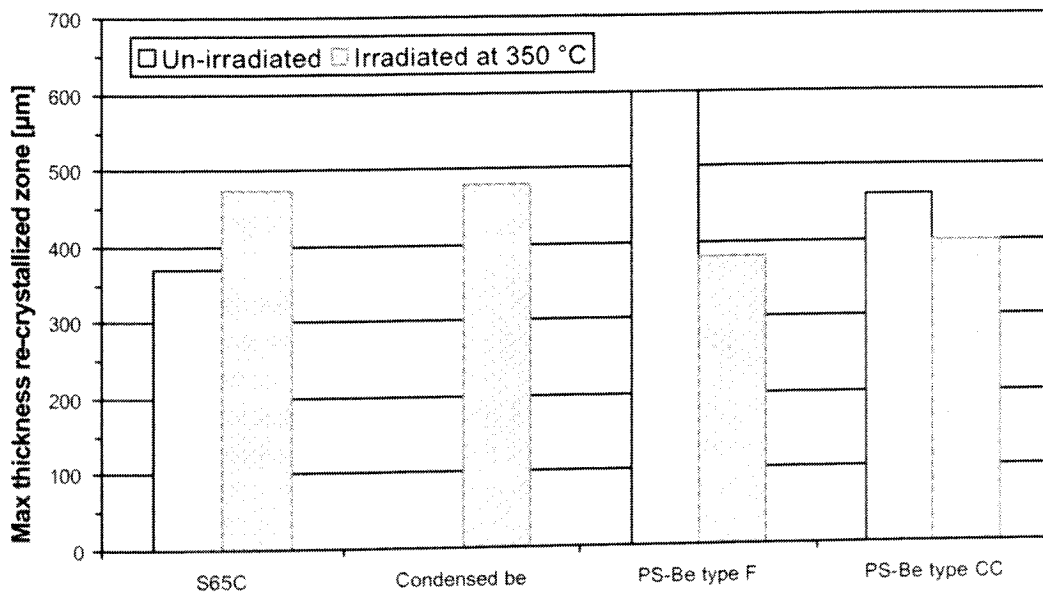


Figure 5.35 - First test campaign. Mean value of maximum thickness of re-crystallized zone after 5 EB shots at  $13.5 \text{ MJ/m}^2$ . Comparison between un-irradiated and irradiated grades

Taking into account all the investigate aspects related to the erosion damage after thermal shock tests, the Be grade S65C confirms its best performance with respect to the other grades also after neutron irradiation.

### 5.3.4 Second test campaign

During this test campaign the material erosion of test coupons un-irradiated and irradiated both at 350°C (0.35 dpa) and 700°C (0.35 dpa) have been compared after thermal shock tests. The investigated materials include the grade S65C by Brush Wellman, three Russian grades (DShG200, DShG56, and TR-30), PS-Be (Los Alamos National Laboratory) and condensed Be (D.V. Efremov Institute, St.Petersburg). All the three Russian grades have been produced by power metallurgical methods (ref. chapter 2). DShG200 is a coarse grain material. TR-30 has a fine grain structure and a relative high oxygen content; this material is expected to show good dimensional stability under neutron irradiation. TShG56 covers an intermediate grain size.

#### 5.3.4.1 Loading conditions

A list of the investigated grades together with the applied loading condition is reported in Table 5.5. Each sample was loaded by 5 EB shots of 13.5 MJ/m<sup>2</sup> incident energy density. The pulse duration of the shots was 5 ms. All tests have been carried out at room temperature.

Table 5.5 - HHF tests during the second test campaign. Investigated grades and applied loading conditions.

Beryllium grades	S65C, DShG200, TShG56, TR30, Condensed Be, PS Be
Beam current [mA]	360
Acceleration voltage [kV]	120
Loaded area [mm <sup>2</sup> ]	4x4
Number of shot	5
Pulse duration [ms]	5
Power density [MW/m <sup>2</sup> ]	~ 2700

#### 5.3.4.2 Experimental features

To achieve the most accurate comparison of the material behaviour before and after neutron irradiation, Be samples un-irradiated, irradiated at 350°C and at 700°C have been tested in sequence without any break of vacuum.

As usual for a given incident power the fraction of that power deposited in the material has been monitored by electrical current measurements. For each test coupon the current absorbed during the first and the fifth e-beam shot has been recorded. Figure 5.6 to 5.9 show the absorbed current behaviour of S65-C un-irradiated and irradiated samples, which was monitored during the electron beam shot. It should be noted that, different from the first test campaign, totally consistency of absorbed current behaviours exists between un-irradiated and irradiated specimens. This has been obtained by the use of a specially designed sample holder, which allowed the remote-controlled mounting of test coupons by mechanical manipulator.

Figure 5.36 shows the copper holder on which un-irradiated and irradiated samples of the same grades have been mounted for testing. As already observed during the first test campaign, due to a possible pollution of the deflection system of the electron gun, the distributions of the electrical current on the samples was not always very accurate.



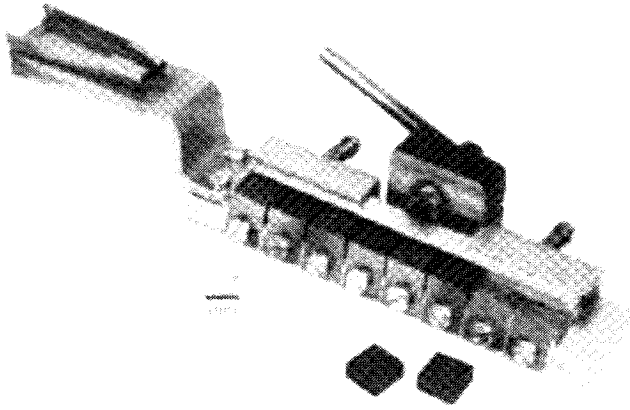


Figure 5.36 – Improved sample holder realized during the second test campaign for thermal shock testing of neutron-irradiated Be specimens.

Sometimes, instead of the planned square shape load area, a more circular crater shape has been observed after testing. This effect should never be minimised in establishing the correlation erosion damage vs. absorbed power density. In fact, if e.g. the energy is deposited on a circular area of 4 mm diameter, the energy density increases by ~27 % compared to a square shaped area of 4x4 mm<sup>2</sup> and the obtained erosion damage has to be ascribed to a higher value of energy absorbed by the sample.

#### 5.3.4.3 Thermal shock damage comparison

After the thermal shock loading the material erosion has been quantified by two independent methods: weight loss measurements and 3D surface profile determined by a laser microprofilometer. A rather large scattering of the results has been found, probably due to the limited number of test coupons available for testing. In general each series of test comprised two un-irradiated samples, three samples irradiated at 350°C and three irradiated at 700°C.

Figure 5.37 shows the weight loss comparison of the investigated Be grades.

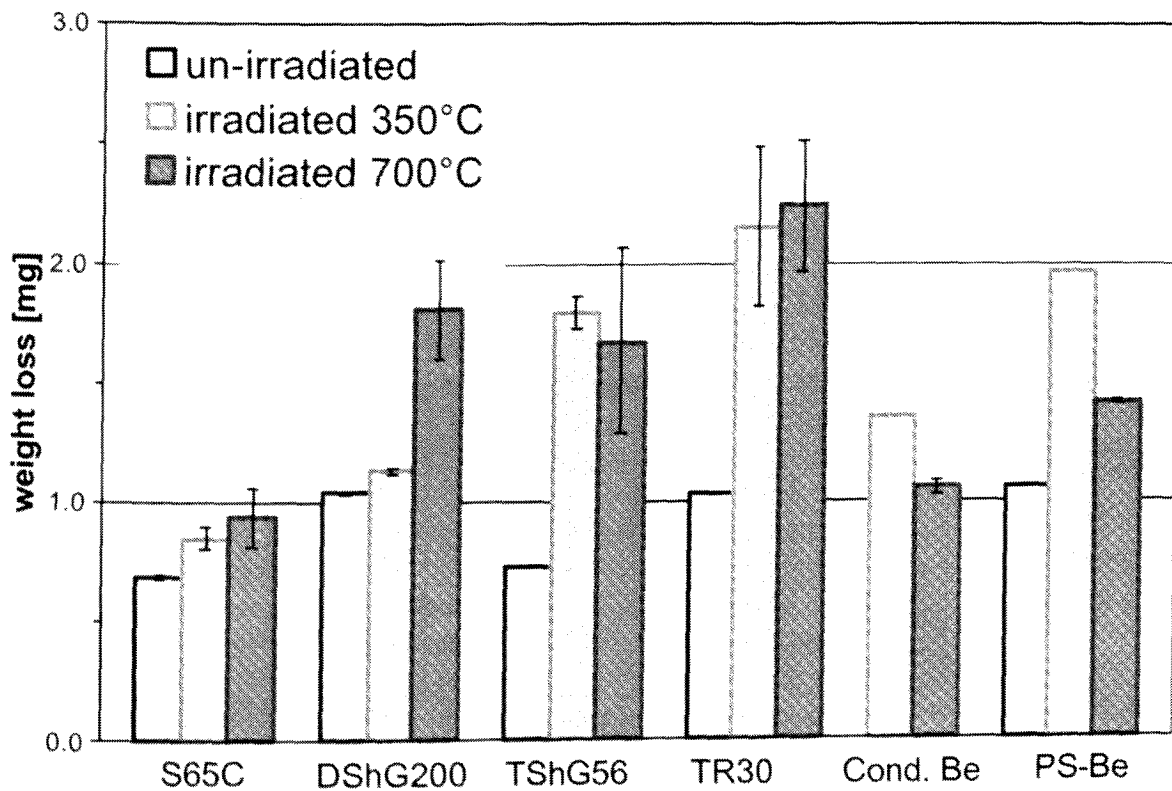


Figure 5.37 - Second test campaign. Mean weight loss after 5 EB shots at 13.5 MJ/m<sup>2</sup>. Comparison between un-irradiated and irradiated Be grades.

As in test campaign 1, all materials shown bigger erosion after neutron irradiation and except for DShG200 and PS-Be little differences are observed for the two irradiation temperatures. The values of the mean weight loss per electron beam pulse and the corresponding standard deviation are reported in Table 5.6. The Be grade S65C presents always the best erosion behaviour compared to the other grades, also after neutron irradiation.

Table 5.6 - Second test campaign. Mean weight loss per pulse after 5 EB shots at 13.5 MJ/m<sup>2</sup>.

	Un-irradiated		Irrad. 350 °C, 0.35 dpa		Irrad. 700 °C, 0.35 dpa	
	weight loss [mg]	standard deviation	weight loss [mg]	standard deviation	weight loss [mg]	standard deviation
S65C	0.137	0.010	0.170	0.009	0.187	0.024
DShG200	0.208	0.001	0.227	0.003	0.361	0.042
TShG56	0.146	0.001	0.359	0.014	0.334	0.078
TR30	0.207	0.002	0.430	0.067	0.448	0.055
Cond. Be	0.163	0.002	0.271	--	0.211	0.005
PS-Be CC	0.212	0.002	0.393	--	0.283	0.008

Results from laser profilometry seem to confirm the trend of weight loss measurements. Figure 5.38 shows the maximum crater depth comparison between un-irradiated and irradiated samples. During some profilometry measurements many errors have been detected, due to anomalous reflection of the laser beam on the loaded surface. As consequence, the evaluation of the maximum crater depth was not possible for these samples, which are therefore not indicated in Figure 5.38.

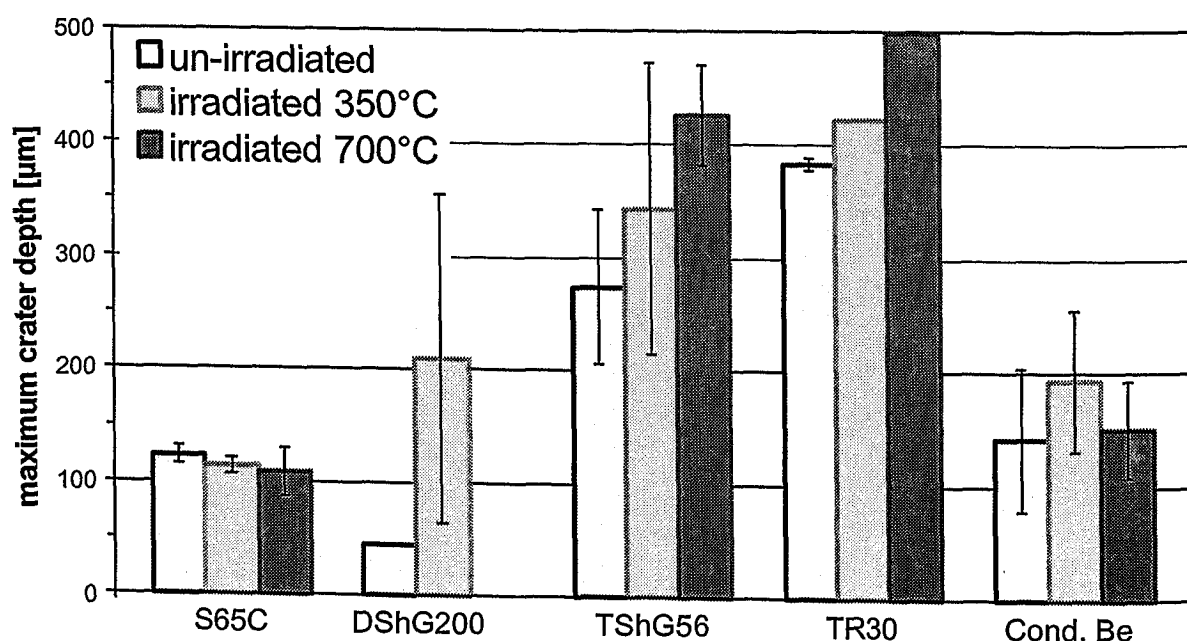


Figure 5.38 - Second test campaign. Mean value of maximum crater depth after 5 EB shots at 13.5 MJ/m<sup>2</sup>. Comparison between un-irradiated and irradiated Be grades.

Deeper craters have been observed after neutron irradiation for all Be grades with exception of S65C which did not show an appreciable increase. Nevertheless, sometimes it has been

noted that these maximum values correspond to deep holes inside the loaded area (see Figure 5.41), the origin of which is probably attributable to the presence of gas bubbles in samples. For the Be grade S65C an evaluation of the medium crater depth by means of the UBM software (cf. paragraph 5.2.3) has been carried out. The estimated values are reported in Figure 5.39.

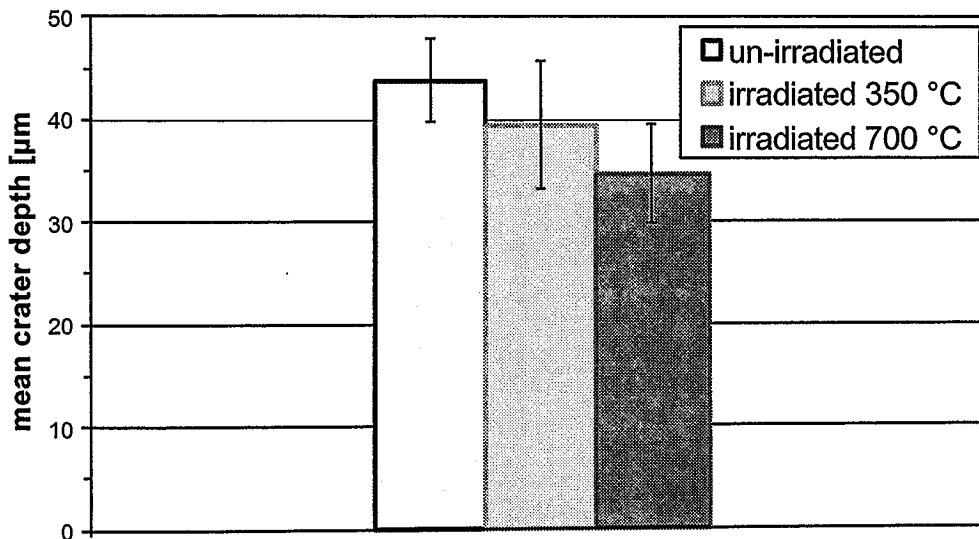


Figure 5.39 - Second test campaign. Be S65C mean value of crater depth after 5 EB shots at 13.5 MJ/m<sup>2</sup>. Comparison between un-irradiated and irradiated samples.

These values have been calculated on the assumption that homogeneous erosion occurred at the loaded area and have been obtained by dividing the “free” volume of the crater by the area of the crater.

#### 5.3.4.4 Post-mortem analysis

Beside material losses, the formation of cracks in the re-crystallised zone and in the base material will have strong impact on the integrity of the Be armour of PFCs. The surface status of all samples after thermal shock tests has been investigated by optical microphotography. Microphotographs of the craters have been taken through an image scanner. Metallographical examination and comparison of the erosion damage before and after neutron irradiation has been carried out. The preparation of samples for metallography has been done in a remote-controlled way inside the hot cell. This complicated way of operating is the cause of a not optimal quality of some pictures.

Figure 5.40 to 5.49 show surface area scans and corresponding pictures of metallographic sections of all investigated Be grades respectively un-irradiated, irradiated at 350°C and 700°C. All test coupons have been sectioned at the centre of the spot and metallographic pictures have been taken in a plane perpendicular to the loaded surface.

The surface's morphology of all test coupons after testing show severe melting and a dense crack pattern throughout the loaded area. The zone inside the crater appears both rough and polished and bright. An increased number of cracks in case of irradiated material is recognizable for all Be grade. Dynamical overflowing of the melt before re-solidification is observed on all samples. Sometimes the surface of the test coupons is covered with globular objects of resolidified Be, clear indication that during the EB shots melt splashing due to the formation, growth and bursting of bubbles inside the liquid layer took place [220, 221]. In this

connection, it should be noted that under realistic tokamak conditions, splashing of liquid Be-droplets and loss of the developed melt layer due to electromagnetic forces during the plasma disruption may result in an enhanced erosion, which can critically shorten the lifetime of PFCs and easily contaminate the plasma boundary layer [222 - 225].

Diverse crater shapes after the EB shots can be occasionally observed on Be specimens. A quite good uniformity of the loaded area has been achieved on samples of the same grades, which have been tested in sequence without any break of vacuum.

### **Be S65C**

In Figure 5.40 surface area scans and corresponding pictures of metallographic sections of Be S65C grade before and after neutron irradiation are shown.

The fine grain, homogenous zone of the base material is easily recognisable from the heat affected zone in all samples (Figure 5.40 d to f).

The re-crystallized material shows a columnar grain structure with grains orientation perpendicular to the loaded surface according to the direction of the thermal gradient. The maximum thickness of the melt zone does not increase after neutron irradiation and it has been estimated approximately 260  $\mu\text{m}$ .

Numerous thermally induced cracks perpendicular to the surface are present both in un-irradiated and irradiated samples (Figure 5.40 g to i). No enhanced cracking is observed after neutron irradiation and in all specimens intergranular cracks only extend to the bottom of the melt layer and not into the base material. This pattern of cracks contributes to the release of thermally induced stresses during the cold down phase of the PFCs.

More porosity is present in the neutron irradiated samples, which also present cavities in the melt layer after electron beam loading. The formation of pores in the melt layer arises from coalescence of gases present in the material during the liquid phase. The tritium and helium production due to neutron irradiation in the HFR reactor at 700°C has been calculated to be  $3.6 \cdot 10^{18}$  atoms/g Be, which corresponds to a concentration of 55 ppm. During disruption simulation experiments, these gases will form bubbles in the melt layer [218] but the contribution of other gaseous impurities (BeO) which may remain trapped between the grains of Be powder during the manufacturing process cannot be excluded. As already mentioned in the previous paragraph, due to the location of samples inside the hot cell, it was not possible to carry on the scanning electron microscopy for investigating the origin of this porosity.

### **Be DShG200**

In Figure 5.41 surface area scans and corresponding pictures of metallographic sections of the DShG200 Be grade before and after neutron irradiation are shown.

Severe melting is observed on the surface of all samples after thermal shock test but no cracks patten through the loaded area has been detected both on the un-irradiated and irradiated at 700°C sample. A crack inside the melting rim is recognizable on the test coupon irradiated at 350°C. This sample presents also a deep hole inside the loaded area. Theis hole was already detected by the laser profilometry measurement.

Figure 5.42 shows the 3D area scan of the sample irradiated at 350°C and 0.35 dpa shown in Figure 5.41-b. The bright spot visible in Figure 5.41-b correspond to a hole approximately 400  $\mu\text{m}$  deep.

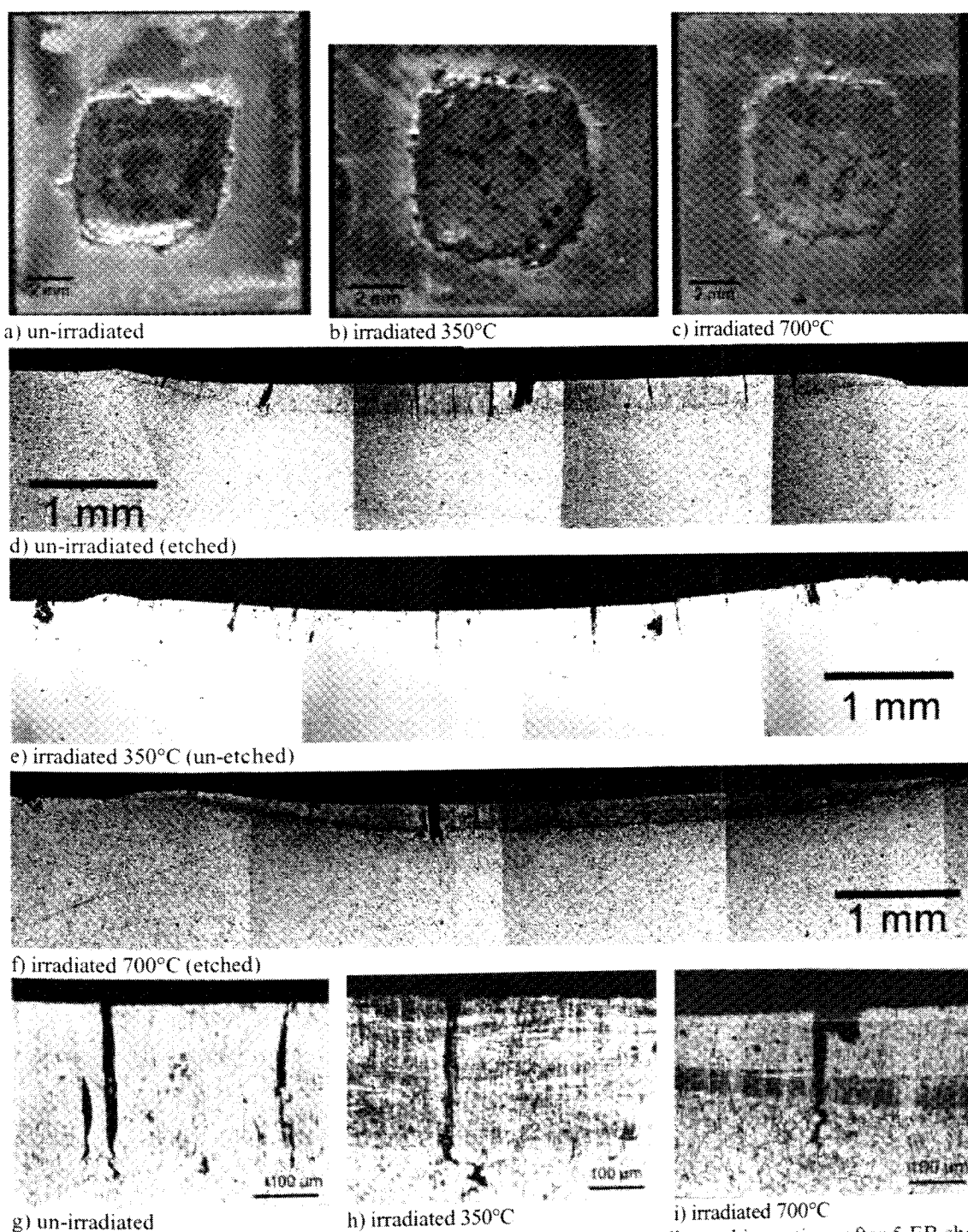


Figure 5.40 – Second test campaign. Be S65C surface area scans and metallographic sections after 5 EB shots at 13.5 MJ/m<sup>2</sup> incident energy density. Comparison between samples un-irradiated (Id. no. M82 S28), irradiated at 350°C and 0.35 dpa (Id. no. S14) and irradiated at 700°C and 0.35 dpa (Id. no. S32).

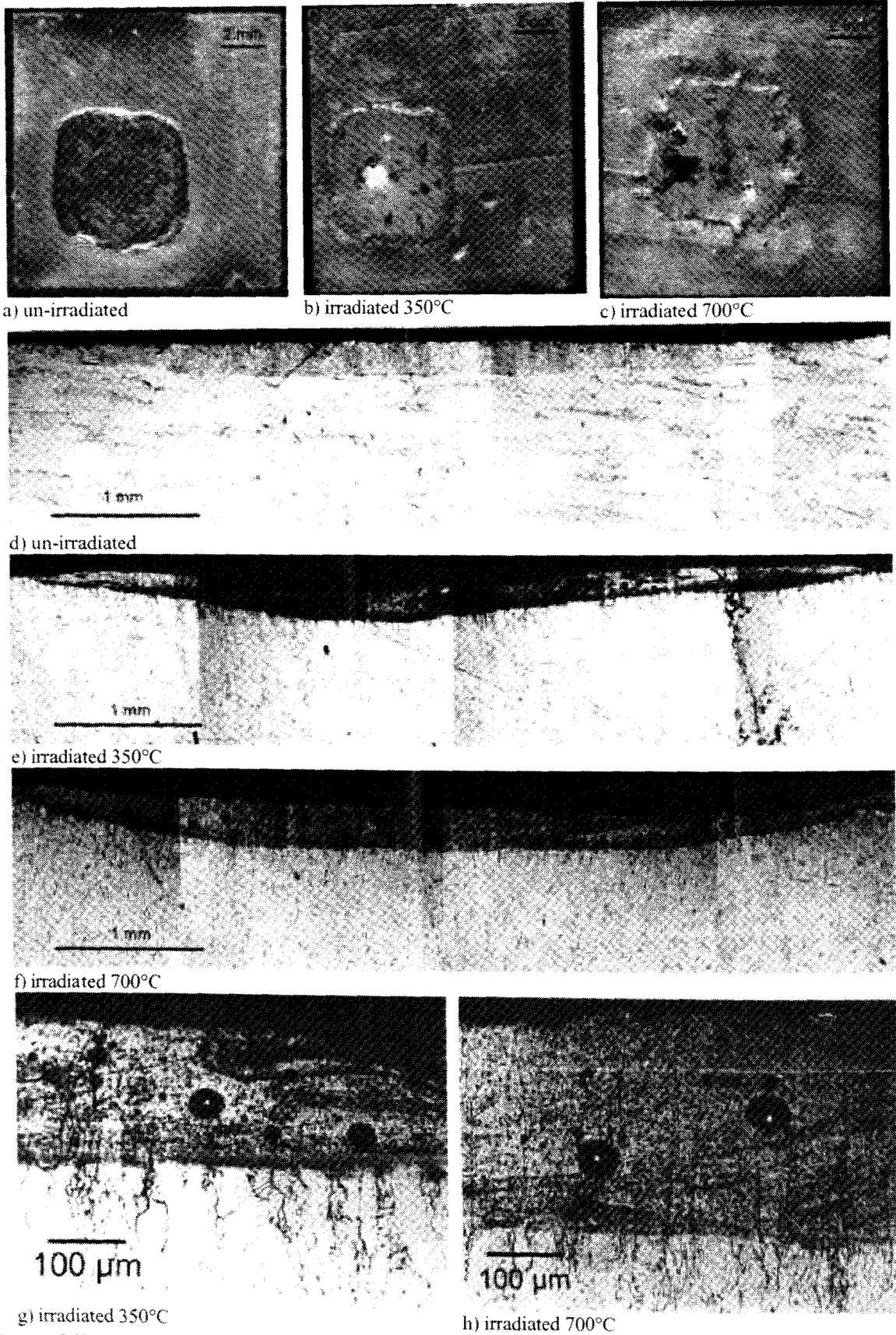


Figure 5.41 – Be DShG200 surface area scans and metallographic sections after 5 EB shots at  $13.5 \text{ MJ/m}^2$  incident energy density. Comparison between samples un-irradiated (Id. no. M90 1), irradiated at  $350^\circ\text{C}$  and  $0.35 \text{ dpa}$  (Id. no. 1.1) and irradiated at  $700^\circ\text{C}$  and  $0.35 \text{ dpa}$  (Id. no. 1.5).

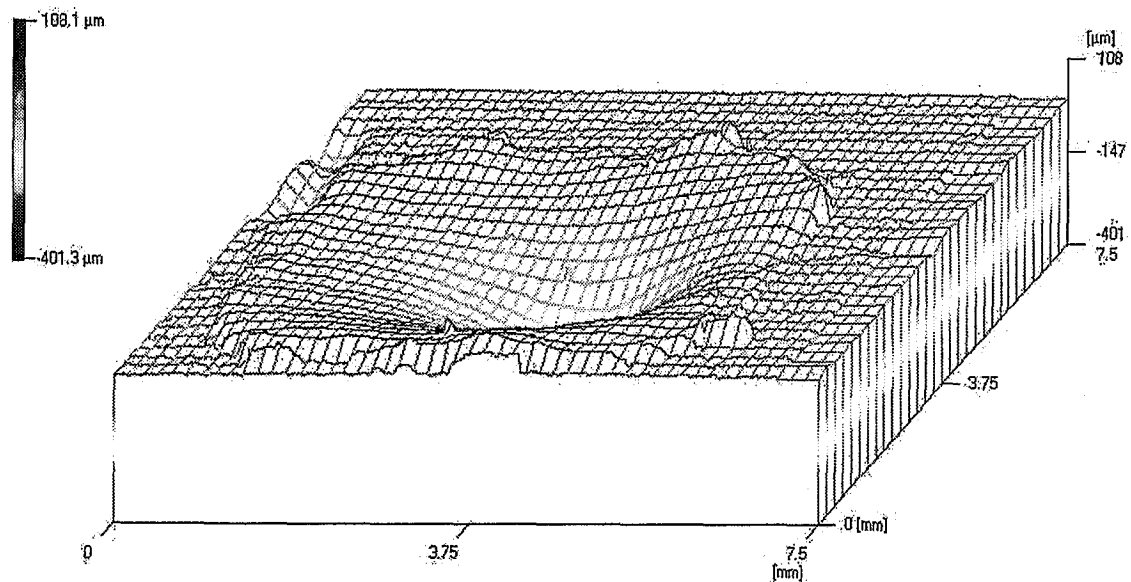


Figure 5.42 - 3D laser profilometry of DShG200 sample irradiated at 350°C and 0.35 dpa (Id. no. 1.1) after 5 EB shots at 13.5 MJ/m<sup>2</sup> incident energy density.

Also for these samples the re-crystallized zone characterized by the columnar grain structure is easily recognizable from the homogenous unaffected base material. The thickness of the melt layer has been measured ~220 μm on the un-irradiated sample, ~240 μm on the sample irradiated at 350°C and ~300 μm on the sample irradiated at 700°C.

Also the examination of the metallographic section does not show cracks both in the un-irradiated sample and in the sample irradiated at 700°C. The sample irradiated at 350 °C shows a crack perpendicular to the loaded surface, which extends in the base material below the melt layer (Figure 5.41-e).

Both irradiated samples show enhanced porosity with respect to the un-irradiated material and numerous pores/bubbles in the re-crystallized zone.

### Be TShG56

Figure 5.43 shows surface area scans and pictures of the metallographic sections of the TShG56 beryllium grade.

Thermally induced cracks are present both in the un-irradiated and irradiated samples. The re-crystallized zone is characterized by the columnar structure of the grain and is optically distinguishable from the homogeneous region with very fine grain structure of the base material. The thickness of the melt layer has been measured approximately 240 μm on the un-irradiated sample and ~360 μm on both irradiated samples.

Cracks move perpendicular to the sample's surface and go slightly beyond the molten zone.

Enhanced porosity in the irradiated samples, with formation of cavities inside the melt layer is observed.



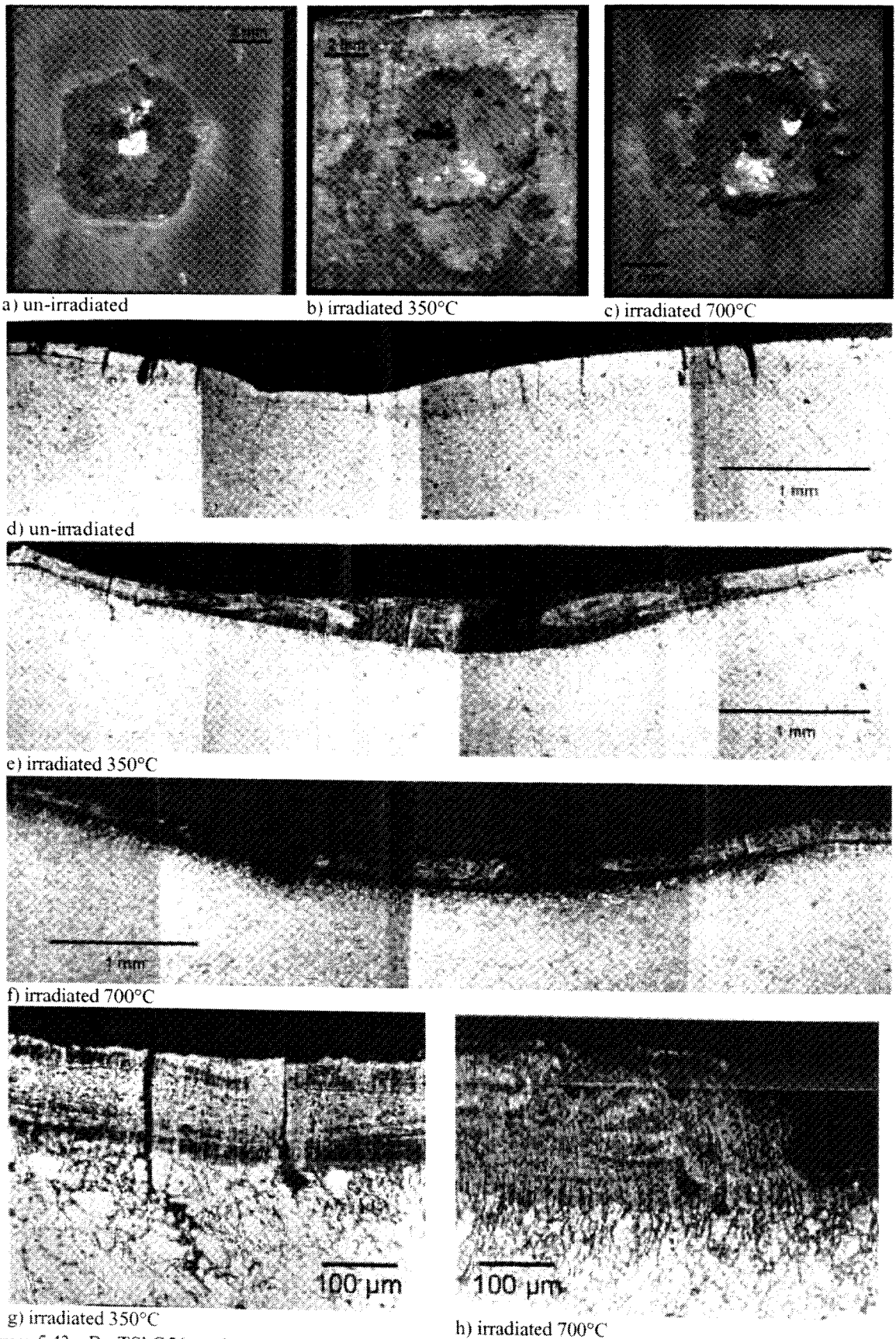


Figure 5.43 - Be TShG56 surface area scans and metallographic sections after 5 EB shots at  $13.5 \text{ MJ/m}^2$  incident energy density. Comparison between samples un-irradiated (Id. no. M91 2.8), irradiated at 350 °C and 0.35 dpa (Id. no. 2.1) and irradiated at 700 °C and 0.35 dpa (Id. no. 2.11).



Figure 5.44 and Figure 5.45 show surface area scans and pictures of the metallographic sections of the TR30 beryllium grade un-irradiated and irradiated, respectively.

Both un-irradiated and irradiated samples show severe damage after thermal shock test. The surface of the un-irradiated sample (Figure 5.44-a) is characterized by a very regular crater shape with respect to the irradiated samples. The square shape loaded area surrounded by the melting rim was also accurately reproduced by the 3-D area scan by laser profilometry (Figure 5.44-b). An enhanced splashing of liquid Be-droplets seems to be occurred on the irradiated test coupons, especially for that one irradiated at 700 °C (Figure 5.44-c).

The thickness of the re-crystallized zone, characterized by the columnar structure of grains, has been measured approximately 200  $\mu\text{m}$  on the un-irradiated specimen and 300  $\mu\text{m}$  on the irradiated samples. The un-irradiated sample shows cracks, which go beyond the melt layer and penetrate deep (up to 1.5 mm) into the base material (Figure 5.44-d). One crack extends to the sample's base (Figure 5.44-c). Cracks move both perpendicular and parallel to the surface. Both irradiated samples show deep cracks which extend beyond the melted layer and extend parallel to the loaded surface resulting in detachment of material (Figure 5.45-c and Figure 5.45-d).

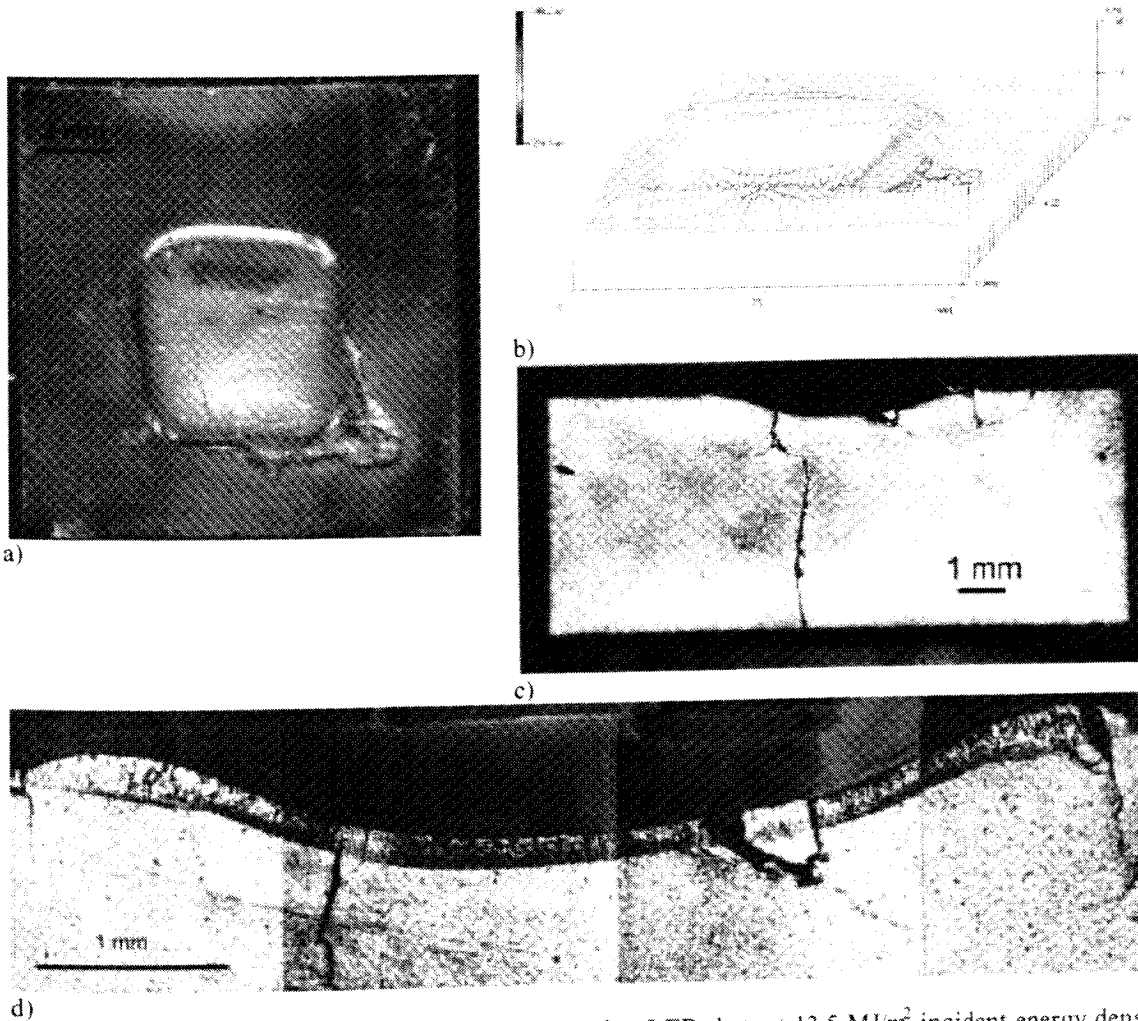


Figure 5.44 - Be TR30 un-irradiated (Id. no. M92 3.19) after 5 EB shots at 13.5 MJ/m<sup>2</sup> incident energy density: a) surface area scans; b) 3D area scan by laser profilometry; c) – d) pictures of metallographic section perpendicular to the surface.

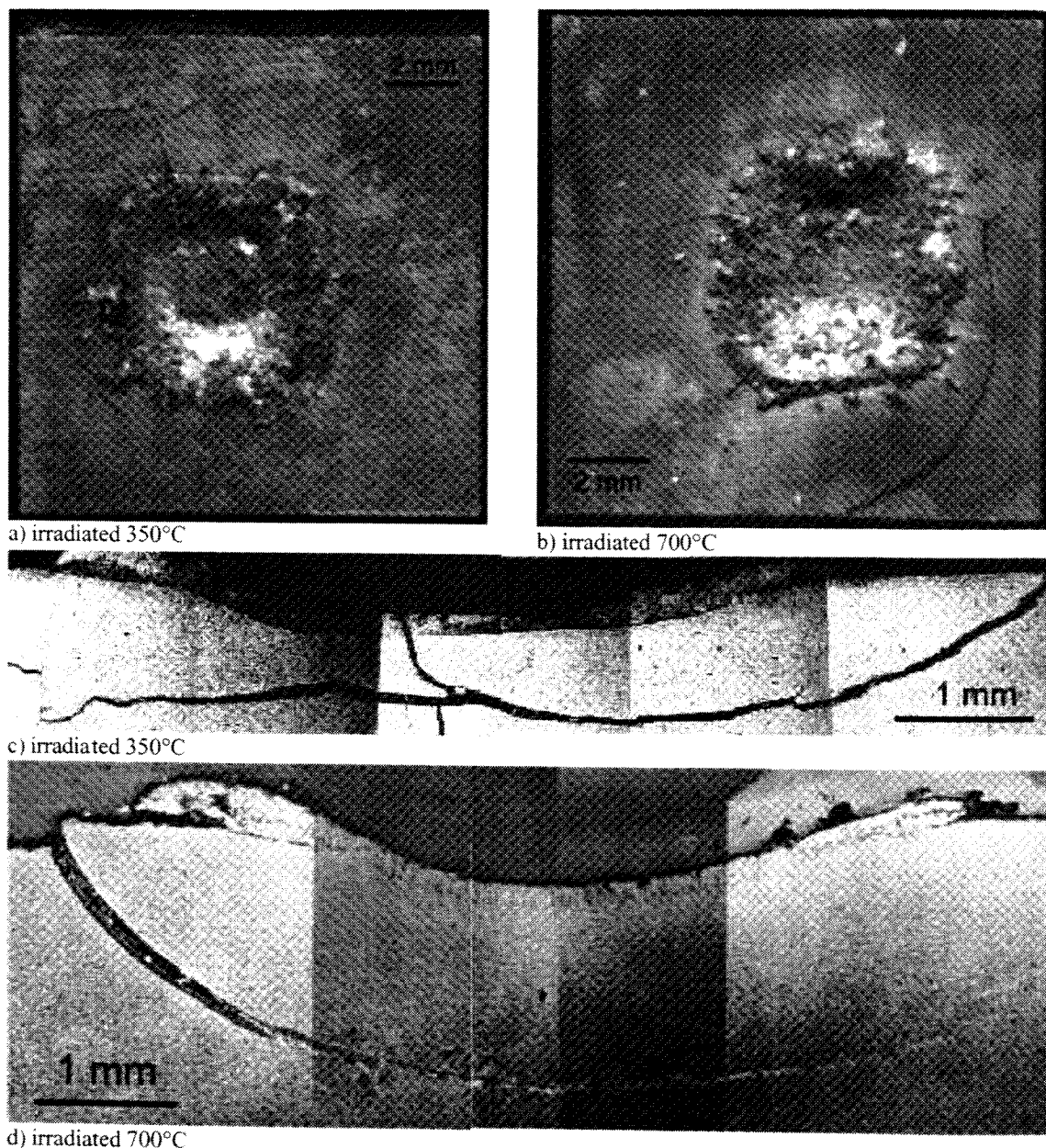


Figure 5.45 - Be TR30 surface area scans and metallographic sections after 5 EB shots at  $13.5 \text{ MJ/m}^2$  incident energy density. Comparison between irradiated samples at 350 °C and 0.35 dpa (Id. no. 3.2) and 700 °C and 0.35 dpa (Id. no. 3.6).

### Condensed Be

Figure 5.46 shows surface area scans, 3-D area scan by laser profilometry and pictures of the metallographic sections of condensed Be un-irradiated and irradiated, after thermal shock test. Condensed Be specimens present the peculiarity of elongated grain's shape also in the base material due to their fabrication method (cf. chapter 2). All test coupons consist of a layer of beryllium condensed onto a pre-existent layer of the same material resulting in a non homogenous junction (see line in Figure 5.46-g to Figure 5.46-i).

A very regular square shape of the loaded area is observed on all sample. Swelling of the central area inside the melt rim is observed on all samples and has been detected also by laser profilometry measurements (Figure 5.46-d to Figure 5.46-f). No enhanced cracking is observed after neutron irradiation. In all samples cracks are perpendicular to the surface and extend to the base material (Figure 5.46-l to Figure 5.46-m).

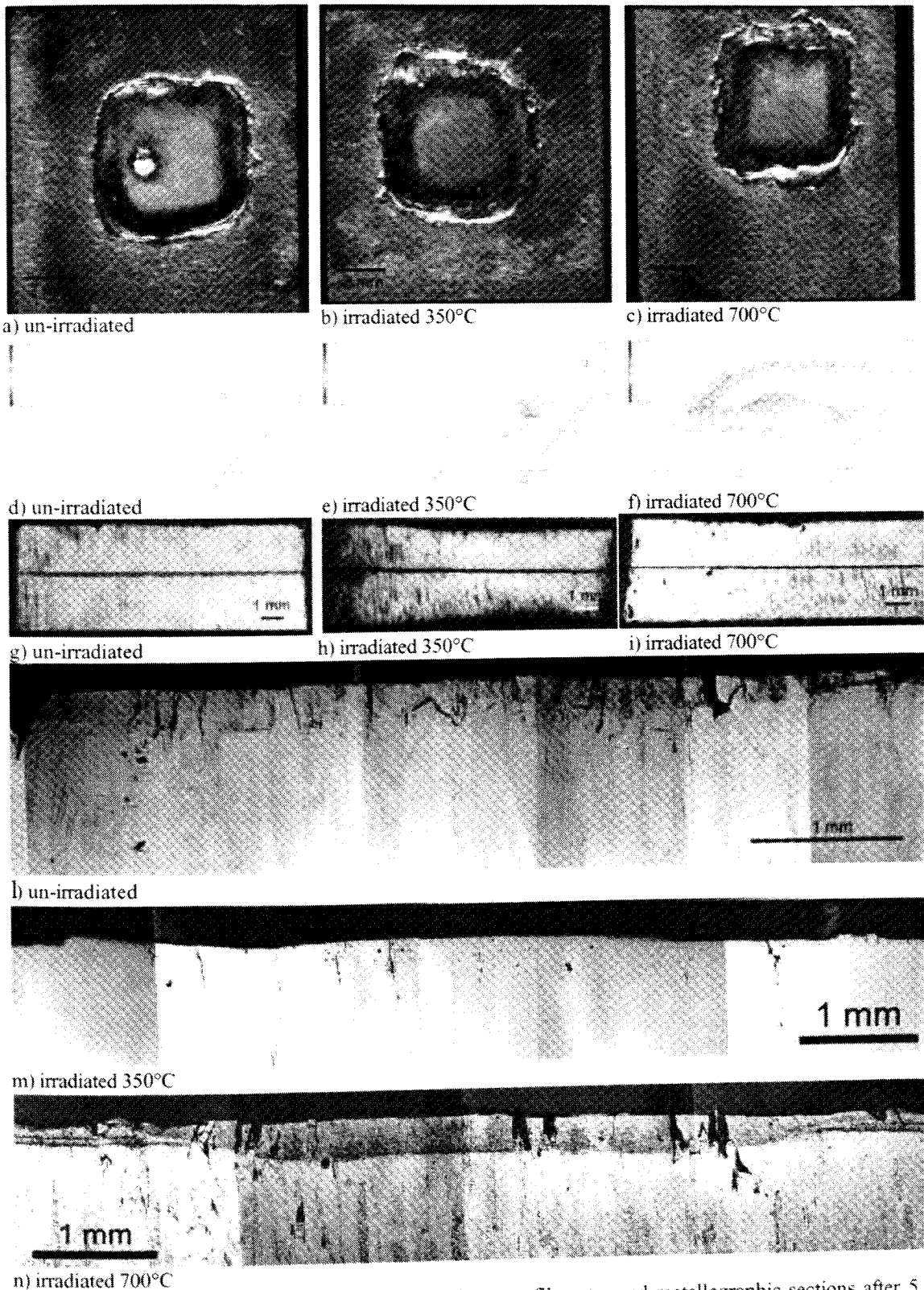


Figure 5.46 - Condensed Be surface area scans, 3-D laser profilometry and metallographic sections after 5 EB shots at  $13.5 \text{ MJ/m}^2$  incident energy density. Comparison between samples un-irradiated (Id. no. M93 4.12), irradiated at  $350^\circ\text{C}$  and  $0.35 \text{ dpa}$  (Id. no. 4.3) and irradiated at  $700^\circ\text{C}$  and  $0.35 \text{ dpa}$  (Id. no. 4.8).

The thickness of the melted layer has been measured  $\sim 300 \mu\text{m}$  both for un-irradiated and irradiated test coupons. Also for this material, more porosity, especially in the melted area, characterizes the irradiated samples after the e-beam load.

### PS-Be

Figure 5.47 to 5.49 show surface area scans and pictures of the metallographic sections of PS-Be samples (type F) un-irradiated, irradiated at 350°C and 700°C respectively.

Severe damage after 5 electron beam shots at 13.5 MJ/m<sup>2</sup> has been detected both in case of un-irradiated and irradiated samples.

The typical stratified structure due to their fabrication process (cf. Chapter 2) characterizes these samples (Figure 5.47-d, Figure 5.48-b and Figure 5.49-b). Un-melted particles between the layers are recognisable in all specimens.

Only a slightly increase of porosity is observed in the material after neutron irradiation due to the fact that cavities originate mostly from coalescence of gas particles (argon) entrapped during the production of the test coupons. Therefore the contribution of helium or tritium produced during neutron irradiation is not considered to be relevant.

Deep cracks perpendicular to the surface are observed within the resolidified zone and in the base material on un-irradiated and irradiated samples. Cracks go not only perpendicular to the surface but also in parallel direction, along the different layers of material. These particular pattern is ascribed to the fabrication method. The un-melted particles cause a non homogenous junction between the layers which provokes delamination of the material. This crack behaviour would suggest that large part of the Be surface could detach if the tile is subjected to thermal fatigue after a disruption.

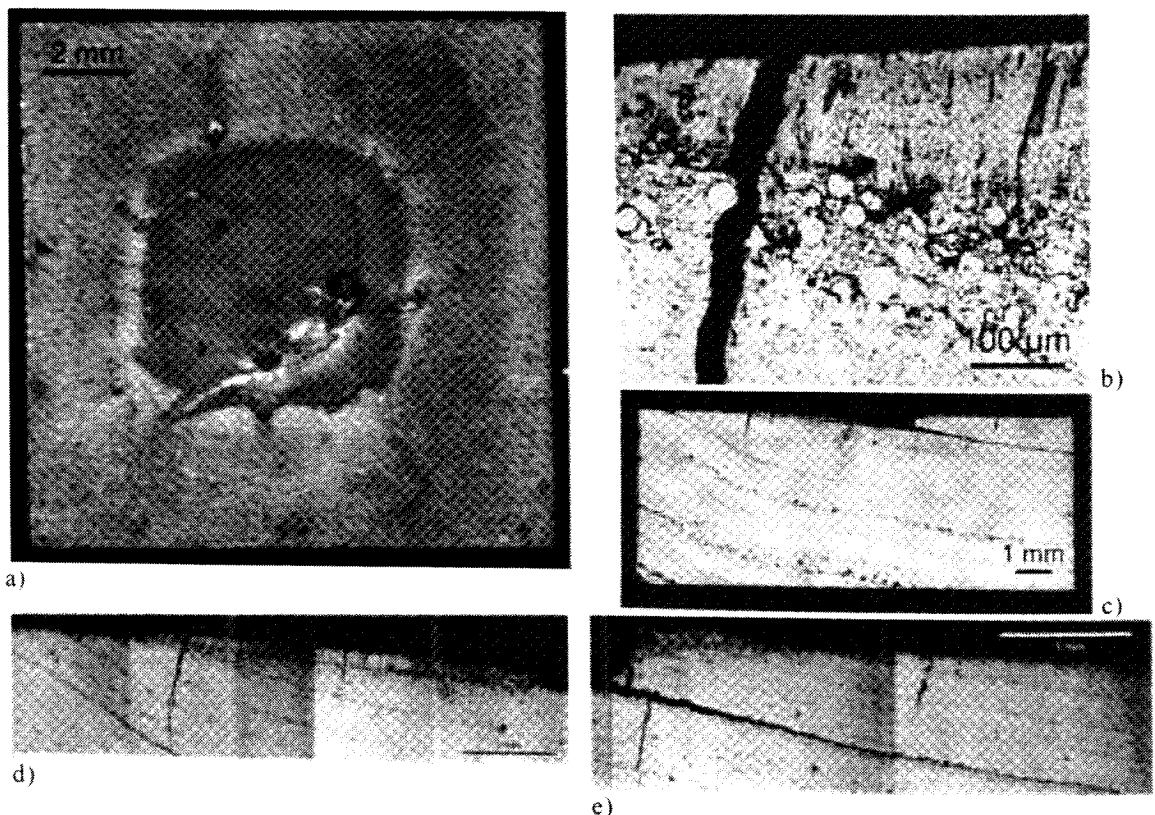


Figure 5.47 - Un-irradiated PS-Be sample (Id. no. M119 8) after 5 EB shots at 13.5 MJ/m<sup>2</sup> incident energy density; a) surface area scans; b) – e) metallographic sections.



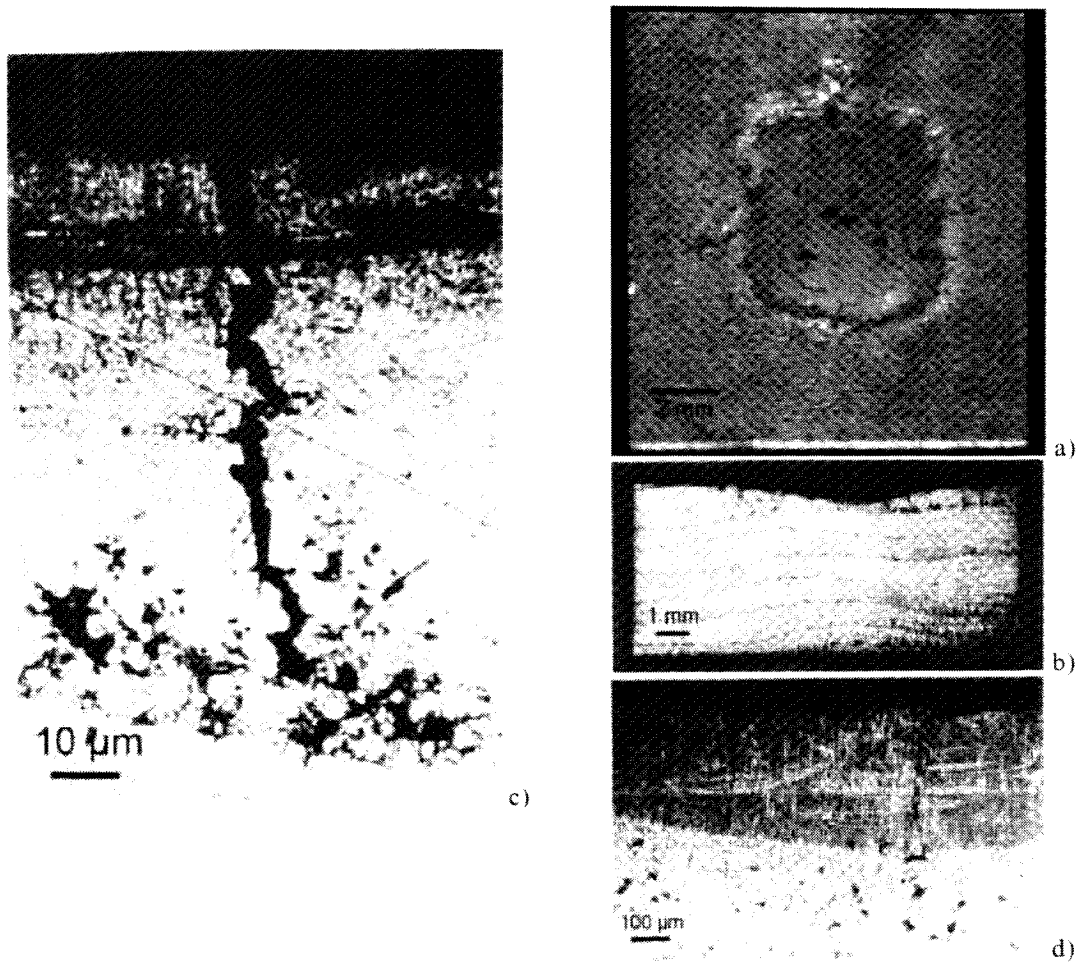


Figure 5.48 - PS-Be sample (Id. no. K1) irradiated at 350 °C and 0.35 dpa after 5 EB shots at 13.5 MJ/m<sup>2</sup> incident energy density; a) surface area scans; b) – d) metallographic sections.

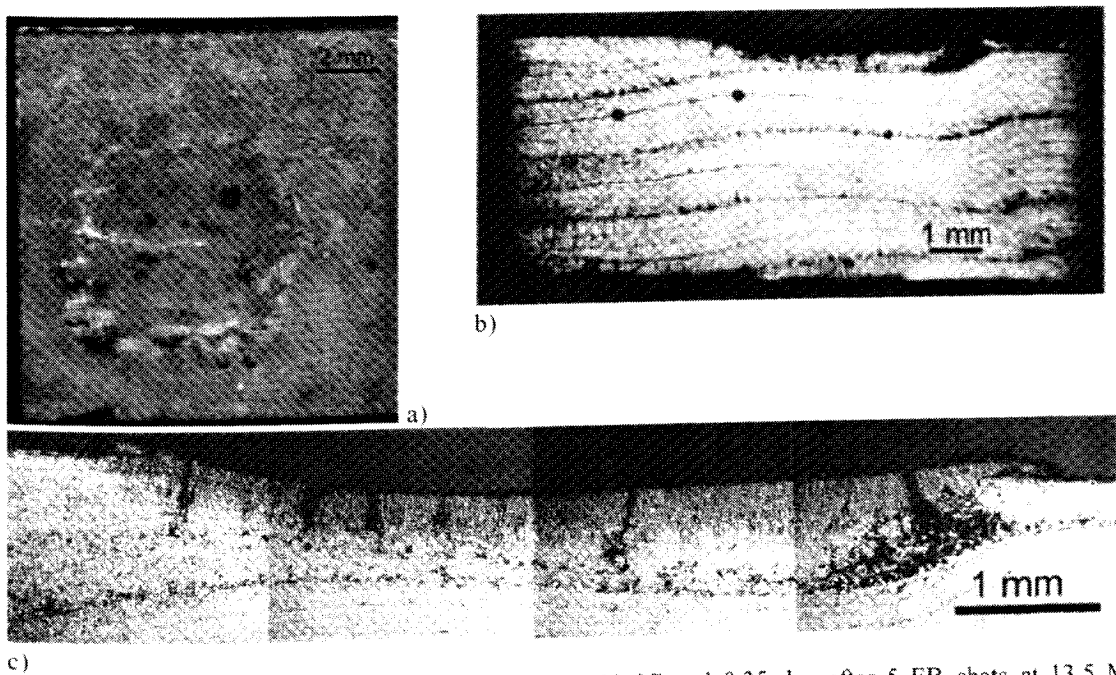


Figure 5.49 - PS-Be sample (Id. no. K2) irradiated at 700 °C and 0.35 dpa after 5 EB shots at 13.5 MJ/m<sup>2</sup> incident energy density. a) surface area scans. b) – c) metallographic sections.

## 5.4 Numerical simulation of the experiments

A computational simulation of the thermal shock test on a Be S65C sample with 5 electron beam shots at  $13.5 \text{ MJ/m}^2$  incident energy density has been carried out. The simulation consists in a 2D finite element (FE) transient thermal analysis based on a sophisticated methodology which takes into account the moving boundary when material vaporization occurs [226].

### 5.4.1 Analysis model

The FE model was generated using very fine meshes in the heating zone and adopting small time steps where change of phase was expected to assure convergence and acceptable accuracy in the results. Taking advantage of the symmetry, only a quarter of the sample has been modelled. In Figure 5.50 the adopted FE model is shown.

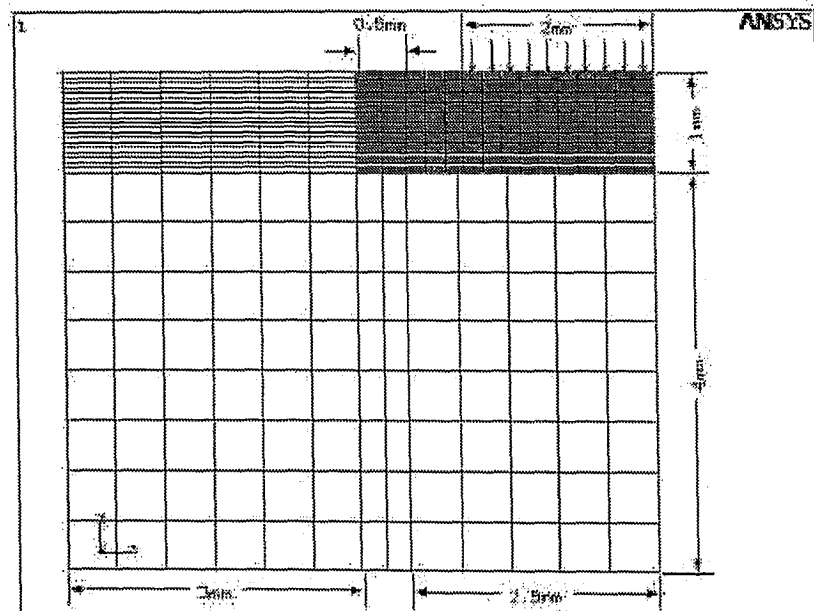


Figure 5.50 - Be sample for thermal shock tests FE analysis model.

A computer routine calculates the quantity of evaporated and melted material making use of the FE code ANSYS [227] to accurately compute the time and space evolution of the temperature, taking into account the moving evaporated and melted layer boundaries. The incoming heat flux, the re-irradiation to an external environment, and the heat transfer to the copper holder are directly applied to the FEM model. For each time-step the temperature distribution is obtained by the FE code. For each finite element of the exposed surface, the erosion rate [194, 195, 228] is calculated from a gas kinetic relation in function of the actual surface temperature, and the outgoing heat flux due to the evaporation is calculated multiplying the erosion rate by the latent heat of vaporization and the material density. The erosion rate for each element is integrated in time to obtain the total evaporated thickness and its effect on the energy balance in each time step. When an entire element is vaporized, it is eliminated from the model and the boundaries at the applied loading conditions are moved to the element below.

The method is then able to evaluate the predicted shape of the eroded surface. The melting layer is directly computed by the ANSYS code on the base of the material enthalpy.

The material properties have been taken from the ITER Material Properties Handbook [229]. Temperature dependent material properties have been used. Irradiation effects on the material properties have not been considered.

## 5.4.2 Thermal loads and input data

The incoming heat flux and the re-irradiation to an external environment were directly applied to the FE model. As input data the result of the test performed on the Be sample irradiated at 350°C during the first test campaign (Id. no. M77 S12; Figure 5.25) has been used. A heat convection ( $h = 500 \text{ W}\cdot\text{m}^{-2}\cdot\text{K}^{-1}$ ,  $T_{\text{bulk}} = 20^\circ\text{C}$ ) has been applied at the bottom of the sample to simulate the heat transfer to the sample copper holder.

Three analyses have been performed, in order to take into account experiment uncertainties in the heat flux distribution (i.e. shape of the loaded area) and in the incoming heat flux (cf. paragraph 5.3).

The heat load histograms during each e-beam shot for the three load cases are shown in Figure 5.51 and in Table 5.7. In load case 1 the assumption that electron thermal emission takes place during the test has been considered. Therefore a uniform spatial heat flux distribution over a  $4\times 4 \text{ mm}^2$  load area, constant for 5 ms has been adopted. In load case 2 the beneficial effect of the vapour shielding has been taken into account. Accordingly a uniform spatial heat flux distribution over a  $4\times 4 \text{ mm}^2$  load area, having the load histogram as the behaviour of the absorbed current has been assumed. Finally, in load case 3, a uniform spatial heat flux distribution over a circle of 4 mm diameter according to a circular crater shape, assuming that vapour shielding takes place, has been considered. To simulate the circular crater shape an axi-symmetric model was used.

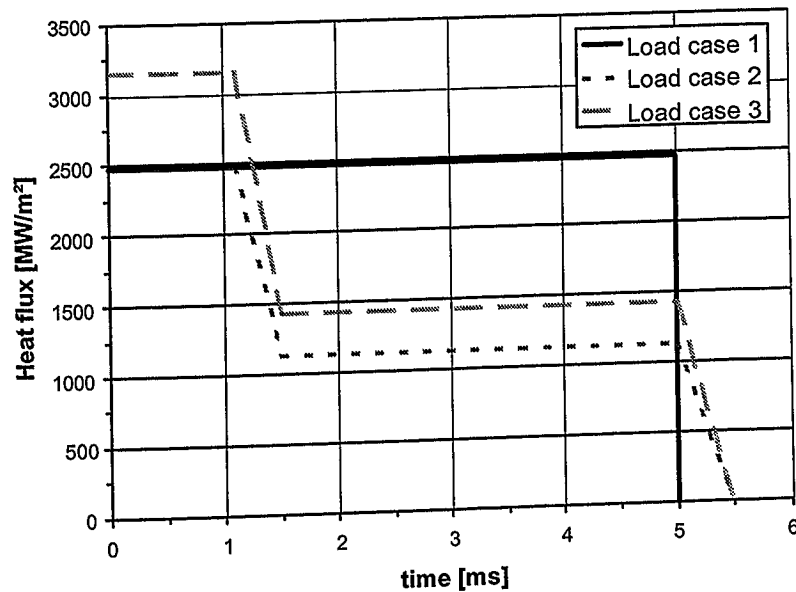


Figure 5.51 - HHF test engineering load histograms during one EB shots.

Table 5.7 - HHF test engineering load histograms.

Time [ms]	Heat flux [MW/m <sup>2</sup> ]		
	Load case 1	Load case 2	Load case 3
0	2457	2475	3151
1.1	2457	2475	3151
1.5	2457	1125	1432
5	2457	1125	1432
5.5	0	0	0

### 5.4.3 Results

The results obtained for load case 1, i.e. simulating electron thermal emission during the tests, showed a maximum crater depth value which was much higher than the experimental value. However, this discrepancy between analytical and experimental results has been already observed in previous disruption simulation experiments with electron beams [230]. The disagreement between calculations and experiments for melt layer depth and evaporation rate can be ascribed to the substantial convection which takes place in the melt layer formed during the electron beam shot. This convection is due to the momentum transferred from the electron beam to the melt and this mechanism can explain the observed discrepancies between experimental results and calculations as far as melt depth and evaporation is concerned. In fact, in the calculation the heat is assumed to be transported from the surface to the bottom by conduction exclusively but, if convection takes place during the EB shot, the transport of heat is increased. More heat at the bottom of the melt layer means an increase in melt depth, as observed during the test. Similar considerations as for the melt depth hold for the evaporation. The evaporation at the surface is strongly dependent on the surface temperature. A high heat transfer to the bottom of the melt decreases the surface temperature and reduces the evaporation, as it has been observed during the experiments. In addition it should be noted that, the thermal shock simulation has been carried out performing 5 EB shots at high power densities which caused multiple melting and re-solidifications. The re-solidified material may have somewhat different properties (e.g. due to higher porosity), which influence the calculation results [226].

Figure 5.52 resumes the results obtained for the load case 2. Figure 5.52-a to 5.52-e present the evolution of the sample crater during the EB shots obtained by the analytical simulation. In Table 5.8 the values of maximum crater depth and thickness of the melt layer obtained at the end of each load cycle are reported.

The results of load case 2, i.e. taking into account the beneficial effect of vapour shielding, underestimate the experimental results. In fact, the maximum crater depth and the maximum thickness of the melt layer after 5 thermal load cycles have been estimated  $\sim 280 \mu\text{m}$  and  $\sim 120 \mu\text{m}$ , respectively; whereas the maximum crater depth and the maximum thickness of the melt layer which have been measured on the Be samples after the thermal shock tests were  $500 \mu\text{m}$  and  $475 \mu\text{m}$ , respectively.

The analysis results which match the experimental values best in terms of total material loss are those obtained for load case 3.

The maximum crater depth and the maximum thickness of the melt layer which have been computed were  $550 \mu\text{m}$  and  $155 \mu\text{m}$  respectively. Therefore a good agreement is found in the evaporated layer thickness but still a significant difference is found in the melt layer thickness.

Therefore the results of the analyses suggest that a more complex simulation should be performed for modelling the thermal shock experiments. For example the heat deposition due to the electrons slow down in the material should be taken into account as space dependent volumetric heating.

The observed drop of the current absorbed by the test coupon may originate both by vapour shielding and electron thermal emission.





## 5.5 Thermal shock tests on pre-heated Be samples

### 5.5.1 Objectives

All thermal shock tests described so far have been performed on cold (i.e. not preheated) test specimens. PFCs in future thermonuclear fusion reactors will experience severe thermal shocks primarily during plasma operation, i.e. at elevated temperatures. Plasma disruptions on the first wall are expected to occur at surface temperatures above 200°C (cf. Chapter 1). Under these conditions Be behaves more ductile compared to room temperature. Hence, additional tests on few un-irradiated Be test coupons have been carried out under experimental conditions which take care of this effect [231]. The erosion damage of the Be grades S65C and TR30 at different temperatures after thermal shock test has been investigated.

### 5.5.2 Experimental details and loading conditions

The test coupons, which have been used for pre-heated tests were halves of samples used for fracture mechanics tests before.

These samples have been mounted on a copper holder which was thermally isolated from the movable support structure. A defocused electron beam with low power density was used to heat up the copper holder including the test coupons to temperatures slightly above the experimental conditions. Thermal shock loading by means of a focused beam has been performed in the cool down phase after having achieved the envisaged temperature range. The actual sample temperature has been monitored by two colour pyrometer and infrared camera.

In Table 5.9 the applied loading conditions on test coupons are reported. Each sample has been loaded by 1 electron beam shots of 5 MJ/m<sup>2</sup> incident energy density.

The pulse duration of the shots was 5 ms. For both Be grades, seven samples have been tested. The temperature range 250-550 °C has been investigated at temperature steps of 50°C.

Table 5.9 - HHF test on pre-heated Be samples

Beryllium grades	S65C, TR30
Beam current [mA]	217
Acceleration voltage [kV]	120
Loaded area [mm <sup>2</sup> ]	5x5
Number of spot	1
Pulse duration [ms]	5
Power density [MW/m <sup>2</sup> ]	~ 1040
Temperature range [°C]	250 - 550

### 5.5.3 Test results

The erosion damage has been estimated by laser profilometry, optical microscopy and metallography. For each sample, the maximum crater depth after e-beam loading has been measured. Figure 5.53 shows the obtained values as function of the temperature for the two grades.

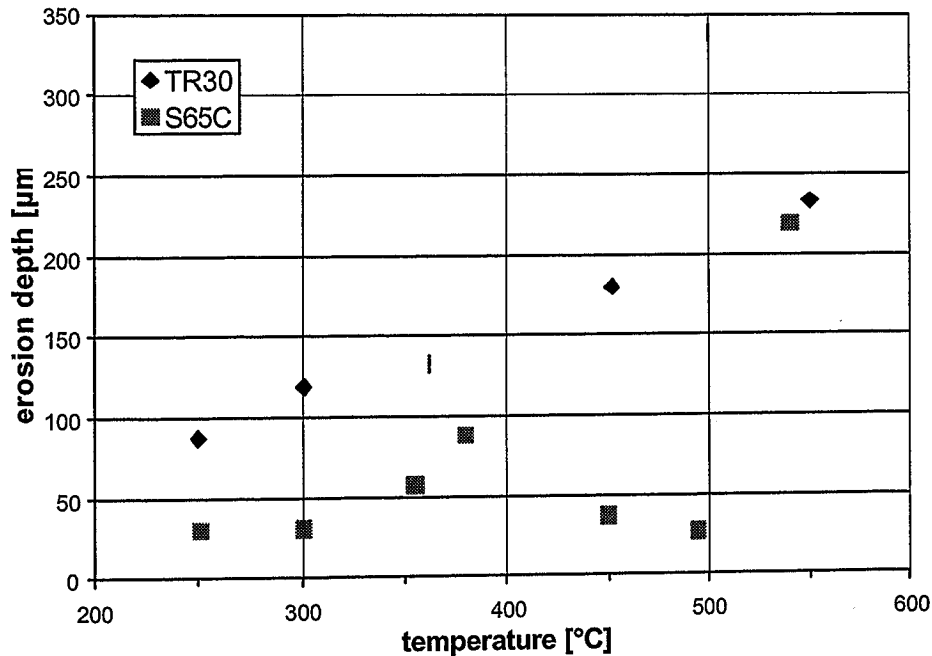
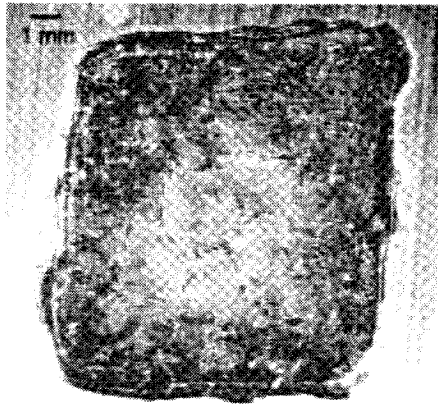


Figure 5.53 - Maximum crater depth vs temperature after 1 EB shot at 5 MJ/n<sup>2</sup> energy density.

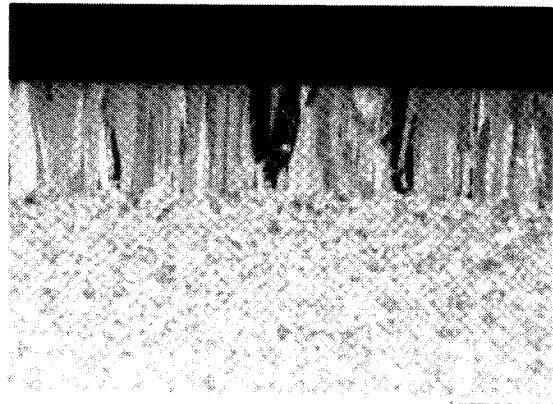
The effect of the sample temperature below 500°C seems to be significant on the TR30 grade but irrelevant for the S65C grade. Be grade TR30 shows bigger erosion values at higher temperatures. Microphotographs of all samples have been taken after electron beam loading to optically compare surface changes at the different exposure temperatures.

After the exposure to the electron beam load, the specimens were sectioned at the centre of the spot and metallographic pictures have been taken in a plane perpendicular to the surface of samples.

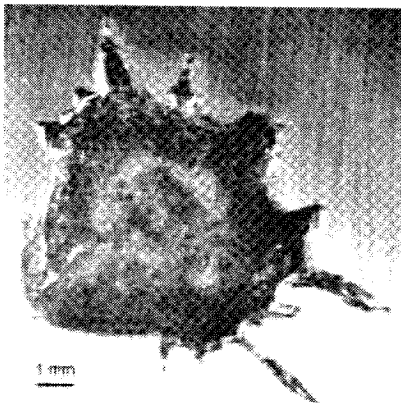
Figure 5.54 shows surface area scan and pictures of the corresponding metallographic sections of three Be S65C samples, which have been tested at 250°C, 450°C and 540°C. In Figure 5.55 equivalent pictures of three Be TR30 specimens, which have been tested at 250°C, 450°C and 550°C are presented. In all test coupons thermal induced cracks move perpendicular to the loaded surface and, except for the Be S65C test coupon, which has been tested at 380°C (Figure 5.54-d), they extend to the base material remaining inside the molten zone. No relevant difference in cracking is observed on the samples tested at higher temperature but an increased dynamic motion of the melt material is observable by the microphotographs, both for the S65C and TR30 grade.



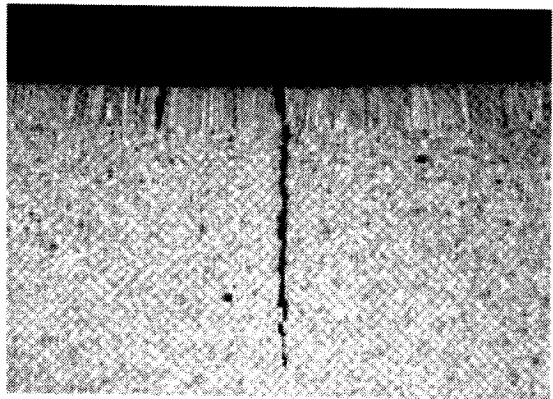
a)  $T = 250\text{ }^{\circ}\text{C}$  (Id. no. M81 13)



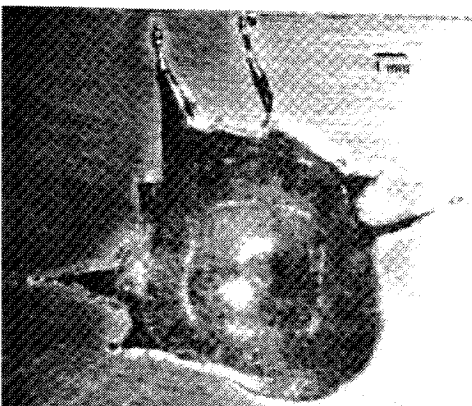
b)  $T = 250\text{ }^{\circ}\text{C}$  (Id. no. M81 13)



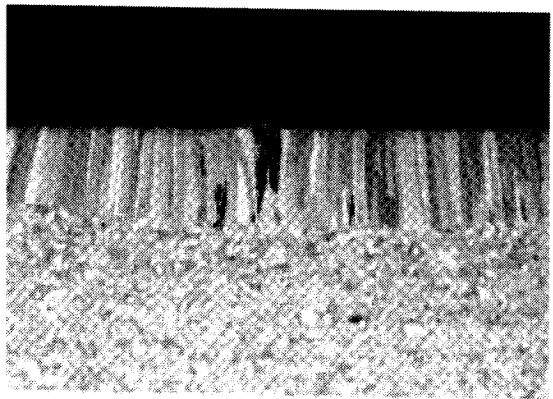
b)  $T = 380\text{ }^{\circ}\text{C}$  (Id. no. M81 7)



d)  $T = 380\text{ }^{\circ}\text{C}$  (Id. no. M81 7)

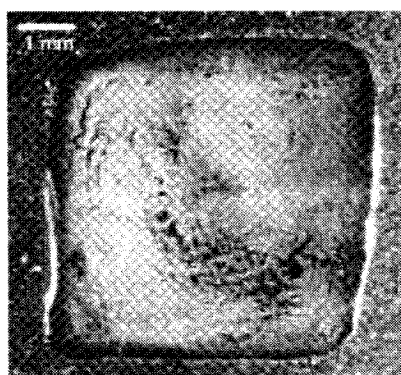


e)  $T = 540\text{ }^{\circ}\text{C}$  (Id. no. M81 23)

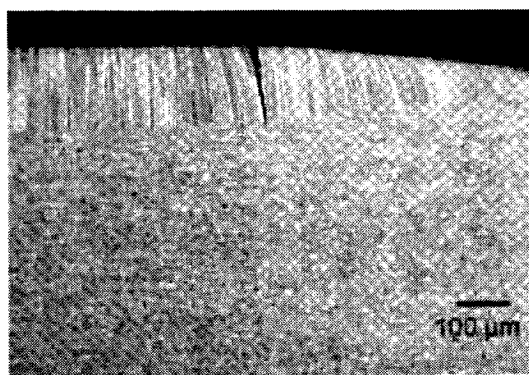


f)  $T = 540\text{ }^{\circ}\text{C}$  (Id. no. M81 23)

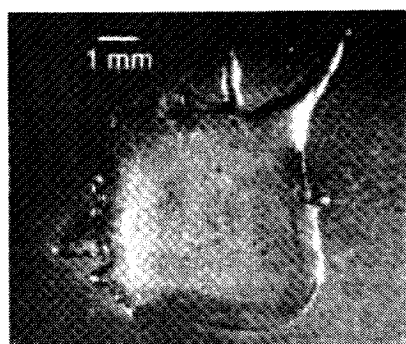
Figure 5.54 - Microphotographs and metallographic sections of Be S65C test coupons after 1 EB shot of 5 MJ/m<sup>2</sup> at different temperatures.



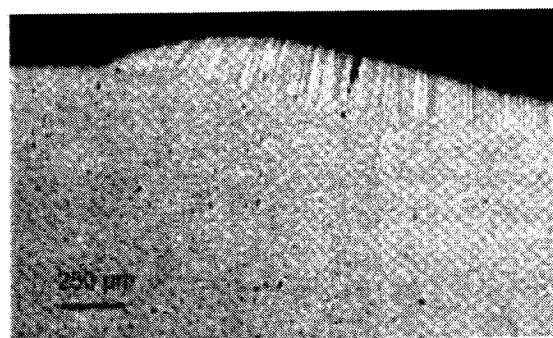
a) T = 250 °C (Id. no. M92 3.17)



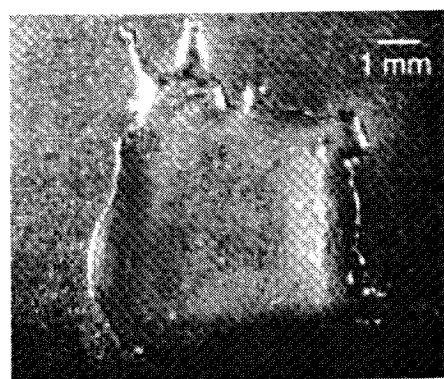
b) T = 250 °C (Id. no. M92 3.17)



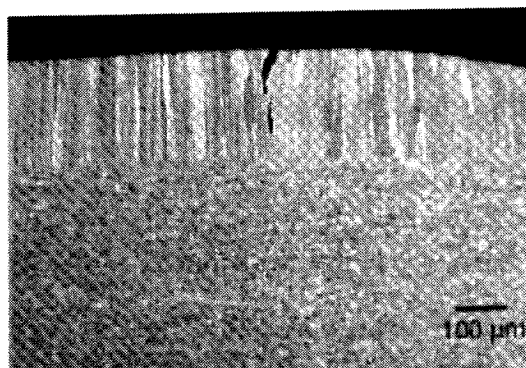
b) T = 450 °C (Id. no. M92 3.27)



d) T = 450 °C (Id. no. M92 3.27)



e) T = 550 °C (Id. no. M92 3.23)



f) T = 550 °C (Id. no. M92 3.23)

Figure 5.55 - Microphotographs and metallographic sections of Be TR30 test coupons after 1 EB shot of 5 MJ/m<sup>2</sup> at different temperatures.

## 5.6 Conclusion and recommendations for future work

Thermal shock tests on several Be grade samples have been carried out in the electron beam facility JUDITH at Forschungszentrum Jülich, Germany. The behaviour of the different Be grades before and after neutron irradiation has been compared. The results from two test campaigns have been presented. The erosion behaviour of the irradiated test coupons has been compared with un-irradiated tests specimens. The results of the two test campaign should not be mixed but within each campaign the same tendencies have been found.

All Be grades show an enhanced erosion after neutron-irradiation, but the amount of erosion is lowest for S65 and for the condensed Be. For most Be grades no enhanced cracking is observed after neutron irradiation. Only TR30 and PS-Be, which showed large cracks beyond the melt layer before neutron irradiation, show an increased crack sensitivity after irradiation. Measurements of the thermal conductivity of Be after neutron irradiation and tensile tests have been carried out [218]. No thermal degradation has been detected after neutron irradiation but a loss of ductility is found. The increased erosion for neutron-irradiated Be grades therefore cannot be ascribed to a decrease in the thermal conductivity of the bulk Be and it is attributed to a reduction of ductility after irradiation. No large differences are observed for the two irradiation temperatures. In Be the neutron induced embrittlement and brittle destruction during e-beam loading with transient heat pulses may be favoured.

The electrical current absorbed by the test sample during the electron beam shot has been monitored. A drop of this current from the initial value has been detected. The amount of the drop and the time at which it occurs, depends from the experimental set-up. The origin of this drop could be ascribed both to a shielding of incoming electrons from the mass of the evaporated material and to the thermal emission of electrons from the metal.

More investigation for fully understanding the origin of the drop of the current which is absorbed by the test coupons should be performed. In order to detect the thermally emitted electrons, the test should be repeated with an improved experimental set-up. The Faraday cage should be connected to a positive Voltage with a resistor of <100 Ohm to avoid a negative Voltage with respect to the vacuum chamber. A small positive potential could then attract the low energy electrons emitted from the metal. If the improved set-up made it possible to measure the thermionic current accurately, the well known temperature of the Be surface would enable a determination of Richardson's constant for beryllium:

$$J = AT^2 e^{-W/kT} \text{ [A/cm}^2\text{]}$$

where A is Richardson's constant, T is the temperature in Kelvin, W is the work function of the metal and k is Boltzman's constant.

In the described procedure for determining the Richardson constant from the above equation a constant value for the Be work function has been assumed. It should be noted that this value could change when the electron thermionic emission takes place from the liquid metal.

Computational simulations of the thermal shock test have also been carried out for investigating the origin of origin of the drop of the absorbed current. Further

improvements are necessary in the analysis model for further clarifying the disagreement between experimental and computational results.

Because PFCs in future thermonuclear fusion reactors will experience severe thermal shocks primarily during plasma operation, i.e. at elevated temperatures (above 200°C), additional tests on few un-irradiated Be test coupons have been carried out under experimental conditions which take care of this effect. The erosion damage of the Be grades S65C and TR30 at different temperatures after thermal shock test has been investigated. The effect of the sample temperature below 500°C seems to be significant on the TR30 grade but irrelevant for the S65C grade.

## 6 ACTIVELY COOLED MOCK-UPS

### 6.1 Thermal fatigue test of Be/Cu joints produced by brazing

One of the main requirements to use Be as a candidate for PFCs in ITER is providing a reliable joint between Be and the Cu heat sink structure. Several techniques of joining such as brazing and hot isostatic pressing (HIP) are under consideration (cf. Chapter 2).

The applicability of the joining techniques was evaluated essentially by testing small actively cooled mock-ups under relevant heat fluxes produced by an electron or ion beam. Mock-up testing is the most proper way to evaluate the thermal fatigue resistance of the joint [232 - 236]. It is not easy to adequately model by numerical analysis methods the local stress state at the discontinuity between dissimilar materials, not to mention the difficulty in defining the constitutive law of the joint [237]. To be fully representative, the mock-up and the test facility should ideally reproduce the real geometry and dimensions of the component, and its actual operating conditions. This is never the case. Size effects are important, because the probability to find a flaw in a joint scales more than inverse linearly with the mock-up size and its geometrical complexity. An other limitation is the testing facility, because the only one that reproduces correctly the mechanical, thermal and neutron loads that the PFCs are subjected to will be the ITER machine itself. Even for the thermal loads, the existing facilities are not able to fully reproduce the load pattern. Due to intrinsic limitation or to the limited availability, ion and electron-beam facilities are used with the shortest duration of the heating cycle, compatible with the condition of near thermal steady-state. In many instances, to reduce the testing time, the test is performed at a heat flux well above the nominal one. Even considering all these limitations, high heat flux testing remains the only way of achieving a preliminary experimental validation of the component design and of its manufacturing technology. The criteria of mock-ups reliability are attainment and repeatability of temperature steady state in the joint at each heating level during the screening test and existence and conservation of the thermal contact in the joint.

#### 6.1.1 Objectives

During the normal operation of ITER, the Be/Cu joint will be stressed by cyclic heat loads, which may cause a fatigue failure. The thermo-mechanical properties of different non-irradiated Be/Cu joints have been investigated by electron beam simulation before [238 - 241]. Thermal fatigue endurance is a necessary but not sufficient prerequisite for the joint. In fact, all PFCs will suffer irradiation with 14 MeV neutrons generated in the fusion process. The influence of neutron irradiation will play an important role in the selection of the joining technologies. This is particularly true for the first wall components, where the joint will experience a rather high fluence. According to one of the repair schemes envisaged for the primary wall [233], the armour is refurbished several times by plasma spraying new Be onto the old eroded Be surface. Therefore, the joint has to withstand the total fluence of the BPP (ITER FDR), while the armour will be periodically renewed. According to an alternative repair scheme, based on rebrazeable rheocast alloys, a sacrificial element including a new Be armour and a new Be/Cu joint will replace the damaged one. In this case, the requirement on the joint lifetime under neutron irradiation is less stringent.

In order to study the degradation effects caused by the fast neutrons, samples have been neutron-irradiated in the HFR at Petten. In this irradiation experiment (PARIDE 1), beside thermal shock samples and mechanical test samples, actively-cooled Be/CuCrZr mock-ups were irradiated up to 0.35 dpa at 350°C (cf. Chapter 4). Post irradiation experiments have been performed in the EB facility JUDITH, to comparatively investigate the thermo-



mechanical properties of the Be/Cu joints produced by fast brazing after the neutron irradiation.

### 6.1.2 Numerical simulation of the experiment

Parametric Finite Element (FE) thermal analyses of both 3 mm and 8 mm Be tile small scale mock-ups have been carried out. The aim of the analyses was:

- To determine the loading conditions to be applied during the tests for maintaining the temperatures of Be surface and the Be/Cu interface below the allowable values, i.e. 800°C and 400°C, respectively;
- To observe the temperature distribution, which results by heating a reduced surface area of the mock-up.

The origin of the latter point is due to a special feature of the JUDITH facility, which imposes the area covered by the electron beam to be smaller than the total surface area of the mock-up (cf. Paragraph 7.1.3).

The analyses have been carried out with the ANSYS code [242]. The design and the geometrical dimensions of the modelled mock-ups are reported in table 1.

#### 6.1.2.1 Analysis model

As result of a reduced loaded area a thermal gradient on the axial direction of the sample was expected. Therefore a 3D model have been used for the analyses.

Taking advantage of the symmetry only a quarter of the mock-ups has been modelled. In Figure 6.1 the adopted FE model for the 3 mm tile sample is shown. Solid parabolic (20 nodes) elements have been adopted. The brazed interlayer has not been modelled.

The material properties are taken from the ITER MPH [243]. Temperature dependent material properties have been used (cf. Chapter 2). Irradiation effects on the material properties have instead not been considered.

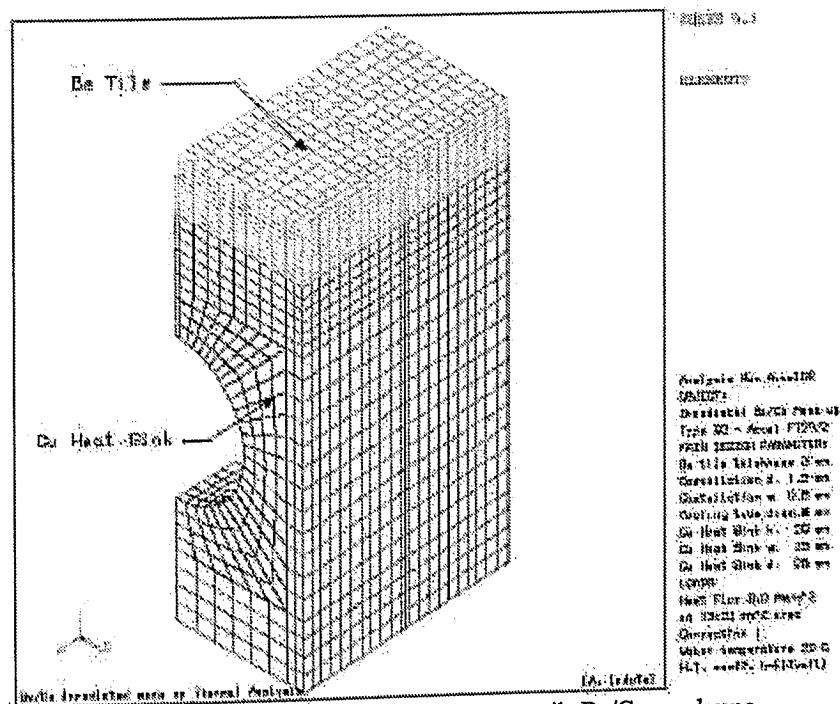


Figure 6.1 - FE analysis model of the 3 mm tile Be/Cu mock-ups.

### 6.1.2.2 Thermal load and input data

For simulating the possible electron beam scenarios, i.e. the possible heated area during tests, three parametric analyses have been performed for each Be/Cu mock-up. The analyses can be classified as follow:

- load case 1: EB incident on the total surface area (25x15 mm<sup>2</sup>);
- load case 2: EB incident on an area reduced of 0.5 mm from the sample edges (24x14 mm<sup>2</sup>);
- load case 3: EB incident on an area reduced of 1 mm from the sample edges (23x13 mm<sup>2</sup>).

Because the surface of the samples is heated by a very narrow EB of <1mm diameter which is scanned at a very high frequency, the incident heat flux has been applied in the FE model, besides on the Be tile surface, in its castellation. The applied heat flux were 8 MW/m<sup>2</sup> and 6.5 MW/m<sup>2</sup> for the 3 mm and 8 mm Be tile, respectively. For the mock-ups with 3 mm Be tile an additional analysis at 11 MW/m<sup>2</sup> has been carried out.

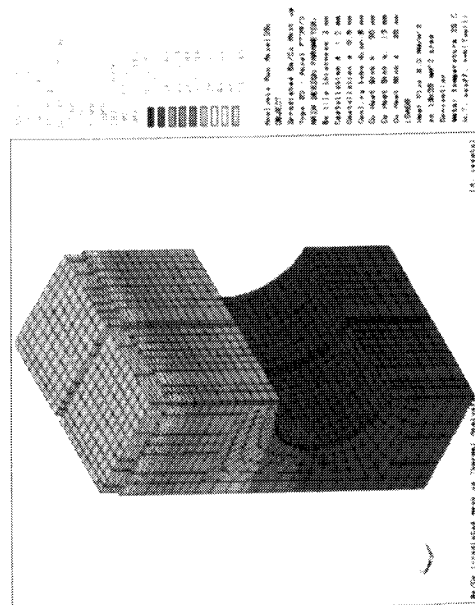
A heat transfer coefficient dependent from the wetted wall temperature has been used in the cooling channel. The heat transfer coefficient vs. wall temperature was computed by means of the EUPITER code [244], which implements the Sider-Tate, the Bergles-Rosenhow and the Thom-CEA correlations in pure forced convection, at the onset of nucleate boiling and in the nucleate boiling regime, respectively. The water coolant parameters, used for input in the EUPITER code, were:  $v = 12$  m/s ( $\sim 36$  l/min),  $P = 4$  MPa and  $T = 20^\circ\text{C}$ . A swirl with a twist ratio of 4 was inside the tube and has been considered by the EUPITER code. By considering the EB incident on the total surface area of the mock-up, the water temperature increase between inlet and outlet has been estimated  $1.19^\circ\text{C}$ . Therefore the coolant temperature for the convection has been assumed  $20^\circ\text{C}$  constant. All other surfaces were assumed to be adiabatic. The loading conditions of the performed analyses have been resumed in Table 6.1.

Table 6.1 - FE analyses loading conditions. Convection conditions:  $T = 20^\circ\text{C}$ ;  $h = h(T_{\text{wall}})$ .

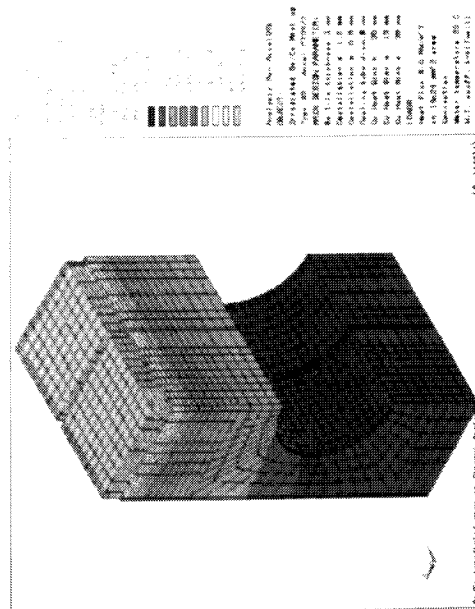
Load case	EB incident area [mm <sup>2</sup> ]	Heat flux [MW/m <sup>2</sup> ]	
		mock-up 3 mm Be tile	mock-up 8 mm Be tile
1	25x15	8 and 11	6.5
2	24x14	8	6.5
3	23x13	8	6.5

### 6.1.2.3 Results

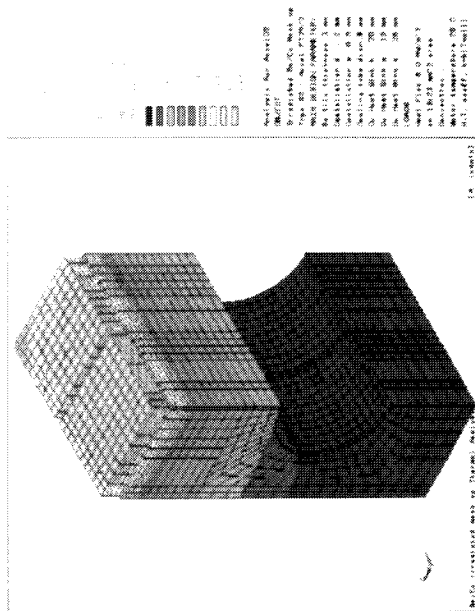
The main resulting data of the 3 mm Be tile mock-up with 8 MW/m<sup>2</sup> incident heat flux are summarised in Table 6.2. Figure 6.2 shows the temperature distribution obtained in the three load cases. Since, even in the most conservative case (load case 1) the maximum Be temperature value is quite a lot below the allowable value ( $800^\circ\text{C}$ ), other FE analyses with higher heat flux values have been carried out. Figure 6.3 shows the temperature distribution obtained with 11 MW/m<sup>2</sup> incident on the total surface area of the 3 mm Be tile mock-up. The temperature values in different regions of the sample are reported in Table 6.3. It should be noted that the temperature of the Be tile is still below the allowable value ( $800^\circ\text{C}$ ).



a) Load case 1 – EB on 25x15 mm<sup>2</sup>



b) Load case 2 - EB on 24x14 mm<sup>2</sup>



c) Load case 3 - EB on 23x13 mm<sup>2</sup>

Figure 6.2 - Be/Cu mock-up, 3 mm Be tile (Id. no FT29/2), steady state temperature distribution. Comparison between three possible heated areas at 8 MW/m<sup>2</sup>.

Table 6.2 - Be/Cu mock-up 3 mm Be tile (Id. no FT29/2) FE analysis results. Comparison between three possible heated areas at 8 MW/m<sup>2</sup>.

Location		Load case 1		Load case 2		Load case 3	
		T [°C]		T min [°C]	T max [°C]	T min [°C]	T max [°C]
Be tile	surface	513		373	481	299	450
	castellation	425		346	396	285	369
Be/Cu interface		306		269	282	235	260
Cu heat sink	inner upper tube	183		169		148	
	inner down tube	63		59		55	

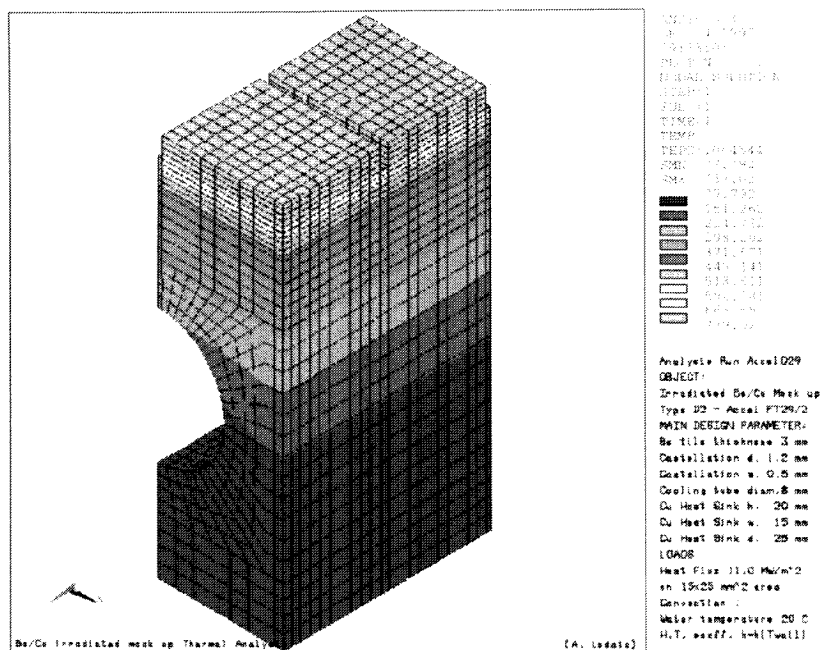


Figure 6.3 - Be/Cu mock-up, 3 mm Be tile (Id. no. FT29/2), steady state temperature distribution. Load conditions: 11 MW/m<sup>2</sup> heat flux on the total Be surface area.

Table 6.3 - Be/Cu mock-up 3 mm Be tile (Id. no. FT29/2), FE analysis results. Load conditions: 11 MW/m<sup>2</sup> heat flux on the total Be surface area.

Location		T [°C]
Be tile	surface	739
	castellation	598
Be/Cu interface		411
Cu heat sink	inner upper tube	232
	inner down tube	78

The following considerations with respect to the analyses on the 3 mm Be tile mock-up can be made:

- the maximum temperature of the Be tile obtained by applying a heat flux of 8 MW/m<sup>2</sup> remains with a large extent below the allowable value (800 °C) in all the three investigated EB scenarios;
- the temperature gradient is only in y direction if the EB is applied on the total surface area and a small gradient in axial direction appears when a reduced surface is heated;
- taking into account that the materials thermal conductivity is slightly reduced after neutron irradiation [245], tests could have been performed at 11 MW/m<sup>2</sup>, the Be surface temperature still remaining below the allowable value.

However, for avoiding the formation of intermetallic phases in the Be/Cu joint (cf. Chapter 2), it is recommended to keep the temperature value at the braze interlayer below 400°C. Therefore during the tests only 9.5 MW/m<sup>2</sup> has been applied.

The main resulting data of the 8 mm Be tile mock-up with 6.5 MW/m<sup>2</sup> incident heat flux are summarised in Table 6.4. Figure 6.4 shows the temperature distribution obtained in the three load cases.

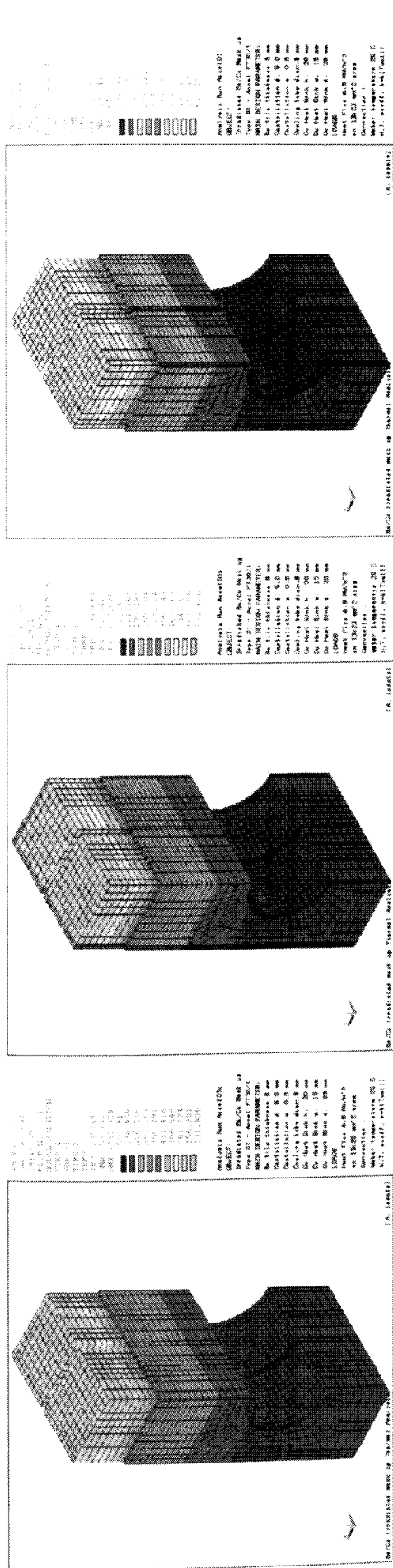


Figure 6.4 – Be/Cu mock-up, 8 mm Be tile (Id. no. FT36/1, FT41/1), steady state temperature distribution. Comparison between three possible heated areas at 6.5 MW/m<sup>2</sup>.

Table 6.4 – Be/Cu mock-up 8 mm Be tile (Id. no. FT36/1, FT41/1) FE analysis results. Comparison between three possible heated areas at 6.5 MW/m<sup>2</sup>.

Location		Load case 1		Load case 2		Load case 3	
		T [°C]	T min [°C]	T max [°C]	T min [°C]	T max [°C]	T max [°C]
Be tile	surface	732	548	673	438	616	
	castellation	410	345	375	299	342	
Be/Cu interface		254	228	232	204	212	
Cu heat sink	inner upper tube	154		136		129	
	inner down tube	56		52		49	

The following considerations with respect to the analyses on the 8 mm Be tile mock-up can be made:

- the maximum temperature of the Be tile obtained by applying a heat flux of  $6.5 \text{ MW/m}^2$  remains with a large extent below the allowable value ( $800^\circ\text{C}$ ) in all the three investigated EB scenarios;
- the temperature gradient is only in y direction if the EB is applied on the total surface area and a small gradient in axial direction appears when a reduced surface is heated;
- temperature value at the braze interlayer remains with a large extent below the allowable value ( $400^\circ\text{C}$ ) in all the three investigated EB scenarios.

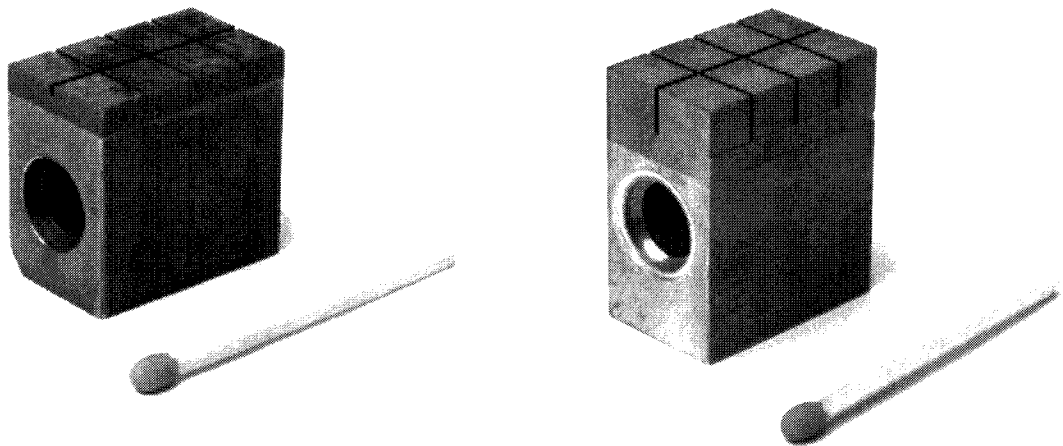
Taking into account that the materials thermal conductivity is slightly reduced after neutron irradiation [245], and that the more realistic dimension of heated area during the tests correspond to the analysed load case 2, a heat flux up to  $8 \text{ MW/m}^2$  has been applied for the screening and thermal fatigue tests on the 8 mm tile mock-ups.

### 6.1.3 Experimental details

Static and cyclic heating tests were carried out with small-scale mock-ups developed mainly for neutron irradiation purposes [246]. The aim of these experiments was on one hand to study the reliability of the joints by screening and thermal fatigue tests, and on the other hand to investigate the heat removal efficiency (i.e. the surface temperature as a function of the absorbed power density change in material properties). The test results were compared to those of corresponding un-irradiated samples.

#### 6.1.3.1 Samples design

All mock-ups investigated were of the flat tile design (Figure 6.5). Be S65C tiles were attached to the CuCrZr copper alloy heat sink by fast brazing. Depending on the producer and production process, the samples differed more or less. These differences cover the braze metals and the sample geometries. Table 6.5 gives an overview on the neutron irradiated mock-ups which were tested in thermal fatigue. The corresponding sample geometries are also indicated. Due to the limited volume in the irradiation capsules the surface area of these samples was limited to  $15 \times 25 \text{ mm}$ . The Be thickness was 3 and 8 mm.



a) mock-up no. FT 29/1

b) mock-up no. FT 36/1 and FT 41/1

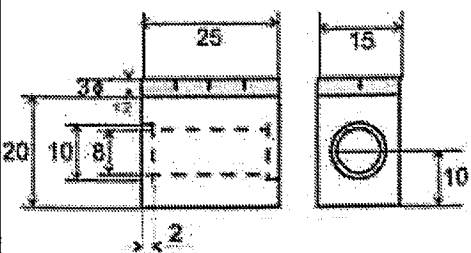
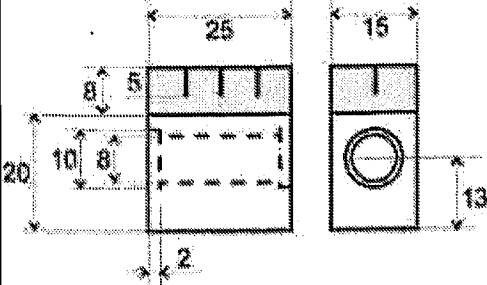
Figure 6.5 - Active cooled samples of Be on Cu for thermal cycle test in JUDITH.

The mock-ups were produced by an induction brazing process proposed by JET [247, 248]. Due to his high capacity in reacting with oxygen, an adherent refractory oxide film (BeO) will rapidly form on Be surfaces. This oxide film will inhibit wetting, flow and melting during brazing (cf. Chapter 2). Therefore parts must be properly cleaned prior to joining. For preventing oxidation during the joining procedure the specimens were produced in a vacuum system. The follow-up of production processes is as follows:

- slow heating to 450°C
- two minutes hold time
- rapid heating (8°C /s) up to 5 – 10 °C above liquidus
- dwell time of 10 to 300 s
- rapid cooling (4°C / s) to T <450°C.

In this brazing process originally InCuSil 'ABA' braze metal containing titanium was used (59% Ag, 27.25% Cu, 12.5% In, 1.25% Ti). But under the operational condition of ITER, silver is strongly activated by neutrons and transmutes to cadmium (with low vapour pressure). Therefore a new joining technique was developed by GEC-Marconi in co-operation with JET [249, 250] which uses a CuMnSnCe braze metal (Cu-60%Mn-9%Sn-30%Ce-1%). For comparison mock-ups with both braze metals were produced and irradiated. For reducing thermal stresses during thermal loads, all samples were castellated after production. In order to save irradiation space, the mock-ups were produced without tube connectors, and the cooling water was supplied through a special clamping mechanism (cf. Chapter 3).

Table 6.5 - Overview on tested Be/Cu mock-ups. Irradiation conditions: 0.35 dpa at 350°C.

Sample type	Producer	Materials combination	Braze metal	Mock-up no.
	Accel	S65C/CuCrZr	InCuSil	FT 29/2
	GEC	S65C/CuCrZr	InCuSil	FT 36/1
	GEC	S65C/CuCrZr	CuMnSnCe	FT 41/1

### 6.1.3.2 Testing procedure and loading conditions

Special techniques for handling of radioactive samples were developed and sophisticated diagnostic systems (water calorimetry, IR camera, pyrometers etc.) have been installed in the facility. The samples were heated by an e-beam of 1 mm diameter approximately, which is swept over the sample surface at frequencies of 50 kHz in x and y directions. The flow rate of cooling water during the test was between 12 and 15 m/s at a pressure of ~4 MPa. A twisted

tape was installed in the cooling channel to enhance the heat transfer. Two types of test were carried out:

- Screening tests: the nominal power was set manually and was switched off a few seconds after thermal equilibrium. No fixed ramp-up or ramp-down values were used;
- Thermal fatigue tests: during each load cycle the mock-up was heated for 10 seconds (after this time 95% of the equilibrium temperature was reached); then it was allowed to cool down for another 10 seconds. Ramp-up and ramp-down times were 0.5 seconds each.

Power densities in the tests were limited by the temperature of the Be tiles. Parametric FE thermal analyses have been carried out to establish the allowable heat flux value to be applied during the tests (ref. Paragraph 7.1.2). In order to avoid evaporation of Be, the temperature was limited to 800°C for safety reasons [251]. According to this limits, maximum power densities between 5 and 9.5 MW/m<sup>2</sup> were achieved, depending on the thickness of Be.

The power absorbed by the mock-ups during the test was determined by water calorimetry. It is calculated from :

$$P_{abs} = C_p \Delta T \Phi$$

where  $C_p$  is the specific heat of water,  $\Delta T$  the of temperature increase, and  $\Phi$  the water mass flow.

Due to the clamping system, no shield plate around the testing specimens can be used in JUDITH [252]. Therefore the e-beam must be restrained to the sample surface. This is achieved by operation with a very narrow e-beam of <1 mm diameter which is scanned at a very high frequency of more than 50 kHz (Figure 6.6-a). The heated area is not completely reproducible, but after the experiment it can be recognized as a discoloration on the sample surface and can be measured (Figure 6.6-b).

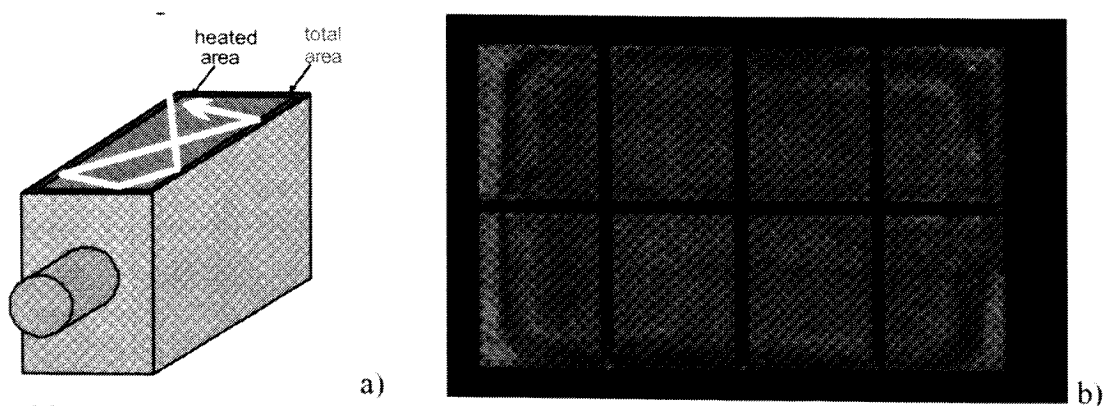


Figure 6.6 – Be/Cu mock-up after test - During the heat loading, the area covered by the EB is a little smaller than the total surface area [252].

Typically the EB stays away 0.5-1 mm from the sample edges [252]. For the calculation of power density, the power was referred to the whole surface area of the mock-ups. In [252] this problem is discussed in detail.

Surface temperature measurements on Be are rather problematic [253]. Temperature distribution on the mock-up surface was controlled by an infra-red camera; a detachment of armor tiles is recognized as an increase of surface temperature. The infra-red camera is a powerful instrument to measure temperature distributions and to control the integrity of the joint, but exact measurement of the surface temperature values is a problem. As a result of previous experiments it was found that Be is rather sensitive to oxidation processes, which



have significant influence on the emissivity value. Therefore, due to the strong fluctuation in emissivity, temperature measurements with one-colour pyrometers and with the IR camera may be inaccurate for Be [254, 255]. In order to overcome this problem, in some experiments a carbon spot of approx. 10 mm diameter was generated by means of graphite spray on the sample surface (Figure 6.11). In fact, the graphite emissivity is rather independent from temperature and surface morphology and is almost constant. For this reason, a special apparatus was built to allow the production of repeatable carbon coatings (spots) on the radioactive mock-ups, by remote operation in a hot cell (Figure 6.7).

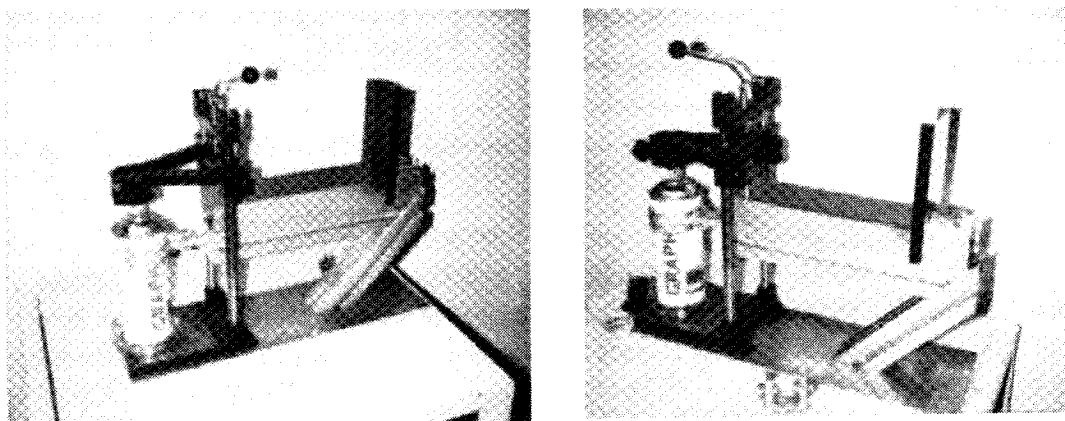


Figure 6.7 - Apparatus for carbon spraying (remote-controlled)

The spraying conditions (thickness of carbon layer, diameter of carbon spot) have been established in calibration experiments. In addition, a two-color pyrometer was used. This pyrometer is able to measure the temperature independently of the emissivity of the material. Unfortunately the minimum working temperature of this pyrometer was 650°C approximately. Therefore it was used only for comparison and calibration at the higher power densities.

#### 6.1.4 Un-irradiated mock-ups test results

Both Be/Cu joining techniques showed a good behaviour during the thermal fatigue tests. A mock-up with the InCuSil braze had an excellent behaviour during 500 thermal cycles at a power density of 4.8 MW/m<sup>2</sup>. A mock-up with the CuMnSnCe braze and a Be armour thickness of 8 mm was loaded up to 1000 cycles at a power density of 5.4 MW/m<sup>2</sup> (absorbed). The flow rate of cooling water during the test was ~12 m/s at a pressure of 4 MPa. The results of these test were reported elsewhere [238-241]. During the thermal fatigue experiment, the surface temperature was measured by a pyrometer. In addition the braze layer temperature was monitored by means of a thermocouple located 1 mm below the joint within the copper body. During the 1000 heating cycles, both temperature curves staid stable and hence no indication of failure was found.

#### 6.1.5 Neutron-irradiated mock-ups 8mm Be tile: results and comparison

Steady state and thermal fatigue test were carried out on the neutron-irradiated mock-ups. One mock-up with CuMnSnCe braze (Id. no. FT 41/1) and one mock-up with InCuSil braze (Id. no. FT 36/1) have been compared with respect to their heat removal efficiency and their thermal fatigue behaviour. During the thermal fatigue experiment the mock-ups were loaded up to 1000 cycles (10 s heating, 10 s cooling). The value of the maximum allowable heat flux has been established by FE thermal analysis. This value was chosen in such a way as to keep the temperature of the Be surface below 800°C (for safety reasons) and to keep the

temperature in the Be/Cu brazing zone below 400°C (to avoid possible partial annealing of radiation defects in Be). The analytical results showed a temperature value of ~250°C at the Be/Cu interface when a heat flux of 8 MW/m<sup>2</sup> is applied on the total surface of the mock-up. In Table 6.6 the exact loading conditions during the test are reported.

Table 6.6 - Loading conditions of neutron irradiated actively-cooled Be/Cu mock-ups.

Sample	Braze metal	Be tile [mm]	Loading conditions			
			Screening		Thermal fatigue	
			Flow rate [m/s]	$\Phi_{abs}$ [MW/m <sup>2</sup> ]	Flow rate [m/s]	$\Phi_{abs}$ [MW/m <sup>2</sup> ]
FT 41/1	CuMnSnCe	8	11.93	up to 7	11.93	~7.5
FT 36/1	InCuSil	8	11.27	up to 7	12.60	~8

Note: Absorbed power density referred to the whole surface area

Figure 6.8 compares the Be surface temperatures as a function of absorbed power density, for the two types of mock-ups, before and after neutron irradiation. The temperature measurement was carried out by means of the IR camera on the carbon spot, and an emissivity of 0.47 was assumed.

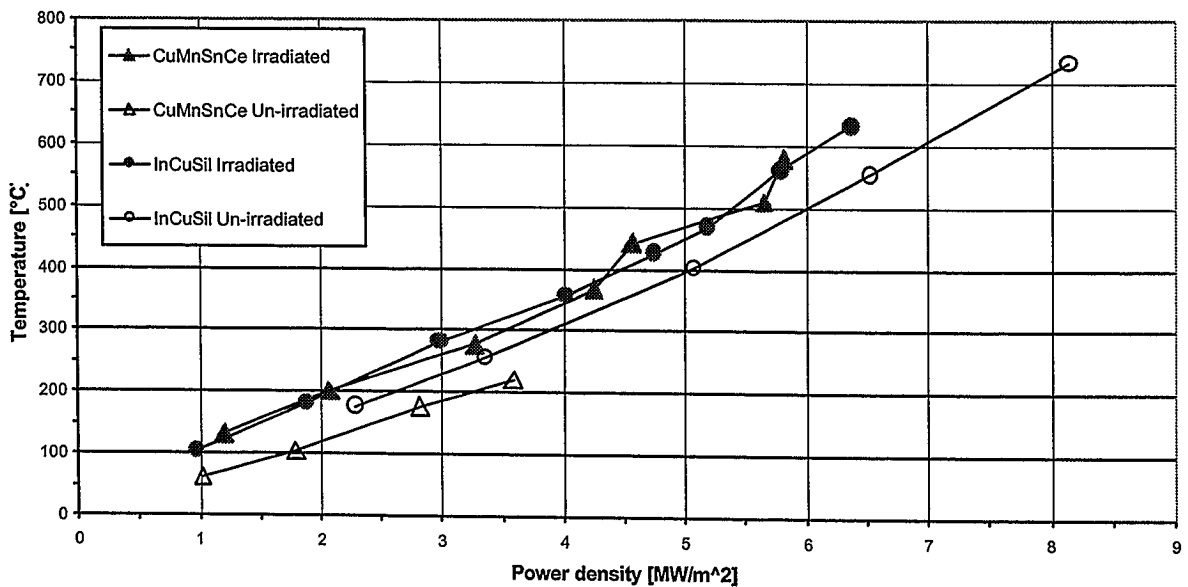
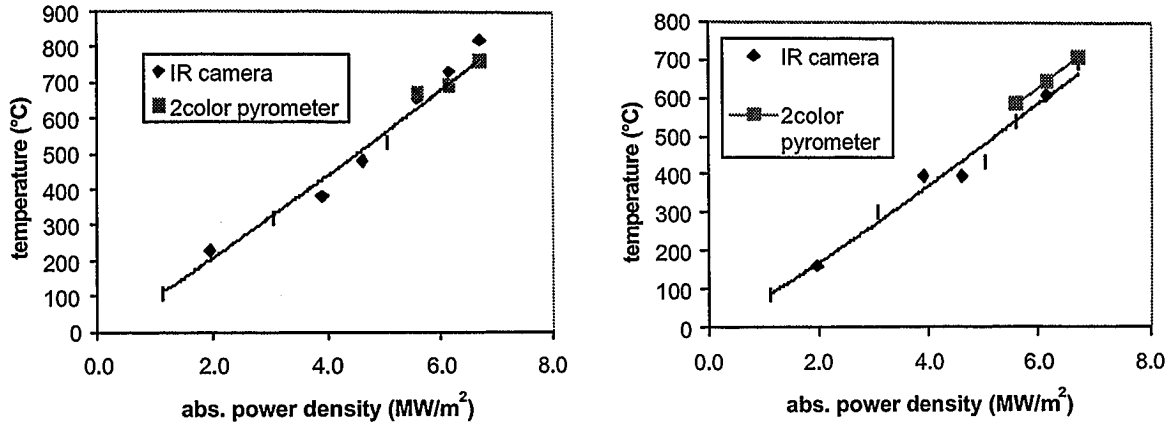


Figure 6.8 - Comparison of maximum surface temperature vs. absorbed power density, before and after neutron irradiation.

The heat removal efficiency is slightly worse after the neutron irradiation. But due to shortage of time pre- and post- irradiation tests have not been carried out on the same mock-ups and this should be taken into account in evaluating the results. Nevertheless, even after neutron irradiation the thermal response shows little difference between the two type of brazes, confirming their good quality.

In Figure 6.9 the comparison between the temperature values by IR camera and two-color pyrometer at the three highest heat loads is shown for both irradiated mock-ups. A good agreement between both kinds of temperature measurement is observed.



a) mock-up no. FT41/1 CuMnSnCe braze

b) mock-up no. FT36/1 InCuSil braze

Figure 6.9 - Thermal response of irradiated mock-ups during steady state heating test. Irradiation condition 0.35 dpa at 350°C.

During the thermal fatigue experiment, the surface temperature of the two mock-ups was measured by pyrometer. Figure 6.10 shows the peak value of the surface temperatures in each load cycle versus the number of cycles. The temperature curves of both mock-ups are stable during the 1000 heating cycles and no indication of failure was observed. The offset between the two curves is due to the different load conditions. This figure also shows that the earlier problems of changes in Be emissivity has been overcome with the introduction of the carbon spot [240]. A constant emissivity  $\varepsilon = 0.47^{14}$  was assumed for the graphite spot during the IR measurements.

The absorbed power density (from water calorimetry) of both mock-ups during thermal cycling has been monitored and a stable behaviour was found during the heating cycles.

The temperature distribution on the sample surface was monitored by the IR scanner. The infra-red images for the sample with CuMnSnCe braze at cycle no. 102 and cycle no. 1000 are shown in Figure 6.11. In addition the temperature profiles along the plotted line during both cycles are shown in this figure.

No relevant changes of the temperature profile are observed. The carbon spot produced by graphite spraying is clearly visible. The temperature distribution shows no instabilities during the experiment.

The infra-red images for the sample with InCuSil braze at cycle no. 2, 105 and 1000 are shown in Figure 6.12.

No indication of failure was found also in the IR images of this sample, but opposite to the mock-up with CuMnSnCe braze, the surface temperature showed some fluctuations during the thermal cycling. The temperature increase during the first 100 cycles is attributed to instabilities of the cooling water. Although the absolute values of temperature changed, no change of temperature distribution was observed during this period. Later however, the apparent surface temperature on the visible beryllium surface increased, while it was more or less constant on the carbon spot.

<sup>14</sup> The emissivity of carbon spot is different from the emissivity of carbon materials which is ~0.9.

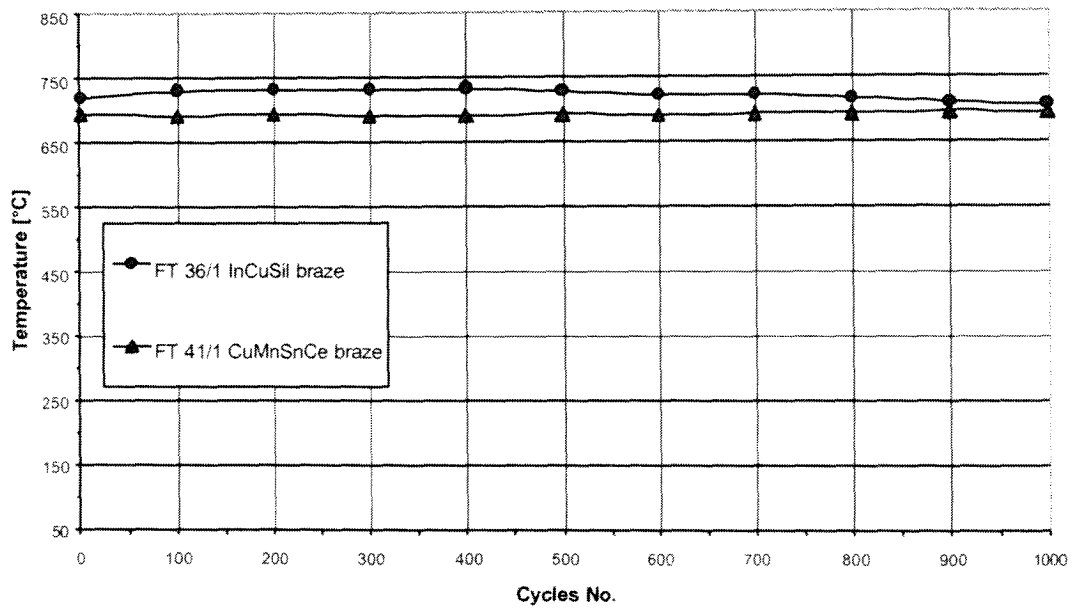
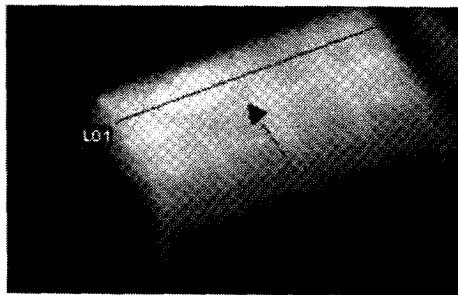
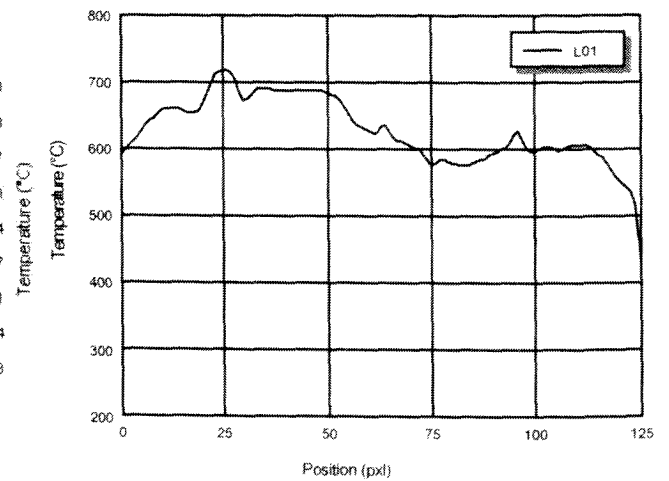


Figure 6.10 - Maximum Be surface temperature during thermal cycling.

Cycle no. 102



Graphite Spot



Cycle no. 1000

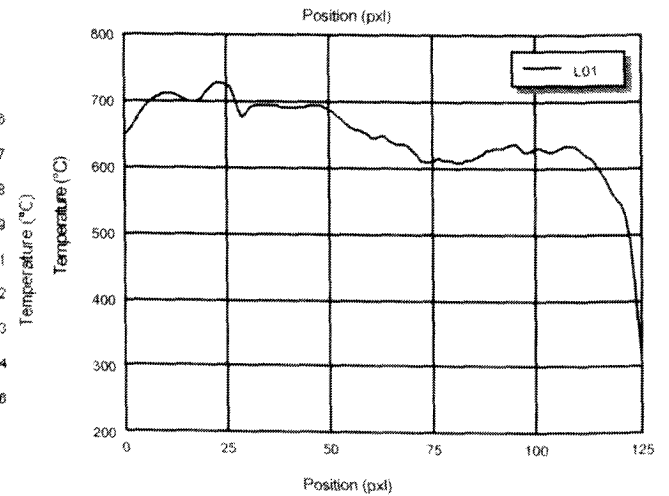
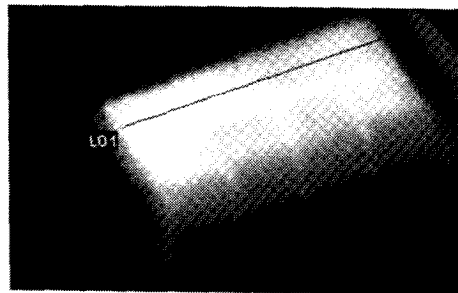
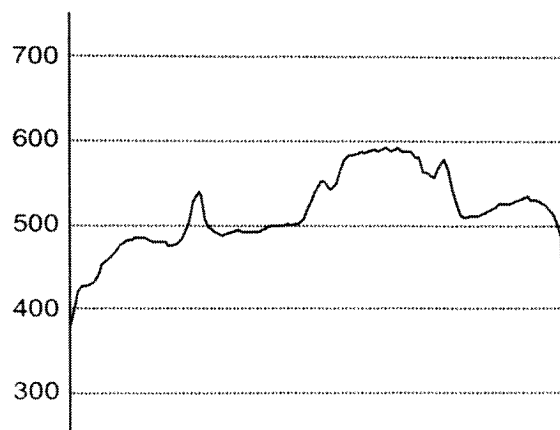
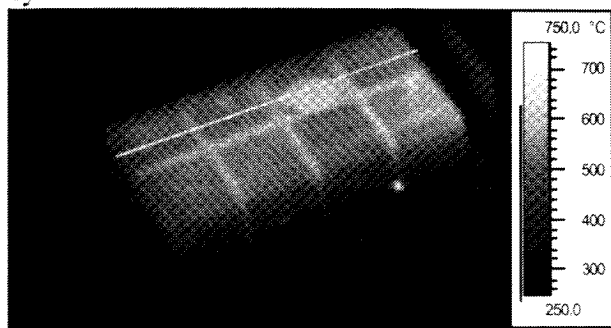
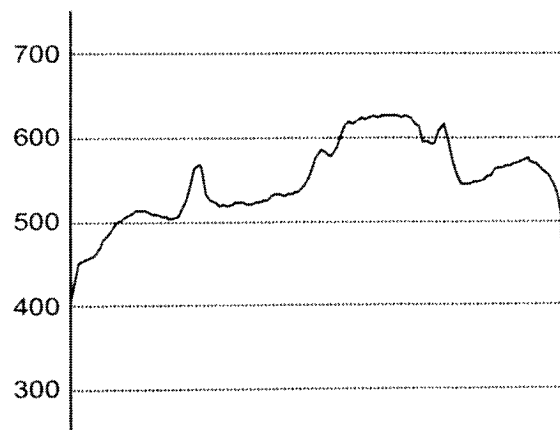
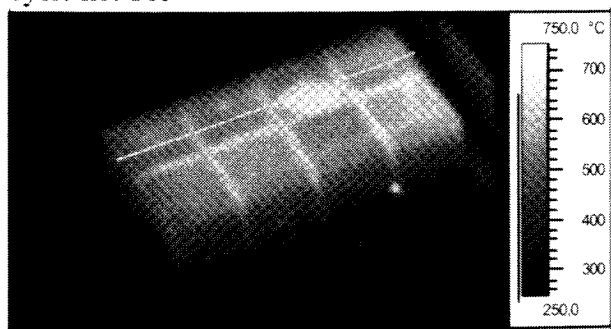


Figure 6.11 - IR images during thermal fatigue test of Be/Cu mock-up with CuMnSnCe braze (Id. no. FT41/1). Absorbed power density:  $7.5 \text{ MW/m}^2$ .

cycle no. 2



cycle no. 105



cycle no. 1000

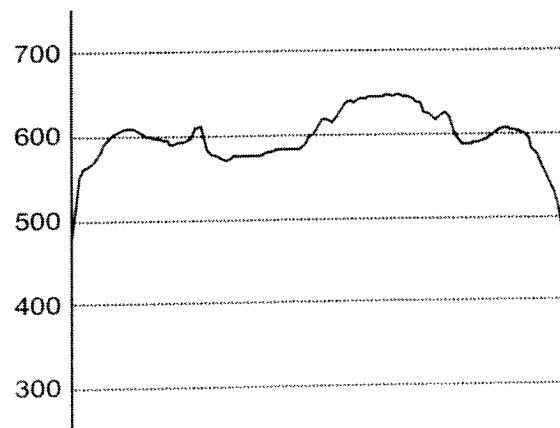
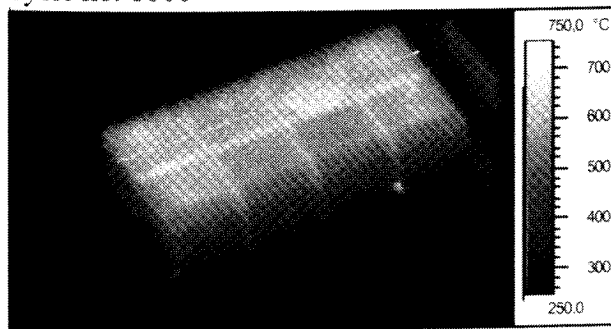
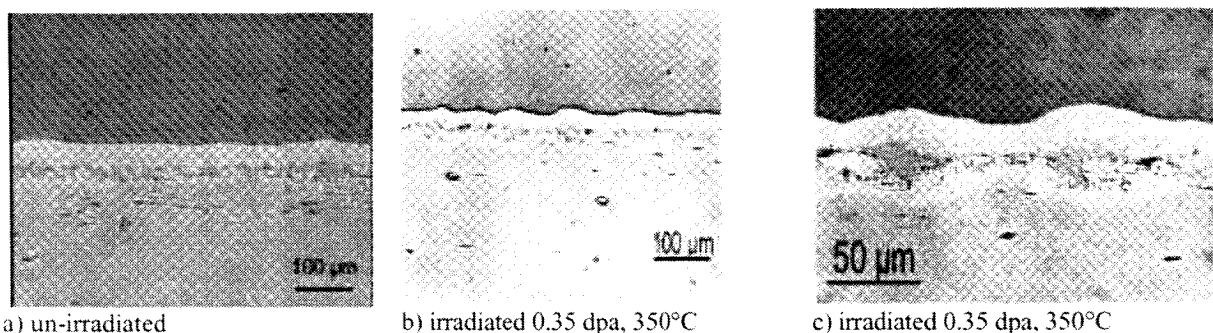


Figure 6.12 - IR images during thermal fatigue test of Be/Cu mock-up with InCuSil braze (Id. no. FT36/1). Absorbed power density: 8 MW/m<sup>2</sup>.

#### 6.1.5.1 Post-mortem analysis

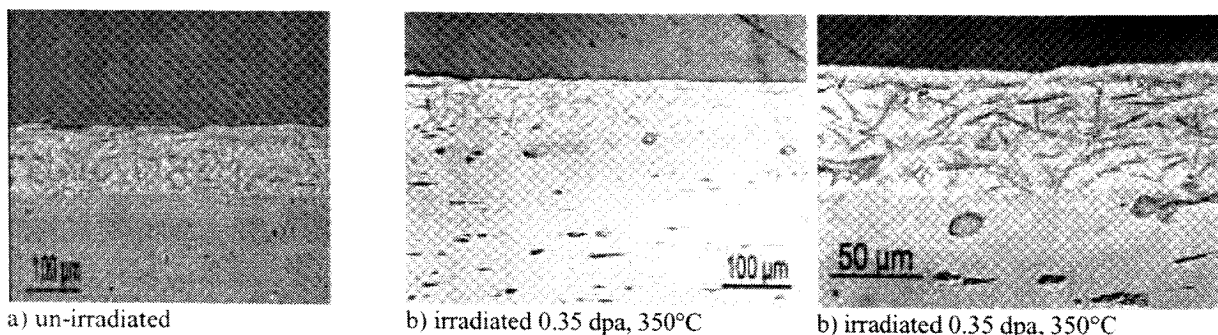
At the end of the thermal fatigue test, the mock-ups were cut and pictures of metallographic sections were compared to those made from un-irradiated joints. Figure 6.13-a shows the metallographic picture of the un-irradiated joint between Be S65C and CuCrZr heat sink with CuMnSnCe braze interlayer. In Figure 6.13-b and c the metallographic section of the correspondent irradiated mock-up with the same braze metal after 1000 cycles at 7.5 MW/m<sup>2</sup> is shown.



a) un-irradiated b) irradiated 0.35 dpa, 350°C c) irradiated 0.35 dpa, 350°C  
Figure 6.13 - Metallographic sections of Be/CuCrZr mock-ups with CuMnSnCe braze interlayer; b) and c) sample no. FT 41/1 after 1000 cycles 7.5 MW/m<sup>2</sup>.

The thickness of the braze is 20 - 50 μm. A large quantity of thin crystallizations, sporadic pores and a waved surface were observed. In the middle of this layer, a thin intermetallic phase is observed. But during neutron-irradiation and during thermal fatigue this layer was stable and did not act as a source for crack initiation. Also in this case no cracking was detected in the braze layer. Apparently no big differences have been found with respect to the un-irradiated mock-ups [239].

Figure 6.14-a shows the metallographic picture of the un-irradiated InCuSil joint between Be S65C and CuCrZr heat sink. In Figure 6.14-a and b the InCuSil braze interlayer of the correspondent irradiated mock-up after 1000 cycles at 8 Mw/m<sup>2</sup> is shown.



a) un-irradiated b) irradiated 0.35 dpa, 350°C b) irradiated 0.35 dpa, 350°C  
Figure 6.14 - Metallographic sections of Be/CuCrZr mock-ups with InCuSil braze interlayer; b) and c) sample no. FT 36/1 after 1000 cycles 8 MW/m<sup>2</sup>.

The 60 - 70 μm braze interlayer shows only sporadic pores and a uniform joint with both beryllium and CuCrZr. The titanium spikes are clearly visible. No cracking was observed in the braze layer.

Both for CuMnSnCe and InCuSil joint the absence of void in the joint area is an indication that good wetting of the materials to be joined occurred. Even after neutron-irradiation and thermal cycling both braze are in a good shape.

### 6.1.6 Neutron-irradiated mock-ups 3mm Be tile test results

Due to the thinner Be layer, higher power densities could be applied compared to the last two mock-ups; and the surface temperatures were lower at equal power densities. Again the value of the maximum allowable heat flux has been established by FE thermal analysis so that the temperature of the Be surface was below 800°C and the temperature in the Be/Cu brazing zone below 400°C (to avoid the formation of intermetallic phases in the Be/Cu joint).

The mock-up was loaded under steady state conditions up to  $9.5 \text{ MW/m}^2$  and afterwards it was loaded in a short term, fatigue experiment up to 100 cycles at the same power density. Figure 6.15 shows the thermal response of mock-up no. FT29/2. No indication of failure was observed (Figure 6.16).

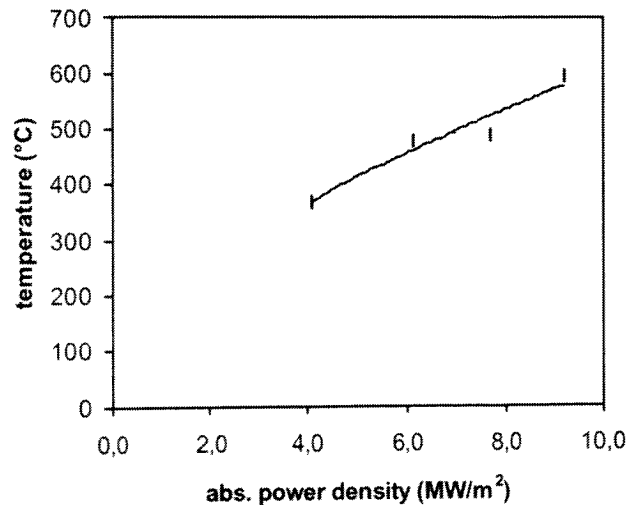


Figure 6.15 - Thermal response of 3 mm Be tile irradiated mock-up (Id. no. FT 29/2) during steady state heating test up to  $9.5 \text{ MW/m}^2$ . Irradiation condition 0.35 dpa at  $350^\circ\text{C}$ .

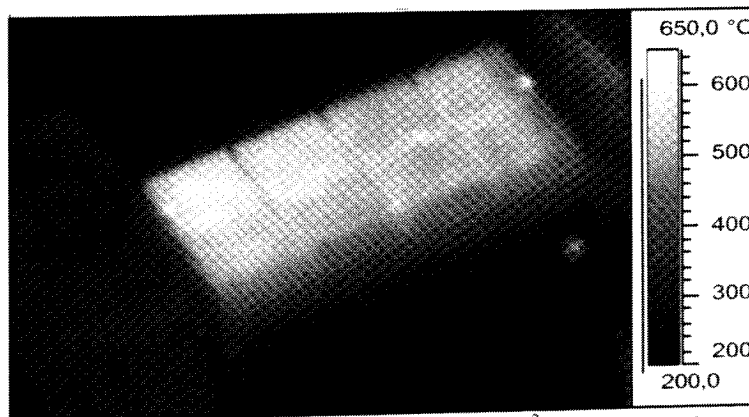


Figure 6.16 - IR image during steady state heating up to  $9.5 \text{ MW/m}^2$  of Be/Cu mock-up no. FT29/2. Irradiation condition 0.35 dpa at  $350^\circ\text{C}$ .

### 6.1.7 Experimental and analytical results comparison

The experimental and analytical temperature values of the Be tile have been compared. The thermal response of the 8 mm Be tile mock-ups (Figure 6.8 and Figure 6.9) have been compared to the FE analyses performed at an absorbed power density of  $6.5 \text{ MW/m}^2$  (Table 6.4). The experimental values have been found in good agreement with the temperatures calculated by FE analyses.

## 6.2 Shear Tests of Be/Cu Joints

In addition to the thermal fatigue test, the quality of the Be-copper joints was characterized by means of mechanical methods. For this purpose, some shear samples were irradiated and after testing the results were compared to those of unirradiated samples [256]. The sample geometry and the sample holder are shown in Figure 6.17.

The load displacement curves of the irradiated samples are shown in Figure 6.18. The results for both types of braze metal are listed in Figure 6.19 and Figure 6.20 respectively. In this evaluation, the result of sample no. FT49/2 has been omitted, due to an irregular failure mode. For the InCuSil braze no influence of the neutron irradiation is observed. The mean value of the post irradiation shear strength for the CuMnSnCe braze is approximately 25% lower compared to the pre-irradiation data. But with respect to the low sample numbers and the large scatter band, this difference is not considered to be significant.

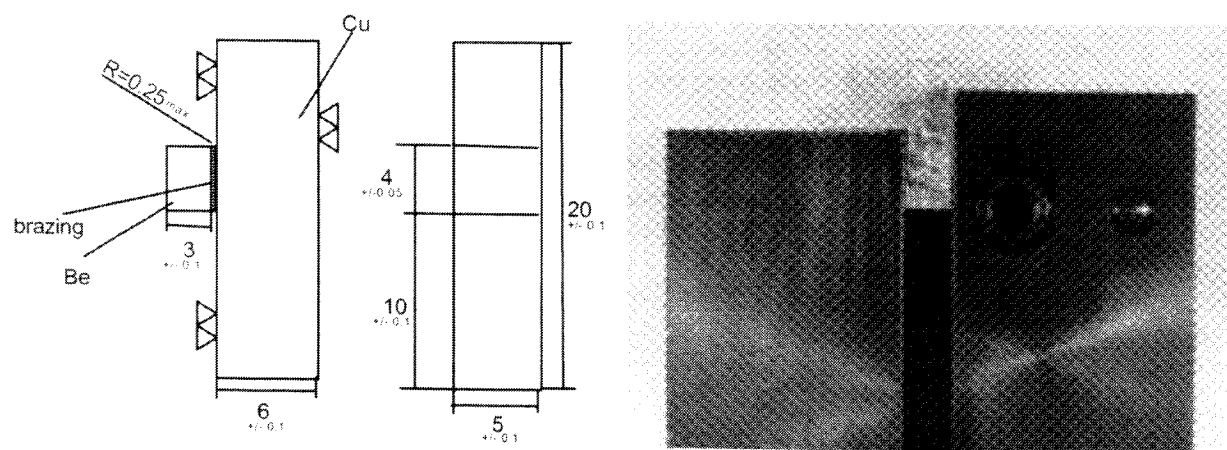


Figure 6.17 - Geometry of shear samples (left) and sample holder for shear testing (right).

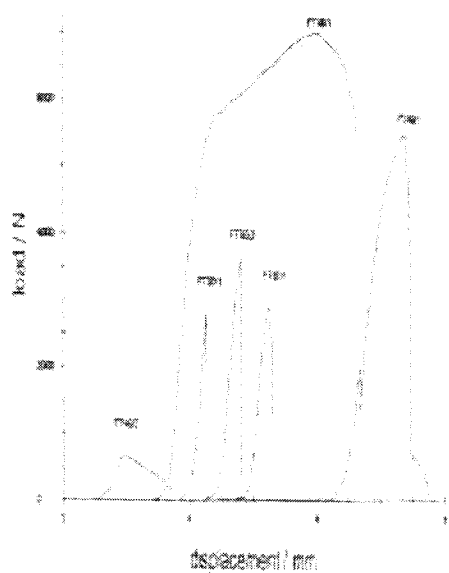


Figure 6.18 - Load displacement curves for irradiated shear samples. FT48, FT49 = InCuSil braze; FT50, FT51 = CuMnSnCe braze.



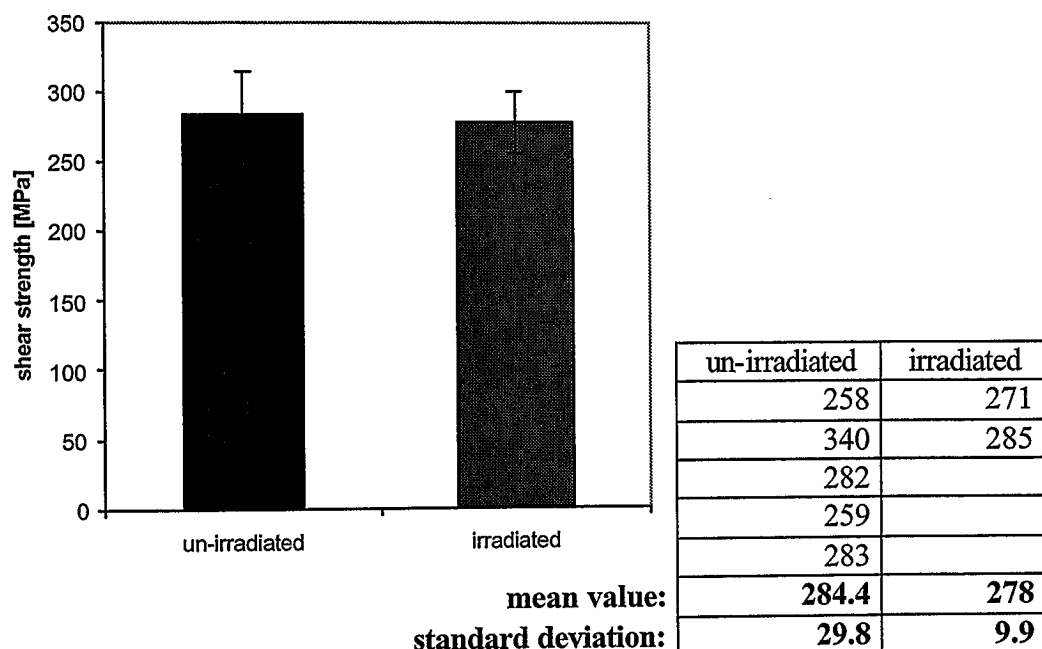


Figure 6.19 - Room temperature shear testing of un-irradiated and irradiated Be/Cu mock-ups with CuMnSnCe braze. Irradiation conditions 0.35 dpa at 350°C.

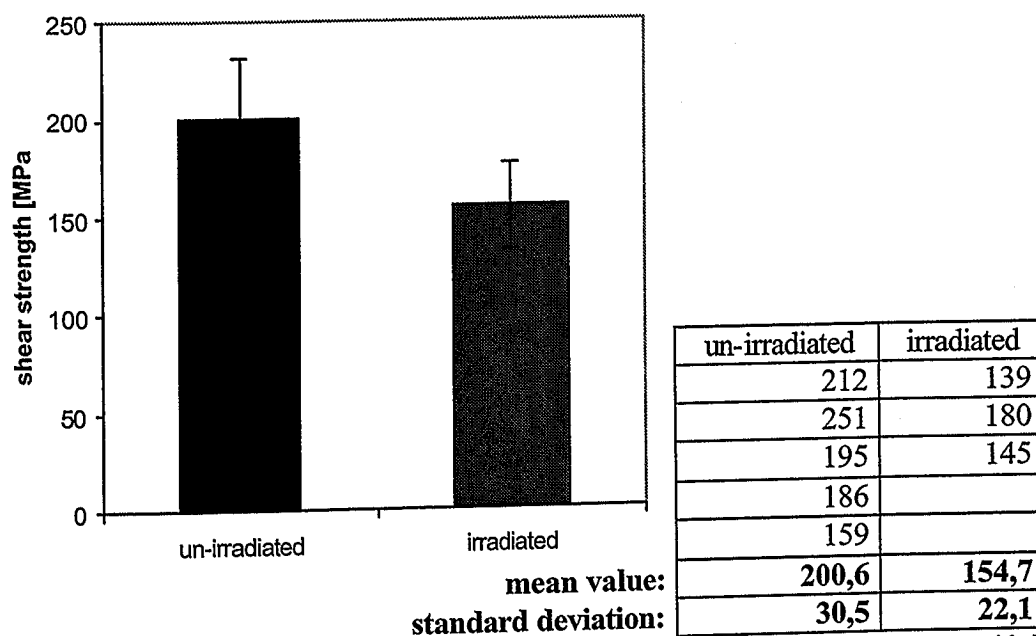


Figure 6.20 - Room temperature shear testing of un-irradiated and irradiated Be/Cu mock-ups with InCuSil braze. Irradiation conditions 0.35 dpa at 350°C.

## 6.3 Pre-irradiation characterisation of PW HIPed mock-ups

### 6.3.1 Objectives

In the frame of the second neutron irradiation campaign PARIDE 3 and 4 (cf. Chapter 4), pre-irradiation characterisation tests on PW small scale mock-ups have been carried out. The aim of these tests was only to check the macroscopic soundness of the joint before irradiation. In these tests, the samples were heated at moderate power densities in JUDITH, and the thermal response was registered by means of the infra-red camera. By this method, it is possible to detect faulty mock-ups and to eliminate them from the neutron irradiation. Another aim of these screening tests is to investigate the change in heat removal efficiency or possible

damage during neutron irradiation by comparison of the heat patterns with the ones which will be measured after irradiation.

### 6.3.2 Mock-ups fabrication

Five PW Be/Cu mock-ups with Be flat tile have been tested. Be S65C tiles, 10 mm thick, were HIPed (cf. Chapter 2) to a heat sink from Glidcop Al25. Three mock-ups have an interlayer of titanium (Id. no. FT66/4 to FT66/6) and two have an interlayer of aluminium (Id. no. FT65/2 and FT65/3). Figure 6.21 shows the photos of one mock-up.

The mock-ups were produced by a Hot Isostatic Pressing diffusion Bonding (HIPB) process (cf. Chapter 2) proposed by CEA/Grenoble [257].

#### 6.3.2.1 Mock-ups with Al interlayer

A thicker Al layer (0.2 mm) was used because beyond its diffusion barrier role it acts as a compliant layer. The DS-Cu used was the grade IG1. The follow-up of production processes is as follows:

- electromachining of the beryllium substrate;
- electromachining of the DS-Cu substrate (corrugate surface, see Figure 6.23);
- degassing of the DS-Cu under vacuum at high temperature;
- deposition of a 10  $\mu\text{m}$  molybdenum coating using Physical Vapour Deposition;
- fabrication of a corrugated 0.2 mm thick, 99.5% pure aluminium interlayer;
- surface preparation of DS-Cu, Al and Be;
- stacking in the canister previously equipped with outgassing tubes;
- EB welding of the canister;
- cleaning of the atmosphere and degassing of the canister using argon flow;
- Sealing of the outgassing tube.

The HIP cycle which was used is reported in Figure 6.22. The HIP temperature of 530°C was adopted by the fact that the higher the bonding temperature, the more stable the joint microstructure under service. However, due to the Al-Cu eutectic melting at 548°C, 530°C can be considered as the maximum joining temperature. The geometry of the mock-up, the nature of the canister and the alloy render difficult the application of the pressure at the interface. Therefore a higher pressure value (150 MPa) has been adopted with respect to previous experiences. Slow cooling and depressurising was applied for the residual stress relieving through creep of the materials.

Figure 6.23 gives a metallographic view of the interface Be/Al/DS-Cu of a mock-up.

#### 6.3.2.2 Mock-ups with Ti interlayer

A 50  $\mu\text{m}$  thick titanium foil was chosen as interlayer. the DS-Cu used was the grade IG1. The procedure may be described as in the following:

- electromachining of the beryllium substrate;
- electromachining of the DS-Cu substrate (corrugate surface, see Figure 6.23);
- degassing of the DS-Cu under vacuum at high temperature;
- fabrication of a corrugated 50  $\mu\text{m}$  mm thick, 99.6% pure titanium interlayer;
- surface preparation of DS-Cu, Ti and Be;
- stacking in the canister previously equipped with outgassing tubes;
- EB welding of the canister;
- cleaning of the atmosphere and degassing of the canister using argon flow;
- Sealing of the outgassing tube.

The HIP cycle which was used is reported in Figure 6.24. Figure 6.25 gives a metallographic view of the interface Be/Ti/DS-Cu of a mock-up.

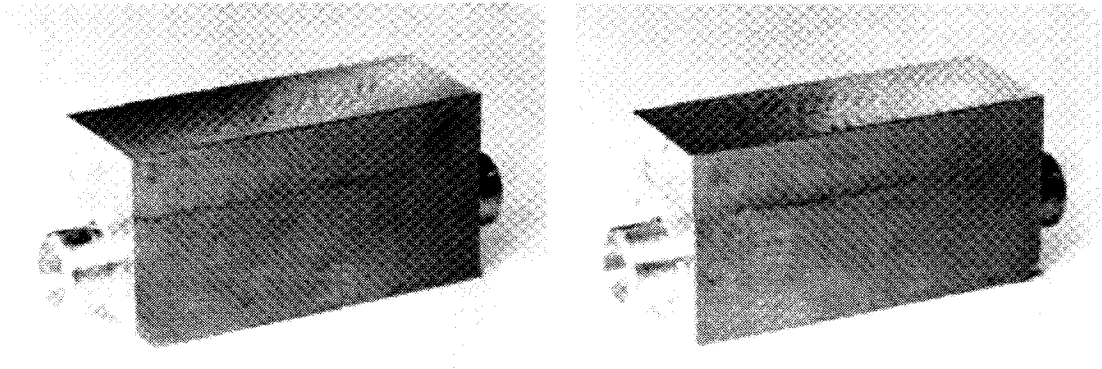


Figure 6.21 - PW mock-up with Ti interlayer (Id. no. FT66/6).

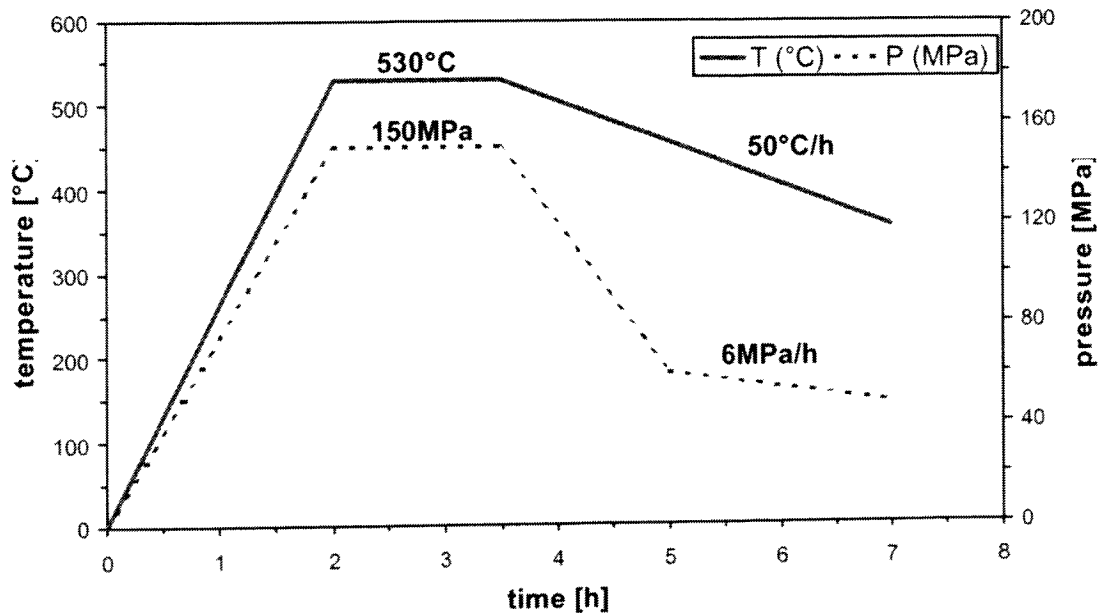


Figure 6.22 - HIP cycle used for the fabrication of mock-ups with an Al interlayer.

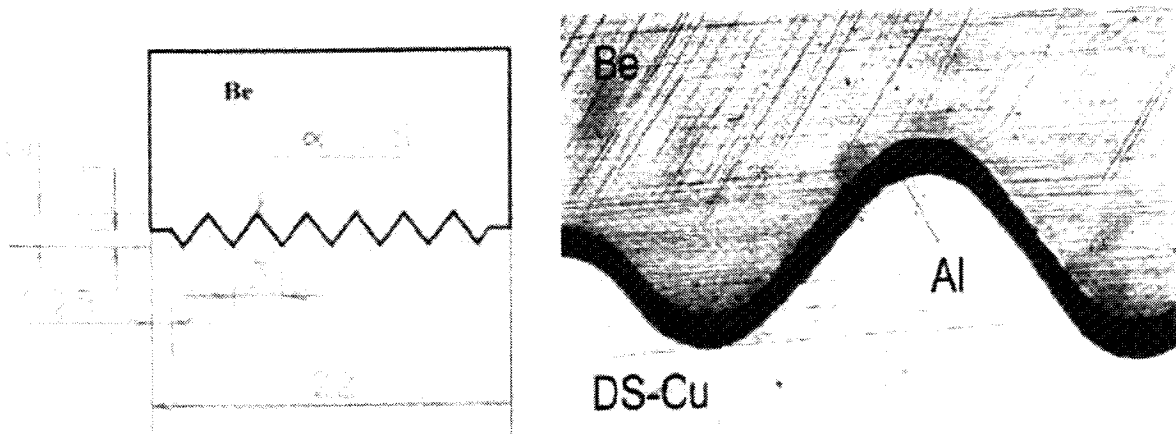


Figure 6.23 - Interface structure of BE/Al/DS-Cu mock-up. Left: scheme of the interface geometry. Right: metallographic view of the interface (x40) [257].

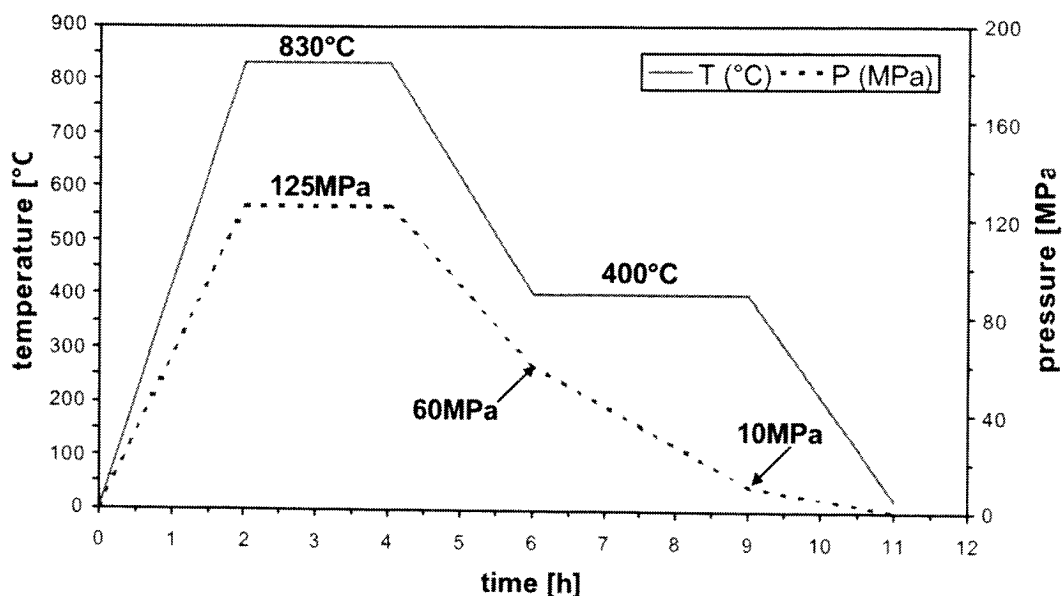


Figure 6.24 - HIP cycle used for the fabrication of mock-ups with Ti interlayer.

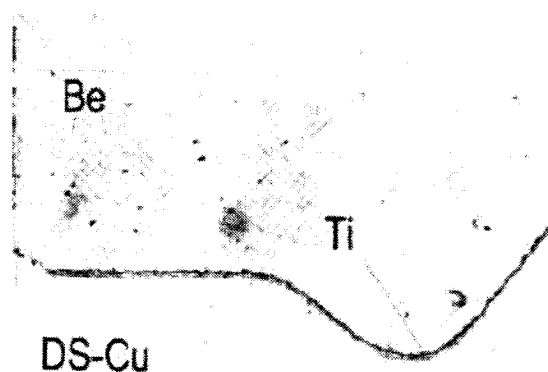


Figure 6.25 - Interface structure of Be/Ti/DS-Cu (x40) [257].

### 6.3.3 Testing procedure and loading conditions

During the electron beam testing, all mock-ups were water cooled and a twisted tape was used to improve the cooling conditions. Water cooling parameter were:  $p = 40$  bars,  $T = 20$  °C,  $\Phi = 24$  l/min ( $v=5$  m/s). All mock-ups were produced with a chamfer on one edge at the lower side. Water supply was achieved from the side of the chamfer, this corresponds to the left side on the infra-red images.

### 6.3.4 Results

In the first experiment with Be flat tile mock-ups, the power density was increased in several steps up to  $2.5 \text{ MW/m}^2$ . Two of the samples with Ti interface (Id. no. FT66/5 and FT66/6) did not show any indication of failure, but for one sample (Id. no. FT66/4) the Be tile detached at  $1.88 \text{ MW/m}^2$  (Figure 6.26). One of the Be mock-ups with Al interface (Id. no. FT65/2) showed a strong local overheating at  $0.75 \text{ MW/m}^2$ . Therefore the second one (Id. no. FT65/3) was tested at reduced power density of  $1 \text{ MW/m}^2$  and it did not show any fault. The test results are resumed in Table 6.7.

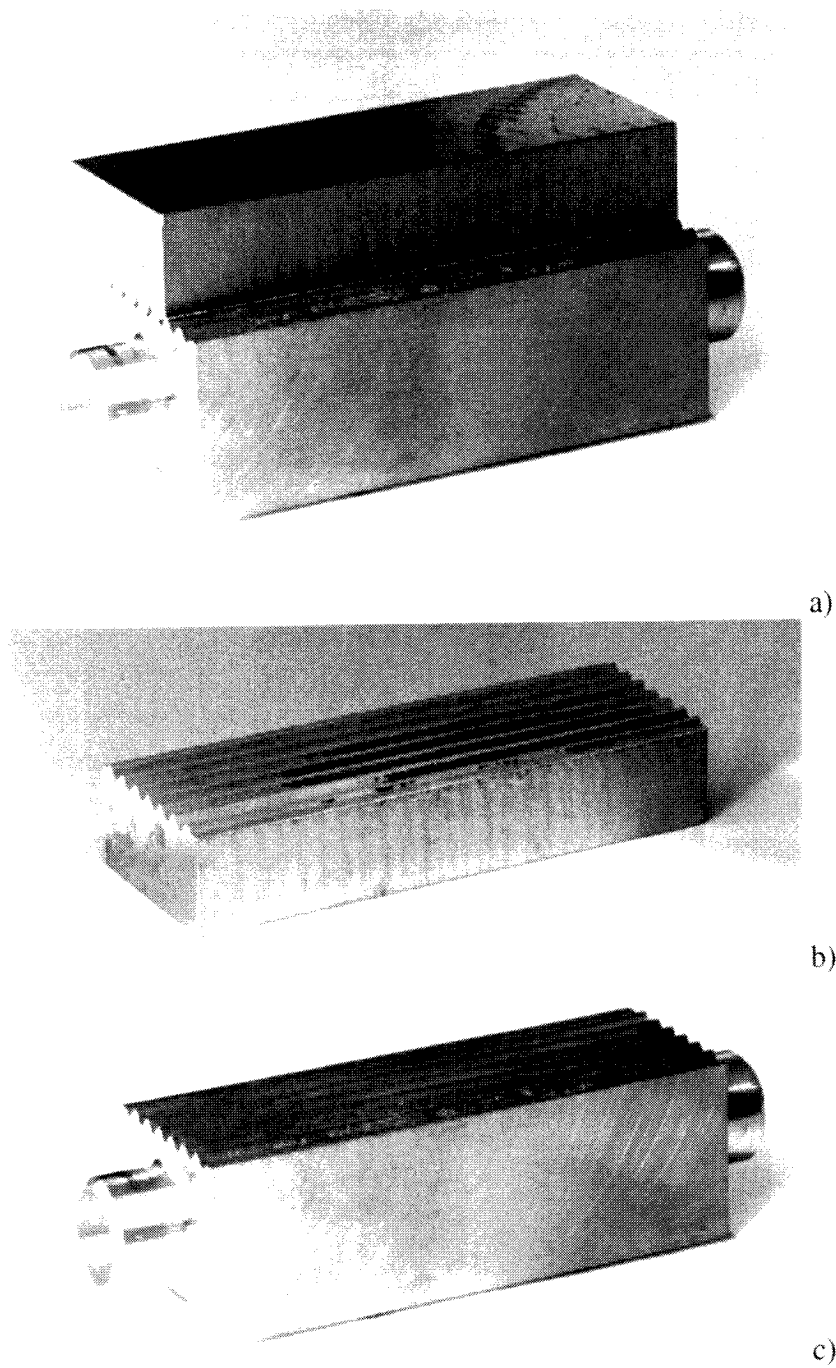
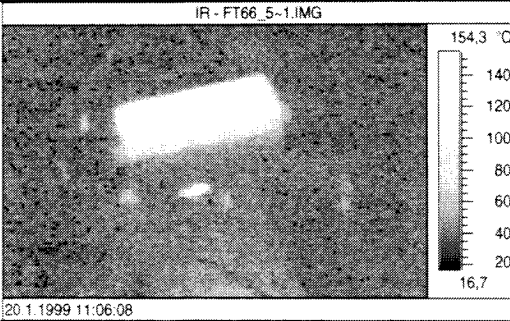
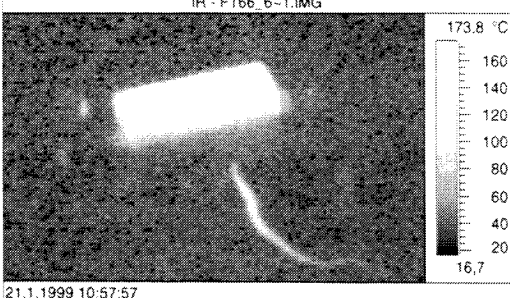
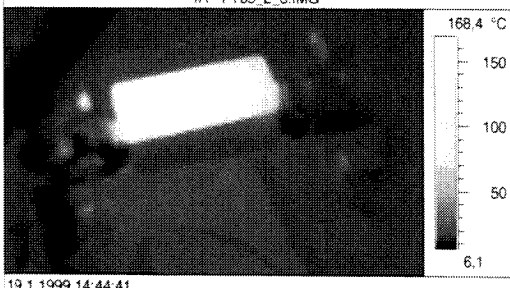
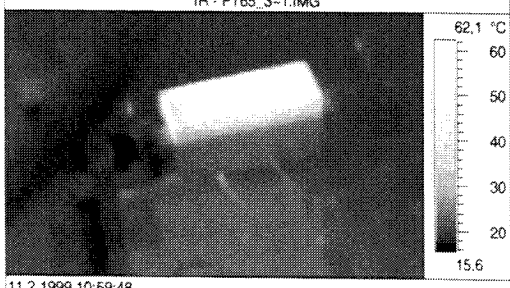


Figure 6.26 - PW mock-up with Ti interlayer (Id. no. FT66/4) after screening test at  $1.88 \text{ MW/m}^2$ . a) mock-up;  
b) Be tile; c) DS-Cu heat sink.

Table 6.7 - Test condition and results of screening test on HIPB PW small scale mock-ups.  
Water cooling parameters: P=40 bars, T=20 °C, Φ=60 l/min.

Interlayer	Id. no.	IR Image	H.F. [MW/m <sup>2</sup> ]	Result
Ti	FT66/4	-	1.88	tile detached
Ti	FT66/5*		2.5	no damage
Ti	FT66/6		2.5	no damage
Al	FT65/2		0.75	increase of surface temperature
Al	FT65/3*		1	no damage

\*Sample selected for neutron experiment PARIDE 4 (200 °C, 1 dpa)

### 6.3.5 Numerical simulation of thermal fatigue experiments

Steady state and transient thermal analyses of PW small scale mock-ups have been carried out. The aim of the analyses was to establish the loading conditions during the post-irradiation thermal fatigue tests. By the steady state analysis the maximum applicable heat flux during the test, for maintaining the temperatures of Be surface below the allowable value (800°C) in the JUDITH facility, has been determined. By the transient analysis the load histogram to be applied during the thermal fatigue tests has been established. The analyses have been carried out with the Ansys code [258]. The design and the geometrical dimensions of the modelled mock-ups are shown in Figure 6.27.

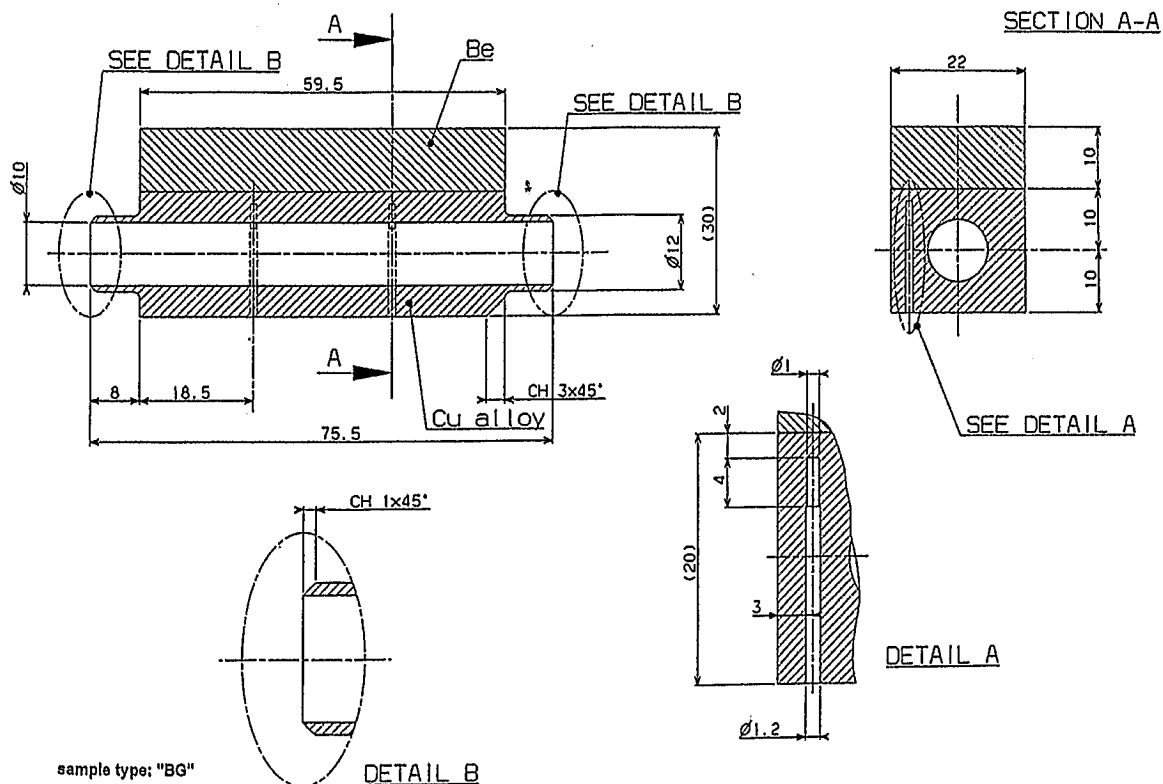


Figure 6.27 - Drawing of PW HIPed Be/Cu mock-ups.

#### 6.3.5.1 Analysis model

A 2D FE model has been used. Taking advantage of the symmetry only half mock-up has been modelled. In Figure 6.28 the adopted FE model is shown. Parabolic plane elements (8 nodes) have been adopted. The interlayer has been not modelled.

The material properties are taken from the ITER MPH [243]. Temperature dependent material properties have been used (cf. Chapter 2).

#### 6.3.5.2 Thermal load and input data

The surface heat flux applied to the Be surface was  $4.6 \text{ MW/m}^2$ . A heat transfer coefficient dependent from the wetted wall temperature has been used in the cooling channel. The heat transfer coefficient vs. wall temperature was computed by means of the EUPITER code [244]. The water coolant parameter, input in the EUPITER code, were:  $v = 5 \text{ m/s}$  ( $\sim 24 \text{ l/min}$ ),  $P = 4 \text{ MPa}$  and  $T = 20^\circ\text{C}$ . The coolant temperature for the convection has been assumed  $20^\circ\text{C}$  constant. All other surfaces were assumed to be adiabatic.

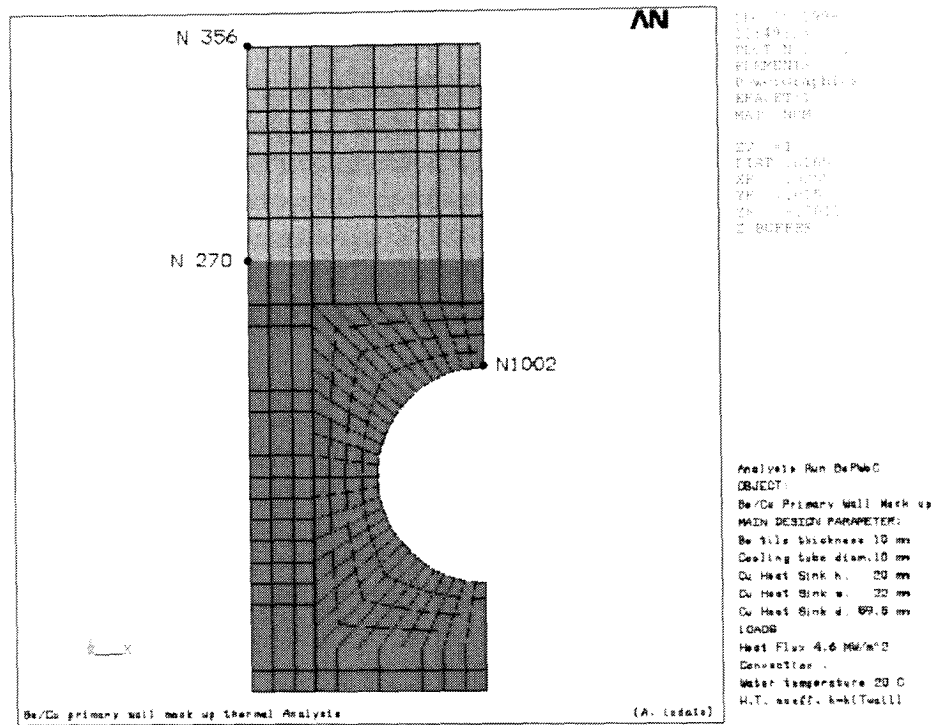


Figure 6.28 - FE analysis model of PW HIPed Be/Cu mock-ups.

### 6.3.5.3 Results

Figure 6.29 shows the steady state temperature distribution. The maximum Be temperature is 753°C. It should be noted that this result is conservative if the area covered by the EB (ref. Paragraph 7.1.3) is smaller then the total sample surface. Figure 6.30 shows the transient temperature behaviour of some selected points of the model. It can see that the steady state condition have reached after 30 s of heating. The start-up time used in the simulation was 0.5 s.

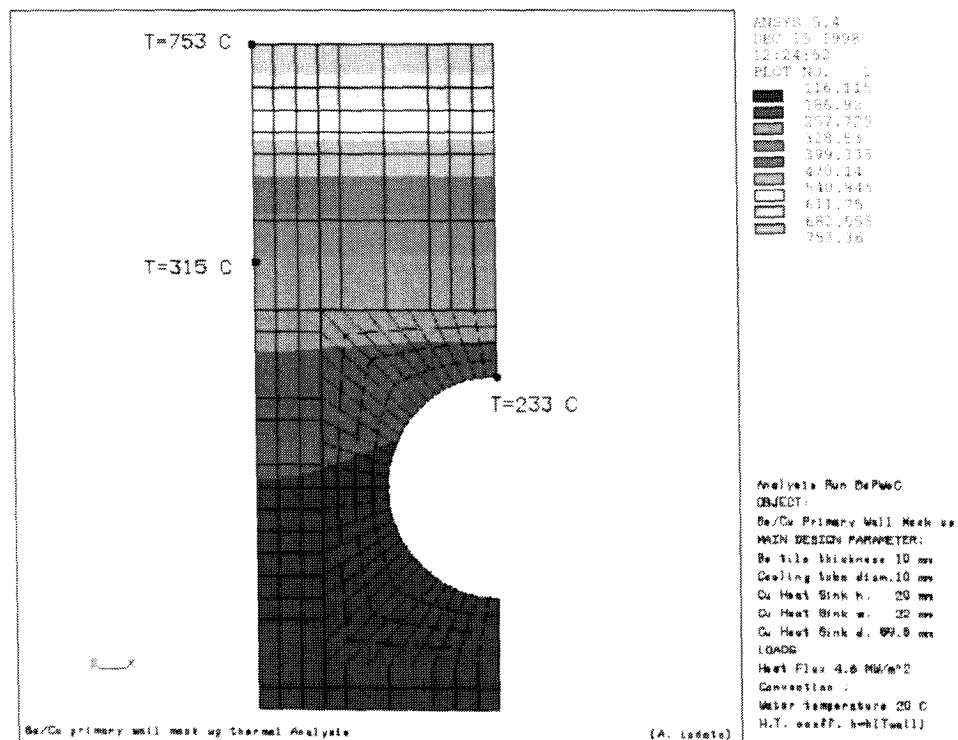


Figure 6.29 - Steady state temperature distribution in PW HIPed Be/Cu mock-ups with 4.6 MW/m<sup>2</sup> incident heat flux.



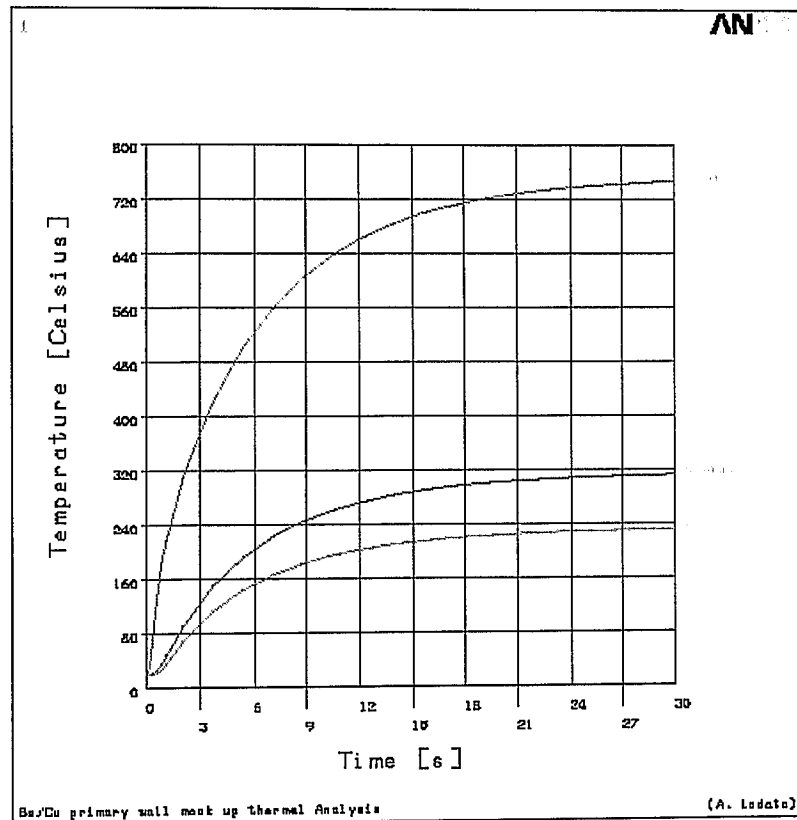


Figure 6.30 - Temperature vs time at selected point (see Figure 6.28). Applied heat flux:  $4.6 \text{ MW/m}^2$ .

## 6.4 Conclusions

The heat removal efficiency and the thermal fatigue behaviour of both 8 mm and 3 mm Be tile mock-ups with CuMnSnCe braze and InCuSil braze before and after neutron irradiation have been compared. The experimental results show that the heat removal efficiency is slightly worse after the neutron damage. Thermal cycling experiments have been performed up to 1000 cycles on the 8 mm Be tile mock-ups and up to 100 cycles on the 3 mm Be tile mock-ups. Absorbed power density were:  $8 \text{ MW/m}^2$  on the 8 mm Be tile mock-ups with CuMnSnCe braze,  $7.5 \text{ MW/m}^2$  on the 8 mm Be tile mock-up with InCuSil braze and  $9 \text{ MW/m}^2$  on the 3 mm Be tile mock-up with InCuSil braze. No significant temperature increase of the surface was observed during the test and no indication of failure was visible. Post-mortem metallography of the braze layer has shown no abnormalities compared to the un-irradiated samples. The irradiation temperature ( $320^\circ\text{C}$ ) and the dose ( $0.3 \text{ dpa}$ ) in this experiment are not fully representative of the operating conditions of the first wall and baffle. At lower temperatures and higher doses ( $150\text{-}230^\circ\text{C}$ ,  $1\text{-}2 \text{ dpa}$ ), embrittlement of Be and radiation hardening of Cu alloys could change the positive picture that comes out from these results. Nevertheless, the experiment demonstrates that there is a range of temperature and dose where neutron irradiation has no negative effects on Be/Cu joints. Further irradiation experiments with more relevant fluence and temperature are planned in the irradiation program Paride 3 and 4 [233].

In addition to the thermal fatigue test, the quality of the Be-copper joints was characterized by means of mechanical methods. Shear tests on un-irradiated and irradiated samples have been performed. For the InCuSil braze no influence of the neutron irradiation has been observed. The mean value of the post irradiation shear strength for the CuMnSnCe braze was

approximately 25% lower compared to the pre-irradiation data. But with respect to the low sample numbers and the large scatter band, this difference is not considered to be significant.

In the frame of the second neutron irradiation campaign PARIDE 4 (200 °C, 1 dpa) pre-irradiation characterisation tests on PW small scale mock-ups have been carried out. The macroscopic soundness of the HIP joints with Ti and Al interlayers has been checked before irradiation. Steady state loads up to 2.5 MW/m<sup>2</sup> have been applied. The Be tile of one sample with Ti interlayer detached at 1.88 MW/m<sup>2</sup>. One sample with Al interlayer showed an increase of the Be surface temperature at 0.75 MW/m<sup>2</sup>. As consequence the second available sample has been tested at 1 MW/m<sup>2</sup>. Experimental and analytical results are in good agreement.

## 7 PORT LIMITER ANALYSES

### 7.1 Introduction

The limiter is a reactor PFC subjected to HHF during the start-up and shut down phases, when the plasma is leaning on its surface (limiter regime), and subjected to normal first wall thermal loads during the burn out phase (divertor regime). A local adjustable limiter design, located at the equatorial ports is the reference solution for the ITER reactor (cf. Chapter 1). In order to minimise the electromagnetic loads and the thermal stresses, a modular structure of SS plates welded together in their rear is used. With this design it will be easier the maintenance (remote handling, repair, substitution), the alignment of the limiter FW (by adjustment and/or shimming from the port) and it will be possible to avoid frontal gaps and penetrations because with the rear access there are not more necessary.

Thermal stresses and strains play a dominant role in the behaviour and the performances of the limiter, and in particular of its FW due to the complex heating cycle, material and geometrical discontinuities, and the presence of manufacturing residual stresses. The reference limiter module (as the primary FW) has been in fact designed in such a way that stresses due to primary loads, such as coolant pressure or electromagnetic effects during plasma disruption, are minimised and can be considered negligible in the FW region.

However due to the high heat flux during the limiter regime, it has not been possible (as in the primary FW case) to assure that stresses in elastic analyses are limited to  $3 S_m$  (at least for the parts of the component where the non ratcheting criterion is applicable). As a consequence it cannot be assumed that the plastic collapse will not be the dominant failure mode and that ratcheting should not occur. Therefore, after performing parametric elastic analyses to design the component, assess its main performances and optimise the coolant lay-out, transient elasto-plastic thermo-mechanical analyses have been carried out to verify the adequacy of the limiter to withstand its thermal loads.

The evaluation of the resulting stresses at the Be/Cu interface remains particularly difficult, because of the presence of geometrical/material discontinuities and of the residual stresses. For this reason:

- the stresses at the node where a singularity is present have been ignored
- in most of the analyses the stress free temperature has been set to room temperature.

With the understanding that the final verification of the joints is being performed by experiments. The prediction of the residual stresses (dependent from the manufacturing process which is extremely difficult to model) is in any case outside the scope of the present analyses. The residual stresses will anyway affect the stress pattern, particularly at the joints so that total stresses can in principle be smaller at working temperature than those without residual stresses. The residual stresses could nevertheless partially be annealed during the thermal cycles.

The design description of the Port Limiter is in [259]. Previous analyses and design are in [260]. An overall description is in [261] and all general design requirement are in [262].

The ANSYS code version 5.3 has been used for all the finite element method analyses.

## 7.2 Analysis model

In order to follow the mutual interactions between the FW and the shield block during the complex limiter heating cycles, a mid plane FW/shield plate cross-section has been modelled for the thermal-mechanical analyses. The model cross-section is shown in Figure 7.1.

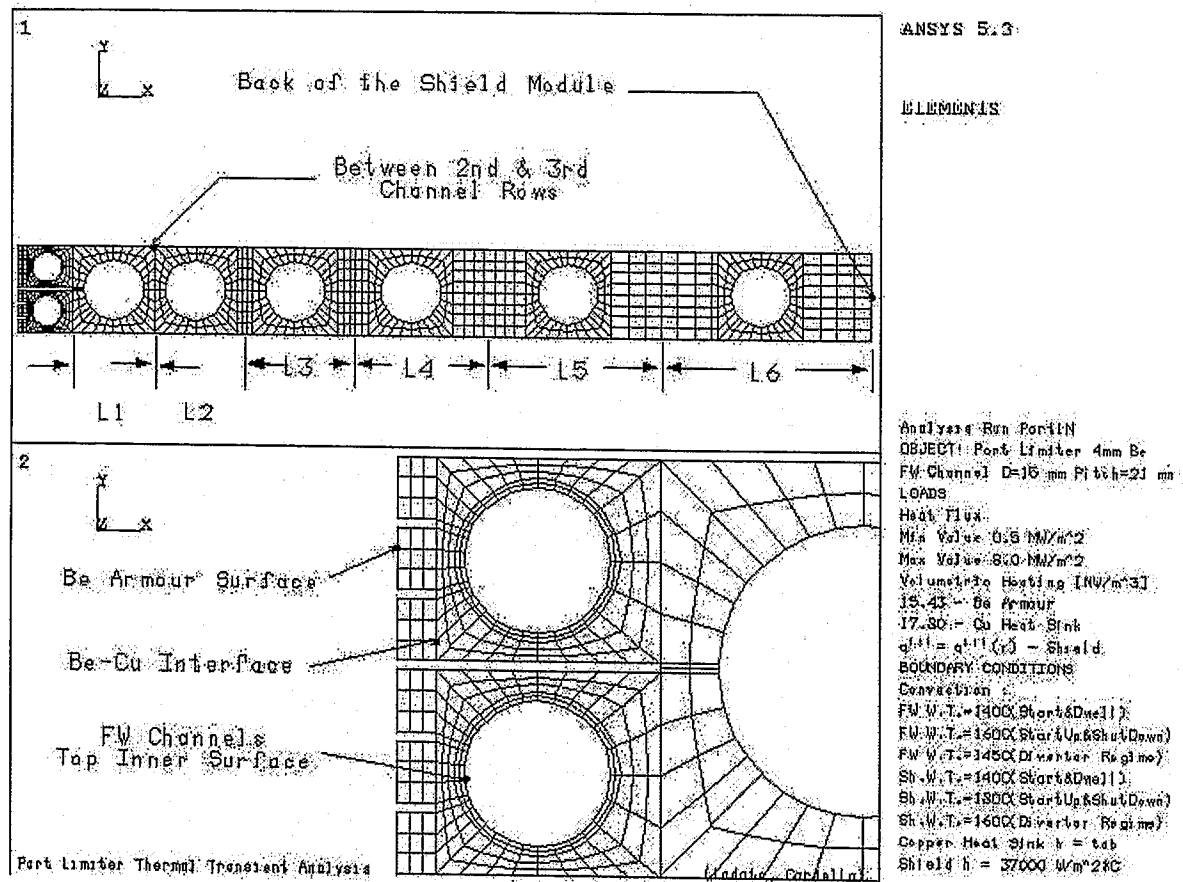


Figure 7.1 - Thermal-mechanical Analysis Model

The material properties are taken from the ITER Material Properties Handbook [263]; the most used are given in chapter 2. In all the thermal analyses material dependent properties have been used. Irradiation effects on the material properties have instead not been considered.

## 7.3 Steady state analyses with elastic material behaviour

In order to size the limiter and to define and optimise the channel lay-out, parametric steady state thermal-mechanical analyses have been performed. The cooling channels have been sized on the basis of thermal-hydraulic considerations. The overall FW dimensions have been instead defined with simple thermal evaluations based on the maximum temperature limits for each material. The channel lay-out has been at first grossly defined on the base of previous analyses and then optimised by varying the coolant pitch in radial direction. In the following only the final cases are reported.

### 7.3.1 Thermal loads and input data

Two main working regimes are identified for the limiter:

- the start-up and shut down [264], characterised by a high heat flux ( $8 \text{ MW/m}^2$  applied to the armour exposed surface) and no volumetric heating and
- the burn, characterised by a moderate heat flux ( $0.5 \text{ MW/m}^2$ ) and volumetric heating which decreases radially outwards (see below)

The volumetric heating can be considered constant in the armour and the Cu alloy part. In the SS shield plate region the heating has been decreased radially interpolating with linear and exponential functions. The values in Table 7.1 have been used.

A heat transfer coefficient dependent from the wetted wall temperature has been used in the cooling channels. The following correlations have been adopted for the heat transfer coefficient:

Single phase	Dittus Boelter
Onset nucleate boiling	Bergles Rosenhow
Fully developed nucleated boiling	Thom

A constant heat transfer coefficient of  $37000 \text{ W/m}^2\text{°C}$  has been used in the shield cooling channels.

Different bulk coolant temperatures were set in the FW and in the SS plate channels during the different operations, as shows in Table 7.2. All other surfaces were assumed to be adiabatic.

Table 7.1 - Port Limiter Estimated Volumetric Heating

Material	Radial location r [m]	Power density [ $\text{MW/m}^3$ ]
Be armour		15.432
Cu in FW		17.808
SS shield	$0 < r < 0.048$	$-93.24 r + 13.44$
SS shield	$0.048 < r < 0.088$	$-72.60 r + 12.44$
SS shield	$0.088 < r < 0.138$	$-39.12 r + 9.503$
SS shield	$0.138 < r < 0.188$	$-43.92 r + 10.16$
SS shield	$0.188 < r < 0.473$	$13.44\exp(-10.416 r)$

r = 0 is taken at the interface between the copper and the shield.

Table 7.2 - Port Limiter Coolant Temperature

	Operation	Start	Start Up	Divertor	Shut Down	Dwell
Location						
F.W.		140	160	145	160	140
Shield		140	180	160	180	140

The boundary conditions for the structural analyses allows a free thermal expansion of the entire component. Two Be armour thicknesses have been analysed, namely 4 and 5 mm.

### 7.3.2 Results

The main resulting data are summarised in Table 7.3 and 1.4. In Figure 7.2 and 1.3 is shown the temperature distribution respectively for the limiter and divertor regime. In Figure 7.2 only the FW region is shown because during the limiter regime the shield is at almost uniform temperature. In Figure 7.4 is shown the Von Mises stress distribution for the divertor regime. The following main considerations can be made:

- The maximum Be temperature with 5 mm tile thickness exceeds the allowable temperature (750°C) in limiter regime. Therefore the more detailed verification analysis is performed only for 4 mm tile thickness.
- The temperature in the armour varies only radially (1D distribution).
- Stresses in the Cu alloy and the SS plates during divertor regime are much below the allowable value and a large margin is left for primary loads.
- The stresses during the limiter regime are negligible in the SS plates but largely exceed the elastic limits in the Be/Cu joint for all the analysed cases; they are not reported (refer to the following elasto-plastic analyses).
- It can be seen from Figure 7.3 and 7.4 that a relatively balanced temperature distribution between the different cooling regions in the SS plates has been achieved, thus minimising the thermal stresses. A reduction of the stresses is also achieved by overcooling the plates (this also reduces the thermal time constant of the massive SS parts, thus decreasing the transient temperature gradients of the component).
- An allowable stress intensity for Be value has not been included in the table. Criteria for beryllium have not been specified yet. The use of the 3  $S_m$  rule may not be appropriate for this material.

Additional steady state thermal analyses have also been performed considering 10 MW/m<sup>2</sup> heat flux during limiter regime. In this case the Be temperature largely exceeds the allowable temperature (854°C already with 4 mm thick Be tiles) and therefore the analyses results will not be reported.

Table 7.3 - Thermal results comparison between Port limiter with 4 and 5 mm Be armour thickness.

Load Conditions	Location		T. range [°C]	T. range [°C]
			Be th. 4 mm	Be th. 5 mm
Limiter Regime	First Wall	Be tile	362 - 704	362 - 793
		Cu heat sink	159 - 398	159 - 398
	Shield	SS block	153 - 166	153 - 165
Divertor Regime	First Wall	Be tile	170 - 186	170 - 190
		Cu heat sink	155 - 172	155 - 172
	Shield	SS block	158 - 218	158 - 218

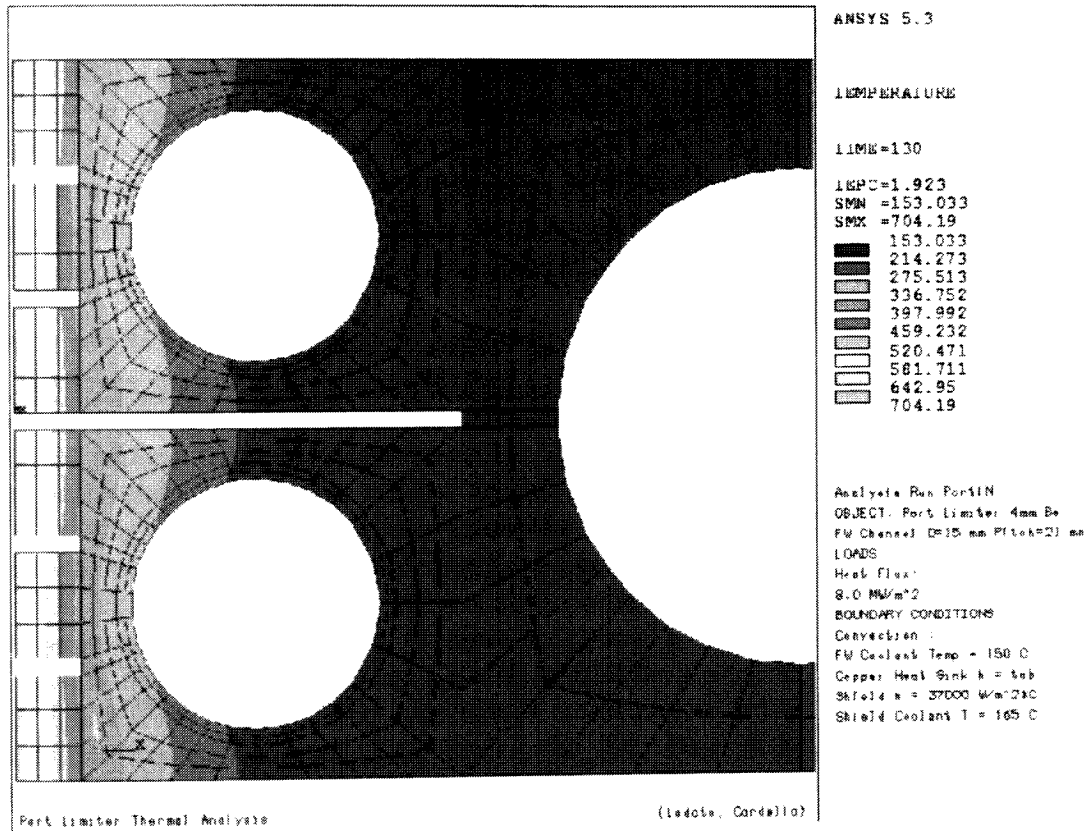


Figure 7.2 - Steady State Temperature Distribution - Limiter Operation

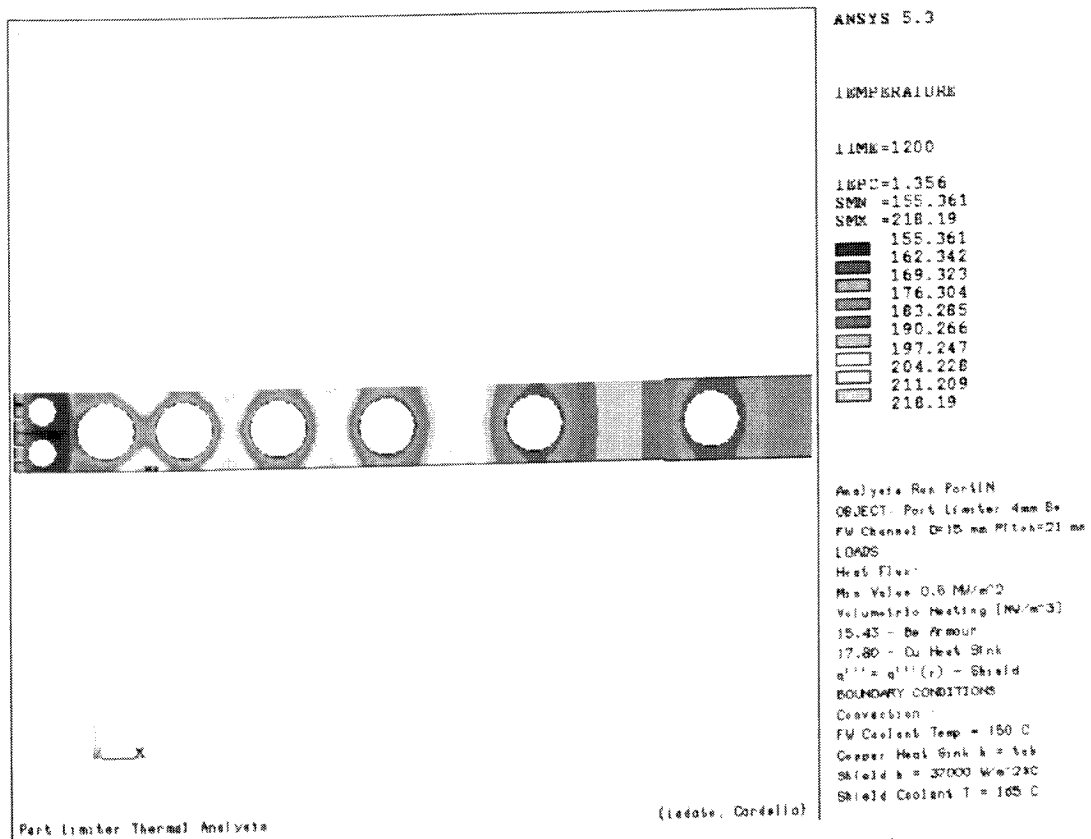


Figure 7.3 - Steady State Temperature Distribution - Divertor Operation

Table 7.4 - Maximum Von Mises stresses in divertor operation.

Location		Max. $\sigma_{VM}$ [MPa] Be th. 4 mm	Max. $\sigma_{VM}$ [MPa] Be th. 5 mm	Allow. S.I. [MPa]
First Wall	Be tile	389 (Cu interface)	375 (Cu interface)	-
	Cu heat sink	93 (Be interface)	92 (Be interface)	660
Shield	SS block	109 (Cu interface & shield tubes)	114 (Cu interface & shield tubes)	510

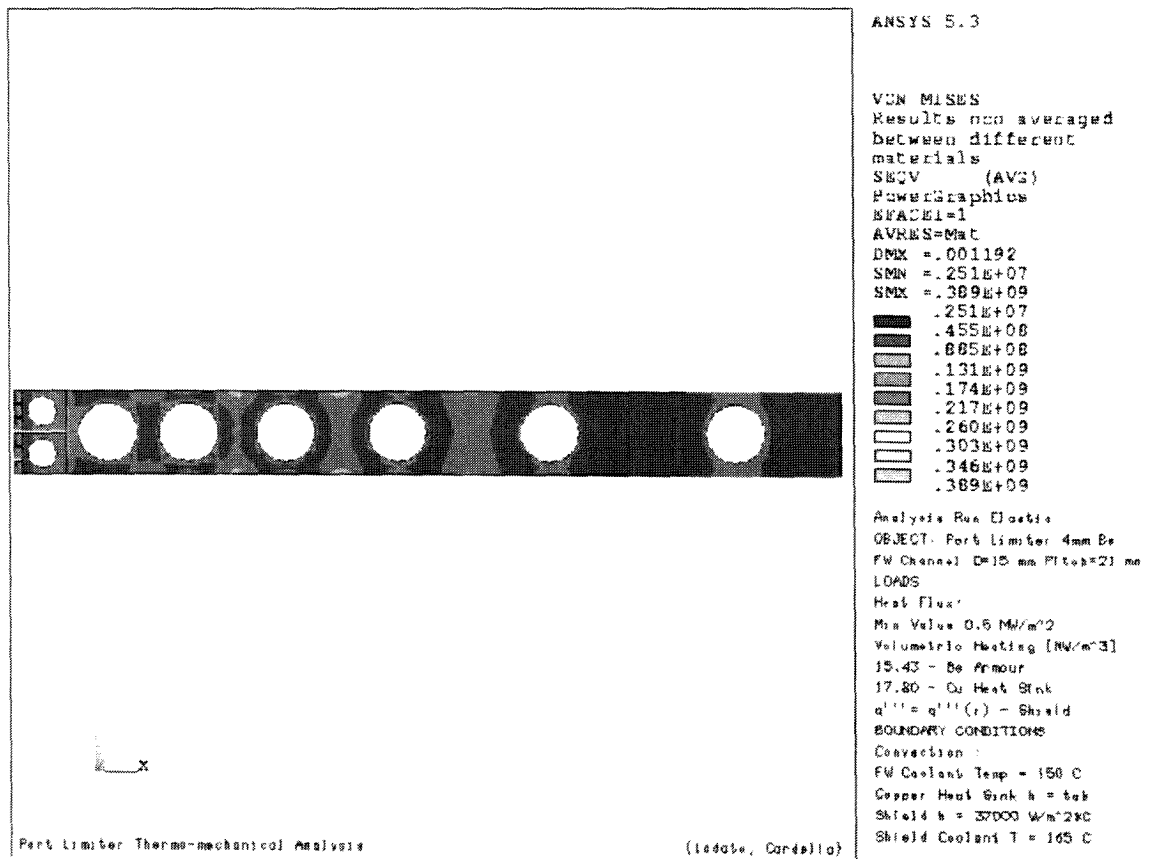


Figure 7.4 - Steady State Von Mises Distribution - Divertor Operation



## 7.4 Transient analysis with elasto-plastic material behaviour

After selecting the final geometry, a final transient elasto-plastic analysis has been carried out. Most of the limiter structure can already be considered as verified by the static elastic analyses. The equivalent stresses are far below the limits for primary and secondary stresses. However in the Be/Cu regions thermal stresses reach the material yield stress already when the component is brought at the initial stand-by operating temperature namely 140°C; thermal stresses at the Be/DS Cu junction are already about 200 MPa (ignoring the discontinuity nodes).

Because of the complex interactions between the first wall and the SS part with their different time constants during the particular limiter thermal cycle, a simplification of the FEM model focusing on the FW would not assure that the solution is appropriate. Therefore it has been decided to perform the inelastic analyses on the entire model.

After performing the transient thermal analysis to evaluate the temperature distribution in the limiter during one thermal cycle, preliminary inelastic analyses have been performed to evaluate the behaviour of the component at the different time steps.

The final full elasto-plastic analysis has been performed using a kinematic hardening model. Five cycles have been analysed. In order to somewhat reduce computer time, memory and disk space, the thermal cycle has been decreased to a total of 1700 seconds, reducing the dwell time of 500 seconds. This reduction is based on the results of the preliminary analyses which show that at the restart of the next cycles the values of the residual stresses and strains have reached a steady state.

### 7.4.1 Thermal loads and input data

Engineering heat load specifications enveloping all practical physics cases have been generated. The resulting load histogram is shown in Figure 7.5 and in Table 7.5. The heat flux reaches 8 MW/m<sup>2</sup>, its maximum value, during the start-up and shut down period. The radial distribution of the volumetric heating is as in the steady state analyses. Its time variation from zero to its maximum value is shown in the same figure and table.

Table 7.5 - Limiter Engineering Load Histogram

Time [s]	H.F. [MW/m2]	V.H. %
0	0.02	0
80	8	0
130	8	0
150	0.5	0
200	0.5	100
1200	0.5	100
1300	0.5	0
1320	8	0
1370	8	0
1500	0	0

All other input data and boundary conditions are the same as in the steady state analyses. Ad hoc time and load steps have been chosen to assure a good convergence and approximation.

### 7.4.2 Results

Figure 7.6 shows the transient temperature behaviour of some selected points of the model. It can be seen by comparison with the load histogram of Figure 7.5 that in the first wall follows the heat flux variation with a time constant of few seconds, The shield part is not influenced

by the heat flux and follows the volumetric cycle with a larger delay. Its longer time constant in the rear shield part is about 400 seconds.

Table 7.6 lists the maximum and minimum temperature values at selected times and locations in the structure.

The maximum deformation values of the shield continuous (welded) part are reported in Table 7.7 (see also sketch of Figure 7.7). The displacement are relative to the limiter centre.

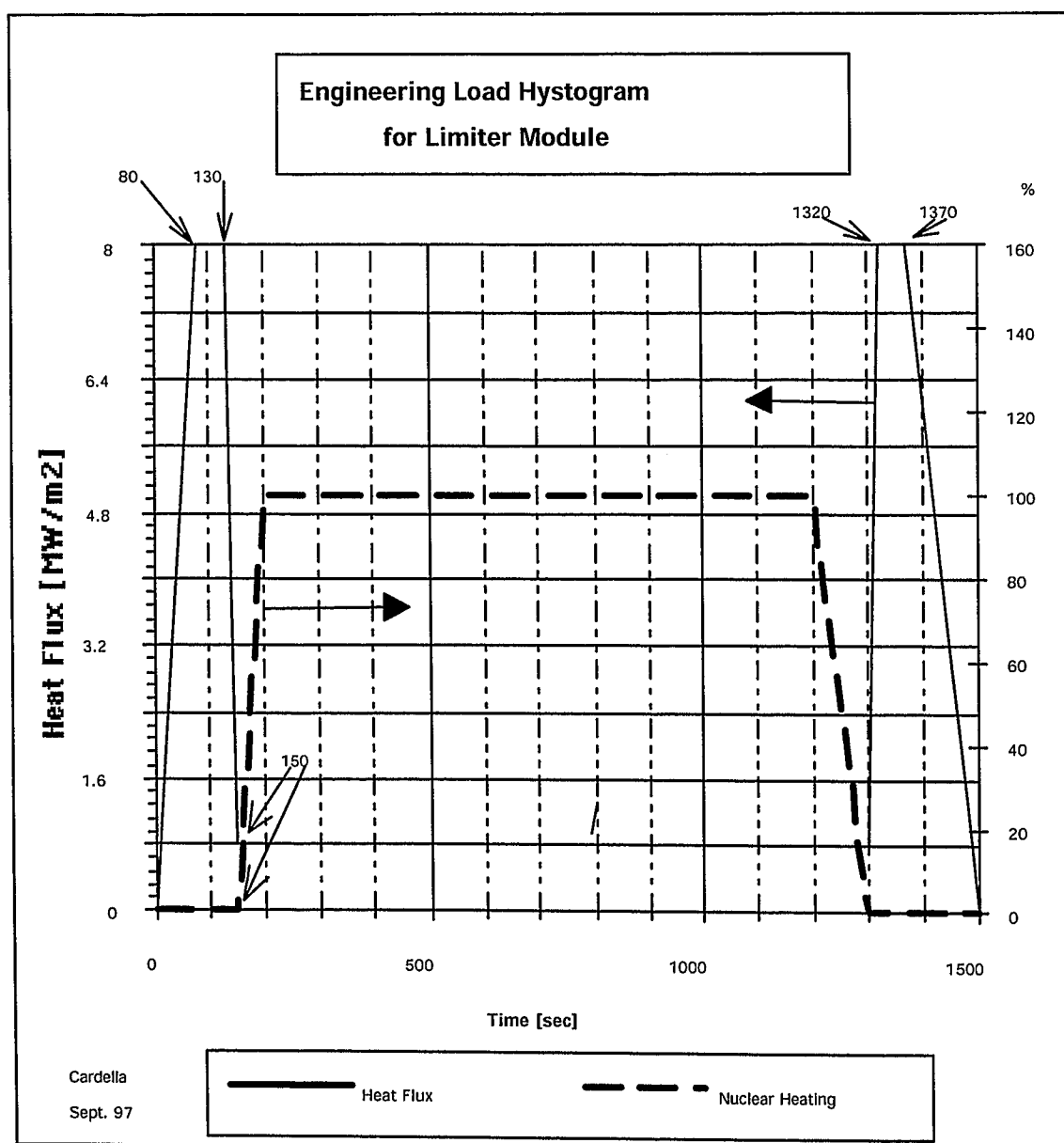


Figure 7.5 - Limiter Engineering Load Histogram

Figure 7.8 and 1.9 show the radial displacement at different times during one operating cycle at external toroidal position (curve b in Figure 7.7) and external poloidal position (curve a in Figure 7.7) respectively. The rear plate deforms (bowing) both in poloidal and toroidal direction with similar radius of curvature.

Table 7.6 - Temperature values at selected times and locations in the structure

Zone	Temperature [°C]									
	Time [s]	80	130	150	700	1300	1320	1370	1500	1700
Be	max	704.4	710.6	194.1	180.5	174.3	689.5	710.6	143.0	140.0
	min	364.5	366.2	173.5	164.5	159.8	359.6	366.2	142.1	140.0
Cu H. S.	max	400.4	403.2	176.8	166.8	161.3	392.7	403.2	142.4	140.0
	min	168.4	168.8	148.3	150.4	146.2	167.3	168.8	140.4	140.0
Shield L1	max	179.5	403.2	176.8	166.8	161.3	392.7	403.2	142.4	140.0
	min	169.7	168.8	148.3	150.4	146.2	167.3	168.8	140.4	140.0
Shield L2	max	179.5	180.0	176.2	213.4	160.6	179.2	180.0	149.5	140.0
	min	165.1	178.3	160.8	162.4	160.0	163.3	177.9	140.3	140.0
Shield L3	max	179.4	180.0	176.2	210.3	162.6	179.1	180.0	153.3	140.0
	min	160.1	175.2	160.9	161.7	160.0	163.2	175.6	140.4	140.0
Shield L4	max	179.4	179.9	175.6	207.1	173.2	179.1	179.9	163.2	142.1
	min	149.1	162.4	160.8	161.1	160.0	163.2	173.3	140.4	140.0
Shield L5	max	179.3	179.9	169.4	202.8	174.4	179.1	180.0	168.2	147.0
	min	144.2	153.3	156.8	160.5	160.1	168.3	172.4	140.4	140.0
Shield L6	max	179.3	179.8	168.3	186.9	173.9	179.0	179.9	168.9	151.3
	min	142.0	148.1	151.0	160.2	160.1	166.0	169.2	140.5	140.1

Note: Shield zones specified in Figure 1

Table 7.7 - Maximum Deformations [mm] of a limiter plate (reference temperature 20 °C)

Radial Positive at Limiter Corners	2.1
Radial Negative at Limiter Corners	3
Toroidal	1.6
Poloidal	3

note: Displacement relative to limiter centre

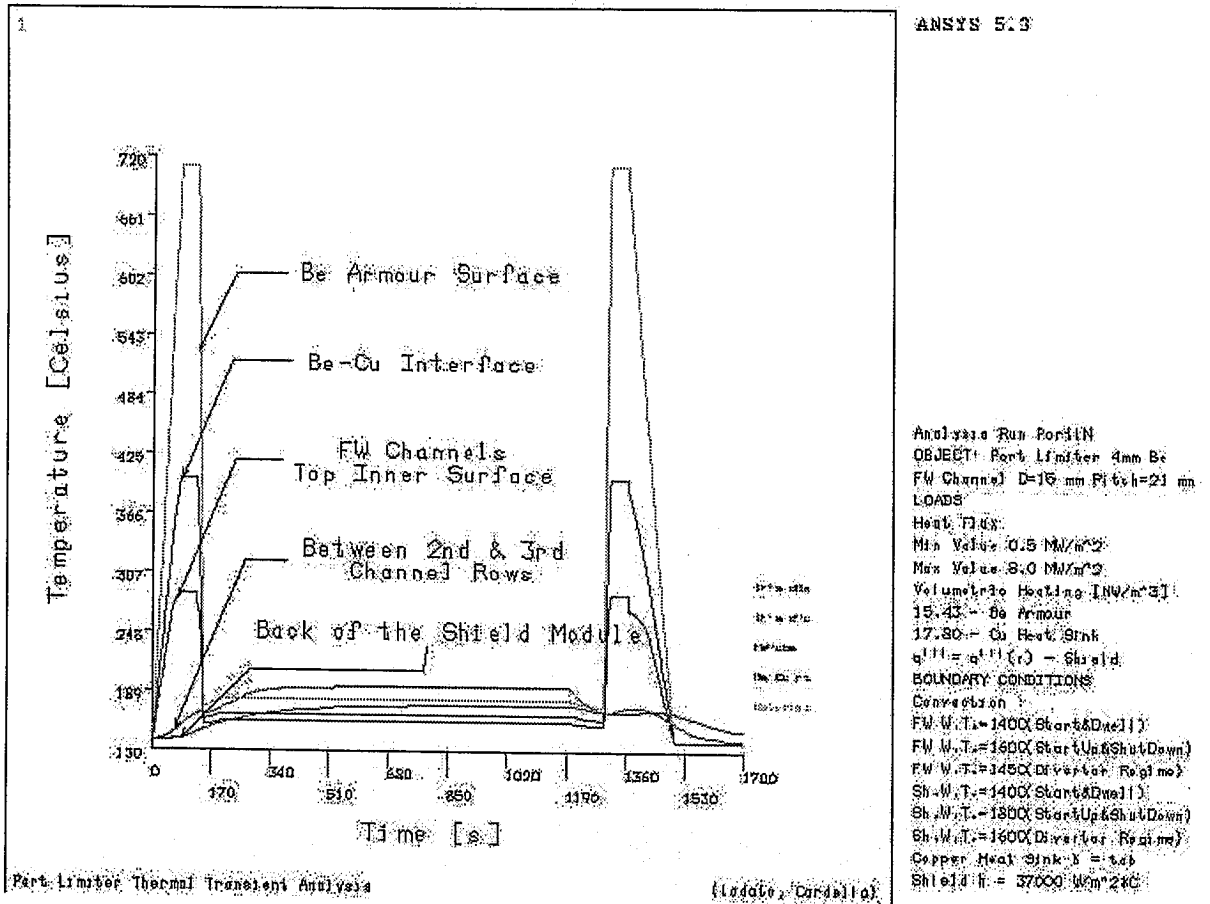


Figure 7.6 - Temperature versus time at selected points

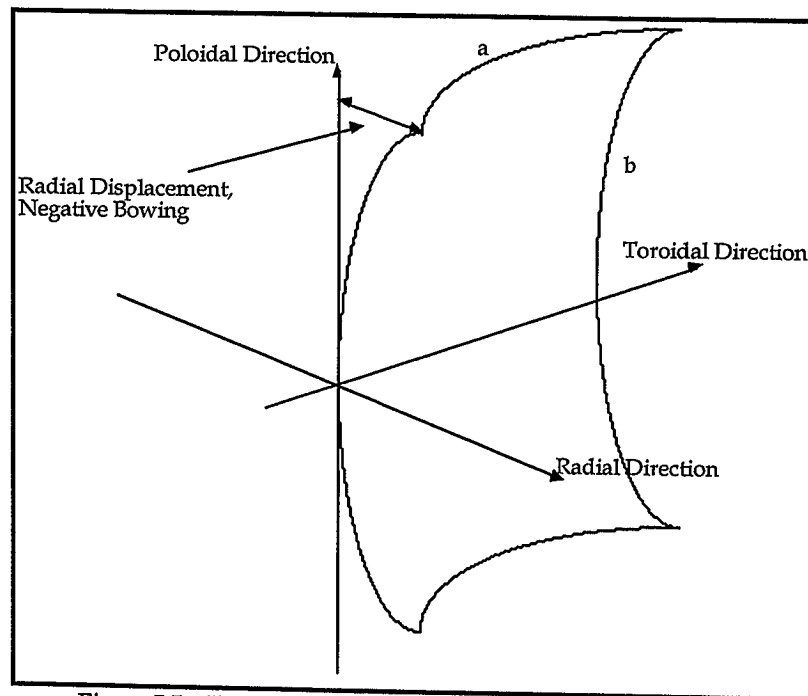


Figure 7.7 - Sketch of a typical limiter deformation (half a plate)

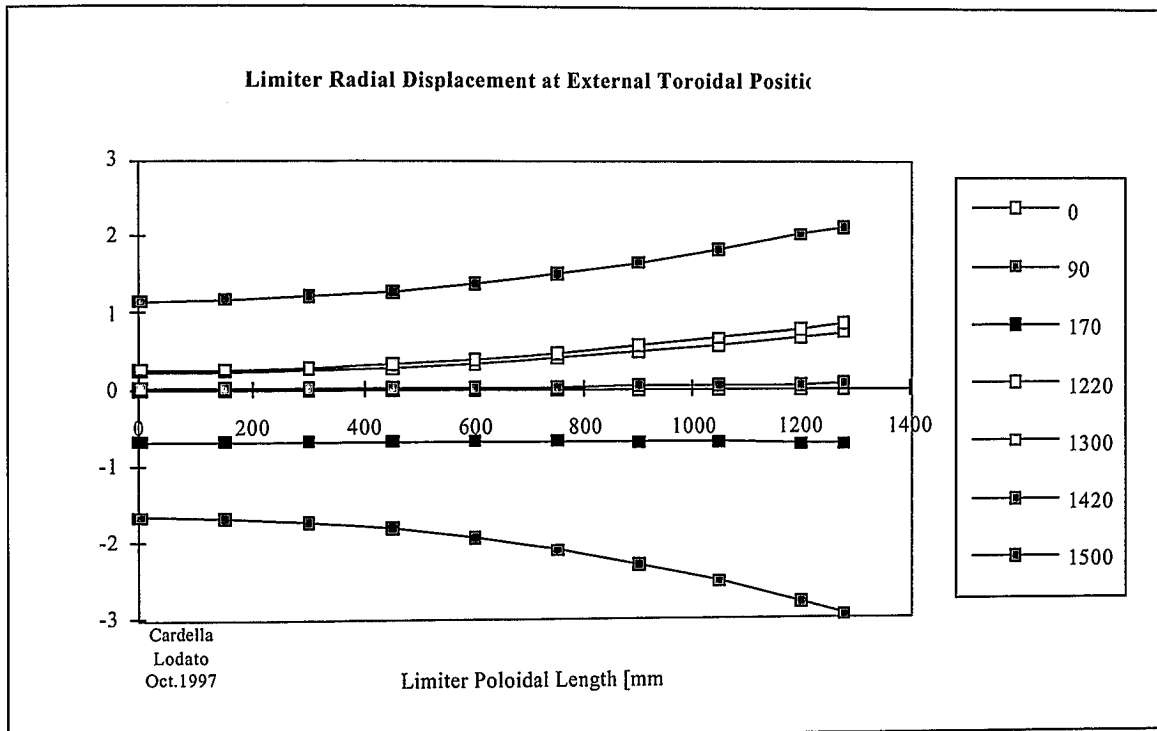


Figure 7.8 - Radial Displacement vs Poloidal Position during one operating cycle

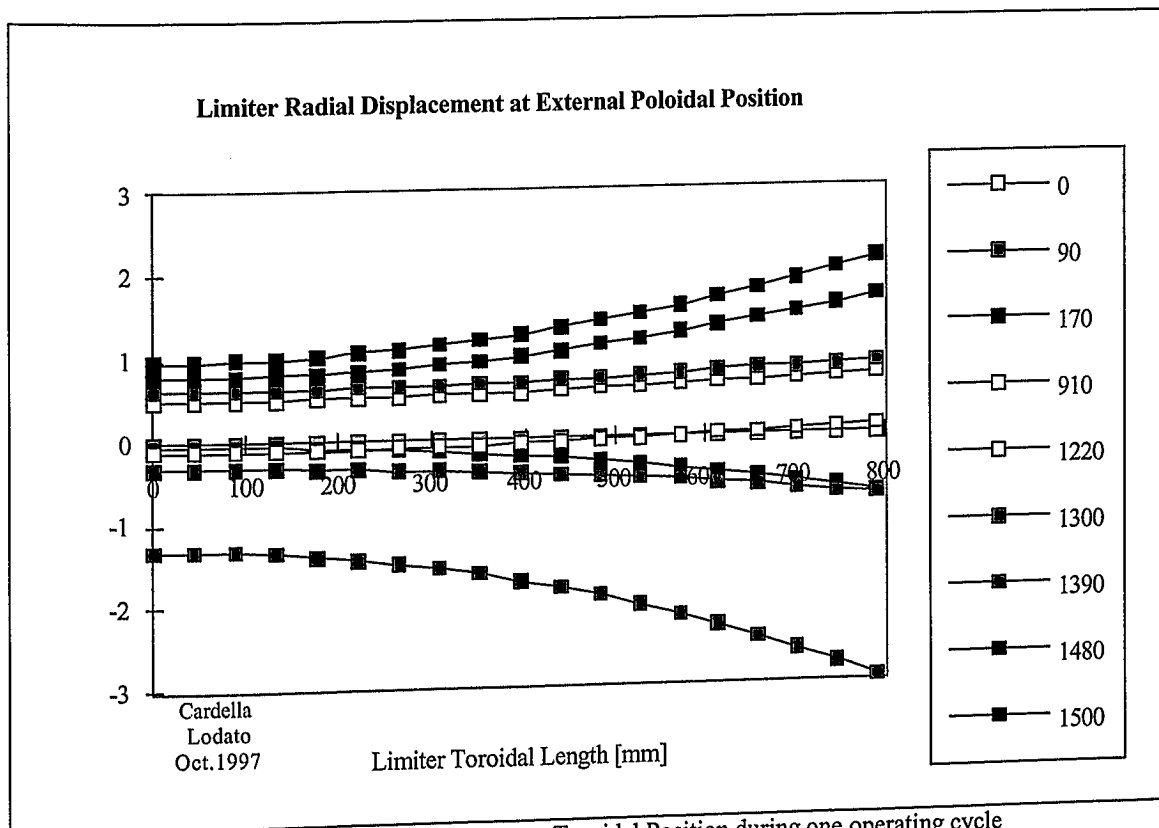


Figure 7.9 - Radial Displacement vs Toroidal Position during one operating cycle

In Figure 7.10 and 7.11 is shown the transient behaviour of the equivalent plastic strain and of the total strain. It can be observed that:

- the maximum plastic strain values are not excessive during the first five cycles. The plastic strains have already reached a stable behaviour at the end of the fifth (third for the Be) cycle so that ratcheting is not expected to be problematic and the plastic behaviour should be accommodated.
- Maximum plastic strains are present in the DS Cu layer near the joint with Be.
- Both in Be and in Cu the strain range is slightly decreasing every cycle.
- The increment in the plastic strain during the divertor regime decreases after the first cycle.
- Reversal of the elastic strain is occurring during divertor regime increasing the total strain range between the limiter and the divertor regimes.
- As expected the SS shield plate remains all the time in the elastic region as shown in both figures.

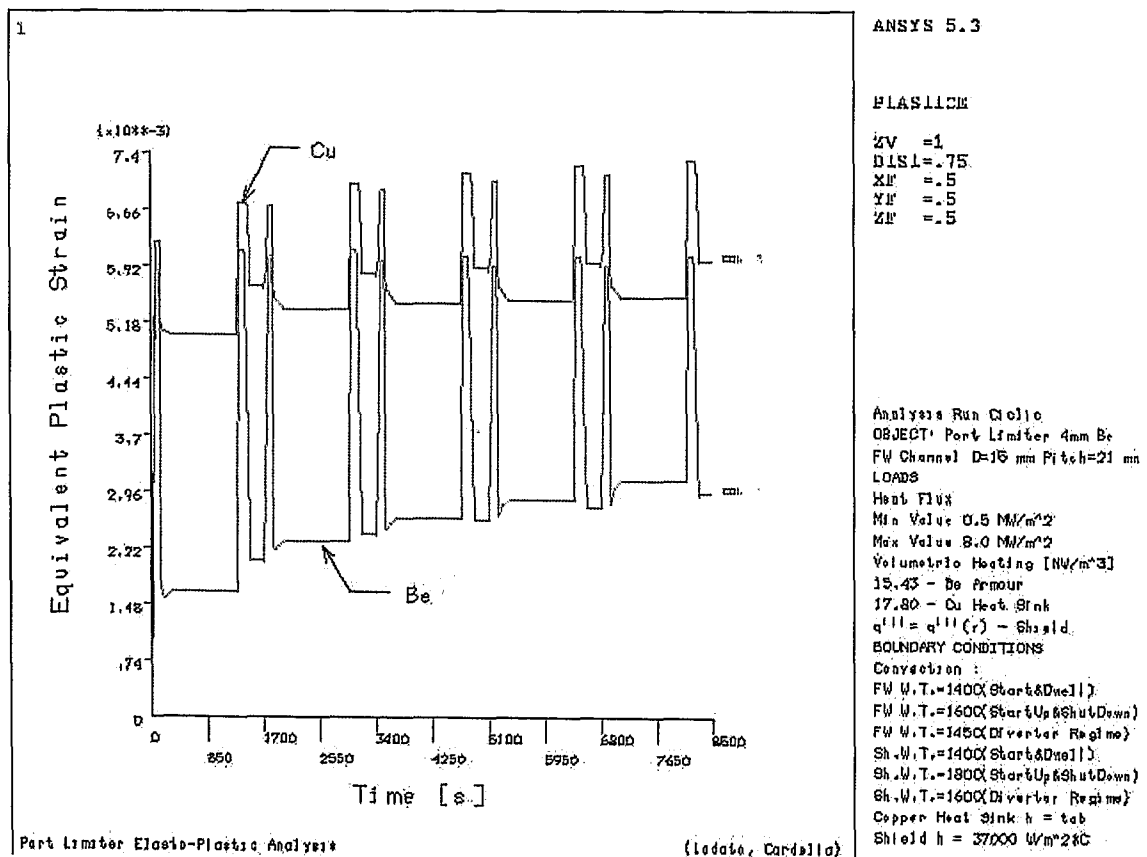


Figure 7.10 - Plastic equivalent strain in Be, Cu and SS regions during 5 cycles.

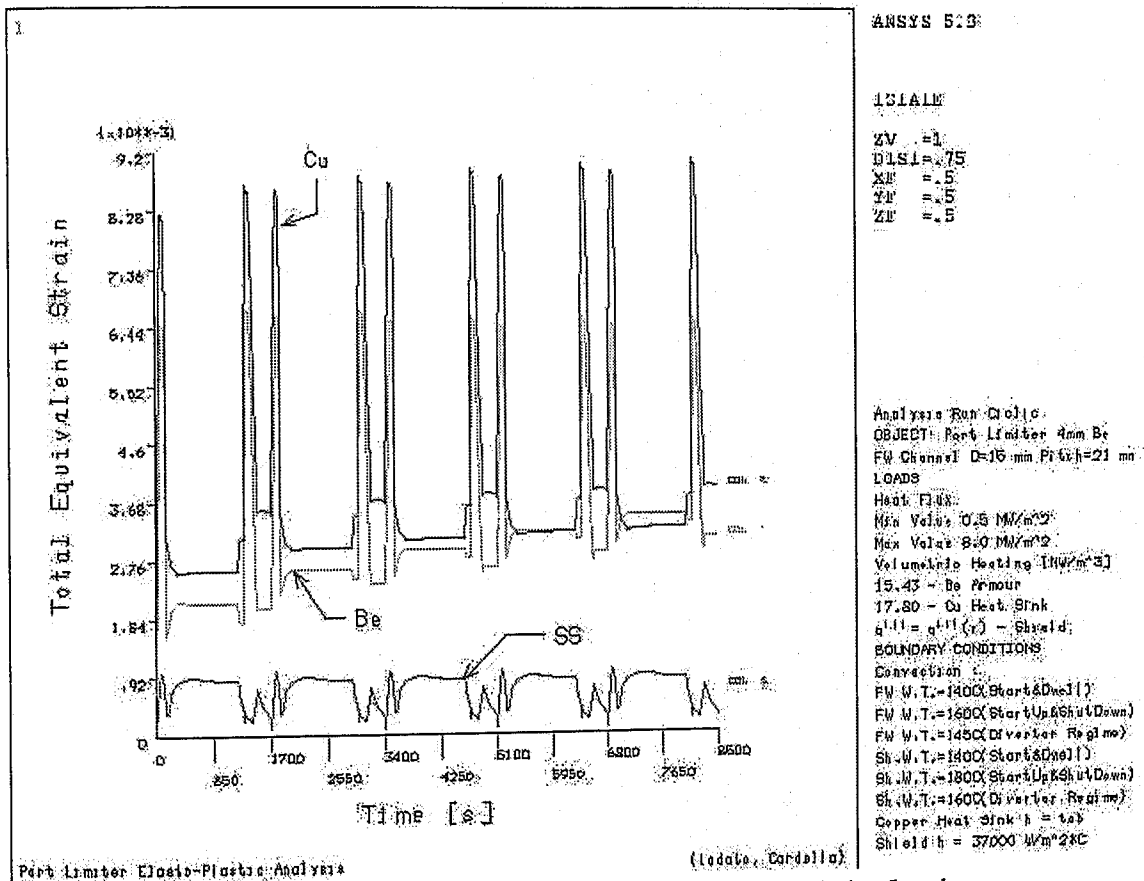


Figure 7.11 - Equivalent total strain in Be, Cu and SS region during 5 cycles.

### 7.4.3 Lifetime estimation

Stresses are within allowable values and the non-ratcheting criterion is satisfied (below 3  $S_m$ ) in most of the limiter structure, except at the beryllium/copper joint where plastic deformations occur locally. According to the inelastic analysis a stable cycling plasticity will occur. However the analyses do not take into account any hardening so that the resulting plastic strain range is conservative (hardening could eventually lead to shakedown). The equivalent maximum elastic stress range, computed in previous elastic analyses, would be at the upper limit of the shakedown region in a Bree diagram, considering that the primary stresses are negligible, so that a suitable lifetime could be predicted. This is confirmed by experiments. If the lifetime is based on fatigue curves, considering the maximum strain range of the copper alloy and the relative curves, the lifetime is limited to about 13000 cycles, see also Figure 7.12. This would imply to change the limiter module at least one time during the BPP. However the use of these curves is considered too conservative.

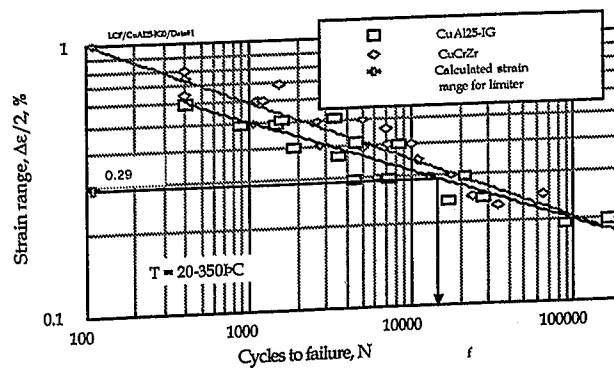


Figure 7.12 - Fatigue Curve for relevant copper alloys (G. Kalinin) [263]

## 7.5 Off normal condition

A VDE is considered highly improbable for the limiter, so that the verification of the FW armour to the related heat shocks has not been performed. In off normal conditions (plasma disruption) the limiter and its attachment system must withstand the electromagnetic loads; the main loads are listed in Table 7.8. The electromagnetic loads due to the variation of the poloidal magnetic field can be considered negligible [265]. Additional electromagnetic loads are due to the overall limiter configuration (the limiter is electrically connected to the vacuum vessel and the electrical currents in the back plate generates induced fields due to the large port opening [8]).

Table 7.8 - EM Loads on Limiter (ITER FDR)

Radial moments	
• due to $B_p$ Variation [7]	
in FW	20 kN·m
in SS plates	60 kN·m
in SS strong back	73 kN·m
• due to the overall limiter configuration *	220 kN·m
Radial pressure due to thermal quench *	0.2 MPa
Poloidal moment on Module due to $B_n$ variation* (results in radial push/pull force)	0.9 MN·m

\*From Ref. [266], this moment is mainly due to the large opening in the back plate and the fact that the limiter is electrically connected to the VV

It can be noted from Table 11 that, due to the slotted design of the limiter structure, large electromagnetic shear forces have been avoided. The above electromagnetic loads affect mainly the supporting structure.

## 7.6 Conclusions

The ITER port limiter design has been described. Due to the slotted design of its structure, large electromagnetic shear forces have been avoided and thermal stresses and deformations have been minimised.

Steady state and transient analyses have verified that no large gradients are generated during the entire limiter thermal cycle in the FW and in the shield part.

Stresses are within allowable values and the non ratcheting criterion is satisfied (below  $3S_m$ ) in most of the limiter structure, except at the beryllium/copper joint where plastic deformations occur locally. It is expected (and it has been preliminary confirmed by experiments) that the plastic strains are not excessive and that a suitable fatigue lifetime can be assured.



## 8 SUMMARY

The behaviour of the different Be grades before and after neutron irradiation has been compared by performing thermal shock tests. The erosion behaviour of the irradiated test coupons has been compared with un-irradiated tests specimens.

All beryllium grades show an enhanced erosion after neutron-irradiation, the amount of erosion, however, is lowest for S65 and for the condensed beryllium. The influence of the two irradiation temperatures seems to be less significant.

Metallography of neutron irradiated beryllium samples showed in general a similar behaviour as the un-irradiated samples before. During thermal shock loading beryllium is molten and after re-solidification a columnar structure is found in the re-crystallized zone containing some cracks perpendicular to the sample surface. More porosity was observed in the melt layer of the irradiated samples with respect to the un-irradiated.

For most beryllium grades no enhanced cracking is observed after neutron irradiation. Only TR30 and PS-beryllium, which showed large cracks beyond the melt layer before neutron irradiation, show an increased crack sensitivity after irradiation. Especially in plasma spray an increase of both crack density and cracks lengths was observed. Different to the other materials, in PS-Be the more severe cracks are parallel to the sample surface following the borders of the spraying layers. Although the weight loss during thermal shock experiments for plasma sprayed beryllium is not dramatically higher than for the other grades, the cracks parallel to the surface may propagate during thermal fatigue experiments and may lead to a detachment of material.

Because PFCs in future thermonuclear fusion reactors will experience severe thermal shocks primarily during plasma operation, i.e. at elevated temperatures (above 200°C), additional tests on few un-irradiated Be test coupons have been carried out under experimental conditions which take care of this effect. Pre-heated tests for simulating the disruption load at working temperature of the material have been performed. The erosion damage of the Be grades S65C and TR30 at different temperatures after thermal shock test has been investigated. The effect of the sample temperature below 500°C seems to be significant on the TR30 grade but irrelevant for the S65C grade.

The heat removal efficiency and the thermal fatigue behaviour of both 8 mm and 3 mm Be tile mock-ups with CuMnSnCe braze and InCuSil braze before and after neutron irradiation have been compared by performing screening and thermal fatigue tests. The experimental results show that the heat removal efficiency is slightly worse after the neutron damage. Thermal cycling experiments have been performed up to 1000 cycles on the 8 mm Be tile mock-ups and up to 100 cycles on the 3 mm Be tile mock-ups. Absorbed power density were: 8 MW/m<sup>2</sup> on the 8 mm Be tile mock-ups with CuMnSnCe braze, 7.5 MW/m<sup>2</sup> on the 8 mm Be tile mock-up with InCuSil braze and 9 MW/m<sup>2</sup> on the 3 mm Be tile mock-up with InCuSil braze. No significant temperature increase of the surface was observed during the test and no indication of failure was visible. Post-mortem metallography of the braze layer has shown no abnormalities compared to the un-irradiated samples.

The irradiation temperature (320°C) and the dose (0.3 dpa) in this experiment are not fully representative of the operating conditions of the first wall and baffle. At lower temperatures and higher doses (150-230°C, 1-2 dpa), embrittlement of Be and radiation hardening of Cu alloys could change the positive picture that comes out from these results. Nevertheless, the experiment demonstrates that there is a range of temperature and dose where neutron irradiation has no negative effects on Be/Cu joints.

In addition to the thermal fatigue test, the quality of the Be-copper joints was characterized by means of mechanical methods. Shear tests on un-irradiated and irradiated samples have been performed. For the InCuSil braze no influence of the neutron irradiation has been observed. The mean value of the post irradiation shear strength for the CuMnSnCe braze was approximately 25% lower compared to the pre-irradiation data. But with respect to the low sample numbers and the large scatter band, this difference is not considered to be significant.

Besides the effect of neutron irradiation on several Be grades and Be/Cu brazed joint, pre-irradiation characterization test on primary FW mock-ups produced by hot isostatic pressing have been carried out. The aim of the pre-irradiation characterization tests was to check the overall soundness of the joints before neutron irradiation. Preliminary FE thermal showed that a heat flux of  $4.6 \text{ MW/m}^2$  could have been applied on the entire surface of the mock-ups, without that the beryllium surface temperature exceeds  $750^\circ\text{C}$ , but the tests have been carried out at a lower heat flux of  $2.5 \text{ MW/m}^2$ . The beryllium-copper joining technique was HIP. Three of them have a titanium interlayer whereas the other two have an aluminium interlayer. A mock-ups with Al interlayer showed an unexpected increase of the beryllium surface temperature (indicating a joint bad condition) already when the applied heat flux was  $0.75 \text{ MW/m}^2$ . Therefore the test was interrupted and the other available mock-up with Al interlayer was tested at  $1 \text{ MW/m}^2$  and selected for neutron irradiation. A beryllium tile of a mock-up with Ti interlayer detached suddenly with an applied heat flux of  $1.88 \text{ MW/m}^2$ . The other two available mock-ups were tested at  $2.5 \text{ MW/m}^2$  and both showed good temperature homogeneity. Taking into account the results of visual examination and non-destructive examination carried out previously, one of the two was selected to be irradiated and the remaining one was kept as reference.

The assessment of the feasibility and adequacy of the ITER port limiter under normal and off-normal conditions has been carried out performing finite element thermo-mechanical analyses. Existing analytical methods have been applied to study this component and to predict its lifetime. Steady state and transient analyses have verified that no large gradients are generated during the entire limiter thermal cycle in the FW and in the shield part. Stresses are within allowable values and the non ratcheting criterion is satisfied (below  $3S_m$ ) in most of the limiter structure, except at the beryllium/copper joint where plastic deformations occur locally. It is expected (and it has been preliminary been confirmed by experiments) that the plastic strains are not excessive and that a suitable fatigue lifetime can be assured.

## 9 APPENDIX - LIST OF ACRONYMS

A	Ageing
ANFIBE	Analysis of Fusion Irradiated Be
BPP	Basic Performance Phase
BW	Brush Wellman
CIP	Cold Isostatic Pressing
CP	Cold Pressing
CTE	Coefficient of Thermal Expansion
CW	Cold Working
dpa	displacement per atom
DS	Dispersion Strengthened
EB	Electron Beam
EDA	Engineering Design Activity
FDR	Final Design report
FEAT	Fusion Energy Advanced tokamak
FW	First Wall
FZJ	Forschungszentrum Julich
hcp	hexagonal closed packed
HHF	High Heat Flux
HIP	Hot Isostatic Pressing
HIPB	Hot Isostatic Pressing diffusion Bonding
IG	ITER Grade
IR	Infra Red
ITER	International Thermonuclear Experimental Reactor
JCT	Joint Central Team
JEBIS	JAERY Electron Beam Irradiation Stand
JUDITH	Juelich Divertor Test Equipment in Hot Cells
LANL	Los Alamos National Laboratory
MAR	Material assessment Report
NRT	Norgett-Robinson-Torrens
PFC	Plasma Facing Component
PFM	Plasma Facing Material
PH	Precipitation Hardened
PKA	Primary Knock-on Atom
PM	Powder Metallurgical
PS	Plasma Spray
PVD	Physical Vapour Deposition
PW	Primary Wall
R&D	Research and Development
RF	Russian Federation
RRA	Rotating Rod Arc
RTO/RC	Reduced technical Objectives / Reduced Cost
SA	Solution annealing
TSC	Tokamak Simulation Code
VA	Vacuum Arc
VDE	Vertical Displacement Event
VHP	Vacuum Hot Pressing
VPS	Vacuum Plasma Spray
WQ	Water Quench

## 10 BIBLIOGRAPHY

- 1 R. Aymar, *ITER achievements by July 1998 and future prospects*, Fusion Engineering and Design 46 (1999) 115-127.
- 2 Final Design Report, IAEA, Vienna, ITER EDA Documentation series No. 16, December 1998.
- 3 R. Aymar, *ITER\_FEAT – Outline Design Report*, ITER Meeting, Tokyo, January, 2000.
- 4 F. Elio, K. Ioki, P. Barabaschi, L. Bruno, A. Cardella, M. Hechler, T. Kodama, A. Lodato, D. Loesser, D. Loustreau, N. Miki, K. Mohri, R. Parker, R. Raffray, D. Williamson, M. Yamada, W. Dänner, Y. Strebkov, H. Takatsu, *Engineering design of the ITER blanket and relevant research and development results*, Fusion Engineering and Design 46 (1999) 159-175.
- 5 A. Lodato, Assessment and experimental verification of plasma facing components for a thermonuclear experimental reactor, Final Report EURATOM Fellowship Contract 5004-CT96-5020, January 2000.
- 6 M. Scheerer, *Entwicklung und Analyse von hochbelasteten Komponenten für Divertoren künftiger Fusionsanlagen*, Dissertation, Rheinisch Westfälische Technische Hochschule Aachen, April 2000.
- 7 R.R. Parker, *Design and issues of the ITER in-vessel components*, Fusion Engineering and Design 39-40 (1998) 1-16.
- 8 A. Cardella, V. Barabash, K. Ioki, M. Yamada, T. Hatano, P. Lorenzetto, I. Mazul, M. Merola, Y. Ohara, Y. Strebkov, *Application of beryllium as first wall armour for ITER primary, baffle and limiter modules*, Fusion Technology 277-398 (2000) 316-333.
- 9 K. Ioki, L. Bruno, A. Cardella, W. Dänner, A. Lodato, D. Lousteau, R. Mattas, K. Mohri, R. Parker, R. Raffray, Y. Strebkov, N. Tachikawa, H. Takatsu, D. Williamson, M. Yamada, *ITER blanket system design*, Proceedings of the 19<sup>th</sup> Symposium on Fusion Technology, Lisbon, Portugal, September 16-20 1996.
- 10 A. Cardella, A. Lodato, H.D. Pacher, R.R. Parker, K. Ioki, G. Janeschitz, D. Lousteau, R. Raffray, M. Yamada, C. Gusic, *The ITER Port Limiter Design*, Fusion Engineering and Design, 43 (1998) 75-92.
- 11 A. Cardella, S. Chiocchio, K. Ioki, G. Janeschitz, R. Tivey, R. R. Parker, L. Bruno, A. Lodato, R. Jakeman, K. Mohri, R. Raffray, G. Vieider, P. Lorenzetto, A. Epinatiev, L. Giancarli, *Design of the ITER EDA Plasma Facing Components*, Fusion Engineering and Design, 39-40 (1998) 377-384.
- 12 K. Ioki, P. Barabaschi, L. Bruno, A. Cardella, W. Dänner, F. Elio, M. Hechler, T. Kodama, A. Lodato, D. Loesser, D. Loustreau, R. Mattas, N. Miki, K. Mohri, R. Parker, R. Raffray, Y. Strebkov, N. Tachikawa, H. Takatsu, D. Williamson, M. Yamada, *ITER first wall/shield blanket*, Fusion Engineering and Design 39-40 (1998) 585-591.
- 13 D. Lousteau, K. Ioki, L. Bruno, A. Cardella, F. Elio, M. Hechler, T. Kodama, A. Lodato, D. Loesser, N. Miki, K. Mohri, R. Raffray, M. Yamada, *Design of the ITER shielding blanket*, Proceedings of the 13<sup>th</sup> Topical Meeting on the Technology of Fusion Energy, Nashville, Tennessee (USA), June 7-11, 1998.
- 14 A. Cardella, K. Ioki, G. Janeschitz, A. Lodato, H. D. Pacher, R.R. Parker, R. Raffray, V. Rozov, K. Skladnov, *The ITER Port Limiter System*, Proceedings of the 20<sup>th</sup> Symposium on Fusion Technology (SOFT), Marseille (France), Sept. 7-11, 1998.
- 15 K. Mohri, A. Lodato, T. Kodama, *Design of inboard module in LAM*, ITER Internal Report G 16 MD 226 98-10-13 W0.1, Garching, Germany.
- 16 A. Cardella, K. Ioki, A. Lodato, T. Kodama, K. Mohri, *RTO/RC ITER Primary Wall Blanket Module Design with Separable Mechanically Attached First Wall*, ITER Internal Report G 16 MD 228 98-12-18, Garching, Germany.

- 17 V. Barabash, K.J. Dietz, G. Federici, G. Janeschitz, R. Matera, S. Tanaka, *ITER plasma facing materials some critical considerations*, Proceedings of the 18<sup>th</sup> Symposium of Fusion Technology (SOFT), Karlsruhe, 22.-26.8.94.
- 18 V. Barabash, J. Dietz, K. Ioki, G. Janeschitz, G. Kalinin, R. Matera, K. Mohri and the ITER Home Teams, *Materials aspects of ITER in-vessel components*, Proceedings of the 17<sup>th</sup> SOFT, Lisbon, September 1996.
- 19 R. Matera, G. Federici, The ITER Joint Central Team, *Design requirements for plasma facing materials in ITER*, Journal of nuclear materials 233-237 (1996) 17-25.
- 20 D.A. Petti, K.A. McCarthy, W. Gulden, S.J. Piet, Y. Seki, B. Kolbasov, *An overview of safety and environmental considerations in the selection of materials for fusion facilities*, Journal of nuclear materials 233-237 (1996) 37-43.
- 21 V. Barabash, M. Akiba, I. Mazul, M. Ulrickson, G. Vieider, *Selection, development and characterisation of plasma facing materials for ITER*, Journal of nuclear materials 233-237 (1996) 718-723.
- 22 K. Ioki, V. Barabash, A. Cardella, F. Elio, Y. Gohar, G. Janeschitz, G. Johnson, G. Kalinin, D. Lousteau, M. Onozuka, R. Parker, G. Sannazzaro, R. Tivey, *Design and material selection for ITER first wall/blanket, divertor and vacuum vessel*, Journal of Nuclear Materials 258-263 (1998) 74-84.
- 23 V. Barabash, G. Federici, R. Matera, A.R. Raffray and the ITER Home Teams, *Armour materials for the ITER plasma facing components*, Physica Scripta, Vol. T81, 74-83, 1999.
- 24 W. D. Manly, D. E. Dombrowski, J. E. Hanafée, L. A. Jacobson, G. J. London, G. R. Longhurst, R. D. Watson, J. L. Yuen, M. A. Ulrickson, *Report of a technical evaluation panel on the use of beryllium for ITER plasma facing material and blanket breeder material*, Sandia Report SAND95-1693, August 1995.
- 25 V. Barabash, M. Akiba, I. Mazul, M. Ulrickson, G. Vieider, *Selection, development and characterisation of plasma facing materials for ITER*, Journal of nuclear materials 233-237 (1996) 718-723.
- 26 B. Wiechers, *Untersuchungen von bestrahlten und unbestrahlten Wolframlegierungen für zukünftiger Fusionsreaktoren*, Dissertation, Rheinisch Westfälische Technische Hochschule Aachen, Februar 2000.
- 27 A.R. Raffray, G. Federici, V. Barabash, H.D. Pacher, H.W. Bartels, A. Cardella, R. Jakeman, K. Ioki, G. Janeschitz, R. Parker, R. Tivey, C.H. Wu, *Beryllium application in ITER plasma facing components*, Fusion Engineering and Design 37 (1997) 261-286.
- 28 V. Barabash, S. Tanaka, R. Matera and the ITER JCT, *Beryllium assessment and recommendation for application in ITER plasma facing components*, Proceedings of the 3<sup>rd</sup> IEA International Workshop on Beryllium Technology for fusion, October 1997, Mito, Japan.
- 29 *Large seven R&D projects for the ITER EDA, L-4 Blanket Project*, Volume 1 ITER Report S A1 RE 2 F, vers. 2, November 1997.
- 30 *Large seven R&D projects for the ITER EDA, L-4 Blanket Project*, Volume 2 Achievements ITER, July 1998.
- 31 P. Lorenzetto, A. Cardella, P. Chappuis, W. Dänner, M. Fèbvre, G. Hofmann, H. Stamm, S. Tähtinen, G. Walsh, *The EU HT test programme of ITER primary wall small scale mock-ups*, Proceedings of 20<sup>th</sup> Symposium on Fusion Technology (SOFT), Marseille (France), Sept. 7-11, 1998.
- 32 V. Barabash, V. Bykov, R. Giniyatulin, A. Gervash, T. Gurieva, K. Egorov, V. Komarov, M. Korolkov, I. Mazul, L. Gitarsky, I. Strulia, V. Sizenev, V. Pronyakin, *Beryllium mock-ups development and ultrasonic testing for ITER divertor conditions*, Proceedings of the 18<sup>th</sup> Symposium of Fusion Technology (SOFT), Karlsruhe, 22.-26.8.94.

- 33 G. Vieider, P. Chappuis, R. Duwe, R. Jakeman, M. Merola, H.D. Pacher, L. Plöchl, F. Rainer, M. Rödig, N. Reheis, I. Smid, *Manufacture and testing of small-scale mock-ups for the ITER divertor*, Proceedings of the 19<sup>th</sup> Symposium of Fusion Technology (SOFT), Lisbon, Portugal, 16.-20.09.1996.
- 34 B.N. Kolbasov, *Review and planning of Russian R&D studies for ITER safety*, Final Report for task S 81 TD 07 FR, WO D328-RF-6, Subtask 2, May 1998.
- 35 G. Vieider, V. Barabash, A. Cardella, P. Chappuis, R. Duwe, H. Falter, M. Fèbvre, L. Giancarli, C. Ibbott, D.M. Jacobson, R. Jakeman, G. LeMarois, A. Lind, M. Merola, H.D. Pacher, A. Peacock, A. Pizzuto, L. Plöchl, B. Riccardi, M. Rödig, S.P.S. Sangha, Y. Severi, E. Visca, *Overview of the EU small scale mock-up tests for ITER high heat flux components*, Fusion Engineering and Design 39-40 (1998) 211-218.
- 36 G. Vieider, M. Merola, F. Anselmi, J.P. Bonal, P. Chappuis, G. Dell'Orco, D. Duglué, R. Duwe, S. Erskine, F. Escourbiac, M. Fèbvre, L. Giancarli, M. Grattarola, G. LeMarois, H.D. Pacher, A. Pizzuto, L. Plöchl, B. Riccardi, M. Rödig, J. Schlosser, A. Salito, B. Schedler, C.H. Wu, *European development of prototypes for ITER high heat flux components*, Fusion Engineering and Design 49-50 (2000) 135-143.
- 37 W. Dänner, A. Cardella, L. Jones, P. Lorenzetto, D. Maisonnier, G. Malavasi, A. Peacock, E. Rodgers, F. Tavassoli, *Major achievements of the European shield blanket R&D during the ITER EDA, and their relevance for future next step machines*, Fusion Engineering and Design 49-50 (2000) 425-433.
- 38 ITER, *Material Assessment Report*, G A1 DDD 1 98-05-28 W 0.3.
- 39 Cardella, A. Lodato, *Electromagnetic Analysis of the Port Limiter*, ITER Internal Report G 16 RI 19 97-05-27 F1, Garching, Germany.
- 40 Cardella, A. Lodato, *ITER Port Limiter Analysis*, ITER Internal Report G 16 RI 20 97-10-22 F2, Garching, Germany.
- 41 F. Elio, K. Ioki, P. Barabaschi, L. Bruno, A. Cardella, M. Hechler, T. Kodama A. Lodato, D. Loesser, D. Loustreau, N. Miki, K. Mohri, R. Parker, R. Raffray, D. Williamson, M. Yamada, W. Dänner, W. Dänner, Y. Strebkov, H. Takatsu, *Engineering Design of the ITER Blanket and Relevant R&D Results*, Invited paper to the 20<sup>th</sup> Symposium on Fusion Technology (SOFT), Marseille (France), Sept. 7-11, 1998.
- 42 A. Lodato, A. Cardella, H. Pacher, K. Ioki, I. Smid, *Effect of the Neutral Beam Shine Through on the First Wall of ITER Thermo-Nuclear Fusion Reactor*, Heat & Technology, Vol. 16, n.1 (1998) 35-40.
- 43 A. Lodato, A. Cardella, *Thermomechanical Analysis of the Separable Mechanically Attached First Wall*, ITER Internal Report G 16 MD 229 98-12-18, Garching, Germany.
- 44 Cardella, A. Lodato, H. Gorenflo, *Updated Thermal and Mechanical Analysis for the ITER FEAT Separable First Wall*, ITER Internal Report G 16 MD 252 99-11-11, Garching, Germany.
- 45 A. Lodato, A. Cardella, R. Matera, *Thermal Analysis of the ITER FW with Replaceable Armour Using a Rheocast Alloy Joining Material*, ITER Internal Report G 16 RI 24 98-03-23 F1, Garching, Germany.
- 46 M. Akiba, I. Mazul, M. Ulrickson, G. Vieider, *Selection, development and characterization of plasma facing materials for ITER*, Journal of Nuclear Materials 233-237 (1996) 718-723.
- 47 E. R. Parker, U. Colombo, *The science of materials used in advanced technology*, John Wiley & Sons.
- 48 F. Aldinger, *Flow and fracture of single crystals*, in: D. Webster, G.J. London (Eds.), *Beryllium Science and Technology*, vol. 1, Plenum Press, 1979, pp. 7-114.
- 49 ITER, *Material Assessment Report*, G A1 DDD 1 98-05-28 W 0.3.

- 
- 50 H. J. Saxton, G.J. London, *Flow and fracture of polycrystalline beryllium*, in: D. Webster, G.J. London (Eds.), *Beryllium Science and Technology*, vol. 1, Plenum Press, 1979, pp. 115-144.
  - 51 Kenneth A. Walsh, *Extraction*, in: D.R. Floyd, J.N. Lowe (Eds.), *Beryllium Science and Technology*, vol. 2, Plenum Press, 1979, pp. 1-10.
  - 52 D. E. Dombrowski, *Manufacture of Beryllium for fusion energy applications*, *Fusion Engineering and Design* 37 (1997) 229-242.
  - 53 *Producing a Defect-free Beryllium and Beryllium Oxide*, Brush Wellman brochure, Cleveland, Ohio, USA, May 1985.
  - 54 *Designing with beryllium*, Brush Wellman brochure, Cleveland, Ohio, USA, 1999.
  - 55 E.B. Deksnis, M.A. Pick, D.E. Dombrowski, *Thermomechanical properties of Beryllium*, JET Joint Undertaking report JET-IR(94)07.
  - 56 D. E. Dombrowski, E. Deksnis, M. A. Pick, *Thermomechanical Properties of Beryllium*, Brush Wellman Technical Memorandum TR-1182, February 1995.
  - 57 W. D. Manly, D. E. Dombrowski, J. E. Hanafée, L. A. Jacobson, G. J. London, G. R. Longhurst, R. D. Watson, J. L. Yuen, M. A. Ulrickson, *Report of a technical evaluation panel on the use of beryllium for ITER plasma facing material and blanket breeder material*, Sandia Report SAND95-1693, August 1995.
  - 58 D. E. Dombrowski, W. J. Haws, P. McKeighan, *Comparison of Elevated Temperature Properties of HIP'd Impact Ground Beryllium (S-65-H) and HIP'd Gas Atomized (GA) Beryllium*, Proceedings of the 4<sup>th</sup> IEA International Workshop on Beryllium Technology for fusion, September 15-17, 1999, Karlsruhe, Germany.
  - 59 R.G. Castro, P.W. Stanek, K.E. Elliot, J.D. Cotton, R.D. Watson, *Optimizing the thermal conductivity of vacuum plasma-sprayed beryllium for fusion application*, *Journal of nuclear materials* 226 (1995) 170-177.
  - 60 Graham I. Turner, *Grain size effects*, in: D. Webster, G.J. London (Eds.), *Beryllium Science and Technology*, vol. 1, Plenum Press, 1979, pp. 145-179.
  - 61 S. P. Abeln, M. C. Mataya, R. Field, *Elevated temperature stress strain behaviour of beryllium powder product*, Proceedings of the 2<sup>nd</sup> IEA International Workshop on Beryllium Technology for fusion, September 1995, Jackson Lake Lodge, Wyoming.
  - 62 A.M. Khomutov, D.A. Davydov, V.A. Gorokhov, I.B. Kuprijanov, V.S. Mikhailov, Ya.D. Pakhomov, *Status of Beryllium materials for fusion application*, *Journal of nuclear materials* 233-237 (1996) 111-119.
  - 63 D.E. Dombrowski, W.J. Haws, P. McKeighan, *Comparison of elevated temperature properties of HIP'd impact ground beryllium (S-65-H) and HIP'd gas atomized (GA) beryllium*, Proceedings of the 4<sup>th</sup> IEA International Workshop on Beryllium Technology for fusion, September 15-17, 1999, Karlsruhe, Germany.
  - 64 A. James Stonehouse, *Impurity effects in beryllium*, in: D. Webster, G.J. London (Eds.), *Beryllium Science and Technology*, vol. 1, Plenum Press, 1979, pp. 181-206.
  - 65 Donald Webster, *Recrystallization and grain growth in beryllium*, in: D. Webster, G.J. London (Eds.), *Beryllium Science and Technology*, vol. 1, Plenum Press, 1979, pp. 207-234.
  - 66 R. G. Castro, P. W. Stanek, K. E. Elliott, *The structure, properties and performance of plasma-sprayed beryllium for fusion application*, Proceedings of the 2<sup>nd</sup> IEA International Workshop on Beryllium Technology for fusion, September 1995, Jackson Lake Lodge, Wyoming.
  - 67 Ian W. Dunmur, *Plasma-sprayed beryllium*, in: D.R. Floyd, J.N. Lowe (Eds.), *Beryllium Science and Technology*, vol. 2, Plenum Press, 1979, pp. 135-175.

- 
- 68 R. G. Castro, R. U. Vaidya, K. J. Hollis, *Characterization of plasma sprayed beryllium ITER first wall mock-ups*, Proceedings of the 3<sup>rd</sup> IEA International Workshop on Beryllium Technology for fusion, October 1997, Mito, Japan.
  - 69 R. G. Castro, K. E. Elliot, R. D. Watson, D. L. Youchison, K. T. Slattery, *Fabrication and high heat flux testing of plasma sprayed beryllium ITER first wall mock-ups*, Journal of nuclear materials 258-263 (1998) 252-257.
  - 70 F. Scaffidi-Argentina, G.R. Longhurst, V. Shestakov, H. Kawamura, *Beryllium R&D for fusion applications*, Fusion Engineering and Design 51-52 (2000) 23-41.
  - 71 I.B. Kupriyanov, V.A. Gorokhov, R.R. Melder, Z.E. Ostrovsky, A.A. Gervash, *Investigation of ITER candidate beryllium grades irradiated at high temperature*, Journal of Nuclear Materials 258-263 (1998) 808-813.
  - 72 I.B. Kupriyanov, V.A. Gorokhov, G.N. Nikolaev, *Development of radiation resistant grades of beryllium for nuclear and fusion facilities*, Proceedings of the 2<sup>nd</sup> IEA International Workshop on Beryllium Technology for fusion, September 1995, Jackson Lake Lodge, Wyoming.
  - 73 R. D. Watson, D. L. Youchison, D. E. Dombrowski, R. N. Guiniatouline, I. B. Kupriyanov, *Low cycle thermal fatigue testing of beryllium grades for ITER plasma facing components*, Proceedings of the 2<sup>nd</sup> IEA International Workshop on Beryllium Technology for fusion, September 1995, Jackson Lake Lodge, Wyoming.
  - 74 M. Rödig, R. Duwe, H. Hoven, W. Kühnlein, J. Linke, G. Pott, A. Schuster, E. Wallura, *Pre-irradiation characterisation of Be- and C-based materials for plasma-facing components*, Final Report NET/ITER Tasks T1, T2, T61, IWE-TN 35/95, 18.12.1995.
  - 75 I. B. Kupriyanov, V. A. Gorokhov, G. N. Nikolaev, *Development of radiation resistant grades of beryllium for nuclear and fusion facilities*, Proceedings of the 2<sup>nd</sup> IEA International Workshop on Beryllium Technology for fusion, September 1995, Jackson Lake Lodge, Wyoming.
  - 76 G. I. Pepekin, A.B. Anisimov, A. S. Chernikov, S. I. Mozherinn, A. A. Pirogov, *Beryllium Coating Produced by Evaporation-Condensation Method and Some Their Properties*, Proceedings of the 3<sup>rd</sup> IEA International Workshop on Beryllium Technology for fusion, October 1997, Mito, Japan.
  - 77 I.B. Kupriyanov, V.A. Gorokhov, R.R. Melder, Z.E. Ostrovsky, G.N. Nikolaev, *Neutron irradiation behaviour of ITER candidate beryllium grades*, Proceedings of the 3<sup>rd</sup> IEA International Workshop on Beryllium Technology for fusion, October 1997, Mito, Japan.
  - 78 M. Rödig, R. Duwe, A. Gervash, A. M. Khomutov, J. Linke, A. Schuster, *Thermal Shock Tests with Beryllium Coupons in the Electron Beam Facility JUDITH*, Proceedings of the 2<sup>nd</sup> IEA International Workshop on Beryllium Technology for fusion, Wyoming, September 1995, pp. 39-57.
  - 79 M.C. Billone, *Recommended design correlations for S-65 beryllium*, Proceedings of the 2<sup>nd</sup> IEA International Workshop on Beryllium Technology for fusion, September 1995, Jackson Lake Lodge, Wyoming.
  - 80 S.P. Abeln, M.C. Mataya, R. Field, *Elevated temperature stress strain behaviour of beryllium powder product*, Proceedings of the 2<sup>nd</sup> IEA International Workshop on Beryllium Technology for fusion, September 1995, Jackson Lake Lodge, Wyoming.
  - 81 A.M. Khomutov, V.A. Gorokhov, V.S. Mikhailov, G.N. Nikolaev, R.Yu. Timofeev, V.M. Chernov, *Temperature-strain rate dependence of mechanical properties of a beryllium of the DShG-200 brand*, Proceedings of the 4<sup>th</sup> IEA International Workshop on Beryllium Technology for fusion, September 15-17, 1999, Karlsruhe, Germany.
  - 82 ITER *Material Properties Handbook*, ITER Doc. S 74 RE 1 78-08-01 W1.5.
  - 83 RF HT, *Assessment and Characterisation of Candidate Cu Based Materials for the First Wall Application*. Analytical Survey, ITER 4.2.42, RDIPE, Moscow 1994.



- 84 M. Fabvre, J.L. Deneville, *CuCrZr Quenching*, EU report, Task T216+. Blanket design + development stage 5. EFET, MC/TS. 96.810.
- 85 S.J. Zinkle, W.S. Eatherly, *Effect of test temperature and strain rate on the tensile properties of high-strength, high-conductivity copper*, Semiannual Progress Report for Period Ending December 31.1996, 165-174, DOE/ER-0313/21.
- 86 S. Sato, Current status of mid-scaled primary first wall module fabrication and proposal for prototype primary first wall module, ITER Blanket Task Meeting, Garching JWS, February 24-26, 1997, ITER Doc. G JH RE 3 97-11-13 F1.
- 87 H. Takatsu, *Main results obtained so far*, Presented on ITER Blanket Task Meeting, Garching JWS, June 24-28, 1996, ITER Doc. G JH RE 4 97-11-13 F1.
- 88 G. Le Marois et. al., *Advanced joining techniques for ITER modules manufacturing*, Note Technique D.E.M. No. 32/97, 12.05.1997.
- 89 V. Barabash, G. Kalinin, R. Matera and the ITER Home Teams, *Joining technologies for the plasma facing components of ITER*, Proceedings of 20<sup>th</sup> Symposium on Fusion Technology (SOFT), Marseille (France), Sept. 7-11, 1998.
- 90 A.A. Gervash, R.N. Giniatouline, I.V. Mazul, A.A. Ganenko, L.S. Gitarskij, V.S. Sizenev, D.A. Davydov, *Metallographic analysis and strength investigation of different Be-Cu joints in the temperature range RT-350°C*, Journal of Nuclear Materials 233-237 (1996) 626-631.
- 91 V. Barabash, M. Akiba, A. Cardella, I. Mazul, B.C. Odegard Jr, L. Ploechl, R. Tivey, G. Vieider, *Armour and heat sink material joining technologies development for ITER plasma facing components*, Proceedings of the 9<sup>th</sup> International Conference on Fusion Reactor Materials, Oct. 1999, Colorado Springs, USA.
- 92 B.C. Odegard Jr, C.H. Cadden, N.Y.C. Yang, *Fusion Engineering and Design* 39-40 (1998) 63.
- 93 H. Kawamura, M. Kato, *Reactivity test between beryllium and copper*, Proceedings of the 2<sup>nd</sup> IEA International Workshop on Beryllium Technology for fusion, September 1995, Jackson Lake Lodge, Wyoming.
- 94 B.C. Odegard, B.A. Kalin, *A review of the joining techniques for plasma facing components in fusion reactors*, Journal of Nuclear Materials 233-237 (1997) 44-50.
- 95 A. Gervash, G. Giniatulin, V. Komarov et al., *Fusion Engineering and Design* 39-40 (1998) 543-550.
- 96 D.J. Butler, D. Dombrowski, *Preliminary results on explosion bonding of beryllium to copper*, Proceedings of the 2<sup>nd</sup> IEA International Workshop on Beryllium Technology for fusion, September 1995, Jackson Lake Lodge, Wyoming.
- 97 R.G. Castro, A.H. Bartlett, K.E. Elliott and K.J. Hollis, *The structure and the thermal properties of plasma-sprayed beryllium for ITER*, 9<sup>th</sup> National Thermal Spray Conference, Cincinnati, Ohio, 1996.
- 98 R.G. Castro, P.W. Stanek, K.E. Elliott, et al., *Physica Scripta* T64 (1996) 77-83
- 99 V. Barabash, M. Akiba, I. Mazul, M. Ulrickson, G. Vieider, *Selection, development and characterisation of plasma facing materials for ITER*, Journal of nuclear materials 233-237 (1996) 718-723.
- 100 C. Ibbott, H.D. Falter, P. Meurer, E. Thompson, M.J. Watson, G. Critchlow, D. Ciric, *Further developments in the brazing of beryllium to CuCrZr*, Proceedings of the 18<sup>th</sup> Symposium of Fusion Technology (SOFT), Karlsruhe, 22.-26.8.94.
- 101 Induction brazing of Beryllium Tiles onto CuCrZr test pieces and divertor mock-up plates, NNC Technical Report, NET94-871, 16 September 1994.
- 102 D.M. Jacobson, S.P.S. Sangha, J.H. Vincent, D.R. Wallis, *Development of processes for attaching Beryllium tiles onto CuCrZr testpieces and divertor mock-up plates*, GEC-Marconi Report MS/20416, November 1995.

- 
- 103 D.E. Dombrowski, *Recent results for bonding S-65C grade Be to copper alloys*, Proceedings of the 2<sup>nd</sup> IEA International Workshop on Beryllium Technology for fusion, September 1995, Jackson Lake Lodge, Wyoming.
  - 104 H. Kawamura, M. Kato, *Reactivity test between beryllium and copper*, Proceedings of the 2<sup>nd</sup> IEA International Workshop on Beryllium Technology for fusion, September 1995, Jackson Lake Lodge, Wyoming.
  - 105 E. Franconi, G.C. Ceccotti, L. Magnoli, *Development of Beryllium bonds for plasma-facing components*, Journal of nuclear materials 191-194 (1992) 493-498.
  - 106 M.G. Nicholas, *An assessment of some brazed Beryllium-copper joints*, Report AEA Industrial Technology AEA-InTec-0665, September 1991.
  - 107 H. Altmann, E.B. Deksnis, C. Ibbott, C. Sborchia, R. Tivey, R. Viola, *An analysis of induction brazed Beryllium on Copper alloy substrates*, JET Joint Undertaking, Abingdon, Oxon, England, OX14 3EA.
  - 108 F. Saint-Antonin, *Development and characterization of Be/Cu alloy HIP joints*, Note Technique D.E.M./S.G.M N 03/96, CEA, CEREM, Jan 1996.
  - 109 F. Saint-Antonin, D. Barberi, G. Le Marois, A. Laillé, *Development and characterization of Be/Cu joint obtained by Hot Isostatic Pressing*, Fusion Technology 1996, pp. 339-401.
  - 110 Lind, J. Collén, *Fabrication of ITER first wall modules from powder by Hot Isostatic Pressing*, Fusion Technology 1996, pp. 411-414.
  - 111 F. Saint-Antonin, P. Bucci, D. Barberi, H. Burlet, A. Laillé, G. Le Marois, *Development of Be/Glidcop joint obtained by hot isostatic pressing diffusion bonding for high in-service temperature*, Proceedings of the 3<sup>rd</sup> IEA International Workshop on Beryllium Technology for fusion, October 1997, Mito, Japan.
  - 112 G.C. Ceccotti, L. Magnoli, *Diffusion bonding as joining technique for fusion reactor components*, Fusion Technology 1992, pp. 216-217.
  - 113 E. Visca, G. Ceccotti, B. Riccardi, G. Mercurio, *Technologies of joining between ITER reference grade Beryllium and Copper alloy by diffusion bonding process*, Fusion Technology 1996, pp. 423-426.
  - 114 J. Linke, H. Bolt, *Thermal stability*, in W. O. Hofer, J. Roth, Physical Processes of the Interaction of Fusion Plasmas with Solids, pp. 177-216, Academic Press.
  - 115 K. Krieger, *Plasma wall interaction in nuclear fusion devices*, in: H.-S. Bosch, Summer university for plasma physics, September 21-25, 1998, Garching, Germany.
  - 116 ITER Design Description Document, Physics, Disruption, July 1998.
  - 117 Plasma Performance Assessments Technical Basis for the ITER Final Design Report, Cost Review and Safety Analysis, 13 July 1998.
  - 118 M. Merola, M. Rödig, J. Linke, R. Duwe, G. Vieider, *Behaviour of plasma facing materials under VDE*, Proceedings of the ICFRM-8, October 26-31, 1997, Sendai, Japan.
  - 119 G. Federici, C.H. Skinner, J.N. Brooks, J.P. Coad, C. Grisolia, A.A. Haasz, A. Hassanein, V. Philipps, C.S. Pitcher, J. Roth, W.R. Wampler, D.G. Whyte, *Plasma material interactions in current tokamas and their implications for next-step fusion reactors*, submitted to Nuclear Fusion, also IPP-report 9/128, PPPL-report 3531, January 2001.
  - 120 G.E. Dieter, *Mechanical metallurgy*, Mc Graw Hill.
  - 121 R. Matera, M. Merola, *Preliminary theoretical and experimental study of the effects of plasma disruptions on the thermal fatigue lifetime of the ITER/NET first wall*, Fusion Engineering and Design 16 (1991) 343-350.
  - 122 D.L. Youchison, R. Guiniatouline, R.D. Watson, J.M. McDonald, B.E. Mills, D.R. Boehme, *Thermal fatigue testing of a diffusion-bonded beryllium divertor mock-up under ITER relevant conditions*, Proceedings of the 18<sup>th</sup> Symposium of Fusion Technology (SOFT), Karlsruhe, 22.-26.8.94.

- 123 A. Gervash, R. Giniyatulin, I. Mazul, *Comparative thermal cyclic test of different beryllium grades previously subjected to simulated disruption loads*, Fusion Engineering and Design 46 (1999) 229-235.
- 124 A. Gervash, I. Mazul, N. Yablokov, A. Ganenko, *Comparative Strength analysis and thermal fatigue testing of Be/CuCrZr and Be/Gludcop joints produced by fast brazing*, Fusion Technology 277-398 (2000) 277-282.
- 125 A. Cardella, A. Lodato, H.D. Pacher, R.R. Parker, K. Ioki, G. Janeschitz, D. Lousteau, R. Raffray, M. Yamada, C. Gusic, *The ITER Port Limiter Design*, Fusion Engineering and Design, 43 (1998) 75-92.
- 126 J. Linke, M. Akiba, M. Araki, H. Bolt, G. Breitbach, R. Duwe, K. Nakamura, J.H. You, *Evaluation of cooling concepts and specimen geometries for high heat flux tests on neutron irradiated divertor elements*, Fusion Engineering and Design 28 (1995) 72-80.
- 127 E. Deksnis, D. Ciric, H. Falter, C. Ibbott, A. Peacock, *Thermal fatigue of Beryllium*, Proceedings of the 2<sup>nd</sup> IEA International Workshop on Beryllium Technology for fusion, September 6-8, 1995, Jackson Hole, Wyoming.
- 128 M. Rödig, R. Duwe, W. Kühnlein, J. Linke, A. Schuster, *Behaviour of Carbon and Beryllium under thermomechanical loads*, Physica Scripta, Vol. T64, 60-66, 1996.
- 129 D. Guilhem, J. Hogan, D. Van Houtte, M. Lipa, T. Loarer, P. Chappuis, T. Hoang, J. Schlosser, R. Mitteau, *Long pulse operation with actively cooled limiters*, Journal of Nuclear Materials 241-243 (1997) 542-547.
- 130 J. Linke, R. Duwe, M. Rödig, A. Schuster, *Thermal cycling of water-cooled divertor mock-ups*, Proceedings of the 17<sup>th</sup> IEEE/NPSS Symposium on Fusion Engineering, 06.-10.10.1997, San Diego.
- 131 M. Rödig, R. Duwe, J. Linke, A. Schuster, B. Wiechers, *Thermal cycling tests of actively cooled Beryllium Copper joints*, Proceedings of the 3<sup>rd</sup> IEA International Workshop on Beryllium Technology for fusion, October 1997, Mito, Japan.
- 132 M. Rödig, R. Duwe, W. Kühnlein, J. Linke, M. Scheerer, I. Smid, B. Wiechers, *Testing of actively cooled high heat flux mock-ups*, Proceedings of the ICFRM-8, October 26-31, 1997, Sendai, Japan.
- 133 T. Hatano, S. Suzuki, K. Yokoyama, M. Akiba, J. Ohmori, T. Kuroda, H. Takatsu, *Fabrication and thermal cycle testing of a first wall mock-up for ITER baffle blanket module*, Proceedings of the 13<sup>th</sup> Topical Meeting Technology of Fusion Energy, June 7-11, 1998, Nashville, Tennessee.
- 134 M. Rödig, R. Duwe, C. Ibbott, D. Jacobson, G. Le Marois, A. Lind, J. Linke, P. Lorenzetto, A. Peacock, L. Plöchl, A. Schuster, Y. Severi, G. Vieider, E. Visca, B. Wiechers, *Thermal fatigue tests with actively cooled divertor mock-ups for ITER*, Fusion Engineering and Design 39-40 (1998) 551-557.
- 135 P. Lorenzetto, G. Le Marois, F. Saint-Antonin, M. Rödig, R. Duwe, W. Dänner, A. Cardella, A. Lodato, *Thermal fatigue testing of a ITER primary wall small scale mock-up*, Journal of Fusion Engineering and Design, 39-40 (1998) 521-528.
- 136 J. Delaplace, *Radiation environments*, Solid State Phenomena Vol. 30 & 31 (1993) pp. 169-178.
- 137 P. Schiller, *Review of material selection for fusion reactors*, Journal of nuclear materials 206 (1993) 113-120.
- 138 H. Ullmaier, H. Trinkaus, *Radiation damage in metallic structural materials*, in: W.O. Hofer, J. Roth, Physical Processes of the Interaction of Fusion Plasmas with Solids, pp. 305-339, Academic Press.
- 139 Y. Quéré, *Radiation effects in solids: a brief history*, Solid State Phenomena Vol. 30 & 31 (1993) pp. 1-6.

- 140 E. Balanzat, S. Bouffard, *Basic phenomena of the particle-matter interaction*, Solid State Phenomena Vol. 30 & 31 (1993) pp. 7-74.
- 141 A. Barbu, G. Martin, *Radiation effects in metals and alloys*, Solid State Phenomena Vol. 30 & 31 (1993) pp. 179-228.
- 142 D.S. Gelles, M. Dalle Donne, G. A. Sernyaev, H. Kawamura, *Radiation effects in Beryllium used for plasma protection*, Fusion Reactor Materials Semi-annual Progress Report, September 1993.
- 143 V. Barabash, G. Federici, M. Rödiger, L.L. Snead, C. H. Wu, *Neutron irradiation effects on plasma-facing materials*, Proceedings of the 9<sup>th</sup> International Conference on Fusion Reactor Materials, Oct. 1999, Colorado Springs, USA.
- 144 C.H. Wu, J.P. Bonal, H. Kwast, F. Moons, G. Pott, H. Werle, G. Vieider, *EU results on neutron effects on PFC materials*, Fusion Engineering and Design 39-40 (1998) 263-273.
- 145 R. Behrisch, V. Khripunov, R.T. Santoro, J.M. Yesil, *Transmutation of plasma facing materials by the neutron flux in a DT fusion reactor*, Journal of Nuclear Materials 258-263 (1998) 686-693.
- 146 F. Scaffidi-Argentina, H. Werle, *Tritium release from neutron irradiated beryllium: kinetics, long-time annealing and effect of crack formation*, Proceedings of the 2<sup>nd</sup> IEA International Workshop on Beryllium Technology for fusion, September 1995, Jackson Lake Lodge, Wyoming.
- 147 D.V. Andreev, V.N. Bespalov, A.Ju. Birjukov, B.A. Gurovich, P.A. Platonov, *Post-irradiation studies of Beryllium reflector of fission reactor. Examination of gas release, swelling and structure of Beryllium under annealing*, Journal of Nuclear Material 233-237 (1996) 880-885.
- 148 L. Coheur, J.-M. Cayphas, P. Delavignette, M. Hou, *Microstructural effects of neutron irradiation in beryllium*, Proceedings of the 4<sup>th</sup> IEA International Workshop on Beryllium Technology for fusion, September 15-17, 1999, Karlsruhe, Germany.
- 149 R. Chaouadi, A. Leenaerts, J.L. Puzzolante, M. Scibetta, *Radiation effects on the mechanical properties of irradiated beryllium*, Proceedings of the 4<sup>th</sup> IEA International Workshop on Beryllium Technology for fusion, September 15-17, 1999, Karlsruhe, Germany.
- 150 I.B. Kupriyanov, V.V. Vlasov, *Helium and tritium behaviour in neutron-irradiated beryllium*, Fusion Technology 277-398 (2000) 350-356.
- 151 M. Dalle Donne, F. Scaffidi-Argentina, *Impurities effect on the swelling of neutron irradiated beryllium*, Proceedings of the 2<sup>nd</sup> IEA International Workshop on Beryllium Technology for fusion, September 1995, Jackson Lake Lodge, Wyoming.
- 152 G. Sernyaev, V. Barabash, M. Chernetsov, A. Kozlov, *Influence of thermocycling heating on bubble swelling of beryllium*, Proceedings of the 18<sup>th</sup> Symposium of Fusion Technology (SOFT), Karlsruhe, 22.-26.8.94.
- 153 I.B. Kuprijanov, V.A. Gorokhov, G.N. Nikolaev, V.N. Burmistrov, *Journal of Nuclear Material* 233-237 (1996) 886.
- 154 G.A. Sernyaev, A.S. Pokrovsky, R.M. Bagautdinov, *Journal of Nuclear Material* 233-237 (1996) 891.
- 155 I.B. Kupriyanov, V.A. Gorokhov, A.M. Khomutov, *Manufacturing and some properties of powder beryllium with high radiation stability*, Proceedings of the 18<sup>th</sup> Symposium of Fusion Technology (SOFT), Karlsruhe, 22.-26.8.94.
- 156 V.Barabash, G.Federici, M.Rödiger, et al., *Neutron effect on plasma facing material*, Journal of Nuclear Materials 283-287 (2000) 138-146.
- 157 D.R. Harries, M. Dalle Donne, F. Scaffidi-Argentina, *An assessment of the tensile and fracture toughness data generated in a beryllium irradiation-test program*, Fusion Technology 277-398 (2000) 338-349.

- 158 I.B. Kupriyanov, R.R. Melder, V.A. Gorokhov, *The effect of neutron irradiation on beryllium performance*, Fusion Engineering and Design 51-52 (2000) 135-143.
- 159 A. Lodato, M. Rödiger, R. Duwe, J. Linke, H. Derz, *High Heat Flux Components with Be Armour Before and After Neutron Irradiation*, Fusion Engineering and Design 49-50 (2000) 255-261.
- 160 M. Rödiger, R. Conrad, H. Derz, R. Duwe, J. Linke, A. Lodato, M. Merola, G. Pott, G. Vieider, B. Wiechers, *Examination of Neutron Irradiated Divertor Materials and their Joints*, invited paper at the 9<sup>th</sup> International Conference on Fusion Reactor Materials (ICFRM), Colorado Springs (USA), Oct. 10-15, 1999.
- 161 M. Rödiger, R. Conrad, H. Derz, R. Duwe, J. Linke, A. Lodato, M. Merola, G. Pott, G. Vieider, B. Wiechers, *Neutron-irradiation effects on high heat flux components – examination of plasma-facing materials and their joints*, Journal of Nuclear Material 283-287 (2000) 1161-1165.
- 162 S. Schiller, U. Heisig, S. Panzer, *Electron beam technology*, John Wiley & Sons, New York-Chichester-Brisbane-Toronto-Singapore.
- 163 V.E. Cosslett, *Introduction to electron optics: the production, propagation and focusing of electron beams*, Oxford and Clarendon Press (1950).
- 164 Robert A. Bakish, , *Introduction to electron beam technology* John Wiley & Sons, Inc, New York-London.
- 165 J. I. Goldstein, H. Yakowitz, *Practical scanning electron microscopy*, Plenum Press, New York-and London.
- 166 Vernon L. Bailey, Jr., *High energy electron beam interaction with materials*, Pulse Sciences, Inc., 600 McCormick St., San Leandro, CA.
- 167 H. Schwartz, *Mechanism of high-power-density electron beam penetration in metal*, in R. Bakish, First International Conference on Electron and Ion Beam Science and Technology, Toronto (1964).
- 168 *Electricity*, Encyclopaedia Britannica Online.
- 169 J. Schou, *Electron emission from solid*, from W. O. Hofer, J. Roth, Physical Processes of the Interaction of Fusion Plasmas with Solids, pp. 269-304, Academic Press.
- 170 Mende, Simon, *Physik Gleichungen und Tabellen*.
- 171 V.S. Fomenko, *Handbook of thermionic properties: electronic work functions and Richardson constants of elements and compounds*, Plenum Press Data Division, New York 1966.
- 172 N. Sakamoto, M. Akiba, H. Kawamura, *New electron beam facility for irradiated plasma facing materials testing in hot cell*, Proceedings of the 2<sup>nd</sup> IEA International Workshop on Beryllium Technology for fusion, September 1995, Jackson Lake Lodge, Wyoming.
- 173 A.M. Hassanein, *Simulation of plasma disruption induced melting and vaporization by ion or electron beam*, Journal of Nuclear Materials 122-123 (1984) 1453-1458.
- 174 D. Quataert, F. Brossa, P. Moretto, G. Rigon, *Electron beam disruption simulation of first wall Material*, SOFT (1984) 401-408.
- 175 G. Rigon, P. Moretto, F. Brossa, *Experimental simulation of plasma disruption with an electron beam*, Fusion Engineering and Design 5 (1987) 299-315.
- 176 M. Rödiger, M. Akiba, P. Chappuis, R. Duwe, M. Febvre, A. Gervash, J. Linke, N. Litounovsky, S. Suzuki, B. Wiechers, D.L. Youchison, *Comparison of electron beam test facilities for testing of high heat flux components*, Proceedings of the 5<sup>th</sup> International Symposium on Nuclear Fusion Technology (ISFNT-5), September 19-24, 1999, Rome, Italy.
- 177 M. Seki, S. Yamazaki, A. Minato, T. Horie, Y. Tanaka, T. Tone, *Improvement of an electron beam facility as a heat source for disruption simulation experiment*, Fusion Engineering and Design 5 (1987) 215-220.

- 178 V. Engelko, R. Kurunov, I. Landman, B. Ljublin, L. Smirnov, H. Würz, *Test of divertor materials under simulated plasma disruption conditions at the SOM electron beam facility*, Proceedings of the 18<sup>th</sup> Symposium of Fusion Technology (SOFT), Karlsruhe, Germany, 22-26 August 1994.
- 179 A. Hassanein, I. Konkashbaev, *Disruption simulation experiments and extrapolation to reactor conditions*, Proceedings of the 20<sup>th</sup> Symposium of Fusion Technology (SOFT), Marseille, France, 7-11 September 1998.
- 180 Hassanein, D.A. Ehst, *Dynamic modeling of plasma-vapor interactions during plasma disruptions*, Journal of Nuclear Materials 196-198 (1992) 680-685.
- 181 J. Linke, M. Akiba, R. Duwe, A. Lodato, H.-J. Penkalla, M. Rödiger, K. Schöpflin, *Material degradation and particle formation under transient thermal loads*, to be published in Proceedings of 14<sup>th</sup> Conference on Plasma Surface Interaction, Rosenheim, Germany, May 2000.
- 182 A.M. Hassanein, A. Konkashbaev, I. Konkashbaev, *Erosion of melt layers developed during a plasma disruption*, Proceedings of the 18<sup>th</sup> Symposium of Fusion Technology (SOFT), Karlsruhe, Germany, 22-26 August 1994.
- 183 A. Hassanein, G. Federici, I. Konkashbaev, A. Zhitlukhin, V. Litunovsky, *Material effects and design implications of disruptions and off-normal events in ITER*, Fusion Engineering and Design 39-40 (1998) 201-210.
- 184 R. Duwe, W. Kühnlein, H. Müstermann, *The new electron beam facility for material testing in hot cells – design and preliminary experience*, Proceedings of the 18<sup>th</sup> Symposium of Fusion Technology (SOFT), Karlsruhe, Germany, 22-26 August 1994.
- 185 R. Duwe, W. Kühnlein, J. Linke, M. Rödiger, *JUDITH – Jülicher Divertor Testanlage in den Heissen Zellen – eine Elektronenstrahlanlage für Materialtests*, Berichte des Forschungszentrum Jülich, Zentralabteilung Forschungsreaktoren und Kerntechnische Betriebe, Institut für Werkstoffe der Energietechnik, Jül-3183.
- 186 M. Rödiger, R. Duwe, H. Hoven, W. Kühnlein, J. Linke, G. Pott, A. Schuster, E. Wallura, *Pre-Irradiation Characterisation of Be- and C-Based Materials for Plasma-Facing Components*, Final Report NET/ITER Tasks T1, T2, T61, IWE-TN 35/95, 18.12.1995.
- 187 R. Conrad, R. May, *PARIDE plasma facing materials for ITER and DEMO*, JRC, Institute for advanced materials, HFR Unit, Petten, Technical Memorandum HFR/95/4242, 15.01.1996.
- 188 M. Rödiger, F. Meuser, G. Pott, *Neutron irradiation HFR-D302 (PARIDE) Samples and loading scheme*, Intermediate Report NET/ITER Tasks T1, T2, T61, IWE-TN 37/95, 22.12.1995.
- 189 M. Rödiger, *Neutron-Irradiation and Post-Irradiation Testing of Beryllium samples and Be/Cu Mock-ups*, Final Report ITER-Task T221/1 (GB5) IWV2-TN 3/2000, 20.09.00.
- 190 M. Rödiger, G. Pott, *Neutron irradiation HFR-D302 (PARIDE)*, Final Report NET/ITER Tasks T1, T2, T61, 20.12.1996.
- 191 J. Linke, R. Duwe, A. Gervash, W. Kühnlein, K. Nakamura, A. Peacock, M. Rödiger, *Pre-irradiation testing of actively cooled Be-Cu divertor modules*, Proceedings of the 2<sup>nd</sup> IEA International Workshop on Beryllium Technology for fusion, September 6-8, 1995, Jackson Hole, Wyoming.
- 192 ITER, *Material Assessment Report*, G A1 DDD 1 98-05-28 W 0.3.
- 193 G. Vieider, M. Merola, F. Anselmi, J.P. Bonal, P. Chappuis, G. Dell’Orco, D. Duglué, R. Duwe, S. Erskine, F. Escourbiac, M. Fèbvre, L. Giancarli, M. Grattarola, G. LeMarois, H.D. Pacher, A. Pizzuto, L. Plöchl, B. Riccardi, M. Rödiger, J. Schlosser, A. Salito, B. Schedler, C.H. Wu, *European development of prototypes for ITER high heat flux components*, Fusion Engineering and Design 49-50 (2000) 135-143.

- 194 R. Raffray, G. Federici, *RACLETTE: a model for evaluating the thermal response of plasma facing components to slow high power plasma transients. Part I: Theory and description of model capabilities*, Journal of Nuclear Materials 244 (1997) 85-100.
- 195 R. Raffray, G. Federici, *RACLETTE: a model for evaluating the thermal response of plasma facing components to slow high power plasma transients. Part II: Analysis of ITER plasma facing components*, Journal of Nuclear Materials 244 (1997) 101-130.
- 196 J. Linke, M. Akiba, H. Bolt, J. van der Laan, H. Nickel, E. van Osch, S. Suzuki, E. Wallura, *Simulation of disruptions on coatings and bulk materials*, Journal of Nuclear Materials 196-198 (1992) 607-611.
- 197 M. Rödig, R. Duwe, A. Gervash, A.M. Khomutov, J. Linke, A. Schuster, *Thermal shock tests with beryllium coupons in the electron beam facility JUDITH*, Proceedings of the 2<sup>nd</sup> IEA International Workshop on Beryllium Technology for fusion, September 1995, Jackson Lake Lodge, Wyoming.
- 198 M. Rödig, R. Duwe, J. Linke, R.H. Qian, A. Schuster, *Degradation of plasma facing materials due to severe thermal shocks*, Proceedings of the 17<sup>th</sup> IEEE/NPSS Symposium on Fusion Engineering, 06.-10.10.1997, San Diego.
- 199 J. Linke, R. Duwe, M. Merola, R.H. Qian, M. Rödig, A. Schuster, *Response of Beryllium to severe thermal shocks simulation of disruptions and vertical displacement events in future thermonuclear devices*, Proceedings of the 3<sup>rd</sup> IEA International Workshop on Beryllium Technology for fusion, October 1997, Mito, Japan.
- 200 J. Linke, R. Duwe, A. Gervash, R.H. Qian, M. Rödig, A. Schuster, *Material damage to Beryllium, Carbon and Tungsten under severe thermal shocks*, Proceedings of the ICFRM-8, October 26-31, 1997, Sendai, Japan.
- 201 M. Rödig, R. Duwe, J. Linke, A. Schuster, *High heat flux tests on Beryllium and Beryllium-Copper joints*, Fusion Engineering and Design 37 (1997) 317-324.
- 202 J. Linke, R. Duwe, W. Kühnlein, M. Rödig, *Thermal shock testing of plasma sprayed Beryllium*, FZJ Report IWE 1, IWE-TN 5/98.
- 203 UBSof for Windows ver. 1.9 UBM Messtechnik.
- 204 M. Rödig, R. Duwe, H. Hoven, W. Kühnlein, J. Linke, G. Pott, A. Schuster, E. Wallura, *Pre-Irradiation Characterisation of Be- and C-Based Materials for Plasma-Facing Components*, Final Report NET/ITER Tasks T1, T2, T61, IWE-TN 35/95, 18.12.1995.
- 205 A. Schuster, *Hochwärmeflußverhalten von Berylliummaterialen und -komponenten für zukünftige Fusionsreaktoren*, Dissertation, Rheinisch Westfälische Technische Hochschule Aachen, 1997.
- 206 Hassanein, D.A. Ehst, *Dynamic modeling of plasma-vapor interactions during plasma disruptions*, Journal of Nuclear Materials 196-198 (1992) 680-685.
- 207 S. Schiller, U. Heisig, S. Panzer, *Electron beam technology*, John Wiley & Sons, New York-Chichester-Brisbane-Toronto-Singapore.
- 208 J. Schou, *Electron emission from solid*, from W. O. Hofer, J. Roth, Physical Processes of the Interaction of Fusion Plasmas with Solids, pp. 269-304, Academic Press.
- 209 Vernon L. Bailey, Jr., *High energy electron beam interaction with materials*, Pulse Sciences, Inc., 600 McCormick St., San Leandro, CA.
- 210 A. Cardella, H. Gorenflo, A. Lodato, K. Ioki, R. Raffray, *Effect of plasma disruption events on ITER first wall plasma facing materials*, Proceedings of the 9<sup>th</sup> International Conference on Fusion Reactor Materials (ICFRM), Colorado Springs (USA), Oct. 10-15, 1999.
- 211 Mende, Simon, *Physik Gleichungen und Tabellen*.
- 212 V.S. Fomenko, *Handbook of thermionic properties: electronic work functions and Richardson constants of elements and compounds*, Plenum Press Data Division, New York 1966.

- 213 R.J. meyer, Hrsg., *Gmelin Handbuch der anorganischen Chemie: Be. Beryllium*, Deutsche Chemische Gesellschaft Berlin, Verlag Chemie Berlin, 8. Auflage, 1930.
- 214 I. Hinz, H.K. Kugler, J. Wagner, eds., *Gmelin handbook of inorganic chemistry*, volume A1 Be Beryllium Supplement The element. Production, Atom, Molecules, Chemical Behaviour, Toxicology, *System number 26*. Gmelin-Institut für Anorganische Chemie der Max-Planck-Gesellschaft zur Förderung der Wissenschaften, Springer-Verlag Berlin, 8<sup>th</sup> edition, 1986.
- 215 L. Berg, ed., *Gmelin handbook of inorganic and organometallic chemistry*, volume A2 Be Beryllium Supplement The Element. Thermal Properties *System number 26*. Gmelin-Institut für Anorganische Chemie der Max-Planck-Gesellschaft zur Förderung der Wissenschaften, Springer-Verlag Berlin, 8<sup>th</sup> edition, 1993.
- 216 *Gmelin handbook of inorganic and organometallic chemistry*, volume A3 Be Beryllium Supplement The Element. Physical Properties (Continued) and Electrochemistry *System number 26*. Gmelin-Institut für Anorganische Chemie der Max-Planck-Gesellschaft zur Förderung der Wissenschaften, Springer-Verlag Berlin, 8<sup>th</sup> edition, 1993.
- 217 J. Linke, H. Bolt, R. Duwe, W. Kühnlein, A. Lodato, M. Rödiger, K. Schöpflin, B. Wiechers, *High Heat Flux Simulation Experiments with Improved Electron Beam Diagnostics*, Journal of Nuclear Material 283-287 (2000) 1152-1156.
- 218 M. Rödiger, *Neutron-irradiation and post-irradiation testing of beryllium samples and Be/Cu mock-ups*, Final Report ITER-Task T221/1 (GB5) IWV2-TN 3/2000, 20.09.00.
- 219 M. Rödiger, R. Conrad, H. Derz, R. Duwe, J. Linke, A. Lodato, M. Merola, G. Pott, G. Vieider, B. Wiechers, *Neutron-irradiation effects on high heat flux components – examination of plasma-facing materials and their joints*, Journal of Nuclear Material 283-287 (2000) 1161-1165.
- 220 A.M. Hassanein, A. Konkashbaev, I. Konkashbaev, *Erosion of melt layers developed during a plasma disruption*, Proceedings of the 18<sup>th</sup> Symposium of Fusion Technology (SOFT), Karlsruhe, 22.-26.8.94.
- 221 A. Hassanein, G. Federici, I. Konkashbaev, A. Zhitlukhin, V. Litunovsky, *Material effects and design implications of disruptions and off-normal events in ITER*, Fusion Engineering and Design 39-40 (1998) 201-210.
- 222 Hassanein, D.A. Ehst, J. Gahl, *Beryllium and graphite performance in ITER during a disruption*, Journal of Nuclear Materials 212-215 (1994) 1272-1277.
- 223 A.M. Hassanein, *Disruption damage to plasma-facing components from various plasma instabilities*, Fusion Technology, 30 (1996) 713-719.
- 224 A.M. Hassanein, I. Konkashbaev, *Lifetime evaluation of plasma-facing materials during a tokamak disruption*, Journal of Nuclear Materials 233-237 (1996) 713-717.
- 225 A. Hassanein, I. Konkashbaev, *Performance and lifetime assessment of reactor wall and nearby components during plasma instabilities*, Journal of Nuclear Materials 258-263 (1998) 645-652.
- 226 A. Cardella, H. Gorenflo, A. Lodato, K. Ioki, R. Raffray, *Effect of Plasma disruption events on ITER first wall materials*, Journal of Nuclear Material 283-287 (2000) 1105-1110.
- 227 ANSYS Finite Element Code, Release 5.4.
- 228 I. Smid, H.D. Pacher, G. Vieider, U. Mszanowski, Y. Igitkhanov, G. Janeschitz, J. Schlosser, L. Plöchl, *Lifetime of Be-, CFC- and W-armoured ITER divertor plates*, Journal of Nuclear Materials 233-237 (1996) 701-707.
- 229 ITER Material Properties Handbook, ITER Doc. S 74 RE 1 78-08-01 W1.5.
- 230 P. Schiller, F. Brossa, M. Cambini, D. Quataert and G. Rigon, *Experimental evidence for melt layer convection during disruption simulation experiments*, Fusion Engineering and Design 6 (1988) 131-136.



- 231 A. Lodato, R. Duwe, H. Derz, J. Linke, M. Rödìg, *Properties of Beryllium as a high heat flux material before and after neutron irradiation*, Proc. 20<sup>th</sup> Symposium on Fusion Technology (SOFT), Marseille (France), Sept. 7-11, 1998.
- 232 J. Linke, G. Breitbach, R. Duwe, A. Gervash, M. Rödìg, B. Wiechers, *High heat flux performance of divertor modules for ITER with beryllium and carbon armour*, Proceedings of the 19<sup>th</sup> Symposium of Fusion Technology (SOFT), Lisbon, Portugal, 16.-20.09.1996.
- 233 ITER, *Material Assessment Report*, G A1 DDD 1 98-05-28 W 0.3.
- 234 A. Gervash, R. Giniyatulin, I. Mazul, R. Watson, *Beryllium armoured mockups for fusion high heat flux application*, Proceedings of 20<sup>th</sup> Symposium on Fusion Technology (SOFT), Marseille (France), Sept. 7-11, 1998.
- 235 G. Vieider, V. Barabash, A. Cardella, P. Chappuis, R. Duwe, H. Falter, M. Fèbvre, L. Giancarli, C. Ibbott, D.M. Jacobson, R. Jakeman, G. LeMarois, A. Lind, M. Merola, H.D. Pacher, A. Peacock, A. Pizzuto, L. Plöchl, B. Riccardi, M. Rödìg, S.P.S. Sangha, Y. Severi, E. Visca, *Overview of the EU small scale mock-up tests for ITER high heat flux components*, Fusion Engineering and Design 39-40 (1998) 211-218.
- 236 R. Giniyatulin, V. Komarov, I. Mazul, N. Yablokov, R. Watson, C. cadden, N. Yang, *Results of HHF tests and metallographic investigation of beryllium HHF mockups*, Proceedings of the 4<sup>th</sup> IEA International Workshop on Beryllium Technology for fusion, September 15-17, 1999, Karlsruhe, Germany.
- 237 A. Cardella, A. Lodato, H.D. Pacher, R.R. Parker, K. Ioki, G. Janeschitz, D. Lousteau, R. Raffray, M. Yamada, C. Gusic, *The ITER Port Limiter Design*, Fusion Engineering and Design, 43 (1998) 75-92.
- 238 M. Rödìg, R. Duwe, W. Kühnlein, J. Linke, A. Schuster, *Behaviour of Carbon and Beryllium under Thermomechanical loads*, Physica Scripta, Vol. T64, 60-66, 1996.
- 239 M. Rödìg, R. Duwe, J. Linke, A. Schuster, *High heat flux tests on Beryllium and Beryllium-Copper joints*, Fusion Engineering and Design 37 (1997) 317-324.
- 240 M. Rödìg, R. Duwe, J. Linke, A. Schuster, B. Wiechers, *Thermal fatigue tests with actively cooled divertor mock-ups for ITER*, ISFNT-4, Tokyo, April 6-11, 1997.
- 241 J. Linke, G. Breitbach, R. Duwe, A. Gervash, M. Rödìg, B. Wiechers, *High heat flux performance of divertor modules for ITER with beryllium and carbon armour*, Proceedings of the 19<sup>th</sup> Symposium of Fusion Technology (SOFT), Lisbon, Portugal, 16.-20.09.1996.
- 242 ANSYS Finite Element Code, Release 5.3.
- 243 ITER Material Properties Handbook, ITER Doc. S 74 RE 1 78-08-01 W1.5.
- 244 M. Merola, G. Vieider, L. Schlosser, U. Mszanowski, I. Smid, *EUPITER: the European thermohydraulic package for plasma facing components*, Proceedings of the specialist's workshop on High Heat Flux Cooling for ITER PFCs, JET, September 23-25, 1996.
- 245 M. Rödìg, *Neutron-irradiation and post-irradiation testing of beryllium samples and Be/Cu mock-ups*, Final Report ITER-Task T221/1 (GB5) IWV2-TN 3/2000, 20.09.00.
- 246 A. Lodato, M. Rödìg, R. Duwe, J. Linke, H. Derz, *High Heat Flux Components with Be Armour Before and After Neutron Irradiation*, Fusion Engineering and Design 49-50 (2000) 255-261.
- 247 C. Ibbott, H.D. Falter, P. Meurer, E. Thompson, M.J. Watson, G. Critchlow, D. Ciric, *Further developments in the brazing of beryllium to CuCrZr*, Proceedings of the 18<sup>th</sup> Symposium of Fusion Technology (SOFT), Karlsruhe, 22.-26.8.94.
- 248 A.T. Peacock, et al. Proceedings of 19<sup>th</sup> Symposium on Fusion Technology (SOFT), Lisbon (Portugal), September 16-20, 1996, p.415-418.

- 
- 249 M. Rödig, R. Duwe, J. Linke, A. Schuster, B. Wiechers, *Thermal cycling tests of actively cooled beryllium copper joints*, Proceedings of the 3<sup>rd</sup> IEA International Workshop on Beryllium Technology for fusion, October 1997, Mito, Japan.
- 250 M. Rödig, R. Duwe, J. Linke, A. Schuster, *Thermal cycling testing of an actively cooled Beryllium-Copper mock-up with CuMnSnCe braze*, Intermediate Report IWE1-TN 25/97, 16.12.1997.
- 251 M.A. Pick, A.D. Haigh, *Operational aspects of using Beryllium – Safety and decontamination*, Proceedings of the 2<sup>nd</sup> IEA International Workshop on Beryllium Technology for fusion, September 6-8, 1995, Jackson Hole, Wyoming.
- 252 M. Rödig, M. Akiba, P. Chappuis, R. Duwe, M. Febvre, A. Gervash, J. Linke, N. Litounovsky, S. Suzuki, B. Wiechers, D.L. Youchison, *Comparison of electron beam test facilities for testing of high heat flux components*, Fusion Engineering and Design 51-52 (2000) 715-722.
- 253 A. Hermann, *Optical surface measurement*, Diagnostics for Experimental Thermonuclear Fusion Reactors, Edited by P.E. Stott et al., Plenum Press, New York, 1996.
- 254 J. Linke, R. Duwe, A. Gervash, W. Kühnlein, K. Nakamura, A. Peacock, M. Rödig, *Pre-irradiation testing of actively cooled Be-Cu divertor modules*, Proceedings of the 2<sup>nd</sup> IEA International Workshop on Beryllium Technology for fusion, September 6-8, 1995, Jackson Hole, Wyoming.
- 255 H.D. Falter, D. Ciric, D.J. Godden, C. Ibbot, *High heat flux exposure tests on monoblocks brazed to a copper swirltube*, JET Joint Undertaking report JET-R(97)04, January 1997.
- 256 T. Floßdorf, *Scherversuche und metallographische Nachuntersuchungen an bestrahlten Be/Cu-Lotverbindungen aus BE PARIDE*, Forschungszentrum Jülich Internal Report ZFK/HZ-TN-16/99, October 1999.
- 257 F. Saint-Antonin, *Development and characterization of Be/Cu alloy HIP joints*, Note Technique D.E.M./S.G.M N 03/96, CEA, CEREM, Jan 1996.
- 258 ANSYS Finite Element Code, Release 5.4.
- 259 A. Cardella, *ITER Port Limiter Design*, ITER report no. G 16 MD 150 97-10-22 F1, Garching Germany.
- 260 A. Cardella, A. Lodato, *ITER Progress in the Limiter Design and Analysis*, ITER report no. G 16 RI 18 96-11-21 F1, Garching Germany 21-Nov.-1996.
- 261 *ITER Design Description Document (DDD)*, G 16 DDD 2 96-11-27 W0.2
- 262 *ITER General Design Requirements Document (GDRD)*, ITER S 10 GDRD 2 95-02-10 F1.0.
- 263 *ITER Material Properties Handbook*, Garching Germany.
- 264 H. D. Pacher, *Start-up Power Loads on ITER Optimised Port Limiters*, NET Internal Note N/I/3340/4/A, Oct. 1997.
- 265 A. Cardella, A. Lodato, *Electromagnetic Analysis of Port Limiter*, ITER memo, G16 RI 19 97-05-27 F1, Garching Germany.
- 266 M. Roccella, *Estimate of the EM Loads on the Shielding Blanket Modules and on the Port Limiter Assuming Port-Limiter Structure*, ENEA, Frascati, Italy, October 1997.

# ACKNOWLEDGEMENTS

In the period from the 1<sup>st</sup> February 1997 to the 31<sup>st</sup> January 2000 under the auspices of the European Commission and within the framework of the Community Fusion Programme in my capacity as holder of a Marie Curie Research Training Grant (proposal No. ERB4001GT96-1842) I was temporarily assigned as a scientific member of the ITER (International Thermonuclear Experimental Reactor). As Grant Holder I carried out the Project "Assessment and experimental verification of the plasma facing components for a thermonuclear experimental reactor". The collection and description of the results of the work carried out in the frame of this project constitute the subject-matter of the present thesis.

As during this period I have been dealing with different challenging topics, I availed myself of the detailed, particularized and circumstantial advice of academics and technicians. I am really grateful to all of them for their enthusiasm, constant patience and generous contribution of time and effort in discussion, insight and suggestions, which have made my doctoral study and research a rewarding experience filled with possibilities for professional growth.

I would like to thank Prof. Dr. rer. nat. F. Schubert for his constant interest in my studies, for caring of my thesis and for taking over the first report.

I would like to acknowledge Univ.-Prof. Dr.-Ing. L. Singheiser for the possibility he gave to me of performing my experimental work at the Institut für Werkstoffe und Verfahren der Energietechnik (IWV 2), Forschungszentrum Jülich, and for taking over the second report.

I am especially indebted to Dr. M. Rödiger and Dr. J. Linke for their advice, encouragement and support, which was of utmost importance during this period, and for their generous contribution of time in valuable discussions.

I would like to express my special thanks to Dr. V. Barabash, whose expertise in nuclear engineering materials made him the best technical consultant.

I would like to acknowledge Dr. M. Merola for the useful discussions and valuable suggestions, which helped me a lot in the wording of my thesis.

My gratitude is extended to Dr. A. Cardella for the knowledge of fusion technology, which I learned from him during the period I was temporarily assigned as scientific member of ITER. I appreciated the opportunity to participate in the work on design of plasma facing components, which made my thesis work more valuable.

I would like to acknowledge the precious assistance of Dr. R. Duwe, H. Klöcker, W. Kühnlein and H. Münstermann in the electron beam experiments and Mrs. G. Gutzeit, who helped me by collecting data during the period I was not in Jülich.

Thanks also to present and recent past members of ITER and EFDA research groups for the technical discussion and for sharing experiences and companionship.

I would like to extend my thanks to my friend Dr. C. Fuchs and to the colleagues of the Forschungszentrum Jülich, who helped me in solving many technical problems.

Forschungszentrum Jülich



Jül-3908  
September 2001  
ISSN 0944-2952